

The Evolution of Early-Type Galaxies



Laura J. Prichard
Christ Church
University of Oxford

A thesis submitted for the degree of
Doctor of Philosophy
Hilary 2018

Declaration

The work presented in this thesis was carried out by me at the Sub-department of Astrophysics, University of Oxford between October 2014 and March 2018 under the supervision of Professor Roger Davies. My research was funded by a Hintze Scholarship, awarded by the Oxford Hintze Centre for Astrophysical Surveys which is funded through generous support from the Hintze Family Charitable Foundation. I hereby declare that no part of this thesis has been submitted in support of another degree, diploma or other qualification at the University of Oxford or elsewhere. Except where otherwise stated or explicit reference to the work of others is made, the work contained in this thesis is entirely my own.

Work presented in Part I of this thesis was carried out as part of the guaranteed observing time programme: The K-band Multi-Object Spectrograph (KMOS) Cluster Survey (KCS). Part I of the thesis (Chapters 2, 3 and 4) is based on work that was peer-reviewed and published in Prichard, L. J. et al., 2017, ‘*The KMOS Cluster Survey (KCS) III: fundamental plane of cluster galaxies at $z \simeq 1.80$ in JKCS 041*’, *Astrophysical Journal*, 850, 203, of which I am the lead author. Research in Part I was based on observations obtained at the Very Large Telescope of the European Southern Observatory (ESO), Paranal, Chile (ESO programme IDs: 095.A-0137(A) and 096.A-0189(A)). The pipeline for the reduction of the KCS data was written by J. Trevor Mendel but the reduction of the data was performed by me. Part II of this thesis is in preparation for submission to the *Monthly Notices of the Royal Astronomical Society*.

The copyright of this thesis rests with its author. No quotation or information derived from it may be published without the prior consent and acknowledgement of its author.

Laura J. Prichard
(March 2018)

The Evolution of Early-Type Galaxies

Laura J. Prichard
Christ Church
University of Oxford

A thesis submitted for the degree of
Doctor of Philosophy
Hilary 2018

Abstract

Early-type galaxies (ETGs) are typically thought of as ‘red and dead’ with little to no star formation and old stellar populations. Their detailed kinematics measured locally suggest an interesting array of formation mechanisms and high-redshift observations are starting to reveal a two-phase evolutionary path for the most massive galaxies. In this thesis, I take a combined approach to studying the formation ETGs. I look to distant quiescent galaxies in one of the densest regions of the early Universe and at the fossil record of a local galaxy to shed light on some of the unsolved mysteries of how ETGs evolved. Using the unique multiplexed instrument, the K-band Multi-Object Spectrograph (KMOS), the evolution of galaxies at both low and high redshift were studied as part of this thesis. I maximised the capabilities of this multi-integral field unit (IFU) near-infrared (NIR) instrument to study different aspects of ETG evolution. With 24 separate IFUs, many quiescent galaxies were efficiently observed in a massive high-redshift cluster as part of the KMOS Cluster Survey. Coupling KMOS spectroscopy with *Hubble Space Telescope* photometry, I studied the ages, kinematics, and structural properties of the galaxies. I then analysed the detailed properties of a massive local ETG with interesting kinematics, IC 1459. Coupling the NIR IFU data from KMOS with a large mosaic of optical data from the Multi-Unit Spectroscopic Explorer, I was able to study the spatially resolved kinematics, stellar populations, and initial mass function of the galaxy. The work presented in this thesis provides some interesting clues as to the formation of ETGs and possible diversity of their evolutionary paths.

For my parents, Helena and Guy

Acknowledgements

Firstly, my sincere and extensive gratitude is given to my supervisor, Professor Roger Davies, for giving me the opportunity to work with you and believing in me throughout this process. You have steered me through some difficult times with the utmost patience and none of this work would have been possible without you. Thank you for your support, mentorship, and insight that has continued to fuel my passion for understanding the Universe. I am thankful for the collaboration, enjoyable meetings with, and help of the entire KMOS Cluster Survey team. I am also extremely grateful to the attendees of *Black Hole Lunch* throughout the course of my DPhil that have provided valuable research insights and good chats about all things. Thanks also to my first supervisor, Professor Raja Guhathakurta, for providing exciting opportunities that started me on my research path in astronomy and for remaining supportive of my career.

Where would I be without the incredible women who have carved the path as scientists along which I walk? Much work is still left to be done to improve diversity in astronomy and academia. I am thankful for the persistence, courage and brilliance of the women who have come before me and I intend to strive to support people from all walks of life who come after me. Thank you to the Oxford Women in Physics Society that are working towards inclusivity and to the incredible women I have met through it. Particular thanks to women involved in the earlier stages of my career, Mrs Catherine Stevens, Professor Paola Caselli, and Dr Alis Deason, for being great examples of women in science and providing the role models I needed to keep climbing to the next step.

Being in Oxford these past few years has not all been easy but has been made unforgettable by some of the incredible people I have met while here. I thank my housemates: Bartie for providing a beautiful home and stability when I needed it most, Riggas (and Sarah) for planning a wedding four days before handing in my thesis to give me great motivation to get it done, and both for all the dinner parties I could have ever hoped for. I am thankful to the other DPhil students, postdocs (particularly the coffee crew), and professors that have made working in this department so enjoyable and when things got tough, providing unfailing support, distraction and pints. My eternal thanks go to Ashling for organising pretty much every aspect of my time here as a student, incredible support, hilarity and mutual love of terrible TV. Office 650 residents past and present – thank you for putting up with me at the worst of times and providing ample opportunity for procrastination and laughs.

Particular mention goes to the incredible friendship of Becky, Marisa, and Josie; I am proud to call you all friends and am so grateful for everything you have done for me. Becky thank you for putting a roof over my head when I was in need, for amazing adventures in Mexico, and for radiating a positivity and energy that I didn't know was humanly possible.

Thanks to my Nonversation, Rally, Squad, and UC Santa Cruz (go Banana Slugs!) friends. Thanks to Helen (who I am so grateful to have met in Santa Cruz), James, Caro, Ettie, Cécile, Amelie, Emily, Harry, and Jo for their visits to Oxford. Special thanks goes to the friendship of my wonderful girls from home and those who have joined over the years (in alphabetical order): Brit, Daisy, Ellie, Frankie, Hannah, Krissy, and Yaz. Thanks for showing me the meaning of loyalty, love, and friendship. Thank you for making me feel valued and for the most incredible memories which we continue to make.

As the late Professor Stephen Hawking put well – *“It would not be much of a universe if it wasn't home to the people you love.”* I acknowledge the love and support of my amazing family; the Universe cannot know the bounds of my love for you. Thanks to my wonderful aunties, uncles and cousins for the memorable occasions, meals, and respite that has got me through some difficult times. To the pillars of my creation – my four diverse and inspirational grandparents: Noreen, and the much-missed Godfrey, Fran and Pat. To my best friend and sister Jo, I would be nowhere without you; thank you for making me laugh more than any other person can. And to my parents to whom this thesis is dedicated, thank you for making me believe that anything I wanted to achieve was within my grasp. Thank you to my father Guy, for your support, love and pride that has seen me through my DPhil. Finally, I acknowledge my proof reader (thanks as I know you are reading this too!) and loving mother Helena. Thank you for being the true definition of strength, dedication and support that has inspired me in everything I have done. I could not have gone through this journey without you there by my side.

“We have peered into a new world and have seen that it is more mysterious and more complex than we had imagined. Still more mysteries of the universe remain hidden. Their discovery awaits the adventurous scientists of the future. I like it this way.”

— Vera Rubin, *Bright Galaxies, Dark Matters*, 1997

Contents

1	Introduction	3
1.1	Background	3
1.1.1	Classifying Galaxies	4
1.1.2	The Classes of Early-Type Galaxies	6
1.1.3	Hierarchical Formation of the Universe	8
1.1.4	Galaxy Evolution in Different Environments	10
1.1.5	Properties of High-Redshift Galaxies	12
1.1.6	The Initial Mass Function	13
1.1.7	Stellar Population Models	15
1.1.8	Possible Evolutionary Paths of ETGs	16
1.1.9	Open Questions About the Evolution of ETGs	17
1.1.10	The K-band Multi-Object Spectrograph	18
1.2	Introduction to Work Presented in this Thesis	19
1.2.1	Part I – The KMOS Cluster Survey: Fundamental Plane of Cluster Galaxies at $z \simeq 1.80$ in JKCS 041	20
1.2.2	Part II – Unravelling the Origin of the Counter-Rotating Core in IC 1459 with KMOS and MUSE	22
1.3	Chapter Summary	25
2	KMOS Data and Spectroscopic Analysis of Galaxies in JKCS 041	30
2.1	The KMOS Instrument	30
2.1.1	Atmospheric Contamination in the NIR	33
2.2	The KMOS Cluster Survey	34
2.2.1	Overview	34
2.2.2	KCS Target Clusters	36
2.2.2.1	JKCS 041 at $z = 1.80$	36
2.2.2.2	Cl 0332-2742 (Cl0332) at $z = 1.61$	39
2.2.2.3	XMMXCS J2215.9-1738 (XMM2215) at $z = 1.46$	39

2.2.2.4	XMMU J2235.3-2557 (XMM2235) at $z = 1.39$	40
2.2.2.5	RCS 2345-3632 (RCS2345) at $z = 1.04$	40
2.2.3	Status and Results of KCS	42
2.2.3.1	Observing Summary	42
2.2.3.2	Summary of Beifiori et al. (2017)	43
2.2.3.3	Summary of Chan et al. (2016, 2018)	46
2.3	KMOS Data of JKCS 041	47
2.3.1	Sample Selection	47
2.3.2	Completeness	48
2.3.3	KMOS Target Selection	50
2.3.4	KMOS Observations	55
2.4	Data Reduction	55
2.5	Data Analysis	59
2.5.1	Cross-Correlation of KMOS Spectra	59
2.5.2	Stellar Kinematics	59
2.5.2.1	Template Spectra	59
2.5.2.2	Fitting Procedure	62
2.5.2.3	Properties of the Spectra	63
2.5.2.4	Correcting Velocity Dispersions	70
2.5.2.5	Uncertainties of the Kinematic Fits	70
2.5.3	KMOS Redshifts	74
2.5.4	Dynamical Masses	74
3	HST Data and Photometric Analysis of Galaxies in JKCS 041	76
3.1	The <i>Hubble Space Telescope</i>	76
3.2	Photometric Data	77
3.2.1	Newman et al. (2014) Reduction and Analysis	78
3.3	Reduction of Photometry	80
3.3.1	Retrieval and Quality Checking of Images	80
3.3.2	Aligning the Images	81
3.3.3	Running ASTRODRIZZLE	83
3.3.4	Sky Subtraction	83
3.3.5	Weight and RMS Maps	85
3.3.6	Calibrating the WCS	88
3.3.7	Derivation of the PSF	88
3.4	Photometric Analysis	90

3.4.1	GALAPAGOS Overview	90
3.4.2	Setting Up GALAPAGOS	93
3.4.2.1	SEXTRACTOR Setup	94
3.4.2.2	Sky Estimation Setup	96
3.4.2.3	Galaxy Fitting Setup	98
3.4.3	Summary of Derived Properties	101
3.4.4	Uncertainties on Light-Weighted Photometric Parameters	103
3.4.5	Comparison of Derived Photometric Parameters	107
3.5	K -Corrections	109
3.6	Light-Weighted Stellar Masses	111
4	Fundamental Plane for Galaxies in JKCS 041 and its Implications	114
4.1	Fundamental Plane	114
4.1.1	Derivation of FP Ages	117
4.2	Structural Evolutionary Effects on the FP Zero-Point Evolution	119
4.2.1	FP Zero-Point and Luminosity Evolution	119
4.2.2	Mass-Sigma and Mass-Size Relations for JKCS 041	120
4.2.3	Effects of Structural Evolution on FP Ages	123
4.3	Overdensity Structure, Dynamics, and Ages in 3D	125
4.3.1	Structure of JKCS 041	125
4.3.2	Overdensity Dynamics	127
4.3.3	Galaxy Ages	129
4.4	Discussion	130
4.4.1	Absorption-Line Spectroscopy at $z \gtrsim 1.80$	130
4.4.2	Comparison of Ages for JKCS 041	130
4.4.3	Comparison of FP Ages to Other KCS Overdensities	131
4.4.4	Structure and Evolution of JKCS 041	132
4.4.5	Speculation on the Lives of the Most Massive ETGs	134
4.5	Conclusions	135
5	KMOS and MUSE Data and Analysis of IC 1459	139
5.1	Mosaic Data	139
5.1.1	KMOS Data	139
5.1.1.1	KMOS Observations	139
5.1.1.2	KMOS Data Reduction	142
5.1.2	MUSE Data	146
5.1.2.1	Overview of MUSE	146

5.1.2.2	MUSE Observations	146
5.1.2.3	MUSE Cube Preparation	146
5.1.3	Telluric Correction	149
5.2	Data Analysis	151
5.2.1	Mosaic Kinematics	151
5.2.1.1	Voronoi Binning	151
5.2.1.2	Spectral Fitting Templates	152
5.2.1.3	Deriving the Kinematics	153
5.2.1.4	Kinematic Maps	154
5.2.2	Extracting Average Spectra	161
5.2.3	Spatially Resolved Stellar Populations	164
5.2.3.1	Uncertainties on the Stellar Population Parameters	169
5.2.4	Spatially Resolved IMF	170
5.3	Discussion	172
5.3.1	Kinematics of IC 1459	172
5.3.2	Stellar Populations of IC 1459	174
5.3.3	Results from Orbital Modelling of KDCs	175
5.3.4	The Profile of the Counter-Rotating Core	177
5.3.5	Spatially Resolved IMF in IC 1459	178
5.3.6	The AGN and Gas Content	179
5.3.7	Possible Formation Mechanisms of IC 1459	180
5.4	Conclusions	184
6	Conclusions	186
6.1	Summary of this Thesis	186
6.1.1	Part I – The KMOS Cluster Survey: Fundamental Plane of Cluster Galaxies at $z \simeq 1.80$ in JKCS 041	187
6.1.2	Part II – Unravelling the Origin of the Counter-Rotating Core in IC 1459 with KMOS and MUSE	188
6.2	Future Work	190
6.2.1	Full-Spectral Fitting of Individual Galaxies in JKCS 041	190
6.2.2	A Different Approach to Full-Spectral Fitting of IC 1459	191
6.2.3	Emission-Line Analysis of IC 1459	191
6.2.4	Future Facilities	192
	Bibliography	193

List of Figures

1.1	Hubble’s ‘tuning fork’ morphological classification scheme	4
1.2	Galaxy colour-magnitude diagrams	5
1.3	The ATLAS ^{3D} ‘comb’ morphological classification scheme	7
1.4	Classifications of ETGs from integral field spectroscopy	7
1.5	Millennium cosmological dark matter simulation	9
1.6	Morphology-density relation for galaxies	11
1.7	Different forms of the initial mass function	14
1.8	Images of IC 1459	24
2.1	KMOS arms and spectrographs	32
2.2	Block diagram of KMOS	33
2.3	Figure of JKCS 041 from Newman et al. (2014)	37
2.4	Four KCS target clusters	41
2.5	KCS cluster mass figure from Beifiori et al. (2017)	44
2.6	Colour-magnitude diagram for JKCS 041 galaxies	47
2.7	HST H_{160} -band image and KCS target galaxies in JKCS 041	49
2.8	Hubble Legacy Archive search and image display	52
2.9	KMOS ARM Allocator configuration for JKCS 041 observations	54
2.10	Galaxy HST image and segmentation map postage stamps	57
2.11	Spectral resolution comparison for KMOS and template libraries	61
2.12	KCS spectra and kinematic fits to quiescent galaxies in JKCS 041 with measured stellar velocity dispersions and velocities	64
2.13	KCS spectra and kinematic fits to quiescent galaxies in JKCS 041 with measured velocities	66
2.14	KCS spectra of star-forming galaxies in JKCS 041	67
2.15	Velocity histograms of bootstrapped spectra of galaxies in JKCS 041	72
2.16	Velocity dispersion histograms of the bootstrapped spectra	73
3.1	Diagram of the Drizzle algorithm mechanism	79

3.2	Raw HST frames and data quality arrays with masking of a ‘hot stripe’	82
3.3	Sky mask from GALAPAGOS-2.2.5B of the HST image of JKCS 041	86
3.4	Error maps of HST images derived in ASTRODRIZZLE	87
3.5	Reduced and calibrated HST images of JKCS 041	89
3.6	Segmentation map of HST image produced in SExtractor	91
3.7	Sky estimation method of GALAPAGOS-2.2.5B	92
3.8	Deriving parameters to determine stars in images for GALAPAGOS	98
3.9	Photometric fits to candidate and member galaxies of JKCS 041	100
3.10	Empirical noise relations derived from the HST images	104
3.11	Results from simulations to derive photometric uncertainties	106
3.12	Comparison of Sérsic indices derived for JKCS 041	107
3.13	Comparison of derived photometric parameters of JKCS 041	108
3.14	K -correction relations derived from models	110
3.15	M_*/L -colour relation for deriving light-weighted stellar masses	112
4.1	Fundamental plane for galaxies in JKCS 041	115
4.2	Relative M/L evolution for galaxies in JKCS 041	117
4.3	Relative M/L evolution for high-mass galaxies in JKCS 041	118
4.4	Mass-velocity dispersion and mass-size relations for JKCS 041 galaxies	121
4.5	Spatial extent and relative velocities of galaxies in JKCS 041	126
4.6	Relative velocity phase-space diagram and histogram	128
4.7	Relative M/L evolution for different galaxy groups of JKCS 041	129
4.8	Comparison of M_{dyn} and M_*^{tot} values	133
5.1	KMOS arms in ‘Mosaic Mode’ arrangement	140
5.2	Median images of three KMOS mosaics of IC 1459	141
5.3	Median image of the MUSE mosaic of IC 1459	147
5.4	MOLECFIT model to a median KMOS spectrum of IC 1459	150
5.5	MUSE relative velocity maps of IC 1459	155
5.6	MUSE velocity dispersion maps of IC 1459	157
5.7	KMOS relative velocity maps of IC 1459	159
5.8	KMOS velocity dispersion maps of IC 1459	160
5.9	Median MUSE and KMOS spectra of three radial bins of IC 1459	162
5.10	Deriving stellar population parameters from MUSE spectra with PPXF	165
5.11	Stellar populations derived from PPXF with regularization of one	167
5.12	Full-spectral fit of median IC 1459 KMOS spectra to measure the IMF	171
5.13	Volumes occupied by orbital families in a triaxial system	176

Acronyms

ΛCDM	Λ cold dark matter	GAIA	Graphical Astronomy and Image Analysis Tool
ADU	Analog-Digital Unit	GALAPAGOS	Galaxy Analysis over Large Areas: Parameter Assessment by GALFITting Objects from Source Extractor
AGN	Active galactic nuclei	GDAS	Global Data Assimilation System
BaSTI	Bag of Stellar Tracks and Isochrones	GMASS	Galaxy Mass Assembly ultra-deep Spectroscopic Survey
BCG	Brightest cluster galaxy	GTO	Guaranteed time observations
BH	Black hole	GUI	Graphical user interface
CANDELS	Cosmic Assembly NIR Deep Extragalactic Legacy Survey	HLA	Hubble Legacy Archive
CMD	Colour-magnitude diagram	HST	<i>Hubble Space Telescope</i>
DEIMOS	DEep Imaging Multi-Object Spectrograph	IC	Index Catalogue
DM	Dark matter	ICM	Intracluster medium
DQ	Data quality array	IFU	Integral field unit
EDisCS	ESO Distant Clusters Survey	IMF	Initial mass function
EG	Eastward-extending group (of JKCS 041)	IR	Infrared
E-MILES	Extended-MILES	ISM	Interstellar medium
ERR	Error map	IVM	Inverse variance map
ESO	European Southern Observatory	JWST	James Webb Space Telescope
ESOREX	ESO Recipe Execution	KARMA	KMOS ARM Allocator
ETG	Early-type galaxy	KCS	KMOS Cluster Survey
FITS	Flexible Image Transport System	KDC	Kinematically decoupled core
FORS2	FOcal Reducer and low dispersion Spectrograph	KMOS	K-band Multi-Object Spectrograph
FOV	Field of view		
FP	Fundamental plane		
FWHM	Full width half maximum		

KROSS KMOS Redshift One Spectroscopic Survey
LEDA Lyon-Meudon Extragalactic Database
LTG Late-type galaxy
MAD Median absolute deviation
MAST Mikulski Archive for Space Telescopes
MCMC Monte Carlo Markov Chain
MILES Medium-resolution Isaac Newton Telescope Library of Empirical Spectra
M/L Mass-to-light ratio
MP Mass plane
MPE Max-Planck Institute for Extraterrestrial Physics
MUSE Multi-Unit Spectroscopic Explorer
NGC New General Catalogue
NIR Near-infrared
NMBS National Optical Astronomy Observatory Extremely Wide-Field Infrared Imager (NEWFIRM) Medium Band Survey
OB Observing Block
PPMXL Position and Proper Motion Extended-L
PPXF Penalised PiXel-Fitting
PSF Point spread function
RMS Root mean squared
ROSAT ROentgen SATellite
SAURON Spectrographic Areal Unit for Research on Optical Nebulae
SED Spectral energy distribution
SExtractor Source Extractor
SF Star forming
SFH Star formation history
SFR Star formation rate
SMBH Supermassive black hole
S/N Signal to noise
SNR Signal-to-noise ratio
SPARK Software Package for Astronomical Reductions with KMOS
SPT South Pole Telescope
SSP Simple stellar population
STD Standard deviation
SWG South west group (of JKCS 041)
UT Unit Telescope
UV Ultraviolet
UVIS Ultraviolet-visible channel
VIRIAL VLT IR IFU Absorption Line
VLT Very Large Telescope
WCS World Coordinate System
WFC3 Wide-Field Camera 3
XMM *X-ray Multi-Mirror Mission*

Chapter 1

Introduction

1.1 Background

A vast conceptual leap in our understanding of the Cosmos came from Immanuel Kant's notion that nebulous emission sources in the sky were 'island universes'. This greatly expanded the perceived horizon of our Universe beyond the gravitationally bound collection of stars that make up our own galaxy, the Milky Way (see e.g., [Binney & Merrifield, 1998](#)). Extensive efforts to map the heavens throughout the 1800s (particularly by Caroline and William Herschel), led to the compilation of the *New General Catalogue* (NGC) and *Index Catalogue* (IC) that are still used today ([Dreyer, 1888, 1895](#)). The observations revealed different types of spiral and featureless nebulae but the confirmation of their extragalactic nature came later. Using the knowledge that Cepheid variable stars could be used as distance indicators ([Leavitt, 1908](#)), [Hubble \(1922\)](#) determined a distance to our massive spiral galaxy neighbour, Andromeda (M31), confirming it was a massive and separate Galactic-like system.

As telescopes and technology have improved, our horizons have expanded, and our picture of the Universe becomes more complex. Ever increasingly large surveys have revealed the importance of understanding galaxies to be able to explain the nature of our Universe from the largest to the smallest scales we deal with as astronomers. Galaxies live in the densest regions of the Universe and act as beacons to trace the large-scale structure of the cosmic web. The formation of galaxies helps us to understand how the stars within them have formed, and ultimately the myriad planetary systems that are being revealed around most stars (e.g., [Borucki et al., 2010](#)). It is clear that understanding how galaxies evolve both on cosmological scales and in detail locally is of vital importance to our understanding of the Universe in its current form and its ~ 13.8 billion-year history ([Planck Collaboration et al., 2016b](#)).

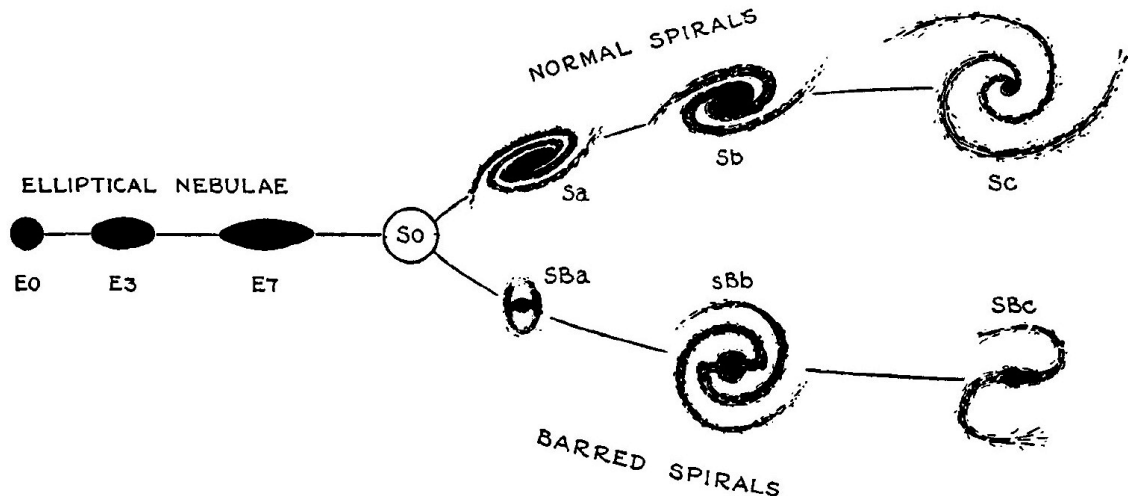


Figure 1.1: The ‘tuning fork’ morphological classification scheme of galaxies devised by [Hubble \(1926\)](#). The ellipticals and S0 galaxies form the ETGs, while galaxies that exhibit spiral arms on the right are LTGs. See Section 1.1.1.

1.1.1 Classifying Galaxies

Continuing his work on understanding galaxies, [Hubble \(1926\)](#) used photographic plates to derive a morphological classification scheme (the ‘tuning fork’ shown in Figure 1.1). Since the classification of galaxies onto the ‘Hubble sequence’, questions have arisen as to how the different types of systems evolved and what determined the distribution of morphological types in the local Universe. In the range of morphological types, smooth ellipticals and S0s are ‘early-type’ galaxies (ETGs) that typically contain older stars, very little dust and gas, and thus have mostly ceased star formation (i.e. ‘quenched’). This ‘red and dead’ population of passive galaxies typically occupy a very narrow region of a galaxy colour-magnitude diagram (CMD; shown in Figure 1.2) termed the ‘red sequence’. On the other end of the scale, complex disc-like ‘late-type’ galaxies (LTGs) are rich in gas and dust and actively star forming (SF). These galaxies are much bluer due to the light given out by young massive stars and they occupy a much broader ‘blue cloud’ on the galaxy CMD (Figure 1.2).

Morphological classifications can be quantified via the definition of various structural parameters. Galaxy brightnesses in different photometric bands (magnitudes), colours (derived from differences in the magnitudes), sizes (often used is their effective radius, R_e , i.e. the radius of the half-light isophote of a galaxy), and profile shapes are used to distinguish their properties. Disc galaxies are well described by exponential light profiles while ETGs are generally well described by a [Sérsic \(1963\)](#) profile with

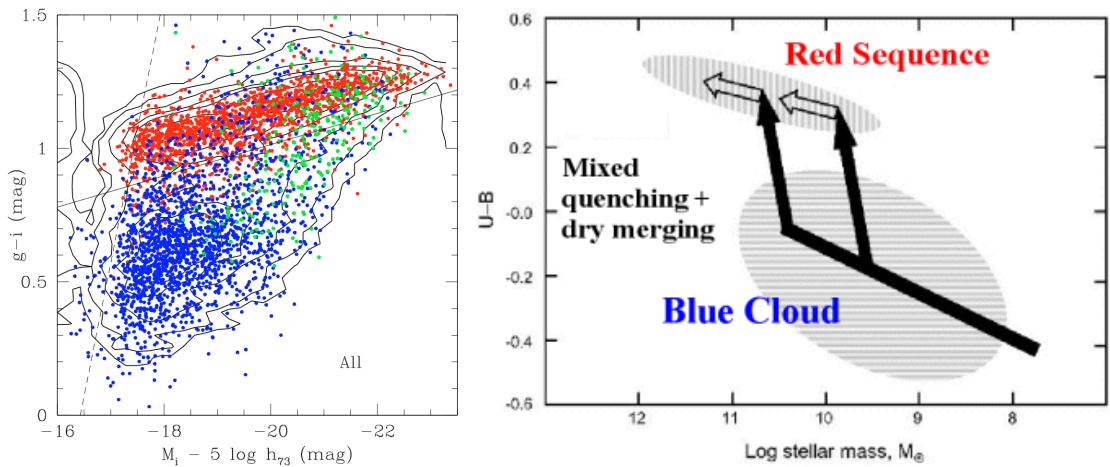


Figure 1.2: Examples of two galaxy CMDs highlighting the narrow ‘red sequence’ of ETGs and ‘blue cloud’ of LTGs. *Left*: Data of the Coma Supercluster from the Sloan Digital Sky Survey (Gavazzi et al., 2010). The galaxies are colour coded as ETGs (red), LTGs (blue), and bulge dominated discs (green). *Right*: Cartoon galaxy CMD (Faber et al., 2007) where mass has been used as a proxy for magnitude on the x -axis and is in the opposite direction to the left panel. The cartoon shows the SF blue cloud and the passive and narrow red sequence. The black arrows show possible evolutionary tracks across the diagram for galaxies. See Section 1.1.1.

different indices (n) that denote the profile curvature.

The spectra of galaxies can be used to measure kinematics, chemical composition, and stellar properties. Spectra of the broad categories of ETGs and LTGs have different purposes for understanding galaxy evolution. LTGs typically have gas-rich disc-like morphologies that are rotationally supported; their spectra can be used to derive rotational velocities (e.g., Binney & Tremaine, 1987). LTGs are typically SF and this will be shown in their spectra by emission arising from the ionized gas around newly formed stars. These bright emission features can be used to measure the star formation rate (SFR) of the galaxy and the metallicity of its gas. The kinematics of ETGs are typically thought of as being dominated by velocity dispersion (e.g., Binney & Tremaine, 1987). As ETGs have little to no SF, their spectra are mostly composed of stellar light. Stars typically show absorption features in their spectra due to atoms in their cooler upper atmospheres absorbing photons emitted from their surfaces. These spectra can therefore be used to study the properties and kinematics of the stellar populations within the galaxy.

Combining the observed photometric and spectroscopic parameters of galaxies has proved a valuable tool in the study of their evolution. There exist a number of scaling relations of LTGs and ETGs that can be used to derive distances and ages of galaxies

(e.g., Faber & Jackson, 1976; Tully & Fisher, 1977; Kormendy, 1977; Djorgovski & Davis, 1987). One of these scaling relations for ETGs is the fundamental plane (FP; Djorgovski & Davis, 1987; Dressler et al., 1987; Jørgensen, Franx & Kjaergaard, 1996). The FP describes the correlation between the size (e.g. R_e), surface brightness and stellar velocity dispersion. The FP zero point is known to be strongly redshift dependent (e.g., van Dokkum & Franx, 1996; van Dokkum & van der Marel, 2007; Holden et al., 2010). If one imagines a simple stellar population (SSP) of stars that is formed at the same time with some initial mass function (IMF), then if left to evolve in isolation, this population will become fainter and redder as the young hot blue stars die earlier. The observed effect is the change in the surface brightness, i.e. mass-to-light ratio (M/L), that drives the shift in the FP zero point as the stars age. Despite this model’s simplicity (requiring the assumption that ETGs are a uniform population), the FP can be a powerful tool for understanding the evolution of galaxies.

1.1.2 The Classes of Early-Type Galaxies

A revolution in our understanding of how galaxies formed came from integral field spectroscopy. Integral field unit (IFU) instruments provide a three-dimensional view of a galaxy whereby for every spatial pixel across the surface of a galaxy, a whole spectrum of light is observed. This is useful for the study of ETGs in that the spatially resolved stellar kinematics and population properties can be measured. Surveys of local ETGs with IFUs revealed a complex picture of the properties of the relatively photometrically featureless galaxies. The Spectrographic Areal Unit for Research on Optical Nebulae (SAURON; Bacon et al., 2001) survey of 48 nearby ETGs (de Zeeuw et al., 2002) revealed that they could be split into two distinct groups. The classes were ‘regular rotators’ – those with disc-like rotation, and ‘irregular rotators’ – those with an interesting array of irregular kinematics (Emsellem et al., 2004). Due to their angular momentum these galaxy classes are often termed ‘fast rotators’ (regular) and ‘slow rotators’ (irregular; Emsellem et al., 2007; Cappellari et al., 2007).

The larger, volume-limited ATLAS^{3D} survey (Cappellari et al., 2011a) confirmed the striking distinction between the two types of ETGs. This led to the proposed revision to Hubble’s classic tuning fork classification scheme in the form of the ‘comb’ (shown in Figure 1.3; Cappellari et al., 2011b). The two ETG classes present a dichotomy and there is not a smooth variation of parameters between them (see Cappellari, 2016, for a review). The fast rotators form a parallel sequence with spiral galaxies and are typically of masses below $M_{\text{crit}} \approx 2 \times 10^{11} M_{\odot}$. The slow rotators are

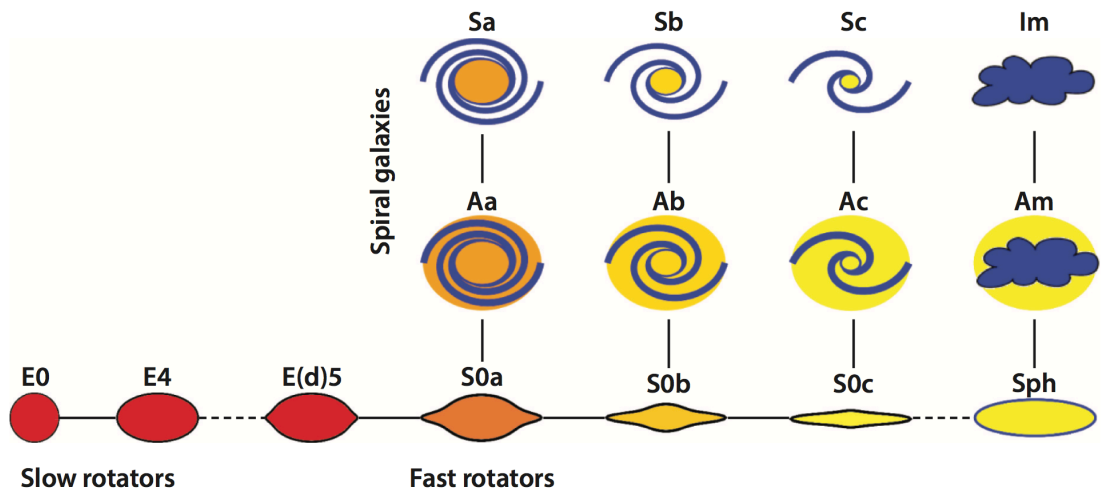


Figure 1.3: The ‘comb’ morphological classification scheme (figure from Cappellari, 2016) proposed as part of the ATLAS^{3D} survey (Cappellari et al., 2011a) as a revision of the classical Hubble tuning fork (Figure 1.1; Hubble, 1926). The galaxies are split into the classical ETG (along the bottom) and LTG (teeth of the comb at the top) morphologies. The ETGs are then split into the slow rotator and fast rotator classifications as a result of the distinct irregular and regular disc-like kinematics (respectively) measured from integral field spectroscopy (Emsellem et al., 2007; Cappellari et al., 2007). See Section 1.1.2.

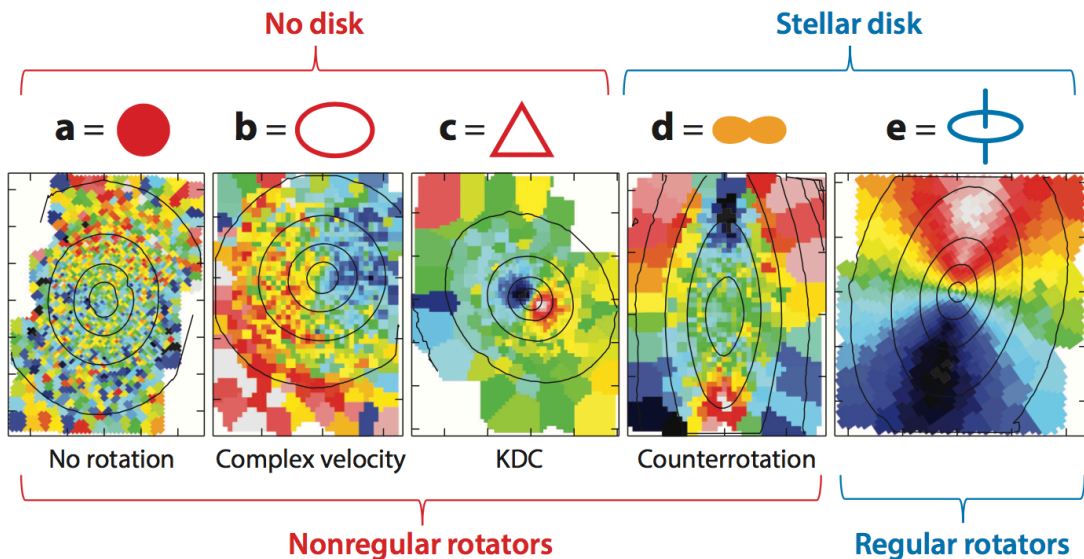


Figure 1.4: Figure from Cappellari (2016) depicting typical examples (taken from Emsellem et al., 2004) of classes and sub-classes of ETG. ETGs are split into nonregular ‘slow rotators’ (left four panels) and regular ‘fast rotators’ (right panel; Emsellem et al., 2004, 2007; Cappellari et al., 2007). The slow rotators are further subdivided into galaxies that show a) no rotation, b) complex velocity, c) KDCs, and d) having two counter-rotating discs (left to right respectively; Krajnović et al., 2011). See Section 1.1.2.

typically more massive than M_{crit} , rarer ($\sim 15\%$ of ETGs), and show an interesting array of kinematics that led to their further sub-classification (Krajinović et al., 2011). The four slow-rotator sub-classes were defined as showing a) no rotation, b) complex velocity (i.e. clear but not bisymmetric or irregular rotation), c) kinematically decoupled cores (KDCs), and d) having two counter-rotating discs. Typical examples of these sub-classes are shown in Figure 1.4.

1.1.3 Hierarchical Formation of the Universe

To provide context of the framework within which galaxy evolution proceeds, I give a brief overview of the hierarchical build-up of structure in the Universe (e.g., Mo, van den Bosch & White, 2010). This assumes a Λ cold dark matter (Λ CDM) cosmology (e.g., Press & Schechter, 1974; Toomre, 1977; White & Rees, 1978). This is based on results from simulations and observations, however it is a simplistic and evolving view. Following the Big Bang and rapid period of inflation at the start of the Universe, small fluctuations in the primordial and permeating radiation field would become the seeds of the densest regions of cosmic web (as shown in Figure 1.5). Dark matter (DM) haloes built around these seeds via gravitational instability and gas fell into these overdensities by radiating away some of its energy. The gravitational collapse of the gas clouds at the centres of the haloes formed the first stars in the Universe from the primordial gas. These ‘Population III’ stars are theorised to be extremely massive and are unlike the stars forming in the Universe today (e.g., Bond, 1981; Abel, Bryan & Norman, 2002). The supernova explosions of these first stars could have populated the pristine gas with metals which would facilitate more efficient collapse of further gas clouds via metal-line cooling to form the first galaxies.

Between $z \sim 14\text{--}6$ ($\sim 0.3\text{--}0.9$ Gyrs after the Big Bang) the Universe was reionized by the ultraviolet (UV) radiation of these first stars, galaxies, or active galactic nuclei (AGN; see Fan, Carilli & Keating, 2006, for a review). The exact feedback mechanisms and contributions of these UV sources to the reionization of the Universe remains unclear and is an active topic of research. AGN are powered by the accretion of material onto supermassive black holes (SMBH) that reside at the centres of all massive galaxies (e.g., Hoyle & Fowler, 1963; Salpeter, 1964; Zel’dovich, 1964; Lynden-Bell, 1969, 1978; Lynden-Bell & Rees, 1971). AGN are thought to play a valuable role in the evolution of galaxies (see Kormendy & Ho, 2013, for a review). The largest DM haloes acquire the most gas first. When they reach a critical point at which their mass limits their growth as infalling gas streams are shock heated (Kereš

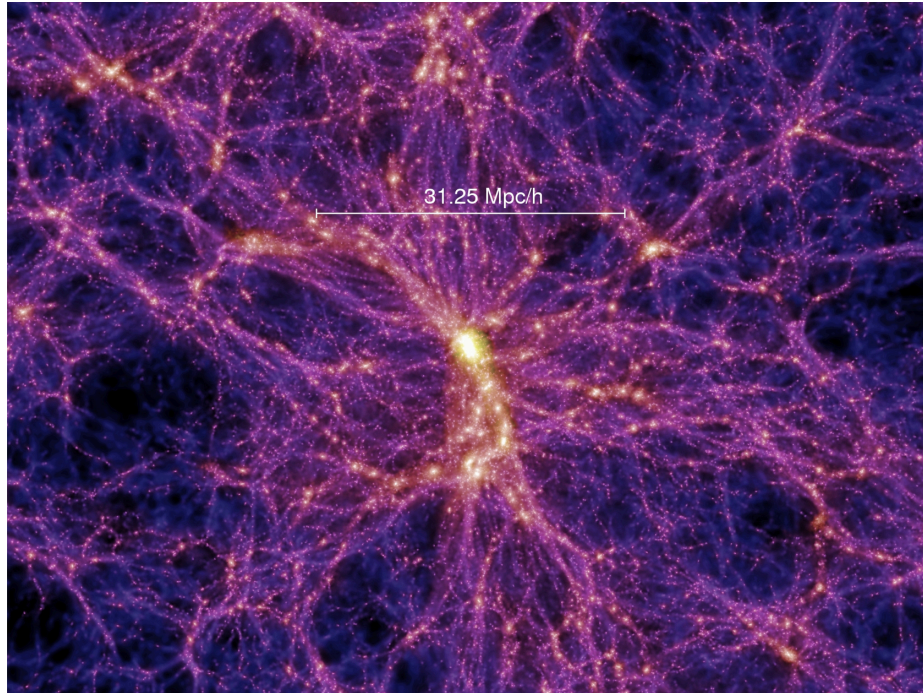


Figure 1.5: Image from the DM cosmological Millennium simulation (Springel, 2005). The cosmic web structure represents an imprint of the small fluctuations in the primordial radiation field of the Universe (higher-density regions are yellow). The central node of the web in the image represents an example of a large DM halo that would have been home to some of the first galaxies. See Section 1.1.3.

et al., 2005; Dekel & Birnboim, 2006) and AGN feedback effects limit the formation of new stars (e.g., Kormendy & Ho, 2013).

As DM haloes hierarchically merge with each other, the central most massive galaxies continually sink to the bottom of the potential well. These galaxies merge with each other and as do their respective SMBHs. It is thought that this would leave an imprint on the stellar kinematics in the galaxy core as the stars are redistributed by the SMBH merging process (e.g., Begelman, Blandford & Rees, 1980; Milosavljević & Merritt, 2001). These massive central galaxies are thought of as the slow rotators that exhibit irregular kinematics. The non-central (i.e. ‘satellite’) galaxies (e.g., Zehavi et al., 2005) in these massive merging DM haloes are prevented from forming new stars. As they move through the large potential well of the DM halo, they cannot effectively accrete new gas (e.g., Larson, Tinsley & Caldwell, 1980) and the resulting cluster dispersion is too large for efficient merging of galaxies (e.g., Ostriker, 1980). These satellite galaxies in the cluster are thought of as the fast rotator galaxies that are not massive enough to sink to the centres of the halo but stop forming stars in the cluster environment. In lower density DM regions of the Universe, evolution

happens later and more gradually due to the slower build-up of gas. These regions form gaseous, turbulent, and clumpy disc galaxies (as seen at $1.5 < z < 2.5$; e.g., Elmegreen et al., 2007; Daddi et al., 2010; Stott et al., 2016).

1.1.4 Galaxy Evolution in Different Environments

Galaxy clusters are the largest gravitationally bound structures in the Universe. Locally, they provide valuable laboratories for understanding the evolution of galaxies in dense environments (e.g., Gunn & Gott, 1972). The most massive cluster in the local Universe is Coma, and it was in this cluster that the detection of a vast amount of invisible mass (i.e. its large DM halo) was measured from the dispersion of its member galaxies (Zwicky, 1933, 1937). The large potential well of clusters causes the intracluster medium (ICM) to heat to extreme temperatures and this can be detected in X-rays (e.g., Felten et al., 1966). The X-ray bright ICM can be used as a marker for detecting massive clusters (e.g., Mullis et al., 2005). Alternatively, the narrow red sequence of the quenched galaxy population (see Section 1.1.1) can be used to identify clusters (e.g., Gladders & Yee, 2000). Clusters of galaxies are valuable cosmological probes as their vast potential wells can be used as magnifying ‘lenses’ of the distant Universe (Zwicky, 1933, 1937, see Kneib & Natarajan 2011 for a review).

As demonstrated in the context of the hierarchical build-up of structure in a Λ CDM cosmology, the densest regions of the Universe result in a different evolutionary path for a galaxy. Observations in the local Universe have long hinted at this environmental effect (e.g., Hubble & Humason, 1931). The morphology-density relation (Dressler, 1980) describes the phenomenon that ETGs are more common towards the centres of galaxy clusters than LTGs (Figure 1.6). It is clear that these environments play a role in the evolution of galaxies. Environmental quenching in the local Universe is typically thought to proceed via the strangulation of a gas supply in the potential well of clusters (Larson, Tinsley & Caldwell, 1980), ram-pressure stripping of material by the hot ICM (e.g., Gunn & Gott, 1972; Kronberger et al., 2008), harassment (e.g., Moore et al., 1996), and tidal interactions (see Boselli & Gavazzi, 2006, for a review). Evidence has also shown that galaxies may undergo some pre-processing in a group environment, where gas-rich mergers and accretion are more likely (e.g., Ostriker, 1980), prior to falling into a cluster (e.g., Zabludoff & Mulchaey, 1998; Mihos, 2004; Dressler, 2004; Fujita, 2004). As shown in the cosmological context, galaxies form first in massive DM haloes and can be ‘mass quenched’ when feedback or internal processes become significant (e.g., Peng et al., 2010; Hopkins et al., 2014) or the gas in the halo cannot cool efficiently (e.g., Birnboim & Dekel, 2003;

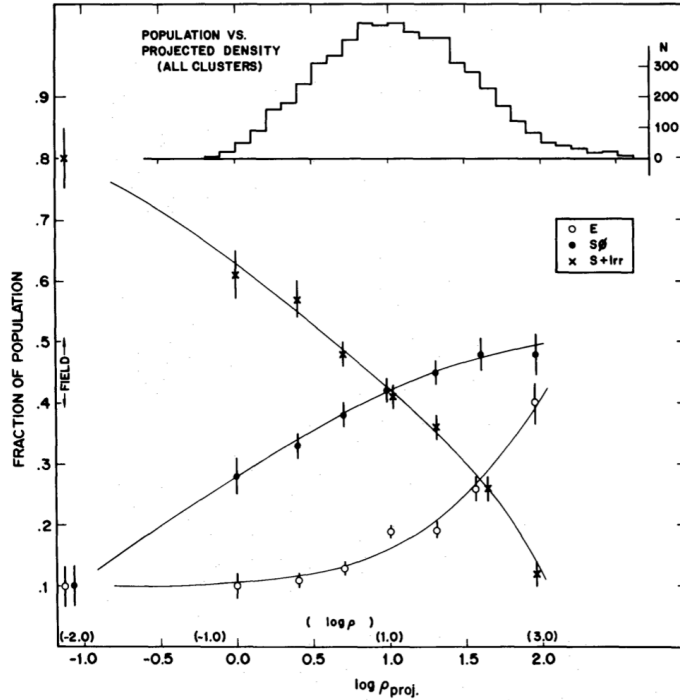


Figure 1.6: Morphology-density relation (figure from [Dressler, 1980](#)). The density is in galaxies per Mpc^3 . Towards higher-density regions (i.e. the centres of clusters) the number of spiral galaxies reduces while the number of ETGs increases. The relation shows the effects of environment on the evolution of galaxies. See Section 1.1.4.

[Gabor & Davé, 2015](#)). The brightest cluster galaxies (BCGs) can often be diffuse and extended which supports the merging mechanism of mass growth for the central galaxies in DM haloes (see Section 1.1.3). However, their evolution is thought of as distinct from other galaxies and there are contradictory theories about their exact evolutionary path (e.g., [De Lucia & Blaizot, 2007](#); [Valentinuzzi et al., 2010a,b](#); [Stott et al., 2010, 2011](#); [Burke & Collins, 2013](#)).

Untangling the effects of environmental quenching (such as those observed in the local Universe) and mass quenching has so far proved challenging. Different studies performed at different redshifts find that mass is the driving quenching mechanism (e.g., [van der Wel et al., 2005](#); [Treu et al., 2005](#); [Quadri et al., 2012](#)), and for mass-controlled studies others find that environment is the main cause of quenching (e.g., [van Dokkum & Ellis, 2003](#); [Newman et al., 2014](#)). It could be that the epoch at which these processes dominate, i.e. driven by differences in the state of the Universe at different times, is the main explanation of these discrepancies. From larger statistical samples, recent studies have shown that mass quenching is most important between $z \sim 1-3$ (e.g., [Darvish et al., 2016](#)) while environmental quenching becomes more effi-

cient and thus more important at lower redshifts (e.g., [Nantais et al., 2017](#)). However, more work has to be done to understand the conflicting results of previous studies to be able to decipher the role environment has to play in the evolution of galaxies. Constraining these transformation processes at high redshift in dense environments is important to resolving the discrepancies in the literature.

1.1.5 Properties of High-Redshift Galaxies

Detailed studies of local galaxies have revealed a complex array of ETG properties and has created many more questions about their evolution. As technology improves we are able to look out to even greater distances to study the properties of ETGs in the early Universe directly rather than from their inferred history from fossil records of local galaxies. These high-redshift galaxy studies have been valuable for improving our understanding of how the evolution of ETGs has progressed throughout the life of the Universe. Results derived from the local Universe are not always in agreement with those from the high-redshift Universe and this has sometimes led to the re-evaluation of our understanding of ETGs or alternatively of the short-comings of our observational methods. There are a number of important biases which must be taken into account when studying galaxies at different epochs. Sample selection factors such as ‘progenitor bias’ ([van Dokkum & Franx, 1996](#)) — where if ETGs evolved from LTGs, then at increasing redshift the sample would be biased toward only the oldest systems — may play a big part in the lack of consensus. The Butcher-Oemler effect ([Butcher & Oemler, 1978](#)), which is the phenomenon that galaxies are bluer in cluster cores at intermediate redshift than at $z \sim 0$, may also affect the sample selection between studies and result in contradictory conclusions.

I give a quick summary of some results from high-redshift galaxy studies that have contributed to our understanding of the evolution of ETGs over cosmic time. Observations show that the peak of cosmic SFR density is at $z \sim 2$ ([Madau et al., 1996](#); [Madau & Dickinson, 2014](#)). It has been shown that much of the star formation in the most massive galaxies happened earlier, with most stars being in place at $z \gtrsim 3$ (e.g., [Ellis et al., 1997](#); [Holden et al., 2004](#)). There is a bimodality between the SF blue and quiescent red galaxies that holds out to $z \sim 3$ (e.g., [Whitaker et al., 2011](#)) which supports this early evolution for some galaxies. Studies have shown that the narrow red sequence holds out to $z \sim 2$ (e.g., [Bell et al., 2004](#); [Cimatti et al., 2008](#)). This is consistent with the picture that SF started early and was quenched early, leaving galaxies in the red sequence to evolve passively (e.g., [Dressler & Gunn, 1990](#); [Heavens](#)

et al., 2004; Thomas et al., 2005; Renzini, 2006; Holden et al., 2010; McDermid et al., 2015).

One of the most interesting discoveries about high-redshift quiescent galaxies is that they are compact (e.g., Daddi et al., 2005; Trujillo et al., 2006a). These very massive ($\sim 10^{11} M_{\odot}$) and compact ($R_e \sim 1$ kpc) galaxies have been termed ‘red nuggets’ (van Dokkum et al., 2008; Damjanov et al., 2009; van Dokkum, Kriek & Franx, 2009; Newman et al., 2010; Whitaker et al., 2012). The masses (e.g., Cappellari et al., 2009; van de Sande et al., 2013) and sizes (e.g., Bezanson et al., 2009; Muzzin et al., 2009) of the red nugget galaxies were independently verified. Based on comparisons with nearby galaxies, the red nuggets must grow in size by a factor of ~ 2 since $z \sim 1$ (e.g., Trujillo et al., 2006b; van der Wel et al., 2008) and a factor of ~ 4 since $z \sim 2$ (e.g., Trujillo et al., 2007; Buitrago et al., 2008) to match the local distribution. Observations of compact, dusty, rapidly SF galaxies (‘blue nuggets’) in the early Universe showed that they could be the progenitors of these compact quiescent galaxies (e.g., Barro et al., 2013, 2014).

1.1.6 The Initial Mass Function

One approach to understanding the evolution of ETGs is to study their IMF; the number of stars of each mass when a galaxy formed. In its simplest form, it is described by a power law where the exponent determines the slope of the IMF. Figure 1.7 shows the mass function (ξ) of some different forms of the IMF. Whether the IMF is universal (i.e., constant over cosmic time and different environments) or not is one of the biggest questions in stellar and galaxy astrophysics (see Bastian, Covey & Meyer, 2010, and references therein). Methods for determining the IMF include individual star counts locally (Salpeter, 1955; Kroupa, 2001; Chabrier, 2003), dynamical modelling (Thomas, Maraston & Johansson, 2011; Cappellari et al., 2012, 2013b), line-strength measurements (e.g. Conroy & van Dokkum, 2012a,b; La Barbera et al., 2013), and strong gravitational lensing (Treu et al., 2010; Auger et al., 2010b; Smith & Lucey, 2013; Smith, Lucey & Conroy, 2015).

The low-mass stars in a galaxy make up the majority of its mass but contribute very little to its stellar light. If one can quantify the low-mass contribution, it allows the derivation of the most fundamental property of a galaxy; its stellar mass. Due to the long main-sequence lives of low-mass stars (i.e., longer than the current age of the Universe), measuring the dwarf-star content of local galaxies is equivalent to probing the low-mass end of the IMF. This area of study therefore crosses the redshift divide and allows us to constrain the conditions of the galaxy at early times by measuring

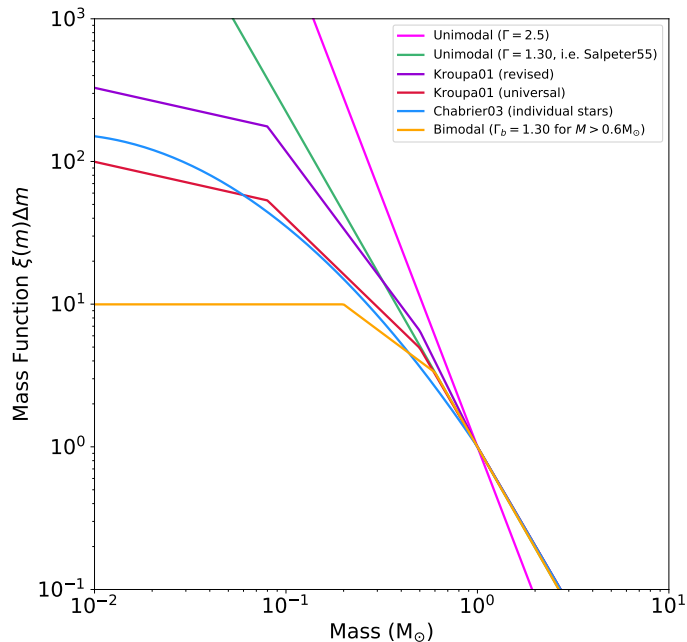


Figure 1.7: Different forms of the IMF; the mass function of stars (ξ) as a function of mass. The logarithmic slope (Γ) and all forms of the IMF shown here are referred to later in this thesis (see Section 5.2.1.2 for a description of the different IMFs). The IMFs with Γ values larger than Salpeter are referred to as bottom-heavy, whilst those similar to Kroupa are referred to as Milky Way like, below this are defined as bottom-light with few low-mass stars. See Section 1.1.6.

the properties of the galaxy in the current Universe. In order to measure the light from faint dwarf stars, high-quality spectra are necessary. This area of study is therefore one that can currently only be performed locally due to the high signal-to-noise (S/N) required. This can be difficult in the near-infrared (NIR), where valuable IMF indicators lie, due to strong contamination from the Earth’s atmosphere at these wavelengths. Stellar absorption features such as NaI (Faber & French, 1980; Schiavon et al., 1997) and FeH (Wing & Ford, 1969; Schiavon, Barbuy & Singh, 1997) can tell us how low-mass star dominated, i.e. bottom-heavy (van Dokkum & Conroy, 2010), a galaxy is. Both the NaI and FeH absorption features are present in the NIR spectra of $M \lesssim 0.3 M_{\odot}$ stars whilst absent or weak in other stars as they are sensitive to surface gravity (e.g., Schiavon, Barbuy & Bruzual A., 2000).

Weighing the contribution of faint dwarf stars in systems has recently seen a resurgence in popularity due to advancements in detector technology and stellar population synthesis models (see Section 1.1.7). This area of research remains challenging and is still active with many studies unable to agree on fundamental results. One method of determining the nature of the IMF (i.e. universal or not) is to measure variations

within just one system. Recent results have measured bottom-heavy IMFs in the centres of ETGs (e.g., [Cenarro et al., 2003](#); [van Dokkum & Conroy, 2010, 2011](#); [Conroy & van Dokkum, 2012b](#); [Smith et al., 2012](#)). So far only a handful of studies have achieved spatially resolved measurements of the IMF on a relatively small sample of galaxies ([Martín-Navarro et al., 2015a,b](#); [Zieleniewski et al., 2015, 2017](#); [McConnell, Lu & Mann, 2016](#); [La Barbera et al., 2016](#); [van Dokkum et al., 2017](#); [Sarzi et al., 2017](#); [Alton, Smith & Lucey, 2017](#); [Vaughan et al., 2018](#)) and there remains some disagreement in their findings.

1.1.7 Stellar Population Models

Vast improvements in the synthesis of stellar populations has improved our understanding of galactic stellar populations (see e.g., [Conroy, 2013](#), for a review). With accurate models of galaxies, one is able to use full-spectral fitting methods (e.g. [Cappellari & Emsellem, 2004](#); [Cappellari, 2017](#)) to derive the properties of the stellar populations from galaxy spectra, including constraining the IMF, by fitting these models to the data. Libraries of model galaxy spectra are spanning increasing parameter space as they grow more complex; covering a large number of ages, metallicities, IMFs, and even α -element abundances (i.e. to measure star formation histories – SFHs). Spectral-fitting libraries are compiled from either empirical (e.g., [Cenarro et al., 2001](#); [Prugniel & Soubiran, 2001](#); [Valdes et al., 2004](#); [Sánchez-Blázquez et al., 2006](#)) or synthetic (e.g., [Munari et al., 2005](#); [Gustafsson et al., 2008](#)) stellar spectra, or SSP models derived from stellar spectral libraries (e.g. [Bruzual & Charlot, 2003](#); [Maraston, 2005](#); [Maraston & Strömbäck, 2011](#); [Conroy, Gunn & White, 2009](#); [Conroy & Gunn, 2010](#); [Sánchez-Blázquez et al., 2006](#); [Vazdekis et al., 2016](#)).

SSPs describe a single age population that evolves with time, however there are a number of other possible population types. The SFHs of galaxies can be traced using the ratio of elements produced when stars die via different mechanisms ($[\alpha/\text{Fe}]$). The mass of a star determines its lifetime and fate, and their chemical outputs can be used to trace the epochs of stellar formation. The spectral libraries are also expanding their wavelength range (now spanning from UV through to mid-IR) and so are expanding the analysis possible to study stellar populations at different redshifts and with different instruments. Their development is a valuable step in the study of ETG evolution.

1.1.8 Possible Evolutionary Paths of ETGs

The earlier picture of ETG formation was divisive where at the peak of the debate it was argued that all ETGs could have been formed via the major merger of gas-rich spirals (e.g., [Toomre & Toomre, 1972](#); [Toomre, 1977](#)) or that none of them were and alternative theories were required (e.g., [Ostriker, 1980](#)). These alternatives included dissipative formation of elliptical galaxies ([Carlberg, 1984](#); [Kormendy, 1989](#); [Kormendy & Sanders, 1992](#)) or monolithic collapse (e.g., [Eggen, Lynden-Bell & Sandage, 1962](#); [Larson, 1974](#)), whereby the continual collapse of a large gas cloud results in a starburst phase, forming a spheroid at very early times. Observations of the detailed kinematics of local ETGs suggest two distinct evolutionary tracks to explain the fast and slow rotator classes; gas-accretion driven evolution for fast rotators and dry-merger driven evolution for slow rotators. The galaxy properties suggest an environmental dependence on this evolution with slow rotators being more common towards the centre of clusters and more massive.

Observations of the high-redshift Universe probe the most massive galaxies at early times. The discovery of extremely compact rapidly SF galaxies (e.g., [Barro et al., 2013, 2014](#)) supports evidence that rapid dissipationless collapses of massive galaxies led to them quenching to form the high-redshift compact red nuggets ([van Dokkum et al., 2008](#); [Damjanov et al., 2009](#); [van Dokkum, Kriek & Franx, 2009](#); [Newman et al., 2010](#); [Whitaker et al., 2012](#)). Simulations have shown that these compact quiescent galaxies could form from dusty turbulent disc galaxies seen in the early Universe (e.g., [Genzel et al., 2006, 2008](#)). A violent disc instability can drive rapid contraction of material in the disc toward the galaxy core (e.g., [Gammie, 2001](#); [Dekel, Sari & Ceverino, 2009](#); [Burkert et al., 2010](#); [Krumholz & Burkert, 2010](#); [Forbes et al., 2014](#)) as can gas rich mergers (e.g., [Barnes & Hernquist, 1991](#); [Mihos & Hernquist, 1996](#); [Hopkins et al., 2006a](#)). Gradients in the IMF could provide clues as to the formation mechanisms of galaxies. Local observations of the bottom-heavy IMFs at the centres of massive slow rotator galaxies could support this channel of growth. It is suggested that this extreme mode of formation could result in the bottom-heavy nature of massive ETG cores (e.g., [van Dokkum et al., 2015](#); [Zolotov et al., 2015](#); [Barro et al., 2016](#); [Kriek et al., 2016](#)).

A current leading theory that is strongly supported by a lot of evidence is the idea of a two-phase growth for the very massive slow-rotator ETGs found in dense cluster environments (e.g., [Oser et al., 2010](#)). The first phase is via a rapid collapse of gas that sparks an intense starburst SF phase as evidenced by high-redshift observations and simulations. The second phase involves the build-up of mass via gas-poor minor

mergers (e.g., Naab et al., 2007; Naab, Johansson & Ostriker, 2009; Hopkins et al., 2009; Feldmann, Carollo & Mayer, 2011; Johansson, Naab & Ostriker, 2012; Lackner et al., 2012; Huang et al., 2016).

What is not yet clear though is whether this two-phase evolutionary path can explain the size evolution required to evolve the high-redshift red nuggets to the local distribution of galaxies. The method of growth would have to dramatically increase the size of the galaxies without increasing their mass or the rate at which they form stars. Major mergers as drivers of expansion have mainly been ruled out as the dominant process as they would increase the mass of the galaxies significantly. Studies have suggested minor mergers can explain the size growth (e.g., Naab, Johansson & Ostriker, 2009; Trujillo, Ferreras & de La Rosa, 2011). The comparison of the stellar density profiles of high- and low-redshift galaxies revealed similar central densities, supporting an ‘inside-out’ growth via minor mergers (e.g., Bezanson et al., 2009; van Dokkum et al., 2010). However, Newman et al. (2012) found that minor mergers can only explain size growth at $z \lesssim 1$ and alternative processes must be responsible at higher redshifts. The adiabatic expansion or ‘puffing up’ scenario has also been explored (e.g., Fan et al., 2008, 2010), in which central AGN eject enough cold gas to significantly distort the gravitational potential of the galaxies, causing them to puff up in size. Although the puffing up of galaxies via AGN or galactic winds from starburst activity could account for some of the size evolution and the quenching of star formation at early times, it might not explain all the size growth observed between $1 < z < 2$ (e.g., Ragone-Figueroa & Granato, 2011).

1.1.9 Open Questions About the Evolution of ETGs

In this section, I have presented the overview of some of the key concepts, results and theories that form the basis of the work presented in this thesis. There are a number of questions that remain about how ETGs evolve, some of which I list here, although this is by no means exhaustive. Some open questions about the evolution of ETGs include the formation of the different types of massive slow rotators. They can exhibit a range of different kinematics; is it possible that all of these can arise from the same formation processes? In the hierarchical model of galaxy evolution, these slow rotators could form and quench first and continue to build up their mass via dry minor mergers. What triggers this first phase of rapid SF? And can this two-phase mechanism of growth apply to non-central galaxies that fall into clusters at a later stage? Is the two-phase model sufficient to explain the array of kinematics displayed by the local ETGs? Despite the growing evidence of a two-phase slow-rotator ETG

evolution, the size growth of galaxies from compact high-redshift galaxies to the local distribution of galaxies may not be able to be explained via minor mergers alone. The role of environment in this formation mechanism is still not well understood at high redshift. Is the quenching of high-redshift galaxies mostly driven by internal processes or the mass of haloes (i.e. mass quenching), or by the environmental processes we are more familiar with at low redshift? The IMF of galaxies as measured from radial gradients may be able to indicate different formation mechanisms. However, whether the IMF changes with redshift and environment is not understood. Clearly there is some work to do in our understanding of the formation and evolution of ETGs to explain the procession of galaxy evolution in a hierarchical universe.

1.1.10 The K-band Multi-Object Spectrograph

Observing the high-redshift Universe has provided some valuable clues about the young lives of the most massive galaxies found locally. However, these studies have been technically challenging and often involved significant amounts of telescope time. A valuable spectral region for studying stellar populations and kinematics is the well-studied rest-frame optical, however at large cosmological distances this region is redshifted to longer wavelengths. To be able to study this rest-frame region above $z \gtrsim 1$, we need NIR wavelengths. Advancements in detector technology have enabled us to explore this region of wavelength space over the last decade (e.g., Moorwood, 2006). Contamination from the Earth’s atmosphere at these wavelengths can be significant, however advanced atmospheric modelling techniques to correct this contamination with high precision have recently become available (Smette et al., 2015; Kausch et al., 2015).

To be able to efficiently observe distant galaxies in the rest-frame optical is of vital importance to constraining the early evolution of ETGs. Likewise, to probe the rest-frame NIR where there are valuable dwarf-sensitive features has been demonstrated to be important for understanding the early stages of galaxy formation. These areas of research were some of the motivation for building the K-band Multi-Object Spectrograph (KMOS; Sharples et al., 2013). This instrument is the first multi-IFU (24 separate pick-off arms) in the infrared (see Section 2.1 for a technical description). Surveys using KMOS’s multi-object efficiency and spatial resolution of the IFUs have shown its value in probing the early stages of galaxy evolution. These include the guaranteed time observations (GTO) programmes: KMOS^{3D} (Wisnioski et al., 2015) of 600 galaxies at $0.7 < z < 2.7$, KMOS Redshift One Spectroscopic Survey (KROSS; Stott et al., 2016) of 800 SF galaxies at $z = 0.8-1$, and Very Large Telescope (VLT)

IR IFU Absorption Line (VIRIAL) survey (Mendel et al., 2015, Mendel et al., in prep.) of 25 massive galaxies ($\log(M_*/M_\odot) \geq 10.9$) at $1.5 < z < 2$. So far KMOS has been somewhat underused in the study of local galaxies, with one example being the KMOS Infrared Nearby Early-Type Survey (KINETyS; Alton, Smith & Lucey, 2017). These studies have shown that KMOS is a valuable instrument for shedding light on the formation mechanisms of galaxies. I intend to demonstrate this fact further with the work presented in this thesis. I couple the NIR spectroscopy of KMOS with photometric observations from the *Hubble Space Telescope* (HST) and optical IFU data from the Multi-Unit Spectroscopic Explorer (MUSE; Bacon et al., 2010) to help build a complete picture of how ETGs evolve.

1.2 Introduction to Work Presented in this Thesis

Many interesting questions remain about the formation of ETGs and how they evolve over cosmic time. As emphasised in a recent review, too often the groups studying local galaxies are unaware of the results of high-redshift galaxy evolution and vice versa (Cappellari, 2016). This results in missed opportunities to advance our knowledge of how ETGs and indeed all galaxies have evolved. This thesis aims to tackle this problem by studying galaxies both in the early Universe and locally to build a more comprehensive view of how ETGs formed and to address some of the open questions relating to how they have evolved.

This thesis comprises two studies that are outlined in two parts. Part I focuses on the investigation of a high-redshift ETG-rich cluster which aims to improve our understanding of how massive ETGs are evolving in dense environments at early times. The use of efficient observations in the NIR (which at $z \sim 1-2$ spans the rest-frame optical) with KMOS has enabled a more comprehensive study of quiescent galaxy formation at $z \sim 2$ than has been previously possible. Part II of this thesis takes a different approach to studying the formation of ETGs by looking in detail at a massive local galaxy with interesting kinematic features. I coupled IFU data at optical and NIR wavelengths to perform a detailed study of the fossil record of a massive local galaxy in order to understand its evolutionary path. Introductions to the two parts of the thesis are given below.

1.2.1 Part I – The KMOS Cluster Survey: Fundamental Plane of Cluster Galaxies at $z \simeq 1.80$ in JKCS 041

In the hierarchical formation model of Λ CDM cosmology, the largest scale structures, such as clusters of galaxies, are the last to be formed (e.g., [Press & Schechter, 1974](#); [Toomre, 1977](#); [White & Rees, 1978](#)). Therefore, galaxy clusters are increasingly rare at high redshift (e.g., [Haiman, Mohr & Holder, 2001](#)). Currently, only a handful of rich overdensities, with a well-defined red sequence (see Section 1.1.1) exist at $1.5 \lesssim z \lesssim 2.5$ ([Kurk et al., 2009](#); [Papovich et al., 2010](#); [Tanaka, Finoguenov & Ueda, 2010](#); [Gobat et al., 2011, 2013](#); [Santos et al., 2011](#); [Stanford et al., 2012](#); [Zeimann et al., 2012](#); [Muzzin et al., 2013](#); [Andreon et al., 2014](#); [Newman et al., 2014](#); [Wang et al., 2016](#), see a recent review by [Overzier 2016](#)).

The evolution of galaxies is connected to their environment; the morphology-density relation ([Dressler, 1980](#)) describes the phenomenon whereby red and dead elliptical galaxies are more common in denser environments, i.e., towards the centre of galaxy clusters. Therefore, processes that occur within these dense environments alter the evolutionary paths of their member galaxies. Probing galaxy evolution in dense environments out to increasingly higher redshift has long been a key focus of extragalactic astronomy (e.g., [Dressler et al., 1997](#); [Stanford, Eisenhardt & Dickinson, 1998](#); [Poggianti et al., 1999](#); [Postman et al., 2005](#)). However, capturing the evolutionary processes within distant quiescent galaxies out to $z \sim 2$ has so far proved challenging for all but the most massive galaxies. Rare, massive, high-redshift overdensities provide a valuable opportunity to observe the largest samples of ETGs out to $z \sim 2$ in order to constrain the evolution of galaxies at these redshifts by studying their stellar light.

Scaling relations of ETGs provide powerful diagnostic tools for probing the evolution of galaxies ([Djorgovski & Davis, 1987](#); [Dressler et al., 1987](#); [Jørgensen, Franx & Kjaergaard, 1996](#)). In the nearby Universe, the existence of the FP was shown to be almost entirely due to virial equilibrium combined with a systematic variation of the M/L ([Cappellari et al., 2006, 2013a](#); [Bolton et al., 2007](#); [Auger et al., 2010a](#), see [Cappellari 2016](#) for a recent review).

The FP zero point is known to evolve strongly with redshift and can be used to determine the stellar ages of galaxies (e.g. [Beifiori et al., 2017](#)). Assuming ETGs are a homologous population, this zero-point evolution can be explained by the M/L evolution of the aging stellar population (e.g., [van Dokkum & Franx, 1996](#); [van Dokkum & van der Marel, 2007](#); [Holden et al., 2010](#)), or alternatively by size evolution ([Saglia et al., 2010, 2016](#)). To construct an FP, deep continuum spectroscopy is required to

obtain accurate absorption-line stellar velocity dispersions. Given the difficulties in obtaining deep enough spectra to measure reliable velocity dispersions for individual galaxies, FPs have only been constructed out to $z \sim 2$ comprising the brightest (typically the central) galaxies. These studies have shown that the FP holds to $z \sim 2$ (Toft et al., 2012; Bezanson et al., 2013; van de Sande et al., 2014).

Performing these types of studies up to $z \sim 2$ has proved costly in telescope time. However, absorption-line studies of galaxies are essential for constraining the kinematics and properties of their stellar content. The first detection of absorption lines at $z > 2$ came from a 29-hour integration of one galaxy at $z = 2.2$ (Kriek et al., 2009); a high velocity dispersion ($\sigma = 510_{-95}^{+165}$ km s⁻¹) was also determined for this galaxy (van Dokkum, Kriek & Franx, 2009). Even with extensive efforts being made to expand this sample of dispersion values at $z \sim 2$, only around a dozen measurements have been obtained directly for individual galaxies at these redshifts (van Dokkum, Kriek & Franx, 2009; Onodera et al., 2010; Toft et al., 2012; van de Sande et al., 2013; Belli et al., 2014; Belli, Newman & Ellis, 2017). A few more have been determined for lensed ETGs at $z > 2$, which negates the need for such long integrations, but these cases are rare (e.g., Newman, Belli & Ellis, 2015; Hill et al., 2016; Toft et al., 2017).

Multi-object spectrographs can improve observing efficiency of high- z galaxies, provided target quiescent galaxies have high spatial density. High-redshift galaxy overdensities with a well-populated red sequence satisfy these constraints. KMOS on the VLT in Chile is a NIR multi-IFU instrument. The IFUs of KMOS were specifically designed to match galaxy sizes at high redshift, and 24 separate targets can be observed simultaneously, thereby vastly improving the efficiency of IFU observations. At $1 < z < 2$, the rest-frame optical region lies in the NIR range of KMOS. Emission and absorption lines in the rest-frame optical are valuable tools for probing the stellar populations and kinematics within galaxies. However, absorption-line studies at this distance are technically challenging, requiring high S/N that can only be achieved from long integration times.

As part of the KMOS GTO project, the KMOS Cluster Survey (KCS; Davies et al., 2015, Davies, Bender et al., in prep.), ETGs in overdensities between $1 < z < 2$ were observed for 20-hours on source, to constrain galaxy evolutionary processes in dense environments at higher redshifts than previously possible. The redshift range covers the peak epoch of cosmic star formation (Madau et al., 1996; Madau & Dickinson, 2014), around 10 Gyrs ago, an important phase in galaxy evolution when their stellar populations were being established. Coupling KMOS data with HST imaging, the

size, age, morphology, and SFHs of the galaxies could be investigated (Chan et al., 2016; Beifiori et al., 2017; Chan et al., 2018).

The highest redshift KCS target, JKCS 041, is an ETG-rich $z \simeq 1.80$ overdensity. JKCS 041 was first identified by Andreon et al. (2009) when detected with diffuse X-ray *Chandra X-ray Observatory* data. The overdensity was spectroscopically confirmed with 19 members, and three candidate members, at $z = 1.803$ with HST grism spectroscopy (Newman et al., 2014, hereafter N14). The total overdensity mass was determined to be in the range $\log(M/M_{\odot}) = 14.2\text{--}14.5$ (Andreon et al., 2014). Further investigation of the overdensity showed that the mass-matched field sample at the same redshift were not as quiescent (N14), providing compelling evidence for environmental quenching. JKCS 041 was therefore an ideal system to target in order to improve our understanding of galaxy evolution out to $z \sim 2$.

In part I of this thesis, I investigated the properties of the highest redshift overdensity in the KCS sample, JKCS 041 at $z \simeq 1.80$. I will present the KMOS spectroscopic data of the galaxies, which when combined with HST imaging (presented in N14), enabled me to construct an FP of galaxies in JKCS 041 in order to determine their mean stellar age. I used dynamical information to construct a three-dimensional view of the observed overdensity members. This is the most detailed study of a high-redshift cluster performed to date and the results of this analysis reveal a complex picture of how massive ETGs and clusters evolve at early times.

1.2.2 Part II – Unravelling the Origin of the Counter-Rotating Core in IC 1459 with KMOS and MUSE

Large IFU surveys of local galaxies have revolutionised our understanding of ETGs (see Cappellari, 2016, for a review). A sub-class of the rarer massive slow-rotator ETGs were galaxies that exhibit KDCs (as had been previously detected e.g., Efsthathiou, Ellis & Carter, 1980, 1982; Franx & Illingworth, 1988; Jedrzejewski & Schechter, 1988; Bender, Doebereiner & Moellenhoff, 1988; Franx, Illingworth & Heckman, 1989; Carollo & Danziger, 1994). KDCs are relatively rare in ETGs as a whole ($\sim 7\%$) but are common among slow rotators ($\sim 42\%$; Krajnović et al., 2011). Another interesting sub class are galaxies with two counter-rotating discs (as previously measured by e.g., Rubin, Graham & Kenney, 1992; Rix et al., 1992) termed ‘ 2σ ’ galaxies due to their distinctive velocity dispersion maps (Krajnović et al., 2011). These galaxies are rare ($\sim 4\%$) and are mostly found in less massive galaxies ($M < 5 \times 10^{10} M_{\odot}$; Cappellari et al., 2013a). There is strong evidence that 2σ

galaxies are composed of two thin counter-rotating discs of different stellar populations (Cappellari et al., 2007; Coccato et al., 2011, 2013; Johnston et al., 2013).

Studies of the stellar populations of galaxies with KDCs have shown old ages and negative metallicity gradients (e.g., Efstathiou & Gorgas, 1985; Franx & Illingworth, 1988; Gorgas, Efstathiou & Aragon Salamanca, 1990; Bender & Surma, 1992; Carollo et al., 1997b,a; Mehlert et al., 1998; Davies et al., 2001; Emsellem et al., 2004; Kuntschner et al., 2010; McDermid et al., 2015). This is similar to ETGs of comparable masses with no KDC. The light profiles of galaxies with KDCs (e.g., Efstathiou, Ellis & Carter, 1980; Läsker, Ferrarese & van de Ven, 2014) are also similar to ETGs without them (e.g., Forbes, Reitzel & Williger, 1995; Carollo et al., 1997b,a; Emsellem et al., 2011; Lauer, 2012; Krajnović et al., 2013).

There is a wealth of evidence that supports a two-stage formation of massive slow rotator ETGs (e.g., Oser et al., 2010). The first phase is thought to be dominated by rigorous star formation (i.e. ‘starburst’) that could be triggered by gas-rich mergers (e.g., Barnes & Hernquist, 1991) or rapid accretion of cold streams (e.g., Dekel et al., 2009; Elmegreen & Burkert, 2010; Dekel & Burkert, 2014; Forbes et al., 2014). The second phase of evolution is thought to be the steady accretion of stars from gas-poor satellites (e.g., Naab et al., 2007; Naab, Johansson & Ostriker, 2009; Hopkins et al., 2009; Feldmann, Carollo & Mayer, 2011; Johansson, Naab & Ostriker, 2012; Lackner et al., 2012). It was originally thought that KDCs had an external origin and provided conclusive proof of major mergers to form ETGs (Efstathiou, Ellis & Carter, 1980; Franx & Illingworth, 1988; Bender & Surma, 1992). Counter rotation could also arise from the accretion of gas or gas rich satellites (e.g., Bertola, Buson & Zeilinger, 1988; Franx & Illingworth, 1988). However, these gas-rich evolutionary scenarios are in conflict with the standard definition of the two-phase path of ETG formation and are therefore difficult to reconcile with the observational similarities of KDC galaxies with other massive ETGs.

Many studies have shown that massive galaxies with KDCs show radially constant ages (e.g., Franx & Illingworth, 1988; Bender, Doebereiner & Moellenhoff, 1988; Rix et al., 1992; Davies et al., 2001; McDermid et al., 2006; Kuntschner et al., 2010; McDermid et al., 2015; Krajnović et al., 2015). These findings support an interesting development in the study of KDCs from dynamical orbital modelling (van den Bosch et al., 2008; Krajnović et al., 2015). van den Bosch et al. (2008) showed that when modelling the galaxy NGC 4365, its KDC was not an orbitally distinct component but actually an observational effect of two smoothly distributed prograde and retrograde populations of stars (explaining the radially constant age) on thick short-axis tube

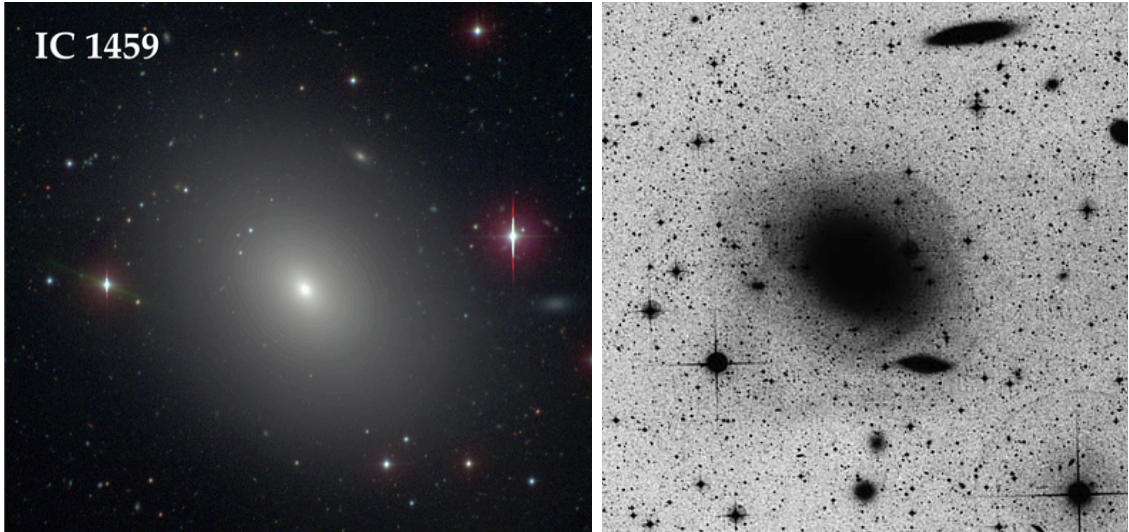


Figure 1.8: *Left*: Image of the E3 galaxy IC 1459 ($\sim 7'$ across) at the centre of the IC 1459 group from the Carnegie Galaxy Survey (Ho et al., 2011). *Right*: Deep image of IC 1459 ($\sim 28'$ across) that revealed tidal features in the galaxy (Malin, 1985).

orbits (as confirmed by Krajnović et al., 2015). The studies found that the net rotation of the KDC arises from the mass imbalance of stars on the prograde and retrograde orbits. Despite this advance in our understanding of KDCs, it is not clear what formation mechanisms would result in prograde and retrograde populations of stars, or what would drive their imbalance in mass fraction at different radii that would result in little radial variation in age.

Radial gradients in the IMF can provide information about the possible evolutionary paths of galaxies. For example, it is thought that a bottom-heavy IMF towards the centres of massive ellipticals supports the two-phase growth channel where the cores are formed first and extremely rapidly (e.g., van Dokkum et al., 2015; Zolotov et al., 2015; Barro et al., 2016). So far only a handful of studies have achieved spatially resolved measurements of the IMF on a relatively small sample of galaxies (Martín-Navarro et al., 2015a,b; Zieleniewski et al., 2015, 2017; McConnell, Lu & Mann, 2016; La Barbera et al., 2016; van Dokkum et al., 2017; Sarzi et al., 2017; Vaughan et al., 2018). As yet, radial measurements of the IMF in a KDC have not been made and could provide valuable clues as to the formation of this interesting class of galaxies.

To help understand the formation of galaxies that exhibit KDCs, I investigated IC 1459; the archetypal massive ETG with a counter-rotating core (Franx & Illingworth, 1988). IC 1459 (shown in Figure 1.8) is a bright ($M_V \simeq -22.3$; Lyon-Meudon Extragalactic Database – LEDA, see Paturel et al., 1997), local ($D = 30.3 \pm 4.0$ Mpc;

Ferrarese & Merritt, 2000), massive ($M \sim 4\text{--}6 \times 10^{11} M_{\odot}$; Cappellari et al., 2002; Samurović & Danziger, 2005) E3 ETG. It is the central galaxy in the gas-rich IC 1459 group of 11 galaxies that is dominated by spirals (group number 15; Huchra & Geller, 1982; Serra et al., 2015). The outer parts of the galaxy and ionized gas in the centre show rotation in one direction, while the central stellar component is rapidly counter-rotating with a maximum velocity $\sim 170 \pm 20 \text{ km s}^{-1}$ (Franx & Illingworth, 1988).

IC 1459 is a gas-rich galaxy that has dust (Malin, 1985; Sparks et al., 1985; van Dokkum & Franx, 1995; Amblard et al., 2017), neutral HI gas (Serra et al., 2015), molecular gas (Prandoni et al., 2012) and ionized gas (Phillips et al., 1986b; Franx & Illingworth, 1988) in its core. A deep image of IC 1459 (shown in the right panel of Figure 1.8; Malin, 1985), revealed tidal features in the galaxy, while Forbes, Reitzel & Williger (1995) found shell-like remnants. IC 1459 hosts a radio-loud AGN that has X-ray jets (e.g., Ekers et al., 1989; Slee et al., 1994; Verdoes Kleijn et al., 2000; Tingay & Edwards, 2015). Mass measurements of the central SMBH differed by an order of magnitude depending on whether it was measured through gas ($M_{\text{BH}} \sim 3.5 \times 10^8 M_{\odot}$) or stellar ($M_{\text{BH}} = 2.6 \pm 1.1 \times 10^9 M_{\odot}$) kinematics (Cappellari et al., 2002). The discrepancy in these measurements was due to strong emission lines obscuring the stellar component and the disturbed orbits of the gas giving an unreliable black hole (BH) mass estimates.

To investigate the evolution of IC 1459, I coupled large field-of-view (FOV) NIR data from KMOS and optical data from MUSE. With the benefit of a three-dimensional view from the two IFU instruments, I was able to accurately separate different kinematic components of the galaxy. The large wavelength coverage enabled me to constrain the stellar population parameters (i.e., age and metallicity) across the kinematically distinct regions of IC 1459. I then used the dwarf-sensitive spectral features in the NIR to measure the spatially resolved IMF of a galaxy with a KDC for the first time. This study highlights the use of KMOS and MUSE for investigating local ETGs and uses novel methods to understand the evolution of IC 1459. The results could indicate unusual formation mechanisms for galaxies with KDCs that step away from the classic two-phase picture that describes other slow rotators.

1.3 Chapter Summary

This thesis is separated into two parts. Part I focuses on work done as part of KCS on the $z \simeq 1.80$ cluster JKCS 041 and is split into three chapters. Chapter 2

details the KMOS data taken as part of KCS and the spectroscopic analysis of the galaxies in JKCS 041. The chapter gives a technical description of KMOS (Section 2.1), an overview of KCS (Section 2.2) including a description of the properties and previous analysis of JKCS 041 (Section 2.2.2.1), details of the KMOS target selection and observations for JKCS 041 (Section 2.3), and a description of the KCS data reduction (Section 2.4). I then describe the spectroscopic analysis which includes kinematic fits to the galaxy spectra (Section 2.5.2), and derivation of their redshifts (Section 2.5.3) and dynamical masses (Section 2.5.4). In Chapter 3, I describe the photometric analysis of galaxies in JKCS 041 using HST data. I give a description of HST (Section 3.1), the photometric data (Section 3.2), and its reduction (Section 3.3). I then detail the photometric analysis performed on the HST images to derive structural properties of the galaxies (Section 3.4) and the estimation of uncertainties of the derived parameters (Section 3.4.4). Light-weighted stellar masses for galaxies in JKCS 041 were then derived (Section 3.6). In the final chapter of Part I (Chapter 4), I describe the construction of the FP for galaxies in JKCS 041 and the derivation of mean ages from its zero-point evolution (Section 4.1). I estimate the effects of structural evolution on the FP ages (Section 4.2). I then investigate the cluster structure in three dimensions and measure ages for different groups of galaxies within JKCS 041 (Section 4.3). I discuss the results found for JKCS 041 in this work in the context of the current literature (Section 4.4) and present a summary of conclusions for Part I (Section 4.5).

Part II of this thesis is focussed on the analysis of IC 1459 with KMOS and MUSE. Chapter 5 first details the KMOS data used for the analysis (Section 5.1.1); a description of the observations (Section 5.1.1.1) and reduction is given (Section 5.1.1.2). I then describe the MUSE data (Section 5.1.2), including a technical description of MUSE (Section 5.1.2.1), an overview of the MUSE observations of IC 1459 (Section 5.1.2.2) and preparation of the cube for analysis (Section 5.1.2.3). I give details of the analysis of the mosaic data (Section 5.2) which includes derivation of kinematic maps (Section 5.2.1) and extraction of average spectra from different regions of the galaxy (Section 5.2.2). I describe the spectral fitting of both the MUSE data to derive stellar population parameters (Section 5.2.3) and the KMOS data to derive the best-fitting IMF (Section 5.2.4). I discuss the results derived for IC 1459 (Section 5.3) and summarise the conclusions of Part II of the thesis (Section 5.4). In Chapter 6 I give an overview of the research performed and main conclusions drawn from results presented in this thesis (Section 6.1). Finally, I give a brief description of my plans for future work (Section 6.2).

Throughout this thesis, I assume Λ CDM cosmology with $\Omega_m = 0.3$, $\Omega_\Lambda = 0.7$, $H_0 = 70 \text{ km s}^{-1} \text{ Mpc}^{-1}$ (these agree well with the latest results from [Planck Collaboration et al. 2016b](#)) and use the AB magnitude system ([Oke & Gunn, 1983](#)).

Part I – The KMOS Cluster Survey:
Fundamental Plane of Cluster Galaxies at
 $z \simeq 1.80$ in JKCS 041

*“Your reward will be the widening of the horizon as you climb. And if you achieve
that reward you will ask no other.”*

— Cecilia Payne-Gaposchkin, *Cecilia Payne-Gaposchkin: An Autobiography and
Other Recollections*, 1996

Abstract

I present data for 16 galaxies in the overdensity JKCS 041 at $z \simeq 1.80$ as part of the K-band Multi-Object Spectrograph (KMOS) Cluster Survey (KCS). With 20-hour integrations, deep absorption-line spectra were obtained from which I derived velocity dispersions for seven quiescent galaxies. This expands the sample of like measurements in the literature at $z \gtrsim 1.80$ by $> 40\%$. I combined photometric parameters derived from *Hubble Space Telescope* images with the dispersions to construct the highest redshift fundamental plane (FP) for quiescent galaxies in a single cluster for JKCS 041. From the zero-point evolution of the FP, I derived a formation redshift for the galaxies of $z_{\text{form}} = 3.0 \pm 0.3$, corresponding to a mean age of 1.4 ± 0.2 Gyrs. I tested the effect of structural and velocity-dispersion evolution on the FP zero point and found a negligible contribution when using dynamical-mass-normalised parameters ($\sim 3\%$), but a significant contribution from stellar-mass-normalised parameters ($\sim 42\%$). From the relative velocities of the galaxies, I probed the three-dimensional structure of these 16 confirmed members of JKCS 041. The bulk of the galaxies formed a fairly relaxed population that extended eastward which could represent the core of the cluster. I discovered that a group of galaxies in the south west of the overdensity had systematically higher velocities which could indicate that they are infalling. I derived mean ages for the galaxies in the different groups from the FP. I found that galaxies in the east-extending relaxed group had a significantly older mean age ($2.1^{+0.3}_{-0.2}$ Gyrs) than those in the infalling south-west group (0.3 ± 0.2 Gyrs). Although based on small numbers, the overdensity dynamics, morphology, and age results indicate that JKCS 041 is in formation and comprises two merging groups of galaxies. The result could link large-scale structure to ages of galaxies for the first time at this redshift. I also noticed that the quiescent galaxies in the infalling group were extremely compact and massive ‘red nugget’ galaxies. The young age measured is consistent with a rapid formation of stars in a starburst phase that has led to the quenching of the galaxies. The results might suggest that the group environment of galaxies falling into a large potential of the cluster facilitates this channel of evolution for massive ETGs. This is the most detailed study of a high-redshift cluster to date and reveals a complex picture of massive ETG and cluster formation in the early Universe.

Chapter 2

KMOS Data and Spectroscopic Analysis of Galaxies in JKCS 041

This first chapter of Part I of my thesis will cover the KMOS element of the project to analyse galaxies in the high-redshift cluster JKCS 041 as part of KCS in order to understand their properties and evolution. I will give details of the KMOS instrument (Section 2.1) and overview of KCS (Section 2.2). I will then detail the KMOS data (Section 2.3), including sample selection (Section 2.3.1), completeness (Section 2.3.2), KMOS targets (Section 2.3.3), and observations (Section 2.3.4). Finally, I will describe the reduction (Section 2.4) and analysis (Section 2.5) of the KMOS spectra of galaxies in JKCS 041.

2.1 The KMOS Instrument

KMOS on the European Southern Observatory (ESO) VLT on Cerro Paranal in Chile is a NIR multi-IFU spectrograph. KMOS was installed on the VLT Unit Telescope 1 (UT1 a.k.a Antu), which is one of four identical 8.2 m telescopes at the Paranal Observatory, during September–October 2012. First light was on 21st November 2012, and early operations started in Period 92 (P92) in October 2013. KMOS is mounted at the Nasmyth focus. To account for the rotation of objects in the FOV during exposures, the instrument itself rotates about the horizontal optical axis to counteract the field rotation. This causes differential flexure upon the instrument that is dealt with during the data reduction processes described in Sections 2.4 and 5.1.1.2.

KMOS has the unique feature of being both a multi-object and integral-field infrared spectroscopic instrument. It can simultaneously observe 24 different targets each with a $2.8'' \times 2.8''$, 14×14 pixel deployable IFU. The IFUs with $0.2'' \times 0.2''$

Table 2.1: Summary of properties of the KMOS gratings.

Grating	Wavelength Coverage (μm)	Pixel Scale (nm/pixel)	Resolving Power (band centre)
<i>IZ</i>	0.779–1.079	0.143	3406
<i>YJ</i>	1.025–1.344	0.165	3582
<i>H</i>	1.456–1.846	0.203	4045
<i>K</i>	1.934–2.460	0.266	4227
<i>HK</i>	1.484–2.442	0.489	1985

spatial pixel scales were designed to sample the optimal infrared seeing at the Paranal Observatory. The 24 configurable arms of KMOS are free to move within a 7.2' diameter patrol field. The arms with the IFUs at the end and the central patrol field are shown in the top panel of Figure 2.1.

The 24 arms feed into three cryogenic grating spectrographs that generate 196 spectra with ~ 1000 Nyquist-sampled spectral resolution elements for each of the 24 targets. The spectra have 2048 wavelength pixels meaning there are more than two times the number of pixels per spectral resolution element to ensure sufficient sampling. These three spectrographs feed to three high-sensitivity NIR detectors: HgCdTe Astronomy Wide Area Infrared Imager with 2k \times 2k (i.e. 2048 \times 2048, 18 μm pixel resolution) Reference pixels and Guide mode (HAWAII-2RG) arrays (from Teledyne Imaging Sensors), each of which receives data from eight of the arms. The back of the instrument with the three spectrographs mounted on it is shown in the bottom panel of Figure 2.1. The instrument is cryogenically cooled to reduce thermal background radiation, which can strongly affect NIR wavelengths. A block diagram of KMOS is shown in Figure 2.2.

KMOS has five grating combinations (*IZ*, *YJ*, *H*, *K*, and *HK*) that each offer different wavelength coverage and span a total range of 0.8 μm to 2.4 μm . The wavelength gaps between the bands (e.g. between *YJ* and *H*) avoid the main atmospheric transmission bands (see Section 2.1.1). The different bands can be chosen based on the science requirements; the most obvious being to cover spectral features at different redshifts. Each band has a different resolution which is defined at a specific wavelength (λ) as the width of a wavelength channel ($\Delta\lambda$) or the difference in velocities (Δv) that can be measured through the Doppler effect: $R = \frac{\lambda}{\Delta\lambda} = \frac{c}{\Delta v}$, where c is the speed of light. A summary of the properties of the KMOS gratings, including wavelength coverage, pixel scale, and resolving power at the centre of each band, are shown in Table 2.1.

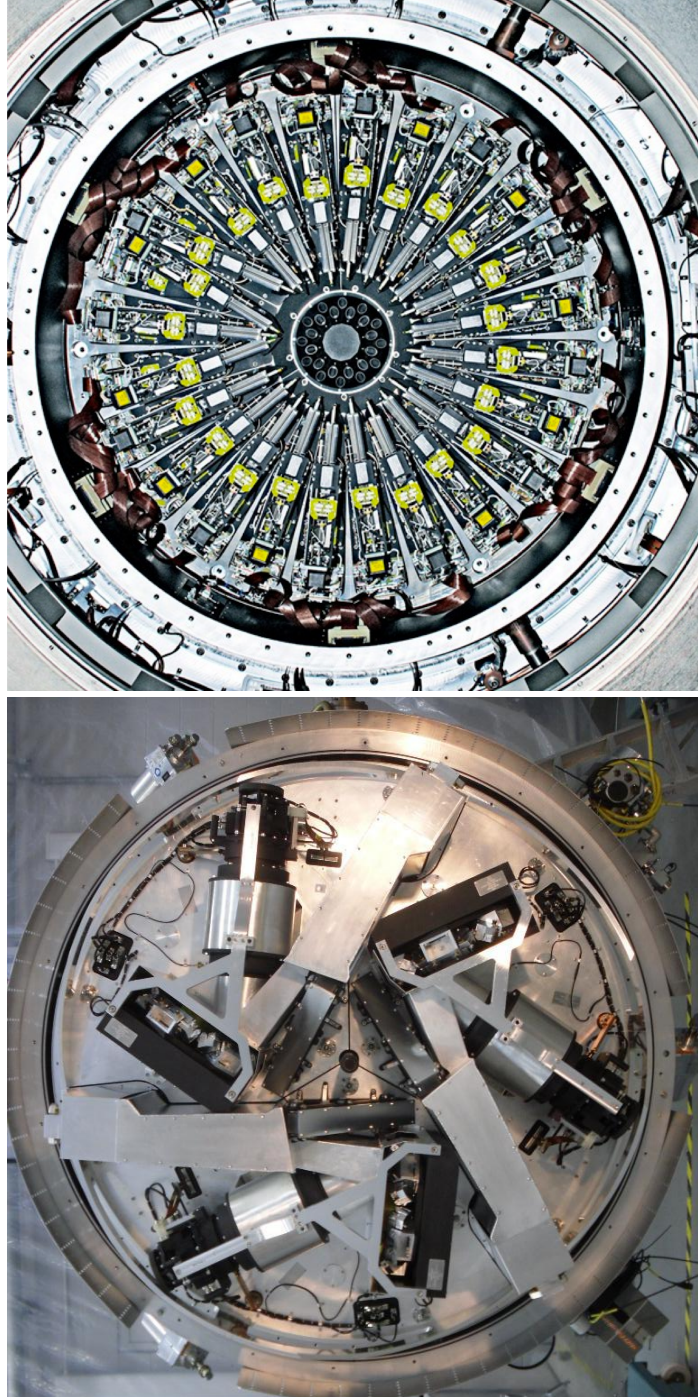


Figure 2.1: *Top:* The 24 pick-off arms of KMOS with the IFUs attached and positioned around the KMOS FOV at the centre. *Bottom:* The three spectrographs mounted on the KMOS cryostat. Both images are ~ 2 m across. Credit: ESO.

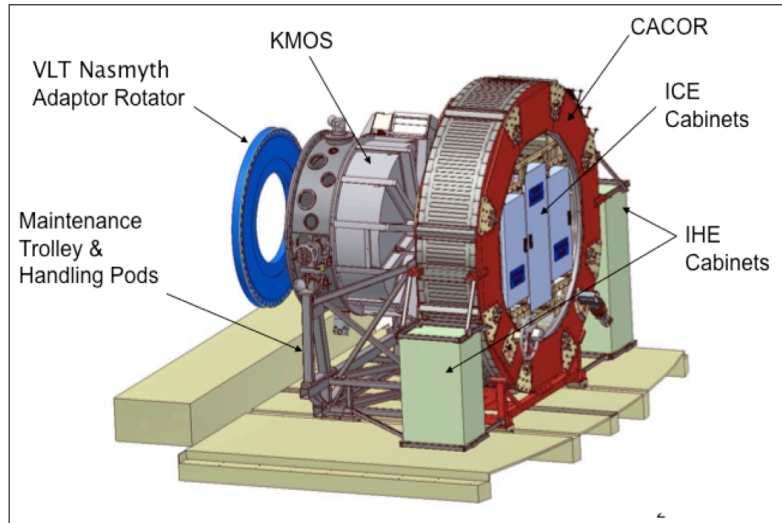


Figure 2.2: Block diagram of KMOS on the Nasmyth focus platform of the VLT UT1. The instrument is cryogenically cooled to reduce thermal background. The Nasmyth Adaptor Rotator keeps the image in a fixed position with respect to the FOV. Acronyms: instrument housekeeping electronics (IHE), instrument control electronics (ICE), and instrument specific cable co-rotator (CACOR). Credit: ESO.

2.1.1 Atmospheric Contamination in the NIR

At NIR wavelengths contamination from the Earth's atmosphere can be significant. Absorption and emission from the atmosphere can affect the shape of the spectrum and also the sensitivity of the observations. One type of contamination is telluric absorption; this is where some fraction of the light from an astronomical object is absorbed by molecules in the Earth's atmosphere. Water, oxygen, and OH are particularly bad for this, and it affects both the optical, but more strongly, the NIR portion of the spectrum. This absorption can be corrected for in a couple of different ways, although no one method can do this perfectly, in a large part due to the rapid variability of the Earth's atmosphere on the timescale of astronomical observations. One way to correct the telluric absorption is to take a spectrum of a standard star, whose spectrum is well understood and modelled, therefore any strong absorption not expected from the star can be assumed to be from the atmosphere. A newer approach is to model the effects of telluric absorption, more details of this method are in Sections 2.4 and 5.1.3. However, these corrections may not be sufficient if the absorption reduces the signal so significantly in certain wavebands that it makes objects unobservable from the ground.

Another type of contamination is emission from molecules in the night sky, these show as extremely bright emission features in the spectra and are typically from OH.

The flux added by these bright lines increases the Poisson noise of the data, reducing the sensitivity of the observations. These bright sky lines, although contaminating the spectra, can have their uses for reducing data. Their widths can be used to quantify the varying line-spread function of instruments such as KMOS, and as they occur at fixed wavelengths, they can be used as wavelength calibrators.

2.2 The KMOS Cluster Survey

2.2.1 Overview

KCS (P.I.s Davies and Bender; [Davies et al., 2015](#), Davies, Bender et al., in prep.) is a 30-night KMOS GTO project and collaboration between researchers at the University of Oxford, Max-Planck Institute for Extraterrestrial Physics (MPE) in Garching, Germany, and Durham University. The aim of the GTO programme was to study ETGs in overdensities between $1 < z < 2$ in order to constrain galaxy evolutionary processes in dense environments at higher redshifts than previously possible. KMOS was designed for such high-redshift, high-density target observations. The KMOS FOV ($\sim 7'$ diameter) covers the cores of most clusters within the KCS redshift range (~ 3.5 Mpc at $z \sim 1.5$). The IFU sizes ($2.8'' \times 2.8''$) are sufficient to cover the entire surface of almost all the galaxies in the target KCS clusters in the redshift range ($\sim 23 \times 23$ kpc at $z \sim 1.5$).

Constraining stellar kinematics and stellar population properties from galaxy spectra is done by measuring the absorption features in the relatively faint continuum light (compared to bright emission lines from SF galaxies) of quiescent galaxies (see Section 1.1.1). Long integrations on large telescopes are required to reach the sensitivity needed to probe the faint stellar continuum light of distant ETGs. KMOS's multi-object capabilities meant that larger samples of absorption-line spectra of ETGs could be built up more efficiently. The allocated GTO time enabled this extended programme to achieve the required sensitivities for constraining the stellar properties of the galaxies in the KCS target overdensities through ~ 20 -hour on-source observations.

The analysis required to study the galaxies in the KCS overdensities falls broadly into two categories; spectroscopic and photometric. The key steps of analysis for the KCS sample are outlined as follows:

1. Using high-resolution HST photometry to select a sample of galaxies in each overdensity to observe with KMOS.

2. Observing around 20 galaxies in each overdensity for ~ 20 -hours on source with KMOS.
3. Reducing the KMOS observations to get one spectrum per KCS target cluster galaxy.
4. Measuring stellar kinematics from the galaxy spectra.
5. Reducing (or re-reducing if already published) HST images and analysing the photometric properties of the galaxies, such as magnitude, size, surface brightness, etc.
6. Combining photometric and spectroscopic properties to construct a FP (see Section 1.1.1) and derive mean galaxy ages.
7. Measuring properties of the stellar populations from full-spectral fitting of the absorption-line spectra.
8. Observing and analysing emission-line galaxies in the target KCS overdensities.

In this chapter, I focus on the first four steps; the target selection, KMOS observations, the reduction, and analysis of the KMOS spectra. Steps 5, 6, and 7 will be covered in Chapters 3, 4, and the future work section of the Conclusions (Section 6.2), respectively.

There are five KCS target overdensities, a summary of which is in Section 2.2.2. The work presented in Part I of this thesis focuses on the highest-redshift KCS target cluster, JKCS 041 at $z = 1.80$, that was the subject of the third KCS paper and published in [Prichard et al. \(2017b\)](#). The first KCS paper, by [Beifiori et al. \(2017\)](#), is an FP study focusing on three other clusters between $z = 1.39$ and $z = 1.61$. The photometric analysis for the clusters in [Beifiori et al. \(2017\)](#) is presented in two papers, [Chan et al. \(2016\)](#), and the second KCS paper, [Chan et al. \(2018\)](#). The final target is a lower redshift cluster at $z = 1.04$. It was used as a backup target for when the other clusters could not be observed, for example, when there was a strong northerly wind that meant only low declination southern targets could be observed. This lower-redshift cluster had less exposure time (~ 10 hours); the photometry for this cluster has been reduced and analysed by a master's student at MPE and will be published in due course. Emission-line studies of SF cluster galaxies (step 8 above) will be done for two clusters at $z = 1.39$ and $z = 1.46$ in a future KCS paper ([Stott et al.](#), in prep.). Ages derived from the full-spectral fitting of the galaxy spectra in the

overdensities in [Beifiori et al. \(2017\)](#) will be covered in an upcoming paper ([Mendel et al., 2018b, in prep.](#)). See Section 6.2.1 on future work for details on full-spectral fitting of galaxies in JKCS 041.

2.2.2 KCS Target Clusters

The target overdensities for KCS were required to be between $1 \lesssim z \lesssim 2$, have many bright red-sequence galaxies, and multi-band HST imaging. Ideally, each overdensity contained ~ 20 sufficiently bright quiescent galaxies on the red sequence and a large number of spectroscopic redshifts. Each target was required to have multi-band HST imaging as it was used in both the reduction of the KMOS spectra (see Section 2.4) and to investigate the photometric and structural properties of the overdensity galaxies (see Chapter 3).

Although the work described in Part I of this thesis will focus on JKCS 041, I give an overview of the properties of each as the KCS results for the other clusters will be used to provide context for the results presented here.

2.2.2.1 JKCS 041 at $z = 1.80$

Part I of this thesis will focus on JKCS 041, the highest redshift cluster in the KCS sample, I therefore give a more detailed overview of past studies of this cluster to provide context for the results. It was first detected as an overdensity of galaxies with similar $J - K$ colours — a modified red-sequence selection method (see Section 1.1.4; [Gladders & Yee, 2005](#)) — from United Kingdom Infrared Telescope Infrared Deep Sky Survey (UKIDSS; [Lawrence et al., 2007](#)) photometry in the Early Data Release ([Dye et al., 2006](#)). X-ray observations of the overdensity were made with *Chandra* and were smoothed with a large Gaussian kernel (with $\sigma \approx 20''$ within the central $30''$) chosen due to the low S/N of the cluster X-ray emission ([Andreon et al., 2009](#)). There are also a few X-ray bright foreground sources in the image, which as seen by the contours from [Andreon et al. \(2009\)](#) (on Figures 2.3 and 2.7), have not been masked prior to smoothing. For these reasons, both the smooth morphology of the X-ray contours and the location of the centroid are both to be taken with caution. A cluster distance of $z \sim 1.9$ was found using photometric redshift (photo- z) measurements ([Andreon et al., 2009](#)). Photo- z s are determined from fitting multi-band photometry with model spectral energy distributions (SEDs). Photo- z s measurement are useful for obtaining redshift estimates for all galaxies within a photometric FOV. These provide redshift errors on the order of $\delta z \sim 0.1\text{--}0.5$ which becomes increasingly significant at lower redshifts.

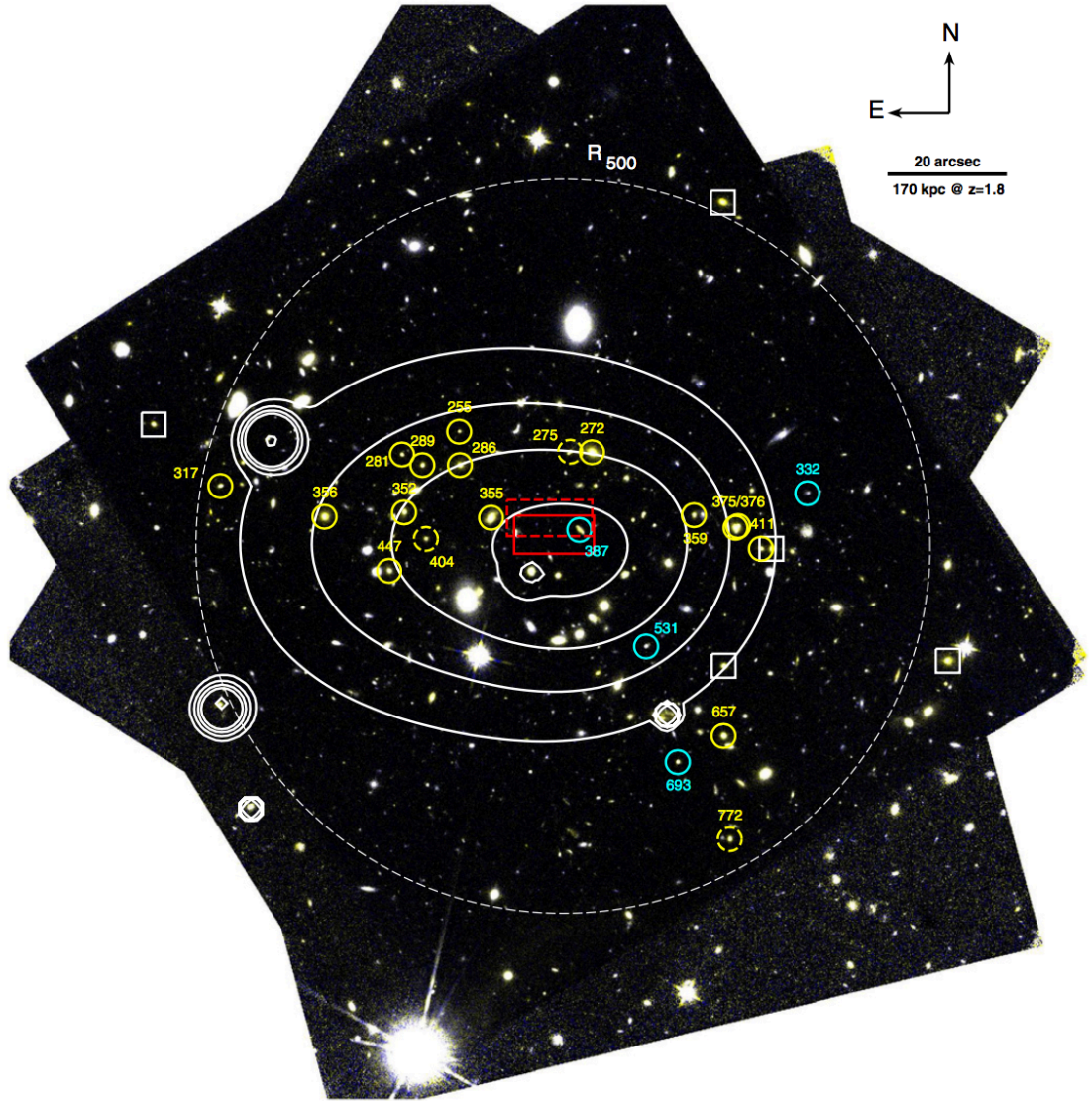


Figure 2.3: HST/WFC3 image of JKCS 041 taken from the spectroscopic confirmation paper (N14). The image is a composite of both HST/WFC3 F160W and F105W bands (see Chapter 3 for a description of the different bands and photometric data). The HST grism spectroscopically confirmed members are shown by the solid circles (blue – SF, yellow – quiescent). The three dashed yellow circles show candidate cluster members: those that are on the red sequence but could not be spectroscopically confirmed. The large white dashed circle represents R_{500} ($\sim 0.5R_{200}$, where R_{200} is the virial radius) and is commonly observed out to for overdensity X-ray measurements. The heavily smoothed X-ray contours from *Chandra* data are shown by the solid white contours (from Andreon et al., 2009). The red rectangles represent the 1σ errors of the confirmed cluster galaxy position centroid (solid) and quiescent galaxy mass-weighted centroid (dashed). The spectroscopically confirmed non-members on the cluster red sequence are shown by white squares (Figure 2.7 shows all confirmed non-members).

The cluster was spectroscopically confirmed at $z = 1.80$ (N14) using HST grism spectroscopy from Wide-Field Camera 3 (WFC3), which at the time was the highest-redshift cluster known. N14 also took companion deep HST images in two NIR bands, F105W (or Y_{105}) and F160W (H_{160}), that I re-reduced and analysed to study the galaxies in JKCS 041 for this work. Full details of the HST filters, these observations, and the analysis performed in N14 and my photometric reduction and analysis are detailed in Chapter 3. The 19 spectroscopically confirmed members were centred on the X-ray emission found by Andreon et al. (2009) as shown in the HST/WFC3 image of JKCS 041 from N14 (Figure 2.3) with confirmed members highlighted.

JKCS 041 is very rich compared to other clusters found at similar redshifts. It has a well-defined red sequence and 15/19 galaxies confirmed by N14 are quiescent. N14 made composite grism spectra of the quiescent galaxies. They showed strong Balmer and metallic absorption lines and were used to derive stellar ages in two stellar mass bins. Comparing the cluster galaxies in JKCS 041 to a mass-matched field sample from Whitaker et al. (2011), N14 found their ages to be similar but that 88% of galaxies in the cluster sample were quiescent compared to $< 50\%$ in the field from the National Optical Astronomy Observatory Extremely Wide-Field Infrared Imager (NEWFIRM) Medium Band Survey (NMBS; Whitaker et al., 2011). These results implied that the cluster environment was more efficient at quenching star formation than the field. N14 concluded that the cluster environment was responsible for quenching $\sim 50\%$ of quiescent galaxies. They also found evidence for a lower fraction of disc-like quiescent galaxies in the cluster that indicated that the dense environment either inhibited growth or more effectively destroyed discs. Lotz et al. (2013) showed that there are high numbers of merger remnants in high-redshift protocluster environments, however, these are not seen in JKCS 041. This implies that JKCS 041 is a more virialised cluster with a dispersion too high to facilitate efficient merging. N14 also noted that there are no AGN (see Section 1.1.3) detected in any of the galaxies in JKCS 041.

JKCS 041 is an extremely massive cluster with $\log(M/M_{\odot}) = 14.2\text{--}14.5$ (Andreon et al., 2014) and will evolve into something of greater mass than the Coma cluster in the local Universe (see Figure 2.5 taken from Beifiori et al. 2017 for model DM halo evolutionary track predictions). The cluster mass was estimated using four methods, X-ray temperature, X-ray luminosity, gas mass, and cluster richness (Andreon et al., 2014). This cluster was not detected in a survey (Culverhouse et al., 2010) of the Sunyaev-Zel'dovich effect (Sunyaev & Zeldovich, 1972), which places a firm upper limit on its total mass.

In the companion paper to that of N14, Andreon et al. (2014) utilised the same HST/WFC3 images to study the properties of the red sequence. Unlike N14, who identified SF galaxies using the colour-colour UVJ selection technique, Andreon et al. (2014) used the colour-magnitude diagram method of selecting red galaxies (see Section 1.1.1) utilising the Y_{105} and H_{160} HST bands. As a result, the two papers have slightly different quiescent and SF populations. With one less SF galaxy identified toward the cluster centre, Andreon et al. (2014) commented that the few SF are away from the cluster core. From the extensive red sequence analysis, Andreon et al. (2014) concluded that due to the quiescent galaxies spanning a range of ~ 5 magnitudes, quenching was already effective 10 Gyrs ago, and that most galaxies were quenched ~ 1.1 Gyrs prior to the epoch of observation.

2.2.2.2 Cl 0332-2742 (Cl0332) at $z = 1.61$

The Cl0332 cluster is a rare case in that it was identified by an overdensity of galaxies in photo- z space (Castellano et al., 2007). It was then spectroscopically confirmed in the Galaxy Mass Assembly ultra-deep Spectroscopic Survey (GMAS; Kurk et al., 2013) which targeted $z_{\text{phot}} > 1.4$ galaxies in the Great Observatories Origins Deep Survey Southern field (Giavalisco et al., 2004) with the VLT/FOcal Reducer and low dispersion Spectrograph (FORS2). Kurk et al. (2009) confirmed 44 members between $1.600 < z < 1.622$ and found that the overdensity comprised two populations. Mass estimates of this cluster are uncertain and range from a virial mass, $M_{200} \sim 6.4 \times 10^{13} h^{-1} M_{\odot}$, from galaxy kinematics that assumes that the cluster is virialised (Kurk et al., 2009), to $M_{200} \sim 1.2 \times 10^{14} h^{-1} M_{\odot}$ by summing the mass of the X-ray groups surrounding the galaxy overdensity (Finoguenov et al., 2015). Utilising deep *Chandra* data, an X-ray source was detected that coincides with a group of quiescent galaxies (Tanaka et al., 2013). This could represent a gravitationally bound subgroup merging with the larger structure. All this evidence implies that Cl0332 is a protocluster – a young cluster in formation and not yet collapsed to a virialised state. Despite this, Cl0332 does show a significant red sequence (Kurk et al., 2009). From analysis of seven stacked spectra, the galaxies in this overdensity were found to have young ages (~ 1 Gyrs), low specific star-formation rates, and low dust extinction (Cimatti et al., 2008).

2.2.2.3 XMMXCS J2215.9-1738 (XMM2215) at $z = 1.46$

XMM2215 was detected in the *X-ray Multi-Mirror Mission (XMM-Newton)* Cluster Survey as an extended X-ray source and was spectroscopically confirmed with Keck

II/DEep Imaging Multi-Object Spectrograph (DEIMOS) with six members at $z \sim 1.45$ (Stanford et al., 2006). With further Keck II/DEIMOS and Gemini Multi-Object Spectrographs spectra, 44 members were confirmed (Hilton et al., 2010). XMM2215 is a massive overdensity ($M_{200} \sim 2.1 \times 10^{14} h^{-1} M_{\odot}$; Stott et al., 2010) but is not fully virialised (Ma et al., 2015) as deduced from the bimodality of the galaxy velocity distribution (e.g. Hilton et al., 2007, 2010), and that there is no clear central BCG (see Section 1.1.4; Hilton et al., 2009; Stott et al., 2010). The red sequence for this cluster comprises relatively low-mass galaxies that have some SF signatures (e.g., Hilton et al., 2009, 2010; Hayashi et al., 2010, 2011, 2014) and has significant scatter (three times greater than Coma). The formation redshift derived from the red-sequence intercept is $z_{\text{form}} = 3\text{--}5$ (Hilton et al., 2009). Some galaxies in the core show evidence of obscured star formation (Hilton et al., 2010; Ma et al., 2015) and AGN (Hayashi et al., 2011).

2.2.2.4 XMMU J2235.3-2557 (XMM2235) at $z = 1.39$

This cluster was detected with *XMM-Newton* and spectroscopically confirmed using VLT/FORS2 with 12 members at $z = 1.39$ (Mullis et al., 2005). It is a very massive ($M_{200} \sim 7.7 \times 10^{14} h^{-1} M_{\odot}$; Stott et al., 2010) and virialised cluster (Rosati et al., 2009; Stott et al., 2010; Jee et al., 2011). Further VLT/FORS2 spectroscopic follow up confirmed 34 cluster members, 16 of which are in the core 1 Mpc and are quiescent (Rosati et al., 2009). Its central core (~ 200 kpc) shows no evidence of star formation, implying it has long been quenched (Strazzullo et al., 2010; Bauer et al., 2011), compared with the outskirts which show a significant number of galaxies with SF signatures (Bauer et al., 2011; Grützbauch et al., 2012). Generally, there is evidence to show that all the massive galaxies have low SFRs (Grützbauch et al., 2012). Age estimates for galaxies within the cluster from either stacked spectra (e.g. Rosati et al., 2009) or the colour and scatter of the red sequence (Lidman et al., 2008) showed that the galaxies in the cluster centre were formed at early times ($z > 3\text{--}4$).

2.2.2.5 RCS 2345-3632 (RCS2345) at $z = 1.04$

RCS2345 is an ETG-rich cluster that was detected as part of the Red-Sequence Cluster Survey (Gladders & Yee, 2005; Gilbank et al., 2007, 2011). It has 34 spectroscopically confirmed members (from Gilbank et al., 2007; Meyers et al., 2012). Mass measurements from weak lensing estimate the mass of this cluster to be $M_{200} \sim 2.4 \times 10^{14} h^{-1} M_{\odot}$ (Jee et al., 2011). This cluster falls in the redshift gap of massive virialised clusters at $0.9 < z < 1.2$. It also helps to bridge the higher-redshift cluster

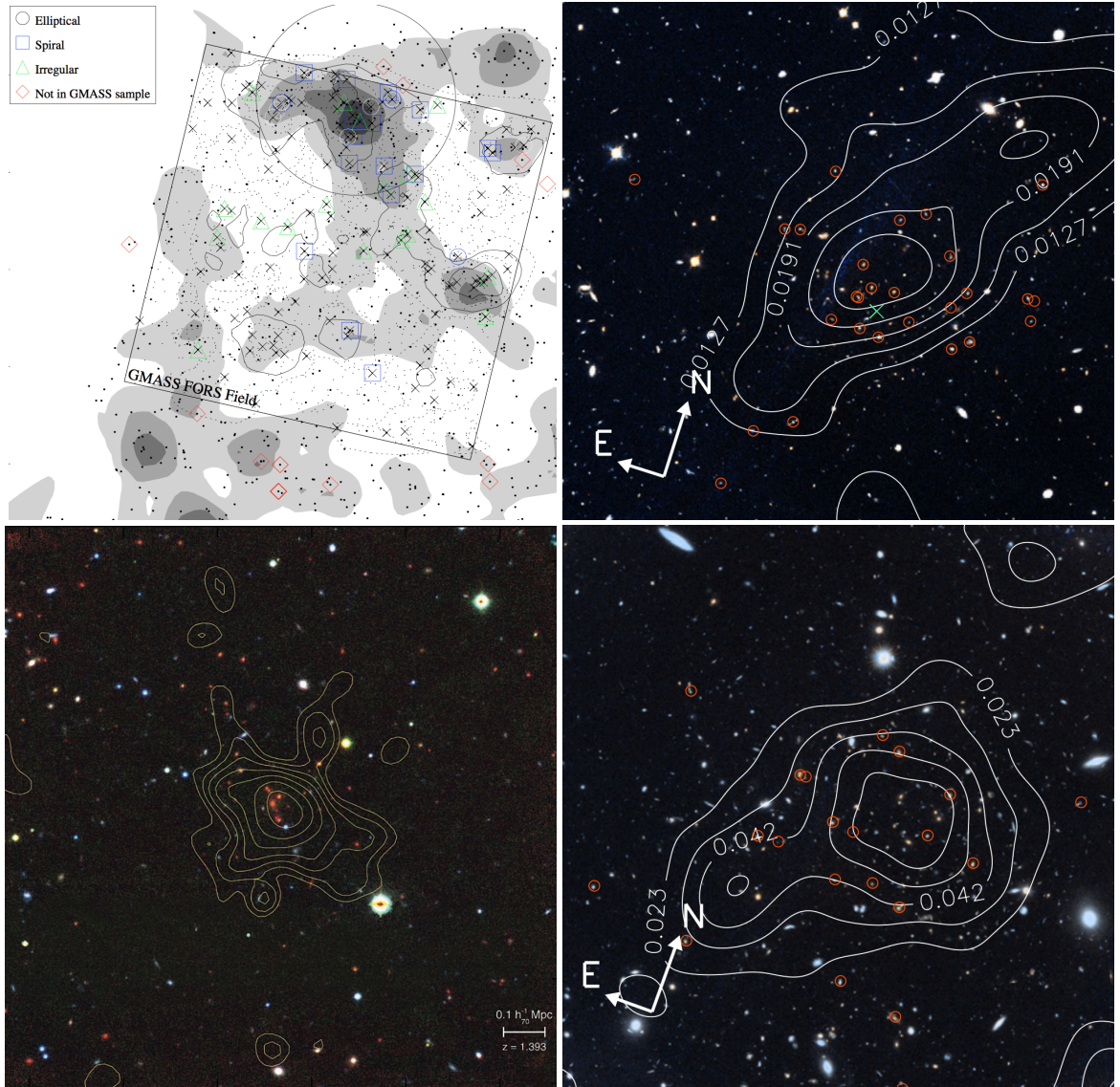


Figure 2.4: Four KCS target clusters. *Top left*: Cl0332 at $z = 1.61$ (from Kurk et al., 2009), ~ 420 kpc across, north is up, east is left. Shaded regions represent $0.0, 0.25, 0.5,$ and $0.75\times$ the maximum overdensity above the median density of galaxies at $z = 1.6$. Galaxies in (large crosses) and out of (small dots) the overdensity redshift range are shown. Confirmed redshift elliptical (circles), spirals (squares), irregular galaxies (triangles), galaxies with late-type spectra (blue symbols), and galaxies not in GMASS (red diamonds) are indicated. *Top right*: XMM2215 at $z = 1.46$ (from Jee et al., 2011) pseudo-colour i_{775} - and z_{850} -band combined image (~ 920 kpc across). Mass contours (white), peak of the *Chandra* X-ray emission (green cross), and spectroscopic members (red circles) are shown. *Bottom left*: XMM2235 at $z = 1.39$ (from Mullis et al., 2005) pseudo-colour K_s -, z -, and R -band combined image, north is up, east is left. *XMM-Newton* X-ray contours (yellow) are shown. *Bottom right*: The backup cluster RCS2345 at $z = 1.04$ (from Jee et al., 2011), same labelling as top right panel. See Section 2.2.2.

analysis of the other KCS targets with the wealth of $z \sim 0.5$ massive clusters which have been targeted as lensing objects that magnify galaxies in the early Universe (see Section 1.1.4).

2.2.3 Status and Results of KCS

2.2.3.1 Observing Summary

Observations for KCS, totalling 30 allocated nights, have run between P92 – October 2013, and P99 – August 2017¹. Observations for the four clusters at $z = 1.39$ – 1.80 were in the KMOS *YJ* band (1.025 – $1.344 \mu\text{m}$) while the lower redshift backup cluster, RCS2345 at $z = 1.04$, was observed in the *IZ* band (0.779 – $1.079 \mu\text{m}$) to target the well-understood rest-frame optical absorption-line indices for all the galaxies. The atmospheric seeing was required to be $< 1''$ for the KCS observations to ensure sufficient data quality. Emission-line studies taken later (P98) were in the *H* band (1.456 – $1.846 \mu\text{m}$) to target bright lines from SF galaxies – e.g. $\text{H}\alpha$ and $[\text{NII}]$. Targets for the emission-line study were red-sequence objects observed for absorption-lines that showed emission in *YJ* ($[\text{OIII}]$, $\text{H}\beta$) and so were observed in the *H* band. An overview of the observations and spectroscopic analysis of the KCS galaxies is given below.

- Of the four main clusters, 106 galaxies were observed in *YJ*; 86 of these were for ~ 15 – 20 hours on source, and 20 were emission-line objects with exposure times of ~ 5 – 10 hours on source.
- 67 galaxies were passive, either determined from the red-sequence or a *UVJ* colour-colour selection. Of these, only around half were at the redshifts of the clusters as there were many interlopers.
- For the spectroscopically confirmed (with KMOS spectra) quiescent cluster members, 26 stellar velocity dispersion measurements were determined.
- Emission-line galaxies in XMM2215 and XMM2235 were observed for ~ 5 hours on source in *H* band in P98.
- Of the 38 emission-line targets, secure redshifts were obtained for 33: 14 in XMM2235 and 19 in XMM2215.

¹The last two nights of KCS time that were to be observed in P99 were lost due to a power cut at Paranal.

- Resolved H α maps were determined for 11 galaxies in XMM2235 and 17 in XMM2215.
- The backup cluster has 20 red sequence galaxies observed for ~ 9 hours on source in *IZ*.

Some of the errors in assigning candidate objects to clusters were due to red-sequence selection; galaxies that are dusty and SF appear redder due to UV light from hot stars being scattered by the dust to redder wavelengths. They then appear to lie on the red sequence in colour-magnitude space. The low spectroscopic confirmation rate could also be driven by inaccurate photo- z measurements that were taken from previous papers when selecting targets for three of the KCS overdensities (Beifiori et al., 2017). The galaxies in JKCS 041 were already spectrophotometrically (see Section 2.3.1) confirmed and so I did not find any non-cluster members in the sample.

2.2.3.2 Summary of Beifiori et al. (2017)

The first paper in the KCS series (Beifiori et al., 2017) gave a survey overview and presented KMOS spectra for three of the KCS targets between $1.39 \lesssim z \lesssim 1.61$ (XMM2235, XMM2215, and Cl0332), and performed an FP analysis for the galaxies within them. As I use similar techniques for the FP analysis of JKCS 041 and place my results in the context of the whole KCS sample, I briefly summarise the relevant methods and results from Beifiori et al. (2017) for reference.

For the three KCS overdensities in Beifiori et al. (2017), there were HST images and extensive ground-based ancillary photometry, the detailed analysis of which was performed in two papers (see Section 2.2.3.3 Chan et al., 2016, 2018). Quiescent galaxies in the clusters were selected from CMDs; the red sequence was fitted and all galaxies within 2σ of the fit were selected. The brightest red sequence galaxies with spectroscopic redshift measurements in the literature were prioritised (to minimise observing time lost on non-cluster members), followed by red-sequence galaxies with no redshift values available, then fainter red sequence or SF galaxies were observed to fill remaining IFUs in the FOV. Around 20 galaxies were targeted in each overdensity, with the spare arms reserved for faint stars (see Section 2.3.4 for more details).

Galaxy structural parameters were adopted from Chan et al. (2016, 2018). Beifiori et al. (2017) measured stellar velocity dispersions from the KMOS spectra using the Penalised PiXel-Fitting method (PPXF, see Section 2.5.2; Cappellari & Emsellem, 2004; Cappellari, 2017) using the Maraston & Strömbäck (2011), SSP models (see Section 1.1.7) based on the ELODIE v3.1 stellar library (Prugniel & Soubiran, 2001;

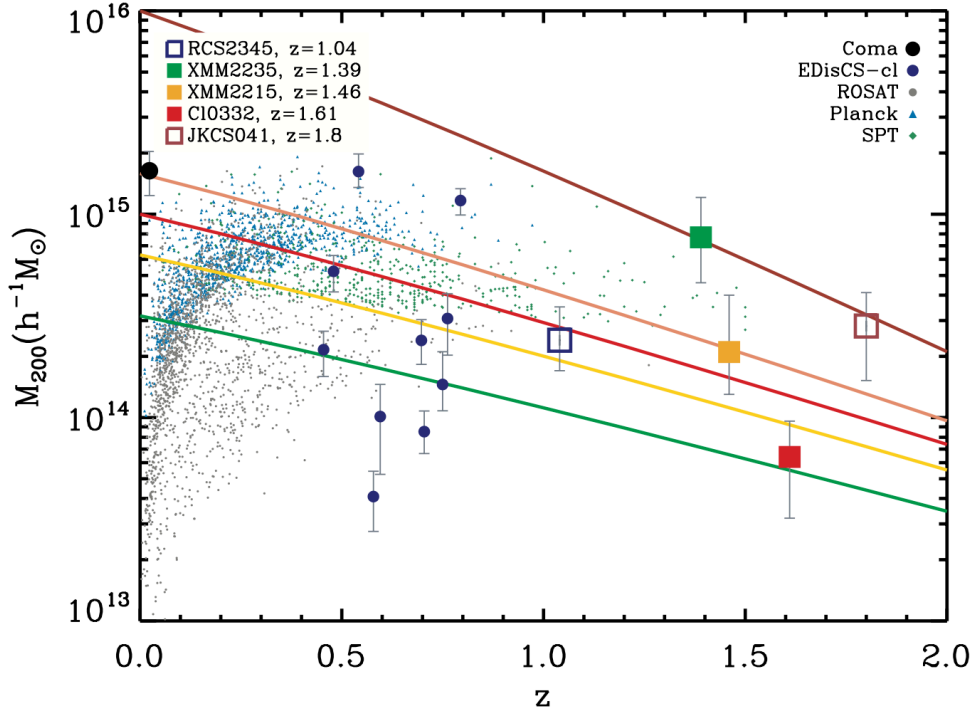


Figure 2.5: This figure (Figure 1. from [Beifiori et al. 2017](#)) shows cluster masses (within the virial radius – M_{200}) of all five KCS targets as made from X-ray data and cluster kinematics (as tabulated in [Stott et al., 2010](#); [Kurk et al., 2009](#), respectively), weak lensing (for RCS2345; [Jee et al., 2011](#)), or X-ray and clustering analysis (for JKCS 041; [Andreon et al., 2014](#)), as a function of redshift. This figure from [Beifiori et al. \(2017\)](#), shows the three clusters analysed in that paper with solid squares, the other two clusters (the backup cluster and JKCS 041) not analysed are shown as unfilled squares. A number of lower redshift comparisons are also given: Coma ([Łokas & Mamon, 2003](#)), ESO Distant Clusters Survey (EDisCS; [Saglia et al., 2010](#)), ROentgen SATellite (ROSAT) Meta-Catalogue of X-ray detected Clusters ([Piffaretti et al., 2011](#)), Planck ([Planck Collaboration et al., 2016a](#)), and South Pole Telescope (SPT; [Bleem et al., 2015](#)). Over plotted are model tracks of the mass accretion history of dark matter halos with different initial masses (M_{in}) derived using the CONcentration-Mass relation and Mass Accretion History code (COMMAH; [Correa et al., 2015a,b,c](#)) with continuous lines ($\log(M_{in}/M_{\odot}) = 16$ in brown, $\log(M_{in}/M_{\odot}) = 15.2$ in coral, $\log(M_{in}/M_{\odot}) = 15$ in red, $\log(M_{in}/M_{\odot}) = 14.8$ in yellow, $\log(M_{in}/M_{\odot}) = 14.5$ in green). Credit: [Beifiori et al. \(2017\)](#).

Prugniel et al., 2007) that span 3900–6800Å. Velocity dispersions for 19 quiescent galaxies were measured in the three clusters. The photometric and spectroscopic values were used to construct FPs and to derive mean stellar ages for the galaxies from the zero-point evolution (see Sections 1.1.1 and 4.1 for more details) for three KCS overdensities: Cl0332, XMM2215, and XMM2235. Using FP analysis, Beifiori et al. (2017) found ages of the galaxies in Cl0332, XMM2215, and XMM2235. These are summarised below.

- For Cl0332 at $z = 1.61$, from four galaxies for which reliable velocity dispersions could be derived (which were all high mass, $\log(M/M_{\odot}) > 11$), Beifiori et al. (2017) derived their mean age from FP zero-point evolution to be 1.32 ± 0.35 Gyrs ($\sim 2.65 \pm 0.35$ Gyrs after the Big Bang).
- For XMM2215 at $z = 1.46$, using six galaxies for which velocity dispersions could be derived, Beifiori et al. (2017) determined their mean age to be 1.85 ± 0.46 Gyrs. For the three most massive galaxies ($\log(M/M_{\odot}) > 11$), the mean age was found to be 1.68 ± 0.28 Gyrs ($\sim 2.62 \pm 0.46$ Gyrs after the Big Bang).
- For XMM2235 at $z = 1.39$, for nine galaxies for which velocity dispersions were derived, Beifiori et al. (2017) measured their mean age to be 1.90 ± 0.50 Gyrs. The mean age for the five most massive galaxies ($\log(M/M_{\odot}) > 11$) was 2.32 ± 0.50 Gyrs ($\sim 2.16 \pm 0.50$ Gyrs after the Big Bang).

The results showed that the galaxies in the three overdensities were consistent with passive evolution and had formation epochs consistent within errors. Although interestingly, Beifiori et al. (2017) found a hint of an older relative formation age for the most massive galaxies in XMM2235 (the more massive and virialised cluster even when taking its redshift into account), compared to the more protocluster like Cl0332. They also found that Cl0332 had very young galaxies with similar ages to that of a field sample (Mendel et al., 2015). This could imply that galaxies in a more virialised and relaxed environment (i.e., XMM2235) undergo accelerated evolution, as found in previous studies (e.g., Gebhardt et al., 2003; Saglia et al., 2010; Strazzullo et al., 2013; Lani et al., 2013; Delaye et al., 2014).

The analysis presented in Part I of this thesis builds upon the work described in Beifiori et al. (2017). I derive the photometric and spectroscopic values for galaxies in JKCS 041 using modified methods or upgraded software and investigate their ages through analysis of the FP. I then extend this analysis to look at the dynamics and structure of the cluster and how galaxy ages differ depending on their location in the cluster.

2.2.3.3 Summary of Chan et al. (2016, 2018)

The photometric analysis for the three KCS clusters analysed in Beifiori et al. (2017) are detailed in Chan et al. (2016) (for XMM2235) and Chan et al. (2018) (for XMM2215 and Cl0332). I adopted similar methods for analysing the photometric data of JKCS 041 for a self-consistent KCS sample. I briefly summarise the analysis performed and results from these three KCS clusters for context with the analysis of JKCS 041 (detailed in Chapter 3).

Chan et al. (2016) studied the photometric structural parameters of 39 quiescent galaxies in XMM2235 at $z = 1.39$. Light-weighted 2D Sérsic profiles were fitted to five HST bands (i_{775} , z_{850} , Y_{105} , J_{125} , H_{160} ; see Chapter 3 for more details on HST filters) using a modified version of a software called Galaxy Analysis over Large Areas: Parameter Assessment by GALFITting Objects from Source Extractor (GALAPAGOS – see Section 3.4 for more details; Barden et al., 2012). Uncertainties for the photometric parameters of these galaxies were derived by simulating a variety of galaxy shapes, sizes, profiles and magnitudes, and randomly placing them into the HST images to test how well their properties could be recovered. I will detail upgrades I made to this suite of simulations for this study in Section 3.4.4. Chan et al. (2016) also produced spatially resolved mass maps, mass-weighted sizes and colour gradients for these galaxies. Mass maps were derived from making $z_{850} - H_{160}$ colour maps and converting this to a mass value following a derived M/L (see Section 3.6 for more details); this method requires two deep photometric bands. Chan et al. (2016) found an average $\sim 40\%$ decrease and at most a $\sim 70\%$ decrease in light-weighted size of the galaxies in XMM2235 compared to a local comparison sample in the same rest-frame band (from Bernardi et al., 2014). Similar trends were seen in the mass-weighted sizes. They found mostly negative colour gradients for the galaxies, implying an age gradient in the galaxy (younger stellar populations towards the outskirts), which is consistent with an inside-out growth mechanism (see Section 1.1.8; Bezanson et al., 2009; van Dokkum et al., 2010; Patel et al., 2013).

In Chan et al. (2018), light- and mass-weighted sizes were derived from optical and NIR HST images, along with resolved stellar-mass maps for the remaining two clusters (XMM2215 and Cl0332) using the same methods described in Chan et al. (2016). The mass-weighted sizes were $\sim 45\%$, $\sim 55\%$ and $\sim 20\%$ smaller than the light-weighted sizes for XMM2235, XMM2215, and Cl0332, respectively. This shows that the stellar mass is more concentrated than the light. Similar results were found to Chan et al. (2016) in that all the high-redshift cluster galaxies in the KCS targets had smaller sizes than local relations from Bernardi et al. (2014) and Cappellari

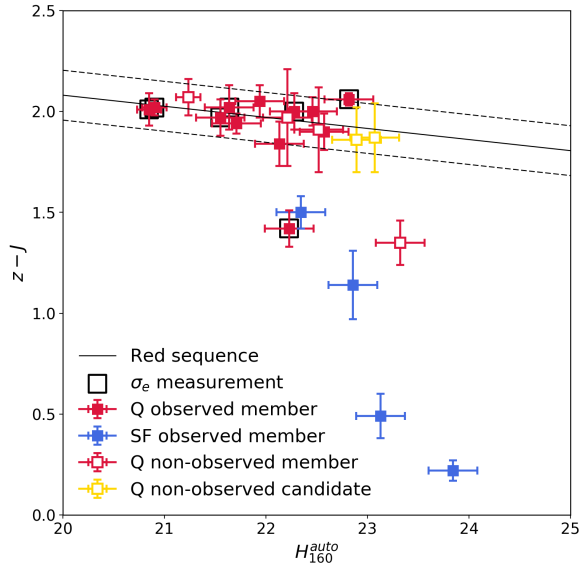


Figure 2.6: Galaxy CMD for confirmed and candidate members of JKCS 041. The quiescent (Q; red) and SF (blue) confirmed member galaxies that have been observed with KMOS (filled squares), and confirmed but not observed (unfilled), are shown along with the unobserved candidate members (unfilled yellow squares; see Section 2.3.3). Those objects for which I derived velocity dispersion measurements are shown by larger black squares (see Section 2.5.2). The best fit to the confirmed red-sequence galaxies is shown by the solid line, while the dashed lines shows the 2σ scatter. The $z - J$ colour (N14) is plotted against my H -band SExtractor total magnitude estimate MAG_AUTO (H_{160}^{auto} ; see Section 3.4). See Section 2.3.1.

et al. (2013a). Chan et al. (2018) found galaxies were $\sim 42\%$, $\sim 55\%$ and $\sim 69\%$ smaller than mass-matched local counterparts for XMM2235 ($z = 1.39$), XMM2215 ($z = 1.46$), and Cl0332 ($z = 1.61$), respectively. Accounting for progenitor bias (see Section 1.1.5) reduces but does not eliminate these trends.

2.3 KMOS Data of JKCS 041

2.3.1 Sample Selection

N14 determined photo- z measurements from multi-band photometry (more details of which are given in Section 3.2.1) and derived grism redshifts for all objects where possible. Spectroscopic redshifts were determined using emission lines where visible (above $H_{160} < 25.5$ mag). Spectrophotometric redshifts were derived by fitting continuum emission and photometric data (for SED fitting) for the ‘continuum’ sample of galaxies (above $H_{160} < 23.3$ mag). Redshift measurements were determined for all other objects within the WFC3 FOV where the data was of sufficient quality to

do so. This meant that they could improve on 79 initial photo- z measurements for objects in the field in addition to the 19 confirmed members (all of these are shown in Figure 2.7). For continuity between our studies, I adopted the galaxy IDs and UVJ classifications from N14 to distinguish between SF and quiescent galaxies.

N14 then constructed a CMD (see Section 1.1.1) for all objects in the field at limiting HST magnitudes of $H_{160} < 25.5$ mag for emission-line objects, and $H_{160} < 23.3$ mag for the continuum objects. Three galaxies on the red sequence could not spectroscopically confirm from grism redshifts (due to contamination); these were flagged as candidate overdensity members. I observed one of these candidate members as part of my KMOS spectroscopic sample (ID 772; see Section 2.3.3) and confirmed its membership, bringing the total number of confirmed galaxies in JKCS 041 to 20.

The galaxy CMD shown in Figure 2.6 is composed of $z - J$ values from ground-based photometry from N14 and my H_{160} total magnitudes derived using the Source Extractor (SEXTRACTOR; Bertin & Arnouts, 1996) MAG_AUTO estimate (H_{160}^{auto} ; see Section 3.4 for more details). In Figure 2.6, I show the confirmed members I observed with KMOS (filled squares), those I did not (unfilled), and indicate whether the galaxies are SF (blue) or quiescent (Q; red) as taken from their classifications on a UVJ diagram (N14). I also include the two candidate members of JKCS 041 (that N14 identified were on the red sequence but could not spectroscopically confirm) that I did not observe (unfilled yellow squares). I show the best fit from a least-squares method to the confirmed red sequence galaxies (solid line) and indicate the 2σ scatter in the red sequence (dashed lines). Also highlighted are the seven galaxies for which I derive velocity dispersion measurements (larger black squares; see Section 2.5.2). JKCS 041 has a well-defined and well-populated red sequence with little scatter, setting it apart in maturity from most overdensities at comparable redshifts.

2.3.2 Completeness

Selection effects for JKCS 041 are difficult to quantify compared to the other KCS overdensities. I was limited in my selection of targets by the density of the confirmed members of JKCS 041. The sample could also be limited by the size of the HST/WFC3 FOV, these effects would then also be present in the sample selection from N14. As discussed in N14, the continuum sample of mostly quiescent galaxies in the WFC3 image for which they derived spectrophotometric redshifts was strictly flux limited ($H_{160} < 23.3$ mag). N14 found that this was an almost mass-complete sample, with 88% completeness at $\log(M_*/M_\odot) > 10.6$ for this magnitude limit at $z = 1.80$. This mass completeness estimate was based on a larger area sample from

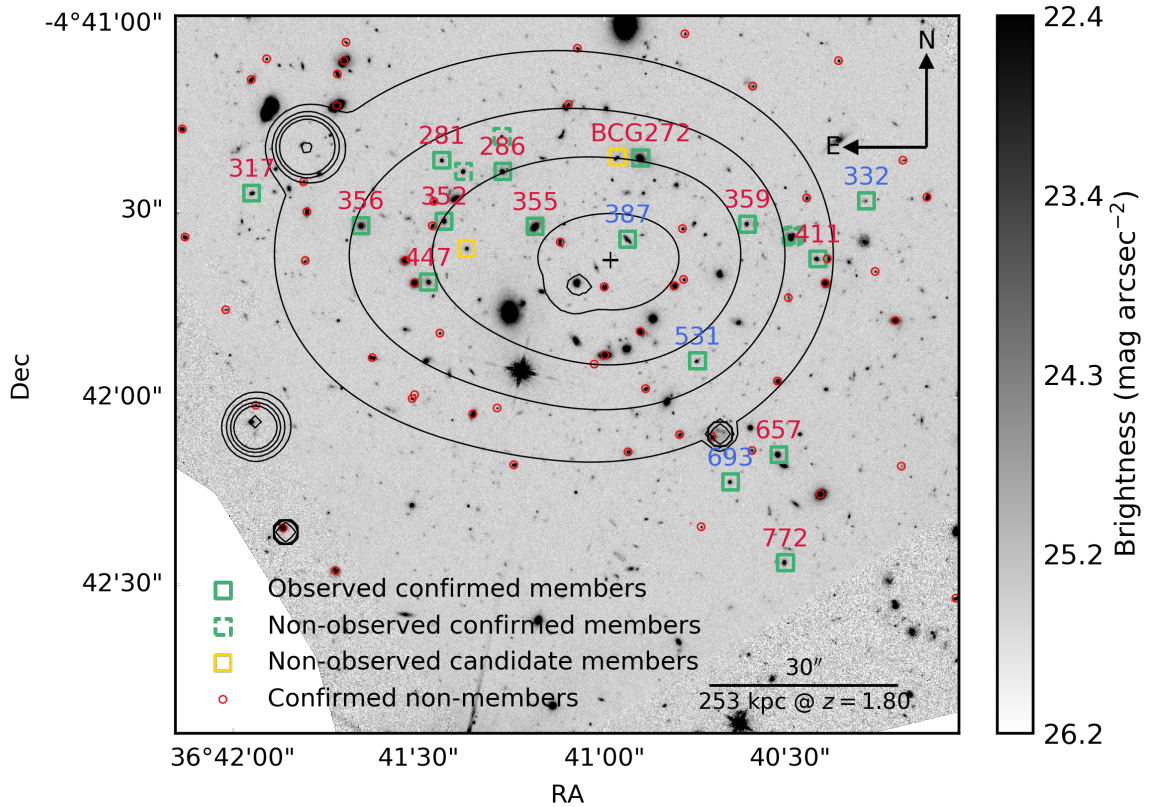


Figure 2.7: HST H_{160} -band image of JKCS 041 (as reduced in Section 3.3). The observed overdensity members (green squares) are shown with their IDs colour coded for whether they are SF (blue) or quiescent (red). The other spectroscopically confirmed members that were not observed with KMOS (dashed green squares), and the unconfirmed candidate members on the red sequence that I did not observe (yellow squares) are all quiescent (N14). The X-ray contours are from Andreon et al. (2009), and the geometric centre of the galaxies is shown with a '+'. All objects confirmed as non-overdensity members with grism redshifts (N14) are shown (small red circles; see Section 4.3 for more details). See Section 2.3.3.

Newman et al. (2012) for this redshift. The two remaining candidate members have $\log(M_*/M_\odot) < 11$, so it is likely that the overdensity members are complete above this mass limit within R_{500} (which is within the WFC3 footprint, see Figure 2.3) of the overdensity centre. For the remaining $10.6 < \log(M_*/M_\odot) < 11$ galaxies, accounting for the two remaining candidate cluster members, the sample is $\sim 78\%$ complete. N14 explained that the completeness for the emission-line sample was harder to quantify.

With so few confirmed member galaxies not observed with KMOS (four) from this parent sample of 20 members, it is difficult to robustly quantify the selection effects of the observed sample beyond the completeness already discussed by N14. As seen on the CMD in Figure 2.6, the galaxies for which I derived velocity dispersions (larger black squares; see Section 2.5.2), fairly evenly span the range of magnitudes I sampled. This helps to reduce any bias (beyond these completeness limits) in the ages I determined from them.

2.3.3 KMOS Target Selection

As shown in Figure 2.7, JKCS 041 is an elongated overdensity that spans $\sim 1.9' \times 1.3'$ (as determined from the extent of the galaxies), which at $z = 1.80$ is $\sim 1.0 \times 0.6$ Mpc in size. Given the relatively tight morphology of the 20 confirmed members compared to the patrol region of KMOS ($\sim 7'$ diameter), the number of galaxies that could be observed with KMOS was limited by the proximity constraint of the IFUs (discussed below). Each IFU is $2.8'' \times 2.8''$ which at $z = 1.80$ is ~ 24 kpc and is sufficiently large to encompass greater than R_e (see Section 1.1.1) of the galaxies.

I designed the observing strategy for JKCS 041, and to determine the optimal configuration for the 24 robotic arms of KMOS and prepare an Observing Block (OB) to feed to the telescope for the observations, I used the KMOS ARM Allocator (KARMA; Wegner & Muschielok, 2008) software. KARMA requires an image of the field to be observed (in order to know where to place the arms), and for this I used the HST images from N14 available from the Hubble Legacy Archive² (HLA). Searching for JKCS 041 returns various results as shown in the top panel of Figure 2.8. As shown on this first page of results from the search, there are a number of images of this field taken between 2008 and 2013. The processing ‘Level’ of the images is indicated in the 6th column; the highest level shown here is 4 which is a combined colour image. The information in this row shows that the colour image has been combined from eight exposures (NExposures) and consists of two bands (F160W and F105W;

²<https://hla.stsci.edu/hlaview.html>

Spectral_Elt column). As can be seen from the far-left columns, there is the option to display this image in an interactive window (shown in the bottom panel of Figure 2.8) and download this as a Flexible Image Transport System (FITS) image. This is a rough reduction so is not ideal for detailed photometric analysis (my reduction procedure is covered in Section 3.3). However, the colour image is fine for selecting targets to observe with KMOS and for gauging rough sizes of the galaxies as used for the reduction of the KMOS spectra (see Section 2.4).

The target list and coordinates of the confirmed members and candidates were taken from Table 1 of N14. For the observations of JKCS 041 with KMOS, observations of stars were also required for a few different purposes: telescope guiding, frame acquisition, and telluric corrections. To identify stars in the KMOS FOV, which is much larger than the WFC3 FOV (see Section 3.1) and so cannot all be identified from the HST image, I used the Aladin Sky Atlas software (Bonnarel et al., 2000; Boch & Fernique, 2014). Within Aladin, one can load different surveys to identify objects in the FOV. The Position and Proper Motion Extended-L (PPMXL) catalogue (Roeser, Demleitner & Schilbach, 2010) contains proper motions for ~ 900 million stars and is valuable for selecting appropriate acquisition, guide, and telluric stars. The motion of an acquisition star can be corrected to account for its position relative to the fixed distant target in the sky (proper motion). However, if the proper motion is too high, then this can increase the uncertainty of the star’s position and lead to a misaligned field. The descriptions and requirements of the stars observed are as follows:

- Guide stars are used to ensure the cluster remains in the VLT UT1 FOV using point sources that are observed at the same time as the galaxies. The VLT UTs have a separate guide sensor on an arm that continually monitors the guide star and so it does not have to be in the KMOS FOV, only close to the observed field. I used a wider Two Micron All Sky Survey image of the field to select this star, and it is defined during the preparation of KMOS OBs. These need to be bright, $R < 12$ mag, and have small proper motions.
- Acquisition stars are used when the telescope moves to the coordinates of the field to be observed. The targets can often not be centred on the IFUs (by up to $1''$ – $2''$ on a $2.8''$ IFU), which for bright objects is fine to adjust on the fly at the telescope, but for the very faint distant objects in JKCS 041, these are not visible with a brief 30 second exposure (or even with a 10-hour exposure!). Therefore, bright foreground Galactic stars are used to acquire an accurate



Hubble Legacy Archive

JKCS 041 [advanced search](#)
Examples: M101, 14 03 12.6 -54 20 56.7 r=0.2d, more...
Requires Firefox, Safari, IE, or compatible browser

[Inventory](#) [Images](#) [Footprints](#) [Cart, 0 kB](#) [Grism Spectra \(ST-ECF\)](#) [Help Center](#)

JKCS 041 RA = 36.683330 Dec = -4.693330 r = 0.200000 [02:26:43.999 -04:41:35.99]

Results 1-20 of 71

Show results per page

Click column heading to sort list - Click rows to select [Add selection to cart](#)
Show selected rows: [First](#) [Mixed](#) [Only](#) [Not](#) [Select all](#) [Reset selection](#)
Text boxes under columns select matching rows [Apply Filter](#) [Clear Filter](#)

Display	PlotCat	Retrieve	RA	DEC	Level	Target	Detector	Aperture	Spectral_Elt	NExposures	ExpTime	StartTime
Display		<input type="checkbox"/> FITS	02:27:02.13	-04:36:15.9	2	VVDS-020179225	NIC2	NIC2-FIX	F160W	4	2559.76	2008-07-08 14:09:05
Display		<input type="checkbox"/> FITS	02:27:02.13	-04:36:15.9	2	VVDS-020179225	NIC2	NIC2-FIX	detection	4	2559.76	2008-07-08 14:09:05
Display		<input type="checkbox"/> FITS	02:26:47.88	-04:31:35.1	2	VVDS-020213000	NIC2	NIC2-FIX	F160W	4	2559.76	2008-07-16 13:57:10
Display		<input type="checkbox"/> FITS	02:26:47.88	-04:31:35.1	2	VVDS-020213000	NIC2	NIC2-FIX	detection	4	2559.76	2008-07-16 13:57:10
Display		<input type="checkbox"/> FITS	02:26:45.19	-04:38:30.5	2	VVDS-020163018	NIC2	NIC2-FIX	F160W	4	2559.76	2008-08-29 01:37:47
Display		<input type="checkbox"/> FITS	02:26:45.19	-04:38:30.5	2	VVDS-020163018	NIC2	NIC2-FIX	detection	4	2559.76	2008-08-29 01:37:47
Display		<input type="checkbox"/> FITS	02:26:07.4	-04:41:03.9	2	SL2SJ022612-044055	PC	WF3-FIX	F606W	3	1200	2007-09-03 16:46:16
Display	PlotCat	<input type="checkbox"/> FITS	02:26:10.44	-04:41:00.6	2	SL2SJ022612-044055	WFPC2	WF3-FIX	F606W	3	1200	2007-09-03 16:46:16
Display		<input type="checkbox"/> FITS	02:26:07.4	-04:41:03.9	2	SL2SJ022612-044055	PC	WF3-FIX	detection	3	1200	2007-09-03 16:46:16
Display	PlotCat	<input type="checkbox"/> FITS	02:26:10.44	-04:41:00.6	2	SL2SJ022612-044055	WFPC2	WF3-FIX	detection	3	1200	2007-09-03 16:46:16
Display	PlotCat	<input type="checkbox"/> FITS	02:26:44.05	-04:41:32.8	2	JKCS041-1	WFC3/IR	IR-FIX	F105W	4	1611.74	2013-02-12 10:48:22
Display	PlotCat	<input type="checkbox"/> FITS	02:26:44.05	-04:41:32.8	2	JKCS041-1	WFC3/IR	IR-FIX	F160W	4	3311.74	2013-02-12 09:03:07
Display	PlotCat	<input type="checkbox"/> FITS	02:26:44.05	-04:41:32.8	2	JKCS041-1	WFC3/IR	IR-FIX	detection	8	4923.48	2013-02-12 09:03:07
Display	PlotCat	<input type="checkbox"/> FITS	02:26:44.05	-04:41:32.8	4	JKCS041-1	WFC3/IR	IR-FIX	F160W/ F105W	8	4923.48	2013-02-12 09:03:07
Display	PlotCat	<input type="checkbox"/> FITS	02:26:44.15	-04:41:42.2	2	JKCS041-2	WFC3/IR	GRISM1024	F105W	1	352.94	2012-10-28 06:42:29
Display	PlotCat	<input type="checkbox"/> FITS	02:26:44.15	-04:41:42.2	2	JKCS041-2	WFC3/IR	GRISM1024	F160W	1	399.23	2012-10-28 09:51:24
Display		<input type="checkbox"/> FITS	02:26:44.15	-04:41:41.5	1	JKCS041-2	WFC3/IR	GRISM1024	G102	1	1102.94	2012-10-28 06:48:51
Display		<input type="checkbox"/> FITS	02:26:44.15	-04:41:41.5	1	JKCS041-2	WFC3/IR	GRISM1024	G102	1	1302.94	2012-10-28 08:15:40
Display		<input type="checkbox"/> FITS	02:26:44.15	-04:41:41.5	1	JKCS041-2	WFC3/IR	GRISM1024	G102	1	1102.94	2012-10-28 07:08:17
Display		<input type="checkbox"/> FITS	02:26:44.15	-04:41:41.5	1	JKCS041-2	WFC3/IR	GRISM1024	G102	1	1302.94	2012-10-28 08:38:26

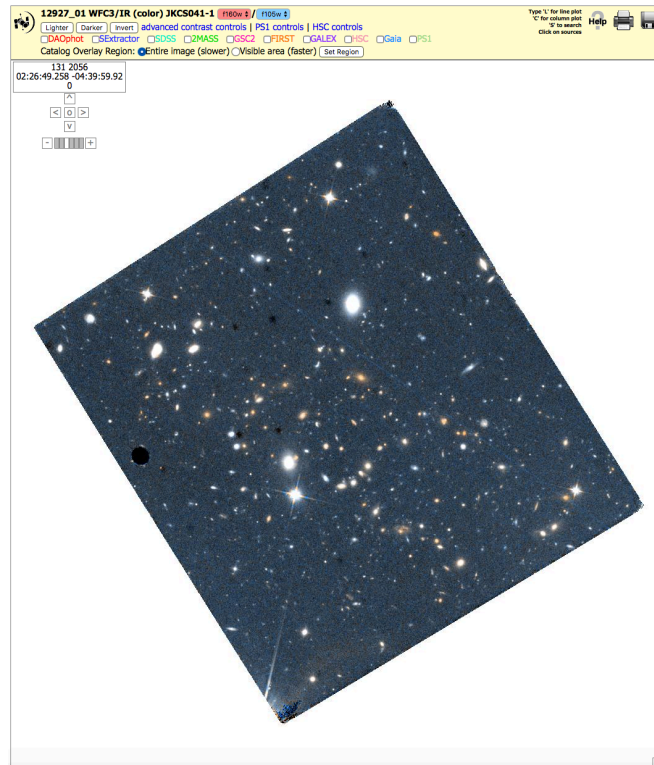


Figure 2.8: *Top*: HLA search results for JKCS 041. The ‘Level’ column indicates the extent of image processing performed, with the highest shown (4) relating to a colour image of two bands (F160W and F105W; Spectral_Elt) combined from eight exposures (NExposures column). *Bottom*: This colour image of JKCS 041 shown in the interactive display window on HLA.

position of the telescope and position angle of the FOV prior to observations. At least three stars is optimal to triangulate the telescope position, and these are selected to ideally be within the HST FOV, have very low proper motions, and have magnitudes $15 < R < 18$ mag (so they do not saturate the KMOS IFUs).

- Telluric or standard stars are observed at the same time as the observations to correct for atmospheric telluric absorption (see Section 2.1.1). These have the same magnitude and proper motion constraints as the acquisition stars. They also have to be stars for which reliable models exist and A0V class stars satisfy this requirement. I observed all the stars within the HST/WFC3 footprint within the required magnitude and velocity ranges, and fortunately one of these was an A0V star.

Once all the stars and galaxy catalogues for the field were compiled, to ensure that despite coming from different sources all were on the same coordinate system, small adjustments were made to their coordinates to ensure they overlaid with objects in the HST/WFC3 image. The HST colour image and tweaked coordinates of the stars and galaxies were loaded into KARMA to find the optimum arm configuration for the OB. The KMOS FOV can be rotated and the arms positioned to get maximum coverage on the selected targets. There are two layers of arms to prevent collisions (shown by the alternate green and blue arms in Figure 2.9), however two arms within the same layer cannot come within $\sim 6''$ (between IFU centres).

Selecting targets to observe was only limited by the density of the targets in the KMOS FOV. In a dense region of four galaxies, where only two could be observed, I prioritised the brightest quiescent members (e.g. IDs 286 & 281 over IDs 289 & 255; see Figures 2.3 and 2.7). I aimed to get the isolated (separated with respect to other members of JKCS 041, $> 6''$) sources, as unresolved pairs were harder to extract reliable 1D spectra from (e.g. IDs 375 & 376; see Figure 3.9). However, I was able to extract spectra for confirmed members with close resolved neighbours (e.g. IDs 359 & 411; see Figure 3.9) as their separation was larger than that of the full width half maximum (FWHM) of the KMOS point spread function (PSF). As I had spare IFUs after targeting all possible quiescent members, I also observed member SF galaxies and quiescent candidate members. I selected targets in order of preference, with the final configuration made to reflect these priorities in each area of the sky:

1. Quiescent, bright, isolated, confirmed overdensity members

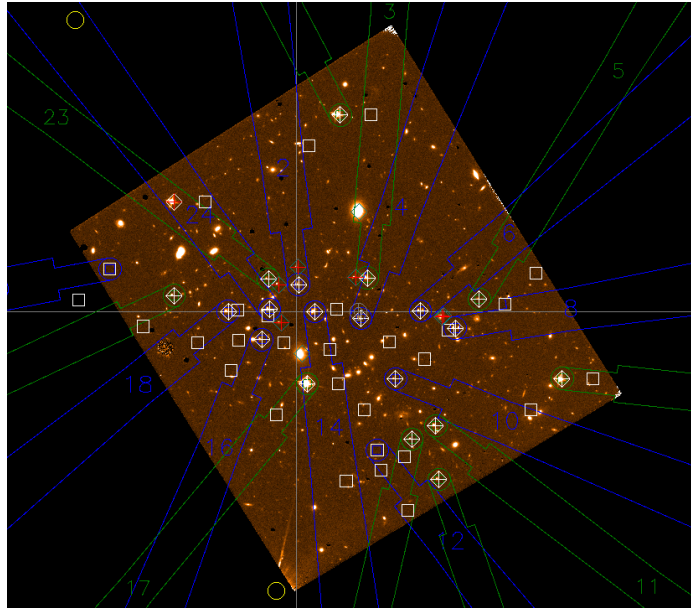


Figure 2.9: KMOS arm configuration designed in KARMA to prepare an OB JKCS 041. The colour HST image from the HLA was used to identify the galaxies and target coordinates came from N14. Stars in the field used for guiding, acquisition, and telluric correction were identified in the PPMXL catalogue (Roeser, Demleitner & Schilbach, 2010) using the Aladin Sky Atlas (Bonnarel et al., 2000; Boch & Fernique, 2014). See Section 2.3.3.

2. SF, isolated, confirmed overdensity members
3. Paired confirmed members
4. Quiescent candidate members

In summary, I targeted 16 galaxies, 15 of these were spectroscopically confirmed, and one was a candidate member. However, with KMOS observations I spectroscopically confirmed the candidate (ID 772) as a member. Of the 16 galaxies observed with KMOS, 12 of these were quiescent (including ID 772), and four were SF (as classified on a UVJ diagram by N14). The HST image in Figure 2.7 indicates those confirmed overdensity members observed with KMOS (solid green squares), showing their IDs colour coded for whether they are quiescent (red) or SF (blue). The green dashed squares indicate the remaining confirmed members not observed with KMOS (four galaxies, all quiescent), due to their close proximity to other targets. I then also show the remaining two candidate cluster members (yellow squares), as those not spectroscopically confirmed by N14 or observed with KMOS, but that lie on the red sequence.

2.3.4 KMOS Observations

As JKCS 041 was only spectroscopically confirmed and results published in June 2014, JKCS 041 was added as a target when KCS had been under way for a few observing periods. A benefit of this was that some of the early problems had been resolved; these included fixing instrumental failures and optimising observing strategies for overcoming systematics or to aid the data reduction. Once the data for JKCS 041 was taken and the pipeline for KCS finalised, I focused on the reduction and analysis of the KMOS spectra of JKCS 041.

The overdensity was observed under ESO programmes 095.A-0137(A) and 096.A-0189(A). In total, 16 galaxies were observed over six nights: 17th–19th September 2015 (P95), 10th–12th October 2015 (P96). The galaxies were observed for ~ 20 hours on source at seeing $< 1''$ in the YJ band ($R \sim 3400$, $\lambda \sim 1\text{--}1.36 \mu\text{m}$). The YJ band was selected for consistency with the other KCS clusters and because it produced an appropriate wavelength range. The reason it was chosen for the KCS clusters was that at $z \sim 1.5$ the valuable strong rest-frame optical absorption lines used for stellar populations analysis ($H\beta$, $H\gamma$, $H\delta$, Mgb , G-band, Fe, CaII) lie in this band. At $z = 1.80$ some of these strong features are shifted out of the rest-frame range, and instead bluer indices move into the band. These features are sometimes weaker but nonetheless can still be used for stellar populations analysis. The next available band (H) is too red and would miss some of the valuable indices so YJ was the obvious choice for JKCS 041 observations.

The observations were taken using a standard nod-to-sky method and object-sky-object observing pattern so that each on-source exposure had an adjacent sky that could be used for the sky correction. OBs were one hour long with 300s exposures (12 per OB), eight of which were on source. To improve the rejection of bad pixels from the final spectra, each exposure was dithered by $0.1\text{--}0''.6$, where the bad IFU pixels are easily identified as those following the dither pattern. The observed sources comprised 12 quiescent galaxies (one of which was previously an unconfirmed candidate member, ID 772), and four SF galaxies.

2.4 Data Reduction

I worked with my collaborator Trevor Mendel to use the pipeline he developed for the KCS observations to reduce the data for JKCS 041. I will summarise the key features of the pipeline and steps of the reduction that produced the spectra analysed in this work. To verify the ability of the pipeline to extract spectra, I accounted for

systematic uncertainties in the values I derived by fitting many realisations of the same spectrum (see Section 2.5.2.5 for more details). The data reduction of the KCS galaxies utilised a combination of routines from the original KMOS reduction pipeline tools (Software Package for Astronomical Reductions with KMOS – SPARK; [Davies et al., 2013](#)) and custom Python software ([Mendel et al., 2015](#)). This reduction was used for the KCS sample in [Beifiori et al. \(2017\)](#) and will be described further in [Mendel et al. \(2018a, in prep.\)](#).

1. The first phase involved making accurate calibration files.
 - (a) The reduction involved first generating standard calibration (darks, flats, wavelength corrections) files using SPARK. See Section 5.1.1.2 for more details on these standard KMOS reduction steps.
 - (b) Standard stars were reduced using the relevant SPARK tool.
 - (c) Then some basic additional custom calibration files were made for the darks and flats to ensure hot pixels propagated through the cubes correctly.
 - (d) The next step involved making much more detailed illumination and wavelength calibrations across and between the IFUs using OH sky line variability. This produced noise corrected flat frames.
 - (e) These corrected flat frames that were extracted from 2D detector space were then converted to 3D cubes as required by the pipeline.

2. Secondly, atmospheric variability and contamination were corrected for.
 - (a) Sky subtraction was done in two steps; first with a simple subtraction of an object frame from its corresponding sky frame.
 - (b) A second order correction was then made for the residuals by stacking spectra per detector. To account for the variability in the sky, OH sky lines were used to derive scaling variations for the observations for each night prior to stacking. The residual sky lines in the stacked spectra were then removed in 2D detector space.
 - (c) To correct for telluric absorption, it was modelled with MOLECFIT ([Smette et al., 2015](#); [Kausch et al., 2015](#)). Using three-hour interval atmospheric data from Global Data Assimilation System (GDAS) and local weather information from the header, MOLECFIT modelled atmospheres as a function of pressure (height), temperature, water column density, and turbulence (see Section 5.1.3 for more details).

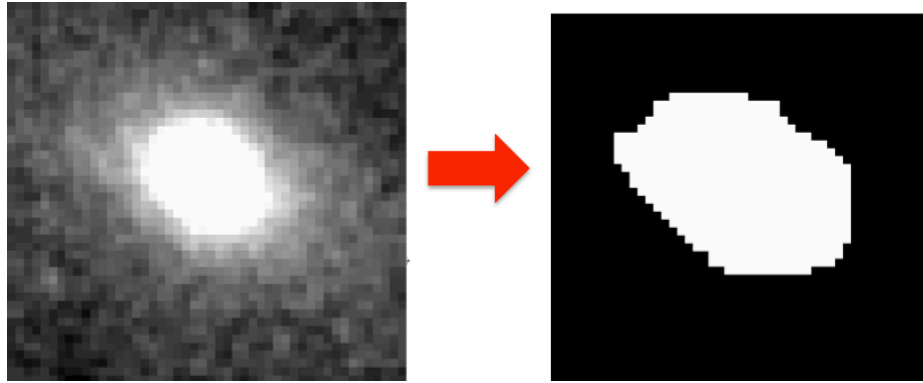


Figure 2.10: Example of an HST postage stamp and corresponding segmentation map (as derived in SExtractor). The stamp sizes match those of the KMOS IFUs ($2.8'' \times 2.8''$) and have been convolved with the KMOS PSF to create source profiles of galaxies. The source profiles are used to optimally extract spectra for the KMOS observations. See Section 2.4.

- (d) This best fit atmospheric model from MOLECFIT was then fitted to the telluric stars, allowing the water column density to vary. This was because the water-column density value was consistently wrong by a small margin. An improved value could then be determined from the fit and corrected for.
3. The following steps describe the determination of the source profiles in each IFU.
 - (a) To determine where the galaxies should be in the IFUs prior to extracting data, model source profiles were produced using HST images.
 - (b) Firstly, a segmentation map (integer mask of sky and object pixels) of the roughly reduced HST colour image of JKCS 041 from HLA (bottom panel of Figure 2.8) was produced in SExtractor. SExtractor required initial parameters to optimally extract sources; at this stage the values from 3D-HST (Brammer et al., 2012) were adopted.
 - (c) Then SWARP (a software for FITS image manipulation; Bertin et al., 2002) was used to cut postage stamps of the galaxies from the HST image and segmentation map to match the size of the KMOS IFUs. An example of a galaxy postage stamp and its segmentation map from SExtractor is shown in Figure 2.10.
 - (d) To enable stacking of the KMOS data for each night, zero points and instrument response curves were determined for each detector per night.
 - (e) From each standard star from the corresponding night, a PSF kernel was determined to convolve the HST images to KMOS data to produce model images.

This was done to estimate what the source’s profile should look like on the KMOS IFU, which was particularly important for recovering data from fainter images or those with bad sky contamination (even after removal).

- (f) Source profile masks were produced (based on the segmentation map postage stamps) indicating regions of object ($= 1$), sky ($= 0$), and second objects in the IFU ($= -1$).
 - (g) Model KMOS frames were produced, with normalised flux to match the expected profile from the PSF matched HST images, for each real KMOS frame of data. An aperture was then made to encompass half the light from the sources (i.e. R_e as determined from SExtractor).
4. Lastly, the 1D spectra were extracted for each galaxy.
- (a) The model frames and source profiles produced in the previous steps were used to optimally extract (Horne, 1986) a single 1D spectrum for each galaxy from within R_e across the whole 20-hour integration.
 - (b) Sky-background information for the extracted source was taken from the neighbouring IFU in case any features in a sky pixel were associated with the galaxy itself. Both the sky and non-sky background subtracted spectra were carried forward through the reduction to check and verify the efficiency of this step.
 - (c) Telluric corrections were derived (see steps 2c and 2d) for each background and non-background subtracted spectrum. Tests allowing for shifts in velocity and stretching were done to minimise the residuals of the model telluric fit to the data.
 - (d) The median continuum level, variance of the data, and sky-line variability were measured. Each pixel contributing to a corresponding pixel on the IFU of an extracted 2D source was quality checked using these three measurements and the outliers were sigma clipped.
 - (e) Then the 1D spectra were produced over the whole 20-hour integration by combining spectra from across the IFU of the 2D extracted source. Sigma clipping was done to remove outliers at each wavelength pixel. This resulted in one average spectrum per galaxy of the 16 observed.
 - (f) As well as these individual spectra, there were also 100 bootstrapped realisations of each galaxy spectrum generated from random replacement of all the input spectra (within R_e from the 20-hour observations) from the final two steps prior to sigma clipping.

Various elements of this reduction were extensively checked. I used the bootstrapped spectra for quantifying the systematic uncertainties of the pipeline by using them to derive uncertainties on parameters derived from the spectra (see Section 2.5.2).

2.5 Data Analysis

2.5.1 Cross-Correlation of KMOS Spectra

With reduced high-resolution ($R \sim 3600$) KMOS spectra, I wanted to improve the redshifts for the individual galaxies from those derived with low-resolution ($R \sim 130$ at 1400 nm) HST grism spectra (N14). With the KMOS spectra, I have improved on the accuracy of the grism redshift measurements for all the 16 observed galaxies. For most (mainly quiescent) galaxies, this was done using kinematic fits of absorption lines (explained in Section 2.5.2). Prior to fitting the galaxies as described below, redshifts were determined through cross-correlation or from emission lines where possible. These initial guesses of redshift were used as starting points for the shift applied to the spectra prior to kinematic fitting.

To cross-correlate the spectra, I used a Maraston & Strömbäck (2011) SSP model based on the Medium-resolution Isaac Newton Telescope Library of Empirical Spectra (MILES; Sánchez-Blázquez et al., 2006). I opted to use a SSP model with a Chabrier IMF (see Section 1.1.6), solar metallicity, and 1 Gyr age. This was a reasonable first-order approximation of the galaxy properties for comparison via cross-correlation. The galaxy spectra were linearly interpolated onto the same grid as the model spectra. The two were then cross-correlated and I found that I could improve on the accuracy of the grism redshifts for 11 out of the 16 galaxies; 10 quiescent and one SF with some weak absorption features. This method provided the starting point for the kinematic fit that was used for a more accurate redshift measurement (see Section 2.5.3). All redshift measurements determined for the observed spectra are in Table 2.2 along with the method used to derive them.

2.5.2 Stellar Kinematics

2.5.2.1 Template Spectra

To derive the stellar kinematics of the galaxies, I fitted the spectra using the PPF³ (Cappellari & Emsellem 2004; as upgraded in Cappellari 2017) software. Line-of-

³<http://purl.org/cappellari/software>

sight velocity dispersions (LOSVDs) are generally well described by a Gaussian fit (Bender, Saglia & Gerhard, 1994), however for high-S/N spectra, useful information can be gained from the profiles of the lines themselves. PPXF works by fitting a simple Gaussian profile when S/N is low but expands to a Gauss-Hermite series (as parameterised by, van der Marel & Franx, 1993; Gerhard, 1993) at high S/N. The minimisation of the χ^2 of the output parameters (velocity, velocity dispersion, and Gauss-Hermite moments for m parameters: h_3, \dots, h_m) that describe the profile is a non-linear least-squares optimisation problem that can be efficiently computationally solved and PPXF fits for them simultaneously in pixel space. PPXF fits an input library of stellar templates or galaxy models to a galaxy spectrum and can be used to derive accurate stellar kinematics from absorption lines. It simultaneously fits for a velocity shift (redshift) and a velocity dispersion (line width). When fitting spectra to derive properties of the stellar populations in a galaxy, the ‘regularization’ parameter is important for extracting useful information from the fit. Regularization is the degree of smoothing applied to the weighting of the templates whilst they are being fitted in order to find the smoothest solution. See Section 5.2.3 for an application of PPXF to extract stellar population parameters.

There are now a number of spectral libraries compiled from either empirical (e.g., Cenarro et al., 2001; Prugniel & Soubiran, 2001; Valdes et al., 2004; Sánchez-Blázquez et al., 2006) or synthetic (e.g., Munari et al., 2005; Gustafsson et al., 2008) stellar spectra, or SSP models derived from stellar spectral libraries (e.g. Bruzual & Charlot, 2003; Maraston, 2005; Maraston & Strömbäck, 2011; Conroy, Gunn & White, 2009; Conroy & Gunn, 2010; Vazdekis et al., 2016). These many libraries differ in wavelength range, resolution, age, metallicity ranges, and α -element abundance (i.e. SFH, see Section 1.1.7; Vazdekis et al., 2016). These SSP models have different codes to generate their predictions. Therefore, results do not always agree between the models. The template library used to fit the spectra therefore requires careful consideration to ensure that the data is best matched in wavelength and resolution as well as having the necessary features to answer the required science questions.

Figure 2.11 shows the wavelength coverage and resolution of both the de-redshifted ($\lambda_{\text{rest}} = \lambda_{\text{obs}}/(1+z)$) KMOS spectra as measured from the bright OH sky lines for each spectrum (blue dashed lines), and their median resolution (thick blue line). I then show the wavelength coverage and resolution of three template candidates: Indo-US Coudé Feed Spectral Library (green line; Valdes et al., 2004), the MILES library (red line; Sánchez-Blázquez et al., 2006), and the ELODIE library (violet line; Prugniel & Soubiran, 2001; Prugniel et al., 2007). The lighter regions indicate

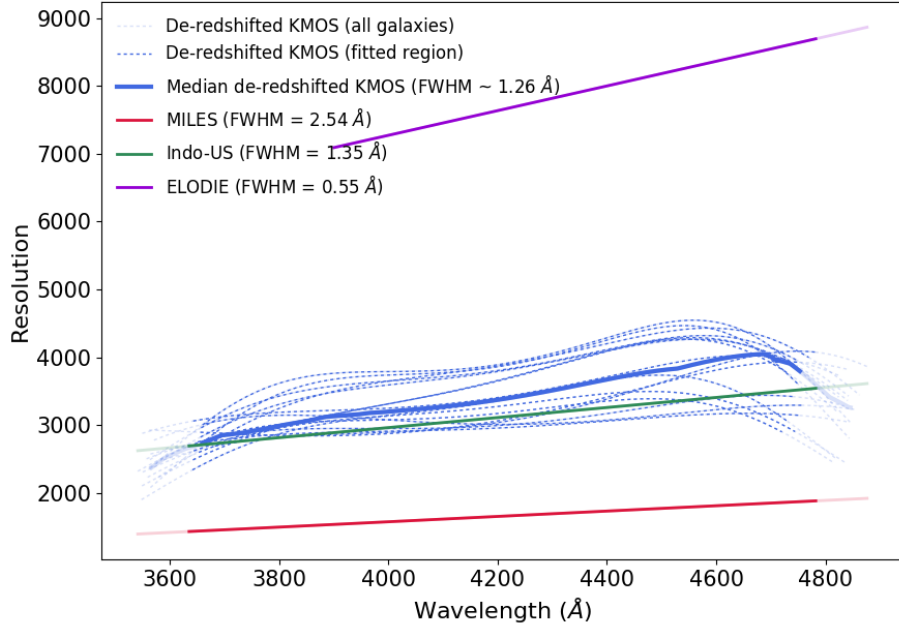


Figure 2.11: Plot of the resolution against wavelength of the KMOS observations and different spectral libraries in order to determine the best templates for kinematic fits. The resolution of KMOS for each galaxy spectrum as a function of wavelength was determined from OH sky lines (blue dashed lines), their median is also shown (thick blue line). I then show the resolution as a function of wavelength for three spectral libraries: Indo-US Coudé Feed Spectral Library (green line [Valdes et al., 2004](#)), the MILES library (red line [Sánchez-Blázquez et al., 2006](#)), and the ELODIE library (violet line [Prugniel & Soubiran, 2001](#); [Prugniel et al., 2007](#)). The faded regions indicate the regions of the KMOS spectra that I did not fit due to poorer quality at the ends.

the regions of the KMOS spectra that I do not fit due to poorer quality at the ends. As can be seen, the ELODIE models have very high resolution, which would suit fitting the KMOS spectra, however, the blue end of the KMOS spectra are not completely covered by their wavelength range. Given the narrow wavelength range of the KMOS spectra when de-redshifted and the presence of valuable absorption features in that range, these were decided not to be the best fit. The other alternative was the Indo-US spectra that had comparable spectral resolution and an appropriate wavelength coverage. Unfortunately, these spectra were combined from numerous different gratings to span the wavelength range. As a result, the library has variable resolution (only a fixed average value is shown in Figure 2.11), which is not ideal for measuring line broadening from spectra.

The templates chosen to fit the galaxies were from the MILES stellar library, made up of 985 stars, spanning 3525–7500 Å, and covering a large range of stellar

atmospheric parameters (Sánchez-Blázquez et al., 2006; Falcón-Barroso et al., 2011). I opted to use the high-resolution (2.54 Å FWHM; Beifiori et al., 2011) MILES stellar library rather than another library or SSP models based on the MILES library (with the same wavelength coverage and resolution). It has been found that stellar spectral libraries can more accurately recover kinematic parameters than SSP models when fitting stellar kinematics, as the influence of template mismatch is reduced (Cappellari et al., 2007). Although in this case, the main limiting factor for accurate kinematics is the spectral S/N and using MILES stellar templates or MILES-based SSP libraries produce values that are consistent within errors. When de-redshifted (assuming $z = 1.80$), the width of each wavelength channel of the KMOS galaxy spectra decreased. The resolving power (R) remains the same, as both the wavelength λ and width of a wavelength channel $\Delta\lambda$ are decreased by a factor of $(1+z)$. However, the average KMOS YJ -band wavelength element FWHM ($\Delta\lambda$) decreased from ~ 3.5 Å FWHM (as determined from the widths of skylines) to ~ 1.25 Å FWHM over a rest-frame wavelength range ~ 3570 – 4860 Å. The resolution corresponds to $\sigma_{\text{KMOS},YJ} \sim 39$ km s $^{-1}$ as compared to $\sigma_{\text{MILES}} \sim 77$ km s $^{-1}$ over this wavelength range. However, due to the stability of its resolution and the wavelength coverage, the MILES stellar library was still the best template option. I therefore had the rare case where the galaxy spectral resolution was smaller than the template resolution in km s $^{-1}$ and had to account for this when setting up and extracting values from the spectral fit to correctly recover the stellar kinematics (see Sections 2.5.2.2 and 2.5.2.4).

2.5.2.2 Fitting Procedure

Prior to fitting with PPXF, I shifted all spectra to the rest frame with initial redshift estimates from cross-correlation where available (see Section 2.5.1) or the grism redshift values from N14. The spectra were rebinned logarithmically with the flux preserved (using PPXF utilities), and the velocity scale (`velscale`) set to the minimum of the input spectra (i.e. determined at the reddest pixel, `velscale` ~ 39 km s $^{-1}$). I did not convolve the spectra to match the resolution of the templates but instead had to correct for this difference in resolution after the fit (see Section 2.5.2.4). The effect on the dispersion measurement after the correction is equivalent to applying a convolution and this method has the advantage of maintaining the data resolution so information derived from the other parameters is not lost. The templates were clipped to 3000–6000 Å (to generously cover the KMOS spectral range), log-rebinned, and normalised. The templates and galaxy spectra were then given to PPXF, which fitted

for velocity, dispersion, and continuum shape simultaneously. The continuum can be fitted with different order additive or multiplicative polynomials. I chose to use additive polynomials in my fits as was done in the previous KCS paper by [Beifiori et al. \(2017\)](#) to account for uncertainties in the continuum shape, flux calibration, and sky subtraction. I chose a fourth-order polynomial to fit the continuum shape but factored in the systematic errors of this choice when estimating errors on the fits (see Section 2.5.2.5).

Some areas of the spectra were affected by strong sky-line residuals even after reduction. The three worst affected bands corresponded roughly to $\sim 3570\text{--}3750 \text{ \AA}$, $4040\text{--}4130 \text{ \AA}$, and $4460\text{--}4600 \text{ \AA}$ in the rest frame. Rigorous masking of these bands could remove up to a third of the spectrum and could cause many fits not to converge due to the lack of continuum data. I therefore derived a method to deal with the worst affected pixels in the spectra without removing too much information so that the fit could be constrained. To determine the bad pixels to mask from the kinematic fit, I first median smoothed each spectrum by five pixels and subtracted the smoothed spectrum from its unsmoothed counterpart. Using this residual subtracted spectrum, I then selected all those pixels that deviated from the median by $> 3\sigma$. I then ‘grew’ these selected bad pixels by ± 1 pixel, creating small masks around them. Masking these bad pixel regions, I then fitted the unsmoothed spectra with PPXF. With this method, I masked between 5–7% of pixels in each spectrum. I found this method could reliably mask bad pixels or poor regions of the spectra that were heavily affected by sky lines and could improve the fits of the galaxies compared to implementing no masking at all. I performed various tests to check the reliability of this masking method. I tried different combinations of three-, five-, and seven-pixel median smoothing, and selected 2- and 3σ outliers from the mean of the subtracted spectrum, but found all methods produced comparable results. Using this preparation of the templates and spectra, and using the masking method described above, I fitted each galaxy and its 100 bootstrapped spectra with PPXF to measure the kinematics.

2.5.2.3 Properties of the Spectra

The spectra of the eight quiescent galaxies (red ID numbers) with dispersion measurements are shown in Figure 2.12. Note that galaxy ID 286 was not deemed reliable due to its low velocity dispersion value and relatively large error (see Section 2.5.2.5). I show the H_{160} image postage stamp of each galaxy with its corresponding ID and present the spectra in order of H_{160}^{tot} Sérsic magnitude. Each postage stamp has size $6.78'' \times 6.54''$ and I have overlaid the size of the KMOS IFUs for reference (green

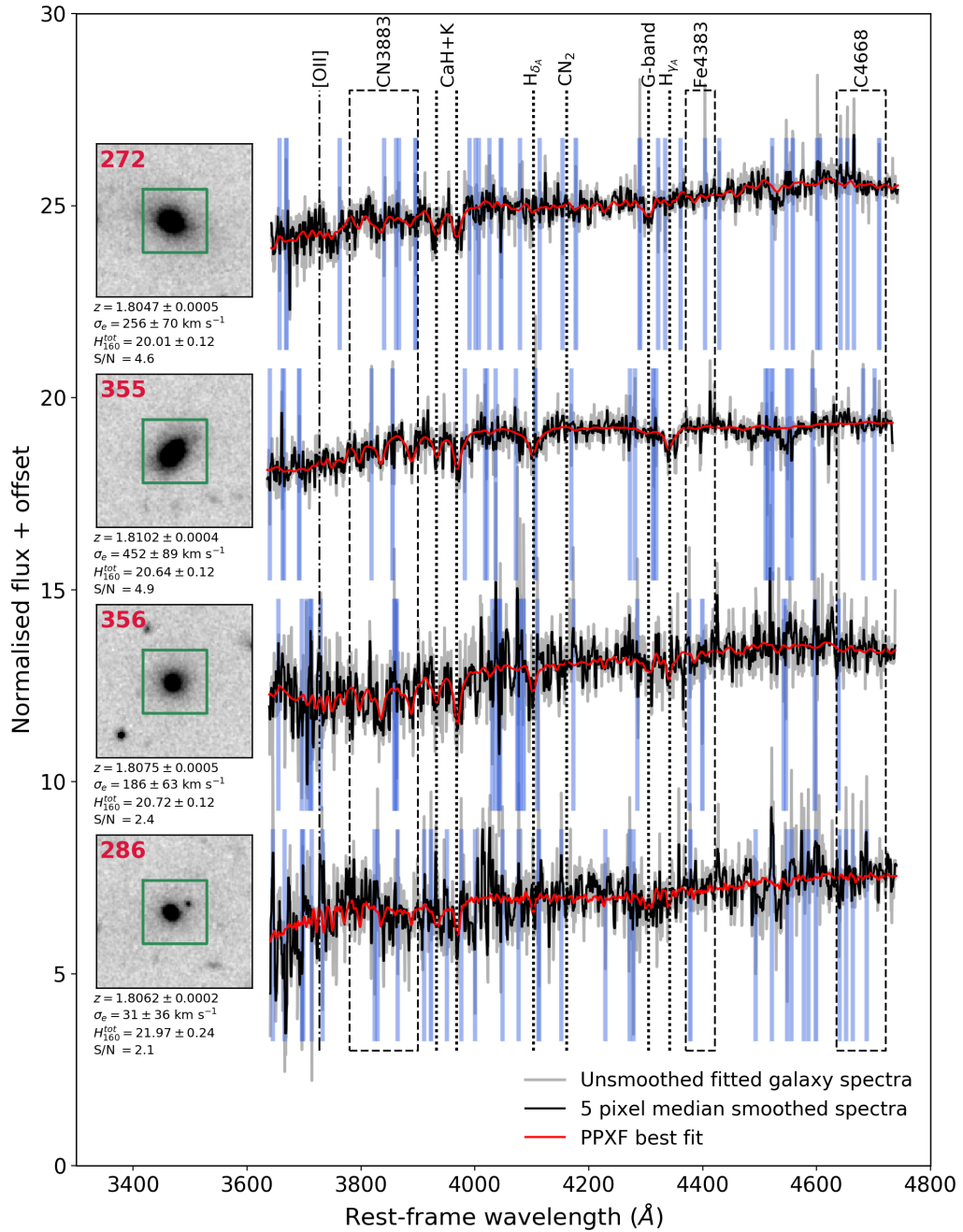


Figure 2.12: KMOS spectra of the eight quiescent galaxies (red IDs on images) in JKCS 041 for which velocity dispersions were derived. The unsmoothed spectra (grey) were fitted with PPXF (best fit shown in red). I masked pixels (blue bands) based on the subtraction of the five-pixel median smoothed spectra (black) and highlighting $> 3\sigma$ outliers from the median of the subtracted spectrum. Next to each spectrum I give the corresponding galaxy ID and H_{160} -band postage stamp, along with the redshift and σ_e as derived from the fit. The 1σ errors were obtained from the bootstrapped spectra. I plot the spectra from brightest to faintest in H_{160}^{tot} , with values derived from GALAPAGOS and errors from simulated galaxies (see Sections 3.4 and 3.4.4). Each postage stamp is $6.78'' \times 6.54''$, the green squares show the size of the KMOS IFUs ($2.8'' \times 2.8''$). Absorption features (dotted lines) or bands (dashed rectangles), and [OII] emission line for reference (dot-dash line), are indicated. Continued on the next page.

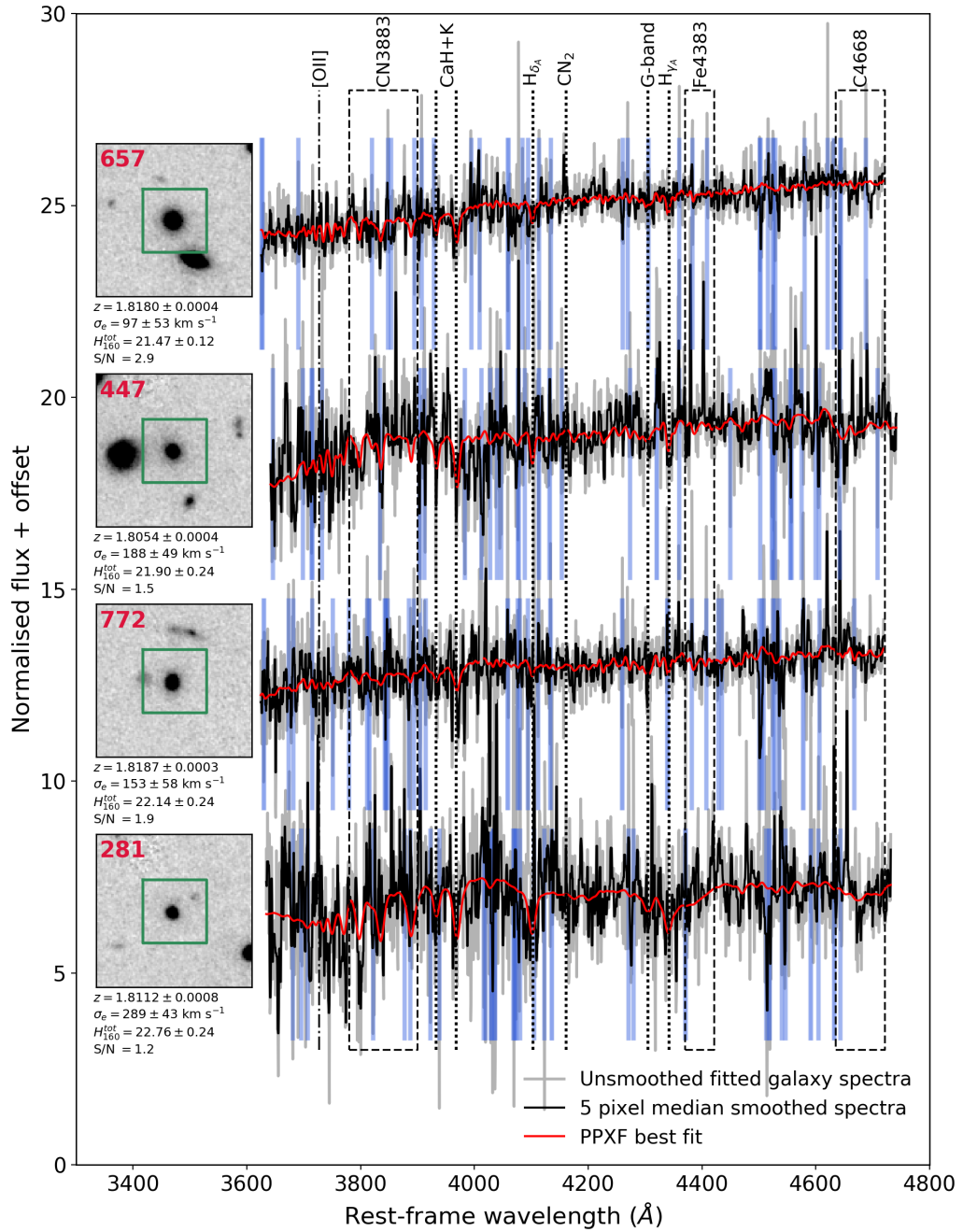


Figure 2.12: Continued. See Section 2.5.2.3.

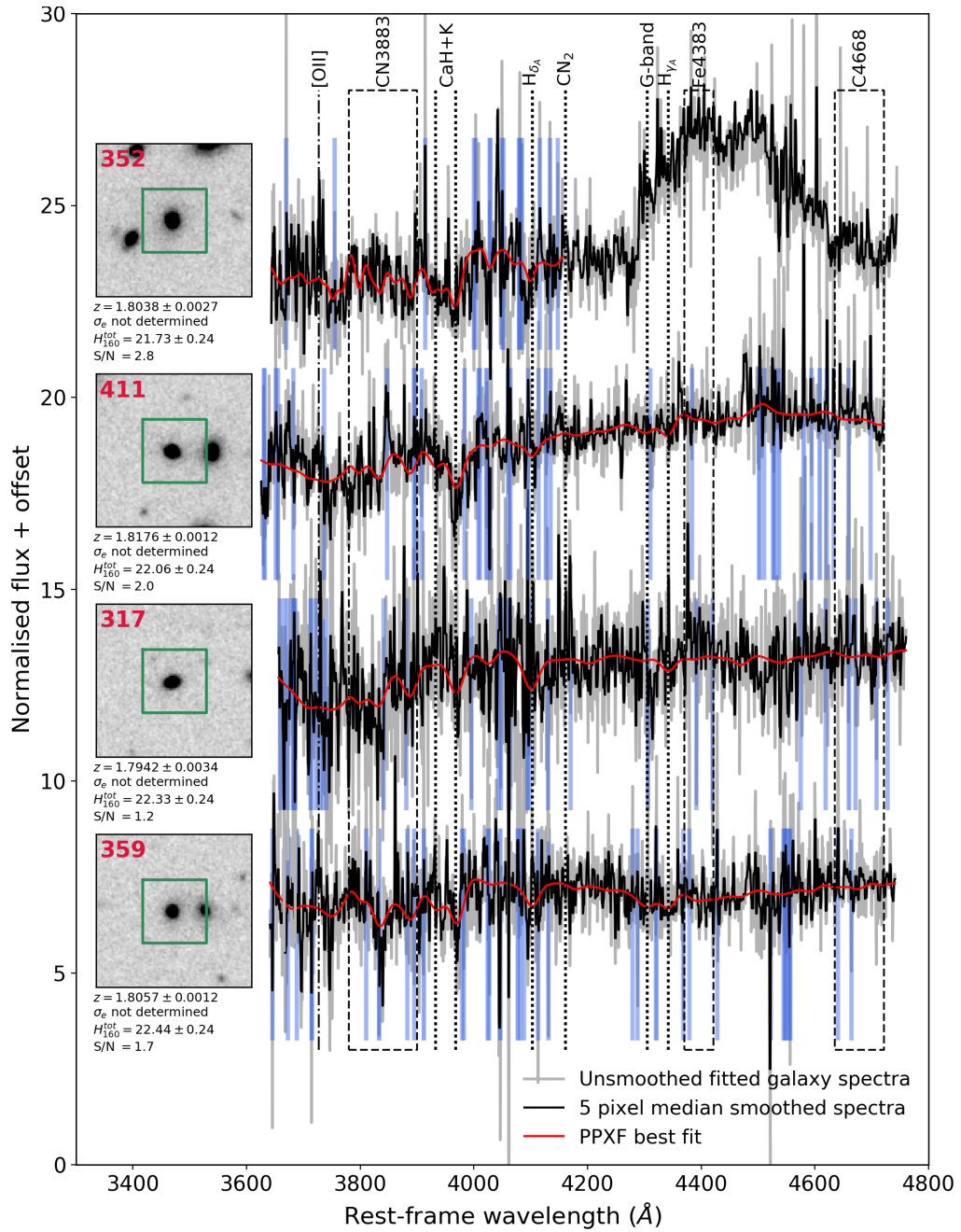


Figure 2.13: KMOS spectra of the four quiescent galaxies (red IDs on images) that were fitted with PPXF but for which no reliable dispersion measurement could be obtained. Labelling conventions are the same as Figure 2.12. However, I show the PPXF fits here along with their redshift values as although the quality of the fits did not enable a dispersion to be measured, I was still able to use them to measure improved redshifts from these data compared to those of N14 (see Section 2.5.3). See Section 2.5.2.3.

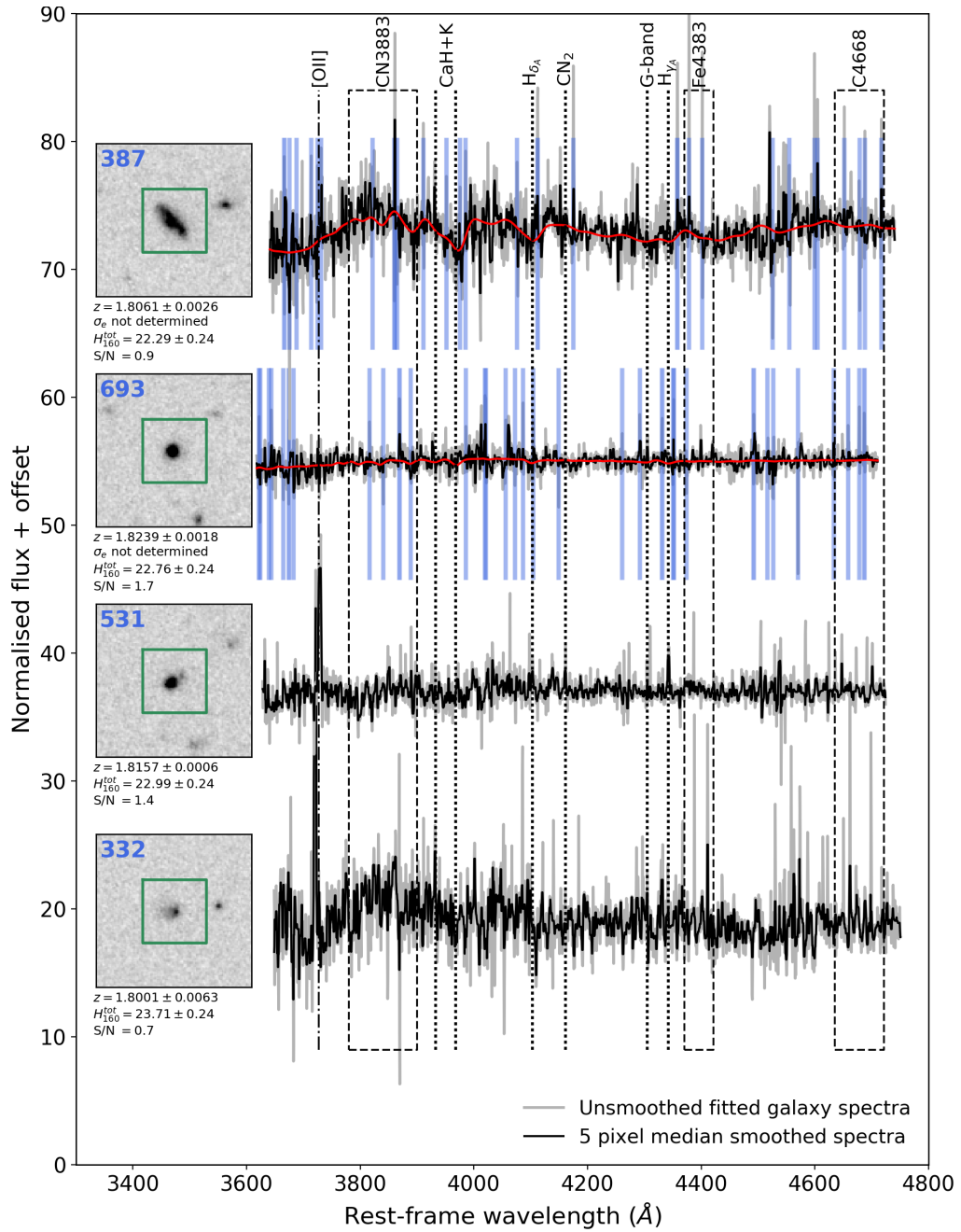


Figure 2.14: KMOS spectra of the four SF galaxies in JKCS 041 (as UVJ selected by N14; blue IDs on images). Labelling conventions are the same as Figure 2.12. For the top two galaxies (IDs 387 and 693), PPXF was used to make an estimate of their redshift even though a dispersion measurement could not be made. The redshift measurements for the bottom two galaxies (IDs 531 and 332) were determined from their bright [OII] emission. Note that the y -axis is different in this plot as compared to Figures 2.12 and 2.13 to accommodate the strong [OII] emission line for the bottom two galaxies. See Section 2.5.2.3.

Table 2.2: Spectroscopic properties of galaxies observed with KMOS. The redshift (z), error (δz) and method of its determination (z -method) are presented, along with the velocity relative to the median redshift (v_{rel}). The seven reliable σ_e values and their corresponding dynamical masses (derived using B -band sizes) are also given. See Section 2.5.

ID	z	δz	z -method	v_{rel} (km s $^{-1}$)	δv_{rel} (km s $^{-1}$)	σ_e (km s $^{-1}$)	$\delta \sigma_e$ (km s $^{-1}$)	$\log(M_{\text{dyn}}/M_{\odot})$	$\delta \log(M_{\text{dyn}}/M_{\odot})$
272	1.8047	0.0005	ppxf	-91	24	256	70	11.91	0.25
355	1.8102	0.0004	ppxf	142	20	452	89	12.05	0.18
356	1.8075	0.0005	ppxf	27	11	186	63	11.46	0.31
657	1.8180	0.0004	ppxf	473	20	97	53	10.24	0.48
352	1.8038	0.0027	ppxf	-130	116	-	-	-	-
447	1.8054	0.0004	ppxf	-61	20	188	49	11.16	0.23
286	1.8062	0.0002	ppxf	-27	11	-	-	-	-
411	1.8176	0.0012	ppxf	456	52	-	-	-	-
772	1.8187	0.0003	ppxf	503	17	153	58	10.48	0.33
387	1.8061	0.0026	ppxf	-32	111	-	-	-	-
317	1.7942	0.0034	ppxf	-543	147	-	-	-	-
359	1.8057	0.0012	ppxf	-49	52	-	-	-	-
693	1.8239	0.0018	ppxf	722	76	-	-	-	-
281	1.8112	0.0008	ppxf	185	35	289	43	11.00	0.13
531	1.8157	0.0006	emission	376	27	-	-	-	-
332	1.8001	0.0063	emission	-289	270	-	-	-	-

squares, $2.8'' \times 2.8''$). I show both unsmoothed spectra (grey; that were used for fitting) and five-pixel median smoothed spectra (black). I also indicate the pixels masked from the fit (blue bands; see Section 2.5.2). I show the PPXF fits to the spectra in red and indicate absorption features (dotted lines) or bands (dashed rectangles), and the [OII] emission line for reference (dot-dash line). For each galaxy, I give its corresponding redshift and stellar velocity dispersions as measured within R_e (σ_e ; as extracted in the KCS pipeline and corrected from the fitted values as explained in Section 2.5.2.4), with 1σ errors from the bootstrapped spectra (see Section 2.5.2.5). As I show normalised flux, I have included the H_{160}^{tot} mag for reference.

In Figure 2.13, I show the four quiescent galaxies (red ID numbers) for which velocity dispersions could not be derived, but for which I used the PPXF fit to derive the redshift (see Section 2.5.3). Again, the spectra are in order of magnitude from brightest to faintest and follow the same labelling as Figure 2.12. For the brightest galaxy spectrum in the figure (ID 352) a prominent bump in the continuum is visible in the red end of the spectrum. This is due to internal reflection from KMOS that has contaminated this portion of the spectrum. To salvage some of the data, I fitted only the blue half of the spectrum to determine a redshift but did not derive a dispersion for the galaxy. The spectrum for the galaxy ID 317 is of poor quality, and thus so is the fit. I derived a poorly constrained velocity for this galaxy but an improvement on the grism redshift from N14 (see Section 2.5.3).

I show the KMOS spectra of the four SF members (blue IDs) of JKCS 041 in Figure 2.14. These are again plotted brightest to faintest and follow the labelling of Figure 2.12. Note that the limits of the y -axis are extended as compared with Figure 2.12 due to the strength of the [OII] emission line (dot-dash line) in IDs 531 and 332. For the top two galaxies in Figure 2.14 with no visible emission, PPXF was used to fit just the velocity to estimate the redshift. For the fainter two galaxies, their strong [OII] emission gave a redshift measurement (see Section 2.5.3). These galaxies are all much fainter in H_{160}^{tot} than the majority of the quiescent galaxies. Looking at their postage stamps, the brightest SF galaxy ID 387 is lumpy and elongated, and is potentially a major merger or disturbed disc. ID 693 looks regular in photometry and does not show any strong emission. For the final two faintest galaxies that show strong [OII] emission, one has a close faint unresolved companion (ID 531), and the other is diffuse, and irregular or disturbed (ID 332).

Table 2.2 gives the spectroscopic properties of all the 16 observed galaxies in JKCS 041. The galaxies are ordered from brightest to faintest in H_{160}^{tot} . The redshift values are given along with the method used to derived them (see Section 2.5.3), as are

the stellar velocity dispersion measurements for the seven galaxies they were reliably derived for.

2.5.2.4 Correcting Velocity Dispersions

As discussed in Section 2.5.2.1, the templates I chose to fit the spectra with (MILES) have a lower resolution than the de-redshifted KMOS spectra. Instead of convolving the data prior to the fits, I corrected the output velocity dispersions using an equivalent procedure. The σ_e had to be determined from the observed value of the dispersion (σ_{obs} – measured by PPXF in the case of no convolution). This was done using the following expressions adapted from Cappellari et al. (2009); Cappellari (2017):

$$\sigma_e = \sqrt{\sigma_{\text{obs}}^2 - \sigma_{\text{diff}}^2}. \quad (2.1)$$

Where σ_{diff} is given by

$$\sigma_{\text{diff}}^2 = \sigma_{\text{temp}}^2 - \sigma_{\text{inst}}^2. \quad (2.2)$$

For JKCS 041 at $z = 1.80$, where σ_{temp} is the resolution of the templates over this wavelength region (σ_{MILES}) which corresponds to $\sim 77 \text{ km s}^{-1}$ over rest-frame wavelength $\sim 3570\text{--}4860 \text{ \AA}$, and here σ_{inst} is the resolution of the KMOS YJ band ($\sigma_{\text{KMOS},YJ}$) and is $\sim 39 \text{ km s}^{-1}$, giving $\sigma_{\text{diff}} \sim 66 \text{ km s}^{-1}$. This left me with eight velocity dispersion values derived from full-spectral fitting with PPXF.

2.5.2.5 Uncertainties of the Kinematic Fits

The errors on the values derived from the kinematic fits were estimated from the fits to the 100 bootstrapped realisations of the galaxy spectra. In Figures 2.15 and 2.16 are histograms of the velocity and velocity dispersion respectively, derived using PPXF on the 100 bootstrapped spectra for each galaxy. The galaxy IDs are shown in the top right of each panel and indicate whether the galaxy is quiescent (red) or SF (blue). The bootstrap values are binned according to the range of values per galaxy but are presented on fixed axes. The values derived for the whole individual spectrum for each galaxy are shown by the arrows. Note the difference relating to Figure 2.13 that galaxy ID 352 with the bump was only fitted in the blue half to get the velocity but shows here as not fitted as these histograms are for the whole spectrum. Also note that in contrast to Figure 2.14, I show fits to the bootstraps of both the galaxies with very strong [OII] emission, but for both I opted to use their emission line for a redshift value and not that from PPXF.

I derived errors on the fits for the individual spectra from the distribution of values from their 100 bootstraps shown in Figures 2.15 and 2.16. To determine the best method of quantifying the spread of the distribution, I show four different estimates; the median absolute deviation (MAD)⁴, the MAD converted to a standard deviation (assuming a normal distribution: $1\sigma = 1.4826 \times \text{MAD}$), the difference between the 16th and 84th percentiles (a 1σ equivalent), and the regular definition of the standard deviation ($\text{STD} = \sqrt{\frac{1}{N-1} \sum_{i=1}^N (X_i - \bar{X})^2}$, where \bar{X} is the mean of the distribution of N points). I opted to use the $1\sigma = 1.4826 \times \text{MAD}$ for the formal error as it is a 1σ measurement that is resistant to outliers. As the values from the fits to spectra with PPXF were not Gaussian in their distribution (non-fits could either hit upper or lower limits set by the software or not deviate from the initial conditions), I opted to use this outlier resistant statistic. This error estimation accounts for both the uncertainties of the fitting method and, by fitting the bootstrap spectra, it allows the systematics of the data reduction pipeline to be quantified. Measuring the distribution of these values is therefore favourable compared to a χ^2 test or Monte Carlo method to estimate the uncertainties of the fit to one spectrum.

To account for any systematics introduced by my choice of order polynomial, I fitted the bootstraps with random order additive polynomials in the range allowed by PPXF of two to eight. The errors from the bootstrapped spectra values therefore reflected the systematic uncertainties of the chosen polynomial order. The errors on the kinematic measurements I derived reflect the ability to reproduce consistent results from the many bootstrapped realisations of each galaxy spectrum. Tests performed for the other KCS targets showed that some of the best quality spectra were extracted from more compact objects and not just from the brightest galaxies. For larger galaxies with more spectra within R_e , the bootstrapped spectra vary more, sometimes producing larger errors despite their higher S/N. Nonetheless, this remains the best estimation of systematic errors for the spectra in my sample. I deemed a stellar velocity dispersion reliable if I was able to fit $> 70\%$ of the bootstrapped spectra and the relative error (i.e. variation in values) I derived from the bootstrapped spectra was $\frac{\delta\sigma_e}{\sigma_e} \lesssim 50\%$. All but one galaxy with a dispersion measurement were within these bounds; galaxy ID 286 had an extremely low dispersion following the correction described in Section 2.5.2.4, and a $\frac{\delta\sigma_e}{\sigma_e} \gtrsim 100\%$. I therefore removed ID 286 from the sample, leaving seven galaxies with reliable dispersion measurements.

⁴The median difference of every point in a distribution (X_i), to the median of the distribution as a whole ($\text{MAD} = \text{median}(|X_i - \text{median}(X)|)$).

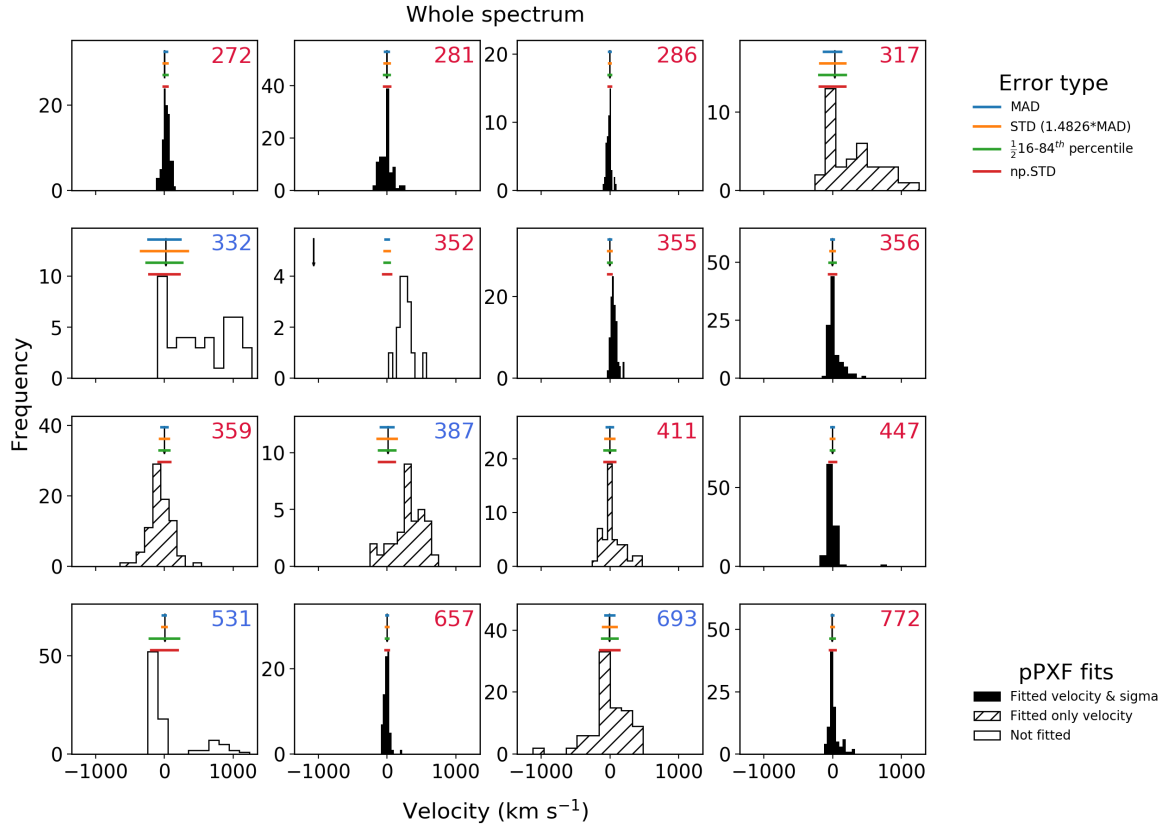


Figure 2.15: Distribution of velocities derived using pPXF for the 100 bootstrapped realisations of the spectra. The galaxy IDs are given in the top right of each panel and show the galaxy is either quiescent (red) or SF (blue). The velocity value derived using the whole individual spectrum for each galaxy is shown by the arrow. The fill of the histograms relates to whether this kinematic fit to the primary spectrum for each galaxy was good (could fit both velocity and dispersion; filled), mediocre (could only fit velocity; hashed), or poor (could not fit the spectrum; unfilled). The different coloured bars show different error estimates derived from the distribution of values from the bootstraps. See Section 2.5.2.5.

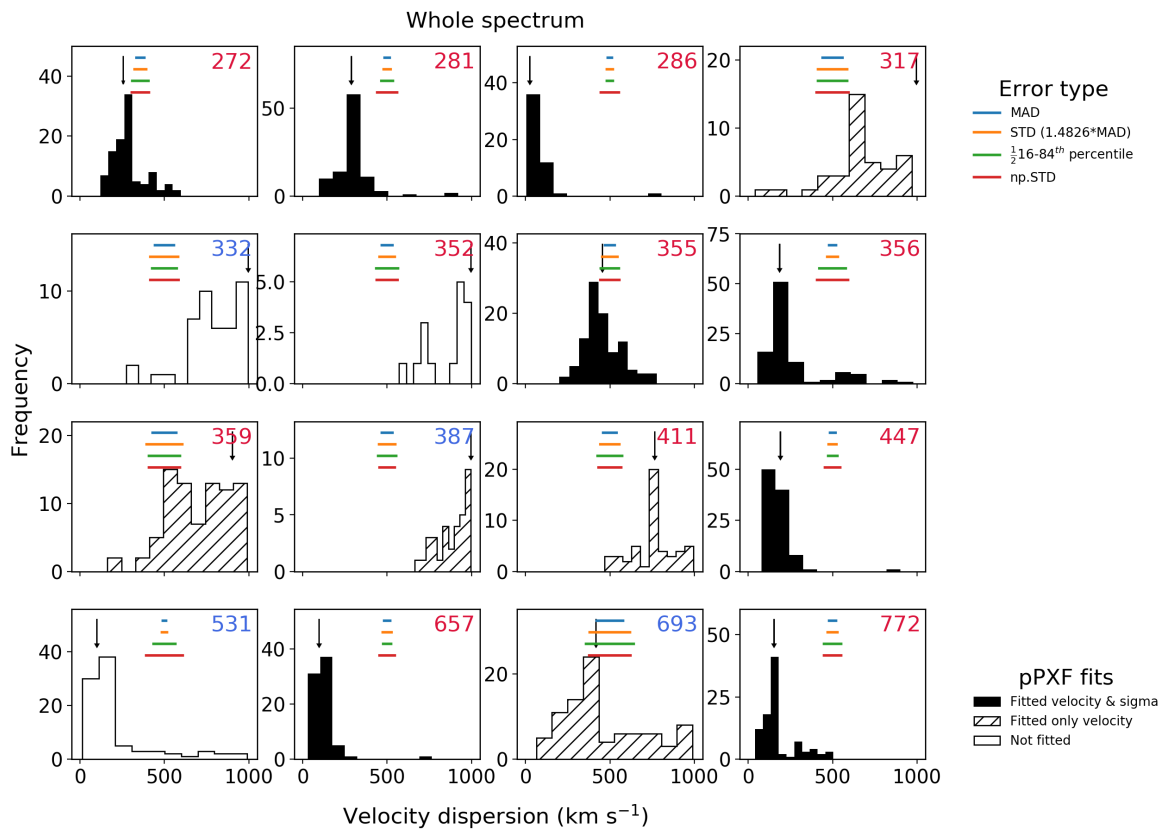


Figure 2.16: Histogram of velocity dispersion measurements derived using pPXF for the 100 bootstrapped realisations of the spectra. The plots have the same labelling conventions as Figure 2.15. See Section 2.5.2.5.

2.5.3 KMOS Redshifts

With the KMOS spectra, I improved on the accuracy of the grism redshift measurements for all the 16 observed galaxies. For most (mainly quiescent) galaxies, this was done using kinematic fits. Even for those galaxies for which I could not derive a reliable value of σ_e , in most cases I was able to determine improved redshift measurements. Velocity measurements were taken from the fits of the individual galaxies and used to determine new redshifts using the following expression from Cappellari et al. (2009):

$$1 + z = (1 + z_{true}) \times (1 + V/c). \quad (2.3)$$

Where z is the measured redshift, z_{true} is the true galaxy redshift, V is the velocity shift derived from the spectrum resulting from the difference between z and z_{true} , and c is the speed of light. The velocity fit for ID 317 is admittedly poorly constrained (Figure 2.15), however, I have used the PPXF value as even with the large errors, I can improve on the accuracy of the redshift from N14. From kinematic fitting, I made improvements in accuracy by around a factor of ~ 4 – 5 for most galaxies compared to the grism redshifts. For two of the SF galaxies (IDs 332, 531), I measured their redshift using the average value derived from each of the two peaks in the strong [OII] $\lambda\lambda 3726, 3729$ Å doublet. All redshift measurements determined for the observed spectra are in Table 2.2 along with the method used to derive them.

2.5.4 Dynamical Masses

For the seven galaxies with reliable σ_e measurements, I estimated dynamical masses using the virial relation. The virial theorem is derived in its simplest form by equating gravitational potential energy to kinetic energy. In the same way that the rotational velocity (v) is used to determine a mass within a Keplerian orbit, the virial theorem uses the velocity dispersion (σ). The kinetic energy of a particle can be given by the following expression:

$$K = \frac{1}{2}v^2 \sim \frac{3}{5}\sigma^2. \quad (2.4)$$

The gravitational potential of a spherical system with a uniform distribution of mass M and radius R is given by:

$$U \sim \frac{3}{5} \frac{GM}{R}. \quad (2.5)$$

Equating the two and rearranging in terms of mass, and assuming that the virial mass (M_{vir}) and radius (R_{vir}) are defined as when the velocity dispersion measured at that

radius is at a maximum (σ_{\max}), gives the following:

$$M_{\text{vir}} \approx \frac{\sigma_{\max}^2 R_{\text{vir}}}{G}. \quad (2.6)$$

To derive the dynamical masses for the seven galaxies with reliable dispersion measurements, I used the form of the relation from [Cappellari et al. \(2006\)](#) (as done in [Beifiori et al., 2014, 2017](#)):

$$M_{\text{dyn}} = \frac{\beta(n)\sigma_e^2 R_e}{G}. \quad (2.7)$$

Where σ_e is the dispersion measured at R_e as is done for the KCS galaxies. The Sérsic index dependent constant $\beta(n)$ is defined by the following equation ([Bertin, Ciotti & Del Principe, 2002](#); [Cappellari et al., 2006](#)) which is accurate to better than 3% at $n = 2\text{--}10$.

$$\beta(n) = 8.87 - 0.831n + 0.0241n^2. \quad (2.8)$$

Here, n describes the distribution of light in the galaxy and is used as a proxy for the distribution of mass in the galaxy. However, this approach does have limitations; the effect of the dark matter contribution within R_e , although expected to be minimal, is unconstrained. In addition, the $\beta(n)$ is derived from idealised, isotropic and spherical galaxies. As I used a rest- B band FP and used these dynamical masses for investigating the effect of structural evolution of the FP shift (see Section 4.2.2 and 4.2.3), I used a B -band R_e (see Section 4.1) to derive my dynamical masses. The dynamical mass estimates and errors for the seven galaxies are shown in Table 2.2.

Chapter 3

HST Data and Photometric Analysis of Galaxies in JKCS 041

In this chapter I describe the photometric analysis of the galaxies in JKCS 041 using the HST images presented in N14. Firstly, I give an overview of HST and its WFC3 instrument in Section 3.1). I then detail the photometric data used in this work (Section 3.2) and the original analysis performed by N14 (Section 3.2.1) for comparison with my results. I will describe the detailed reduction of the HST images prior to fitting the galaxies in Section 3.3. The photometric analysis to extract the structural parameters of the galaxies and the suite of simulations used to derive their uncertainties are described in Sections 3.4 and 3.4.4 respectively. I then compare the photometric values I derive with those of N14 (see Section 3.4.5). Finally, I detail the derivation of the K -corrections (in Section 3.5) for the galaxies as will be used in the FP analysis, and will outline the derivation of their light-weighted stellar masses in Section 3.6

3.1 The *Hubble Space Telescope*

HST was first conceptualised in the 1940s, built in the 1970s and 1980s, and launched in April 1990 (with a repair mission in 1993 to bring it up to its designed imaging performance). It remains the world-leading space-based facility for high-resolution imaging and space-based spectroscopy spanning from ultraviolet (UV) to NIR wavelengths. HST is in space and can therefore make observations in the UV (that is blocked by the atmosphere) and NIR (that is heavily contaminated by the Earth's atmosphere). HST has a 2.4 m diameter mirror and a range of instruments that include cameras, spectrographs, and grisms. It has undergone five servicing missions since its launch; these have extended its life as the world-leading astronomical

observatory beyond its original intended operational lifetime of 15 years¹.

The images from N14 that I used for the photometric analysis of the galaxies were taken using WFC3 (Dressel, 2017) on board HST. This is a fourth-generation instrument, installed in the latest servicing mission in May 2009, that produces wide-field, high-resolution, high-sensitivity imaging from the UV through to the NIR as well as grism spectroscopy. WFC3’s broad wavelength coverage (2000–17000 Å) is enabled by three detectors; two for the UV and optical, and a NIR HgCdTe array for the NIR wavelengths. WFC3 has two channels, one for UV and visible (i.e. optical; ‘UVIS’ channel, 2000–10,000 Å coverage) and one for the IR (IR channel, 8000–17,000 Å coverage). It has a vast range of wide-, medium-, and narrow-band filters (62 in UVIS, 15 in IR) and grisms (one in UVIS, two in IR). The data from N14 (see Section 3.2) described in this chapter is from the IR channel which has a pixel scale of $\sim 0''.128/\text{pixel}$ and a $136'' \times 123''$ FOV.

3.2 Photometric Data

The multi-band HST images used in this work were first presented in N14. Images for JKCS 041 were taken using the infrared filters F160W (H_{160} band) and F105W (Y_{105} band) on WFC3 (GO 12927, Cycle 20, P.I. Newman, October 2012–January 2013). The naming conventions for the IR channel filters are ‘F’ for filter, ‘160’ describes the central wavelength of the channel which translates to a ~ 1600 nm ‘pivot’ wavelength for the F160W filter. The pivot wavelength is a measure of the effective wavelength of a filter that accounts for the integrated system ‘throughput’ (Tokunaga & Vacca, 2005). The throughput describes the telescope and filter’s effectiveness at transmitting the original photon flux through to the output from the detector. It is a function of the transmission of all the elements on a photon’s path through the telescope, instrument and detector (peak system throughput is 0.52 for F105W and 0.56 for F160W). Finally, the ‘W’ defines the width of the band, which in the case of F160W and F105W is wide (~ 270 nm). The F160W and F105W bands are also defined as the WFC3 H and Y bands, respectively. This is a proxy for the commonly used H bands used in ground-based spectroscopy, so I notate them as H_{160} and Y_{105} , respectively, to ease comparison with other surveys.

Images in the H_{160} and Y_{105} bands were taken during a two-orbit visit (see Section 3.3.2) and at different orientation angles of the spacecraft. As well as the photometric

¹http://www.stsci.edu/hst/HST_overview

observations, [N14](#) also made grism observations in two bands G102 (‘blue’ high-resolution grism in the IR channel) with range $\sim 800\text{--}1250$ nm, and G141 (‘red’ low-resolution grism in the IR channel) with range $\sim 1075\text{--}1700$ nm. Prior to the observations of the grism spectra, shorter exposure images (see Section 3.3.2) were made to ensure the correct positioning of the telescope. The main exposures in the H_{160} and Y_{105} bands could therefore be combined with their respective pre-grism images to maximise the total exposure time in each. These combined images result in total exposure times in each band of ~ 4.5 ks in H_{160} and ~ 2.7 ks in Y_{105} . [N14](#) used a four-point dither pattern (the same as was used in the Cosmic Assembly NIR Deep Extragalactic Legacy Survey – CANDELS; [Koekemoer et al., 2011](#)) which aided the removal of bad pixels (as they follow the pattern of the dither and can be easily identified) and to perform sub-pixel shifts help to improve the spatial sampling of the images.

For a self-consistent KCS catalogue in-line with the analysis of [Chan et al. \(2016, 2018\)](#), I re-reduced and analysed the images presented in [N14](#). As shown in Section 2.3.3, there are roughly reduced HST images available on HLA, however for detailed analysis of the structural properties of galaxies, a more refined reduction was required.

3.2.1 [Newman et al. \(2014\)](#) Reduction and Analysis

To highlight the differences between the reduction of [N14](#) and my analysis, and explain any inconsistencies in our derived photometric parameters, I present a brief summary of the photometric reduction and analysis they performed. [N14](#) combined the individual exposures and pre-grism images together via the ‘Drizzle’ algorithm ([Fruchter & Hook, 2002](#)) using the MULTIDRIZZLE software ([Koekemoer et al., 2002](#)). The Drizzle algorithm works by taking the pixels of the contributing image frames and samples their sub-pixel dithering to produce a higher-resolution image. A coarser pixel scale frame can be resampled onto a finer grid by setting the ‘drop’ fraction; the amount by which the original pixel scale is reduced prior to drizzling and this is determined by the user by setting the `pixfrac` keyword. These drops can then be drizzled onto an even finer grid, set by the `pixscale` parameter. This method results in much sharper sub-sampled output images than the observed pixel scale. Figure 3.1 shows an example of the original pixel scale (red squares), the drop pixels (blue squares), and how these map onto the final fine-scale output grid (right-hand side). The output image from the drizzling procedure was chosen to have a final pixel scale of (`pixscale`) $0''.06$; around half the original pixel scale of the input frames (see Section 3.1), which is a reasonable proportion for optimal sampling.

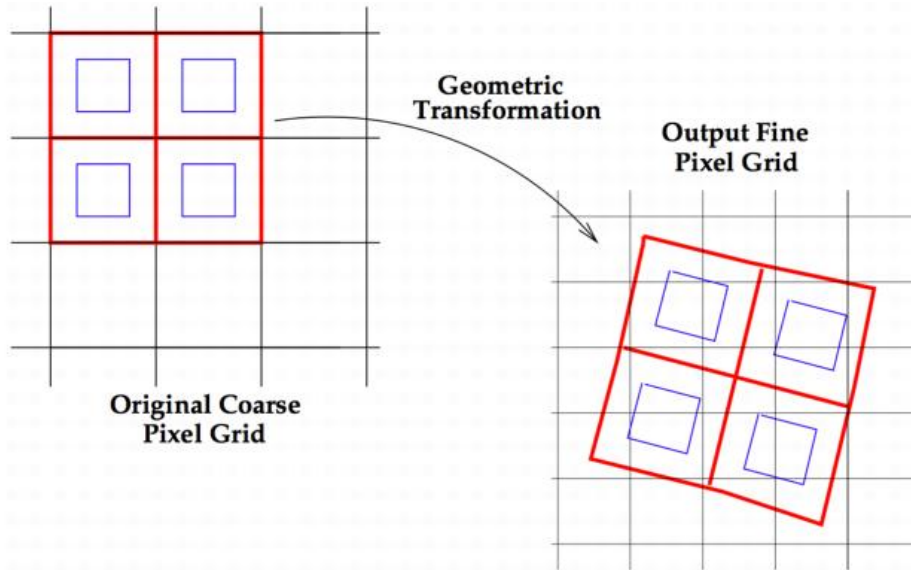


Figure 3.1: Example of the principle mechanism of the drizzling algorithm from the DRIZZLEPAC Handbook (Gonzaga et al., 2012). The large original pixels are highlighted in red and the dropped pixels (denoted by the `pixfrac` parameter) are shown in blue. How these are then mapped onto a final finer-grid output image (scale dictated by the `pixscale` parameter) in order to increase the sampling of the original image is shown on the right. See Sections 3.2.1 and 3.3.

In addition to the HST photometry, N14 also compiled a PSF matched photometric catalogue for galaxies in JKCS 041 comprising *ugrizJHKs* filters from the Canada-France-Hawaii Telescope Legacy Survey and the Wide-field InfraRed Camera Deep Survey (Bielby et al., 2012). In addition, N14 also used observations in the *Spitzer* Infrared Array Camera 3.6 μm and 4.5 μm channels taken as part of the *Spitzer* Wide-Area Infrared Extragalactic Survey (Lonsdale et al., 2003). It is from this catalogue that N14 derived photo- z measurements using SEDs described in Section 2.3.1.

To derive structural properties of the galaxies from the images, Newman et al. (2012, 2014) used GALFIT (Peng et al., 2002) to fit 2D Sérsic profiles simultaneously to all the quiescent galaxies, to account for contamination from neighbouring sources. The Sérsic indices were restricted to $n < 8$. Each galaxy was fitted in a region $2.5\times$ its Kron radius (Kron, 1980). N14 estimated the sky background level by using an 80-pixel width rectangular band around an object and aggressive masking of sources. Getting an accurate measure of the sky in photometric fitting is of particular importance as if it is under- or over-estimated it can significantly affect the derived profile of an object. The smallest member quiescent galaxy (ID 255) could not be fitted as it was too small and not resolved. Apart from this galaxy, all quiescent members

of JKCS 041 confirmed by N14 were fitted with GALFIT. Although, for one galaxy, ID 286, the fit returned a value of $n = 8.0$ which is the upper limit of the input GALFIT parameters and so was not deemed to be constrained. To estimate errors on the derived properties, Newman et al. (2012, 2014) performed tests, adding hundreds of simulated galaxies to the HST images. This method of quantifying the uncertainties in the derived photometric parameters is considered the most accurate as the standard GALFIT errors are considerably underestimated (Häußler et al., 2007). See Section 3.4.4 for details of a similar method used in this work for estimating errors. For JKCS 041, N14 found 1σ uncertainties in R_e were $\sigma_{R_e} = 10\%$ for systems with $R_e < 0''.5$, increasing to 17% for larger galaxies. For n , they got errors of $\sigma_n = 0.4$ when $n < 5$, increasing to $\sigma_n = 0.9$ for more extended profiles having $n = 5-7$. Total fluxes were recovered with a scatter of $\sigma_{\text{mag}} \simeq 0.1$ mag.

3.3 Reduction of Photometry

To reduce the HST images of JKCS 041 for this work, I used ASTRODRIZZLE from DRIZZLEPAC (version 2.0; Gonzaga et al., 2012), which is an updated version of the MULTIDRIZZLE software (Koekemoer et al., 2002) that was used by N14. The reduction steps required prior to applying ASTRODRIZZLE and subsequently for getting the image ready for photometric analysis are outlined in the sub-sections below. These included retrieval and quality checking of HST data, aligning the images onto a common reference frame, running ASTRODRIZZLE, verification of sky subtraction, production of root-mean-squared (RMS) maps, the calibration of the World Coordinate System (WCS), and finally the derivation of the image PSFs.

3.3.1 Retrieval and Quality Checking of Images

All images from WFC3 undergo some calibrations with the CALWFC3 pipeline using reference files particular to the observing mode that correct for instrumental effects. The original raw images, the output calibrated files and the reference files are all available from the Mikulski Archive for Space Telescopes (MAST)². I downloaded all the standard CALWFC3 fully calibrated, flat-fielded products for each exposure (*_flt.fits), association tables (information on dithering between exposures and the pattern used; *_asn.fits) and calibration reference files for JKCS 041 from MAST. Copies of these were made as ASTRODRIZZLE overwrites the original files during the reduction process. For the WFC3/IR data, each flt.fits image consists of five

²<https://archive.stsci.edu/>

extensions: the science image (extension name: SCI), the error array (extension name: ERR), the data quality array (extension name: DQ), the number of samples array (extension name: SAMP), and the integration time array (Deustua, 2016, extension name: TIME).

A visual data quality inspection was done for every `fit.fits` file and their extensions. Examination of the DQ arrays were done to check that the identification of cosmic rays or bad pixels by CALWFC3 was done well. The DQ arrays are similar to the SExtractor segmentation maps (see left panels of Figure 3.2), where all useable pixels are assigned a value of zero, and the bad pixels (or grown bad regions), cosmic rays, and other artefacts are assigned different values depending on their classification. The DQ array therefore acts as a mask for which pixels within the `fit.fits` SCI array are included when being drizzled together. One of the SCI frames for the Y_{105} band showed a bad diagonal row of pixels or ‘hot stripe’. I show an example of the hot stripe that is visible in the identical SCI frames on the left-hand side of Figure 3.2. I then show the DQ frames for this image, the top being before any masking, and the bottom panel after masking. Masking was done by drawing a region around the hot stripe on the SCI image in DS9 and saving this region file. Using the region file coordinates, the poor-quality hot stripe region was assigned the value of 4096 in the DQ array. This ensured that it would not be included in the combined image.

3.3.2 Aligning the Images

The data for each band consisted of some longer exposure science images and shorter exposure pre-grism images. For the H_{160} band, this consisted of four frames with ~ 800 – 900 s, and three ~ 400 s exposures. For the Y_{105} band, there were four shallower science exposures of ~ 400 s and three ~ 350 s pre-grism images. For each band, the longer and shorter pre-grism images were taken during different ‘visits’ which meant that images with different exposure lengths were not aligned to the same reference frame. Broadly speaking, an HST visit is defined as a pointing at a target during which the telescope does not move by more than ~ 1 deg, or if the time between exposures is no longer than one orbit, or if the telescope orientation does not change. For images observed within the same visit, they are aligned to better than 0.1 pixels.

Following a similar technique to Chan et al. (2016, 2018), for each band I used the routine TWEAKREG from DRIZZLEPAC to align the images on to a common reference frame. I selected one of the deeper images for each band to map the other images on to. TWEAKREG works by selecting sources in the reference image, and then in

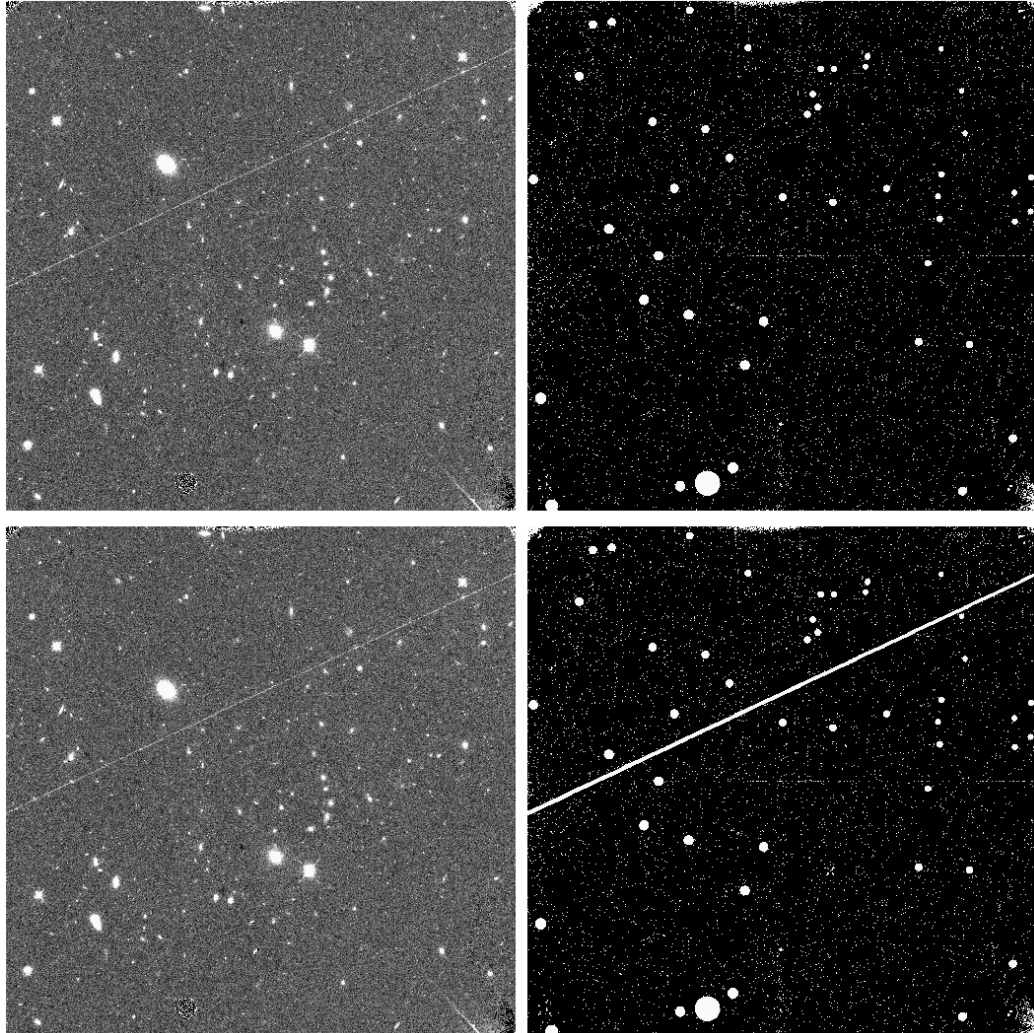


Figure 3.2: An example of the SCI and DQ array extensions of a single `flt.fits` file (a data product of the standard HST/WFC3 CALWFC3 pipeline) for the Y_{105} -band image as shown in the SAOIMAGE DS9 software. The images have linear scaling on the ‘zscale’, which runs from the approximate median image value to the image maximum. I show the same SCI image on the left in both rows but show the before (top right) and after masking (bottom right) of the DQ array in the right-hand columns. The masking was done by defining a region in DS9 to generously encompass the hot stripe seen in the SCI images on the left. I assigned the bad-pixel value of 4096 to all pixels in the masked hot stripe region in the image DQ array (bottom right) so that they would not be included in the combined image. Each panel is 1014×1014 pixels with WFC3 scale $\sim 0''.128$ and total size $\sim 130'' \times 130''$. See Section 3.3.

every subsequent image and mapping one on to the other. The source coordinates for each input image were derived using SExtractor. The inputs for TWEAKREG were a list of the files whose header information needed updating with new WCS³, a file comprising the names of each fit.fits file and its corresponding source catalogue of coordinates, and a reference image onto which the other images were mapped. The output is simply the same input fit.fits files but with shifts applied to their header WCS information (under the user-defined `wcskey` parameter name, TWEAK) so that the final combined image from ASTRODRIZZLE will consist of aligned frames.

3.3.3 Running ASTRODRIZZLE

Aligned exposures were combined into a final higher-resolution output image for each band using ASTRODRIZZLE. This was done through a graphical user interface (GUI) as part of the DRIZZLEPAC software. All the parameters I adopted for running ASTRODRIZZLE (where they differed from the defaults) are summarised in Table 3.1. I describe some of the key parameters and the reasons for choosing them below. See an explanation for selecting the sky subtraction parameters used for ASTRODRIZZLE in Section 3.3.4 and a summary of the values adopted in Table 3.2.

An important parameter in drizzling is the fraction by which the original pixel size is reduced (to avoid convolving the image with the larger-scale camera grid) to produce ‘drop’ pixels prior to being drizzled. Drop size is controlled by the `pixfrac` parameter in ASTRODRIZZLE (linear ratio of the drop size pixel to the original pixel size). This was set to be `pixfrac` = 0.8, as it had to be small enough to avoid convolution with a larger pixel scale frame (i.e. the original scale) but large enough to avoid output pixels having no data in them (see Figure 3.1). The other important parameter is the output pixel scale of the final image (`pixscale`) on to which the drops are drizzled and sub-sampled. I adopted a `pixscale` = 0^{''}.06/pixel for JKCS 041 as this is around half of the original pixel scale, and for consistency with N14.

3.3.4 Sky Subtraction

Starting from the default parameters, I tested how well the sky was being subtracted from the output image during the drizzling process. Accurately quantifying the sky background of each input fit.fits frame is a vital step in the drizzling process in order

³The WCS describes the reference frame in which the positions of objects are defined. Slightly misaligned frames of the same part of the sky can register objects at slightly different positions. There are many different definitions of the WCS and often different surveys and instruments will have different reference frames in which they define object positions.

Table 3.1: Input parameters for ASTRODRIZZLE that differ from the default settings. See Table 3.2 for the non-default sky subtraction parameters. See Section 3.3.3.

Parameter	Input	Description
<code>input</code>	@filelist.txt	A file with a list of file names and paths (file format indicated as a list with the '@' symbol) to be combined.
<code>output</code>	./[filter]_drz	User defined output folder and root name for all products produced in the drizzling process.
<code>wcskey</code>	TWEAK	Header keyword set in TWEAKREG indicating the WCS version to use.
<code>resetbits</code>	0	The pixel values to reset in the DQ arrays. This was set at 0 to prevent astrodrizzle overwriting the masked hot stripe region in the DQ array.
<code>driz_sep_kernel</code>	square	The kernel function for drizzling separate frames onto a common grid.
<code>driz_sep_pixfrac</code>	0.8	Fraction by which to scale pixel size down prior to drizzling for the separate frames (see Figure 3.1).
<code>driz_sep_wcs</code>	Yes	Define custom WCS for separate drizzled images.
<code>driz_sep_rot</code>	0.0	Position angle (deg) of the separate drizzled images' y -axis w.r.t north.
<code>driz_sep_scale</code>	0.06	Absolute pixel scale of the separate drizzled images in arcsec/pixel.
<code>driz_cr_snr</code>	5.0 4.0	Signal-to-noise ratio (SNR) of cosmic ray detection.
<code>final_wht_type</code>	ERR or IVM	The RMS weight-map type, see Section 3.3.5 and Figure 3.4.
<code>final_pixfrac</code>	0.8	Fraction by which to scale pixel size down prior to drizzling for final output image.
<code>final_wcs</code>	Yes	Define custom WCS for the final output image.
<code>final_refimage</code>	none or ./f160_drz_sci.fits	Use reduced F160W band image as the reference for the F105W band.
<code>final_rot</code>	0.0	Position angle (deg) of the final output image y -axis w.r.t north.
<code>final_scale</code>	0.06	Absolute pixel scale of the final output image in arcsec/pixel.
<code>final_units</code>	counts	The units of the output image.

to combine the images onto a final finer grid (as they are effectively sigma-clipped and median stacked using this background value) and for bad pixel and cosmic ray detection. There are a number of user-defined parameters for sky subtraction that can be input to ASTRODRIZZLE. A sky value is estimated (but not subtracted) for each input `flt.fits` image by doing a number of iterative sigma clips and taking an average of the final distribution. The number of iterations, level σ outlier, and the average statistic adopted (e.g., median, mean, mode) is user-defined. The actual sky subtraction is done on-the-fly when drizzling the frames together to an effectively median stacked final image; a minimum sky value of the contributing pixels for each region of the sky (in electrons/arcsec²) is adopted and subtracted.

The background level of a perfectly sky-subtracted image should be zero counts. To determine the background value of the drizzled images from ASTRODRIZZLE, I used an output from GALAPAGOS (described in more detail in Section 3.4) called a sky mask. This is an integer mask, much like the SExtractor segmentation map and DQ images, whereby all the sky pixels have a value of zero, and masked objects are assigned positive integer values. The masking of sources is rigorous, much more so than the source maps from SExtractor; these are some number of Kron radii (parameter set in GALAPAGOS) to conservatively encompass all the extended light from objects. I therefore measured a sky value from an output ASTRODRIZZLE image using a histogram of all the sky pixels (as defined by the sky mask) on the central and deepest part of the image (ignoring the shallower or poorer quality image edges). An example of an H_{160} -band sky mask generated in GALAPAGOS-2.2.5B is shown in Figure 3.3.

The default parameters caused an over subtraction of the sky by ~ 5 counts and so the input parameters were changed to improve this value and to get the sky value as close to a perfectly subtracted value of ~ 0 counts as possible. The final input parameters to ASTRODRIZZLE that were chosen after testing various combinations to optimise the sky subtraction are given in Table 3.2.

3.3.5 Weight and RMS Maps

ASTRODRIZZLE was run twice to produce different weight maps that were used later in the analysis stage; an ERR and IVM map. Figure 3.4 shows H_{160} -band examples of an ERR (left panel) and an IVM (right panel) weight map. The ERR maps show all the background noise (i.e. read noise, dark current, sky background) as well as the Poisson noise of the observed sources. The IVM maps show all the background noise apart from the Poisson noise of the objects. The regions of masked bad pixels are

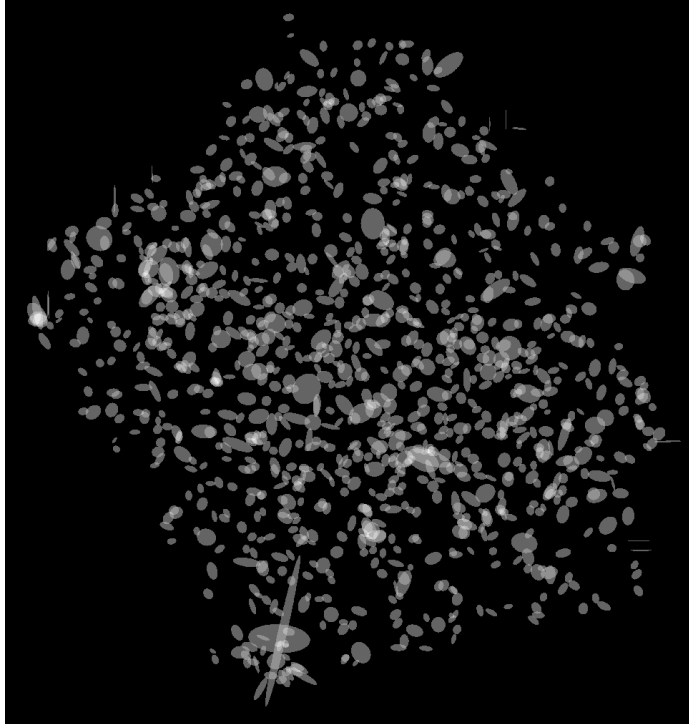


Figure 3.3: An integer sky mask as generated by GALAPAGOS-2.2.5B (see Section and 3.4 for more details) which indicates sky pixel values ($= 0$; black) and rigorous masking of sources ($= 1$ per source; grey). The mask was used to verify the effectiveness of ASTRODRIZZLE at subtracting the sky. Making a histogram of sky pixels as defined by the mask and on the central, deepest part of the frame (ignoring the poor-quality outer edges), gave an accurate estimate of the sky level after subtraction. This was then used to adjust the ASTRODRIZZLE reduction for optimal sky subtraction. The sky map footprint is $\sim 182'' \times 193''$ in size. See Section 3.3.4.

Table 3.2: Sky subtraction input parameters for ASTRODRIZZLE that differ from the default settings. See Table 3.1 for the other adopted non-default parameters. See Section 3.3.4.

Parameter	Input	Description
<code>skystat</code>	mode	Statistic used when taking an average value for each sigma clip and of the final pixel value distribution when determining a sky level to subtract.
<code>skyclip</code>	10	Number of sigma-clipping iterations performed before reading off a sky value.
<code>skylsigma</code>	3.0	Clip sky pixel values with this sigma value below the <code>skystat</code> average.
<code>skyusigma</code>	3.0	Clip sky pixel values with this sigma value above the <code>skystat</code> average.

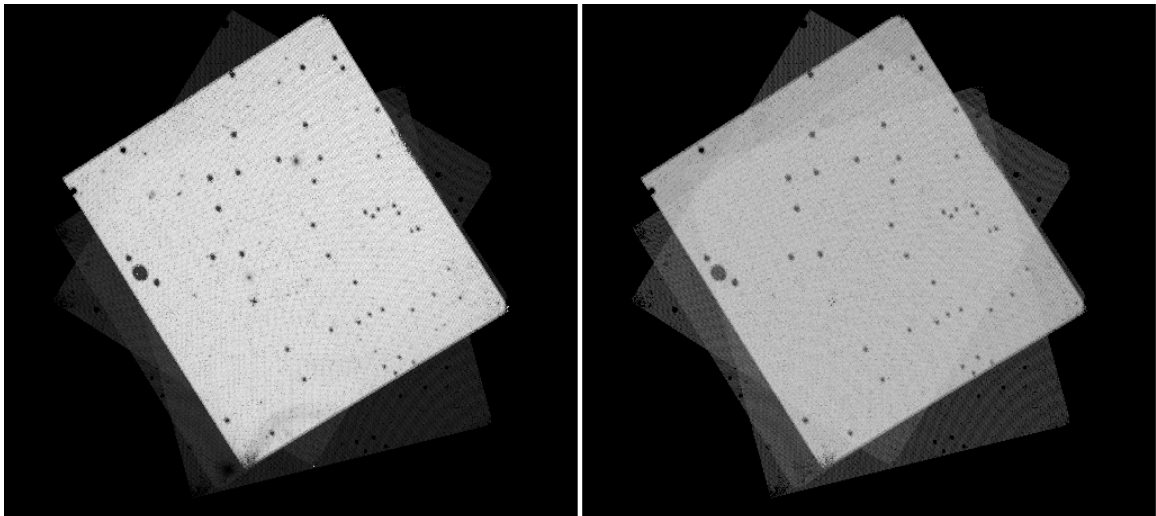


Figure 3.4: Examples of the two different root-mean-squared (RMS) weight maps produced in ASTRODRIZZLE. The error map (ERR; left panel) shows all the background noise whereas the inverse variance map (IVM; right panel) shows all background noise except for the Poisson noise of the objects in the FOV. The ERR maps are used in structural property derivation and the IVM maps are used for source detection with SExtractor. The map footprints are $\sim 182'' \times 193''$ in size. See Sections 3.3 and 3.4.

shown in each (black circles). The ERR maps are useful for when deriving structural parameters as these include the Poisson noise of the objects in the image. The IVM maps are used in source detection with SExtractor as they include only the background noise, making it easier to identify sources (see Section 3.4 for more details).

Once drizzled, a single original pixel can be mapped on to multiple pixels in the finer grid of the output image of the combined drizzled frames. Therefore, the pixel-to-pixel noise in the output image is correlated. A scaling factor is applied to the derived ERR and IVM weight maps to produce RMS maps where this correlation is accounted for. The following relations from Casertano et al. (2000) were used to derive the scaling factor:

$$\sqrt{F_A} = (s/p)(1 - (s/3p)), \quad \text{if } s < p, \quad (3.1)$$

$$\sqrt{F_A} = 1 - (p/3s), \quad \text{if } s > p. \quad (3.2)$$

Where p is the `pixfrac` parameter and s is the fraction of the output drizzled pixel scale to the original pixel scale. For both bands this was $s = 0''.06/0''.128 \approx 0.47$, and $p = 0.8$, therefore $\sqrt{F_A} = 0.4724$. This correction factor was then applied to the

IVM and ERR weight maps to produce the corrected RMS maps using the following expression:

$$\text{MAP}_{\text{RMS}} = \frac{F_{\text{A}}}{\sqrt{\text{MAP}_{(\text{IVM}/\text{ERR})}}}. \quad (3.3)$$

3.3.6 Calibrating the WCS

Now with the final, reduced, drizzled images, I wanted to calibrate their global WCS onto a useful frame of reference. In this case, for consistency between studies, I opted to map my reduced HST images onto the galaxy coordinates published in N14 to aid those utilising both catalogues in future. In order to do this, I used the Graphical Astronomy and Image Analysis Tool (GAIA) in the Starlink library (Berry et al., 2013). GAIA has a user-friendly GUI in which images and coordinates can be loaded, aligned, and header WCS information updated. I loaded both the H_{160} - and Y_{105} -band images into GAIA and the coordinates of the galaxies from N14. I shifted the image to align the galaxies with the coordinates from N14 (by minimising the RMS between the two positions) and saved this information to the header. The final reduced images that were accurately sky-subtracted and WCS calibrated are shown in Figure 3.5 with the Y_{105} band on the left, and the deeper H_{160} band image on the right with the same image scaling. The jagged footprint is from the different telescope orientations for the multi-visit observations.

3.3.7 Derivation of the PSF

A well-defined PSF for each image was essential for the derivation of photometric parameters and the extraction of accurate aperture colours. To derive a PSF for each band, I used the available point sources in the WFC3 FOV; these are the stars that can be distinguished by their bright diffraction spikes, as seen most clearly in the deeper reduced H_{160} image (right panel of Figure 3.5). The PSF was derived using a similar method to Newman et al. (2012) and Chan et al. (2016, 2018); I median stacked the four non-saturated stars from the deepest part of the image, ignoring the very bright star at the bottom of both images. These were the same point sources N14 stacked to make their PSF. The FWHM for the PSF was $0.15''$ for the H_{160} band.

For deriving accurate aperture photometry to calculate galaxy colours ($Y_{105} - H_{160}$), I had to PSF match the images prior to extracting the magnitudes from each band (see Section 3.2.1). I did this by convolving the H_{160} -band image with the Y_{105} PSF and Y_{105} -band image with the H_{160} PSF. I then extracted colours within fixed $1''$ -diameter apertures using SExtractor in dual image mode with the deeper

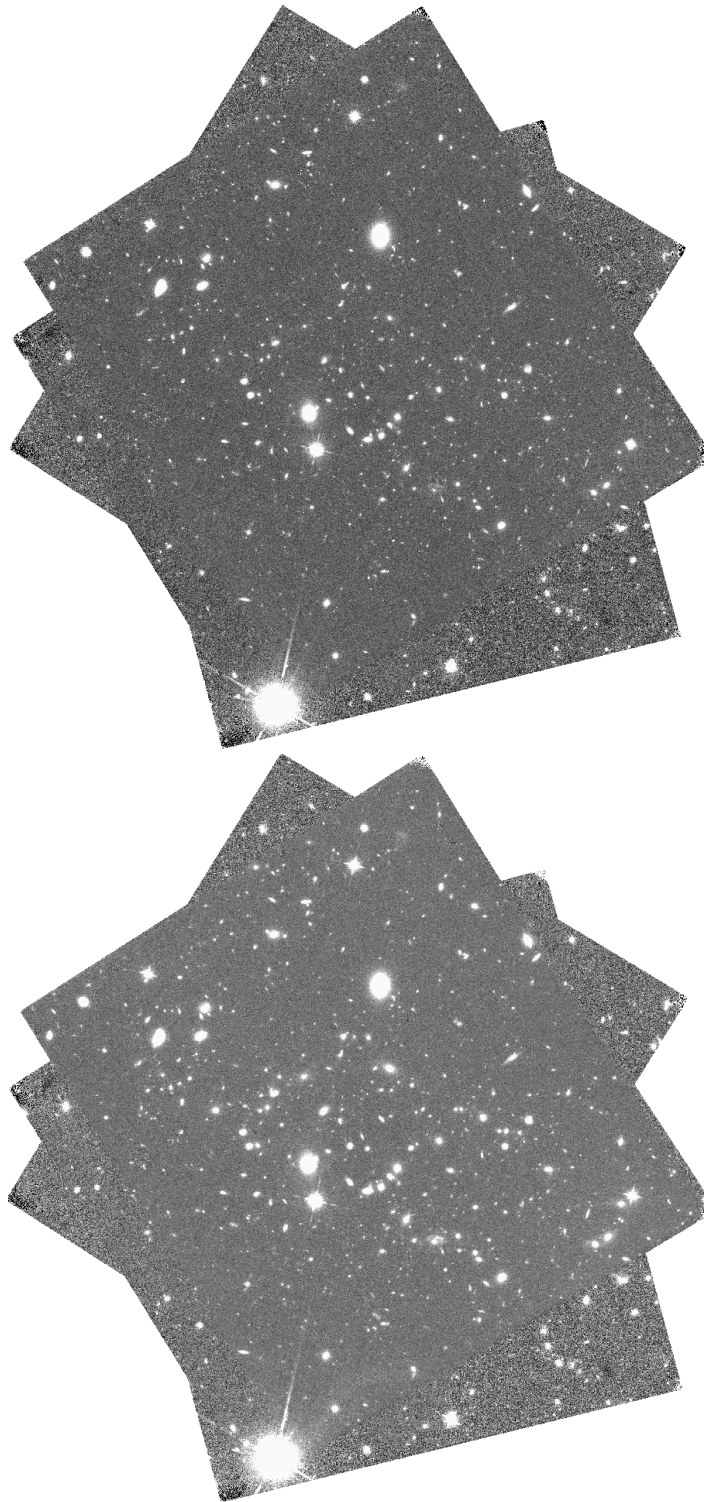


Figure 3.5: The final reduced, drizzled, correctly sky-subtracted, WCS-calibrated HST images in the Y_{105} (top) and H_{160} (bottom) bands. They are both shown on the same scale using linear zscale in DS9. The right-hand H_{160} band is deeper and shows as slightly brighter with more counts and a bit more detail. The footprints of the final images were determined by the different position angles of the telescope during the exposures. The image footprints are $\sim 3030 \times 3224$ pixels with scale $\sim 0''.06$, as set in ASTRODRIZZLE, and total size $\sim 182'' \times 193''$. See Section 3.3.

H_{160} band as the detection image. Dual image mode in SExtractor is a useful function for comparing images of different depths and resolutions. It allows the source catalogue of one image (typically the deeper, higher-resolution image with the most sources) to be that for any other image. For an image which is less deep, fewer sources will typically be detected by SExtractor. Therefore, dual image mode allows the accurate comparison of pixels/regions belonging to a source even if undetected above a user-defined threshold in another band.

3.4 Photometric Analysis

To analyse the photometry, I fitted 2D Sérsic profiles to the galaxies in the images to extract their light-weighted properties. Chan et al. (2016, 2018) performed extensive photometric analysis on the other overdensities in the KCS sample; I adopted similar methods for JKCS 041. In Chan et al. (2016, 2018), light-weighted structural parameters were obtained for the galaxies in the HST images using a modified version of GALAPAGOS (version 1.0; Barden et al., 2012). I give an overview of GALAPAGOS, how it works and its outputs, in Section 3.4.1. I describe setting up GALAPAGOS to analyse galaxies in JKCS 041 in Section 3.4.2. I then give a summary of the light-weighted galaxy properties derived from GALAPAGOS in Section 3.4.3.

3.4.1 GALAPAGOS Overview

The GALAPAGOS software (Barden et al., 2012; Häußler et al., 2013) utilises GALFIT (Peng et al., 2002, 2010), a robust sky-fitting method, and SExtractor (Bertin & Arnouts, 1996) in order to derive accurate photometric parameters from galaxy imaging. GALAPAGOS is an extremely powerful software for large-scale photometric analysis for surveys and some version of it has been used for the Galaxy And Mass Assembly survey (Driver et al., 2009) and CANDELS (Koekemoer et al., 2011). In its latest form (GALAPAGOS-2 and above), as part of the Measuring Galaxy Morphology (MegaMorph) project (Häußler et al., 2013), GALAPAGOS can be used with an adapted version of the new GALFIT (version 3.0.5; Peng et al., 2010) called GALFITM (Häußler et al., 2013) to fit structural properties of galaxies in multiple photometric bands simultaneously.

To analyse the galaxies, each photometric band has its own GALAPAGOS and SExtractor setup file, each with information about the basic properties of the corresponding image. SExtractor is a powerful and widely used software for quickly identifying sources and deriving rough parameters from them. It is flexible and the

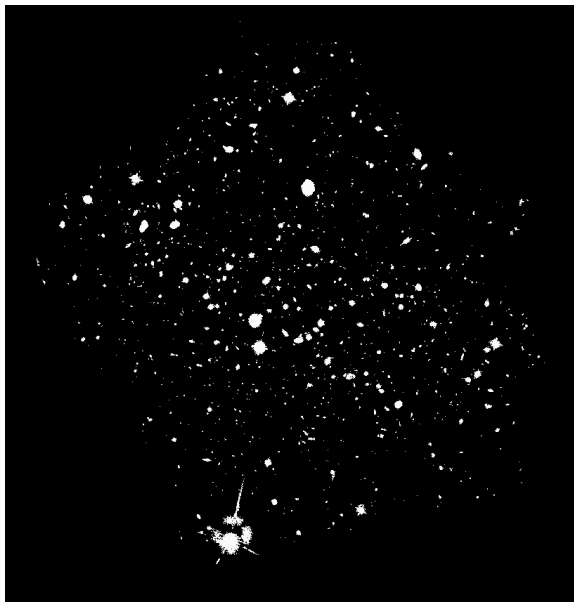


Figure 3.6: A segmentation map of the H_{160} band of JKCS 041 ($\sim 182'' \times 193''$) as produced in SExtractor. SExtractor detects all sources above a user-defined threshold and all pixels belonging to the same object are assigned the same integer value. Basic parameters such as size, magnitude, ellipticity, are measured and catalogued by SExtractor and passed onto GALAPAGOS. See Sections 3.4.1 and 3.4.2.

user can set parameters to control every step and has the ability to choose its outputs. SExtractor is run in GALAPAGOS and it identifies sources, producing a source catalogue and segmentation map (as shown in Figure 3.6 for the H_{160} band), and derives parameters for each source. GALAPAGOS requires a certain set of parameters from SExtractor to run the galaxy fitting; this list is supplied with the software setup file templates and these can be added to. These include source coordinates, ellipticity, size (Kron radius), and magnitude estimates; within a fixed aperture (MAG_APER parameter) and total-integrated magnitude (MAG_AUTO parameter, as given in Figure 2.6). The SExtractor catalogue is fed to GALAPAGOS which then informs the input parameters for some of the next steps.

Next, GALAPAGOS cuts out postage stamps in order to save on processing time. It does this using the Kron radii derived from SExtractor in order to determine a suitable cut-out size. The scale of the stamps in Kron radii is user-defined, and this process produces a postage stamp for each object detected. Following this, GALAPAGOS then estimates the sky background for each object, using rigorous masking of sources (by some factor of Kron radii defined by the user), and a flux-growth curve method (see Figure 3.7). This method works by measuring the sky flux in a series

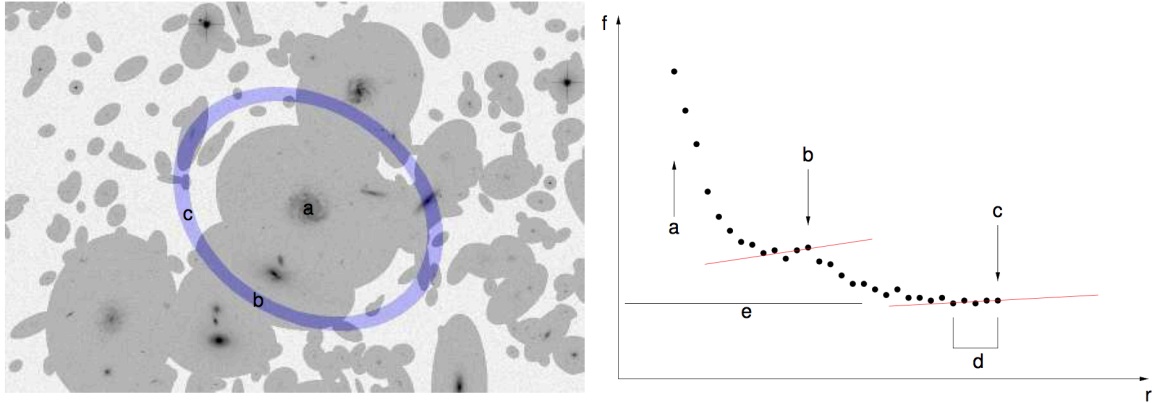


Figure 3.7: Sky estimation figure from [Barden et al. \(2012\)](#). *Left*: An image with galaxies/sources; the dark grey regions show rigorous source masking with ellipses of a user-defined factor of Kron radii larger than the source. The purple region shows an ellipse within which sky is estimated on all non-masked pixels (lighter c regions). The size, separation, and width of the ellipses are set by the user. *Right*: The flux (f) measured within ellipses of increasing radius (r), starting at the central object (a). The slope of the sky-flux curve becomes negative (red lines) for the first time at b, and when it turns over a second time (c) is where the sky value is measured by some number of the last measurements made (d). The background level adopted is shown by e. See Sections 3.4.1 and 3.4.2.2.

of elliptical annuli, the number, size, and separation of which is defined in the setup file. The expanse of the ellipses is not limited by the size of the postage stamps as the whole image is used. The ‘sky’ estimate measured close to the galaxy is likely to contain some diffuse emission from it and the flux-growth curve method addresses this fact. The background will get steadily fainter the further measurements are made from an object (assuming it is isolated). However, when this level plateaus (taken at when the curve gradient goes negative for the second time, see the right panel of Figure 3.7) it indicates that the true sky background has been measured. The strength of this robust sky-fitting method is that it enables accurate fits of diffuse and extended objects. This value of the sky is then fixed for the GALFIT fit; this avoids contamination effects when GALFIT tries to fit sources with many neighbours. I found that because the sky was fixed prior to fitting the galaxies, GALAPAGOS could more reliably extract sources, especially those with close neighbours, as compared to using GALFIT alone.

Finally, it sets up and runs GALFIT using information obtained from the previous steps. GALFIT has long been the most commonly used and versatile method of galaxy fitting used in astronomy. It works by fitting 2D model profiles (e.g., Sérsic, exponential disc) to galaxy images with optimal computational processing, making it ideal for

large surveys. It can also be used for separating different galaxy components, such as bulges, discs, bars etc. GALFIT can be sensitive to input parameters, and not converge on fits if poor initial estimates are given. This is the strength of GALAPAGOS; it utilises the information from SExtractor, fixes the accurate estimation of the sky for each object, and gives GALFIT a sensible range of initial parameters. GALAPAGOS automatically produces a GALFIT setup file and then passes it the galaxy image, a noise array (corrected ERR map from ASTRODRIZZLE, see Section 3.3.5), and a PSF as defined by the user (see Section 3.3.7).

There are a number of input parameters that can be changed in GALAPAGOS to improve or optimise the fit with GALFIT, these are discussed further in Section 3.4.2. To find the best fit, GALFIT minimises the reduced χ^2 (χ_v^2) of the data to the model, as defined by:

$$\chi_v^2 = \frac{1}{N_{\text{dof}}} \sum_{x=1}^{nx} \sum_{y=1}^{ny} \frac{(\text{flux}_{x,y} - \text{model}_{x,y})^2}{\sigma_{x,y}^2}, \quad (3.4)$$

where

$$\text{model}_{x,y} = \sum_{v=1}^{nf} f_{v,x,y}(\alpha_1, \dots, \alpha_n). \quad (3.5)$$

Here, N_{dof} is the number of degrees of freedom in the fit, nx and ny are the image pixel size in x and y respectively. $\text{flux}_{x,y}$ is the image flux at (x, y) , $\text{model}_{x,y}$ is the sum of the nf functions $f_{v,x,y}(\alpha_1, \dots, \alpha_n)$ employed by the user, and $\alpha_1, \dots, \alpha_n$ are the 2D model parameters. The uncertainty on a given (x, y) pixel is $\sigma_{x,y}$.

Photometric parameters are then combined into a single output catalogue, where for each source detected, the SExtractor values and those from the GALAPAGOS fitting are given. GALAPAGOS does most of the preparation and bookkeeping work for the fitting of the galaxies in a sufficiently automated way so that it can be applied to many large data sets. This was therefore the most logical approach for creating a self-similar photometric catalogue for all the KCS target overdensities.

3.4.2 Setting Up GALAPAGOS

For the photometric analysis of the galaxies in JKCS 041, I used an updated and currently maintained version of GALAPAGOS (version 2.2.5b⁴; Häußler et al., 2013). GALAPAGOS-2 and above uses the adapted version of GALFIT3 (Peng et al., 2010), designed to fit multiple bands simultaneously, called GALFITM (Häußler et al., 2013). Although I ran analysis on the different photometric bands separately, to maintain as

⁴Available from Boris Häußler's GitHub page: <https://github.com/MegaMorph/galapagos>.

much consistency as possible between this work and that of [Chan et al. \(2016, 2018\)](#), I used GALFITM (version 1.2.1) for compatibility with GALAPAGOS-2.2.5B. GALFITM handles single bands similarly to GALFIT, the only mentionable difference being the introduction of Chebyshev polynomials (orthogonal polynomials that are useful for interpolation and approximating continuous functions). The Chebyshev polynomials were found to be less degenerate than the structural parameters of the galaxies. Therefore, coefficients of these are fitted rather than the parameters themselves which aids the stability of the fitting process ([Häußler et al., 2013](#)). This can result in a slightly different end point as the code explores parameter space, however, when comparing outputs of the two versions I found them to be extremely consistent and well within the quoted errors (see Section 3.4.4).

Most adaptations made to the original GALAPAGOS used in [Chan et al. \(2016, 2018\)](#) have now been implemented in the currently maintained version (GALAPAGOS-2.2.5B) used for this work, with the exception of running SExtractor in dual image mode. I therefore adapted GALAPAGOS-2.2.5B to run SExtractor in dual image mode with the deeper H_{160} image as the detection band for the fainter Y_{105} image.

The GALAPAGOS-2.2.5B setup consists of seven blocks: A) setting input file locations, B) setting up SExtractor (see Section 3.4.2.1), C) postage stamp creation, D) preparation of the sky calculations (see Section 3.4.2.2), E) GALFIT setup (see Section 3.4.2.3), F) bulge-to-disc decomposition, and G) setup of the output catalogue. Each block can be set to be executed individually, to save on running time, with the exception of block E) which was executed together with block D). The bulge-to-disc decomposition is not used for this analysis, and so I ignore this block. An overview of the important setup steps and parameters are outlined in the sub-sections below.

3.4.2.1 SExtractor Setup

The parameters given in Table 3.3 show the values used in the SExtractor setup files given to GALAPAGOS. I show only the entries that affect the source extraction (i.e. not input and output file names) and a description. These parameters were determined through a combination of utilising parameters adopted in [Chan et al. \(2016, 2018\)](#) and through trial and error to optimise the extraction.

The detection threshold above which a source would be detected was set relatively high (6σ) due to the efficiency of SExtractor at detecting sources in the deep H_{160} -band image. This high threshold did not affect the ability of GALAPAGOS to fit neighbouring secondary sources that were not detected. It was used to conservatively identify non-spurious detections in the image to be fitted as primary

Table 3.3: Input parameters (that affect the extraction of sources) to the SEXTRACTOR setup file that is run in GALAPAGOS. See Section 3.4.2.1.

Parameter	Input	Description
DETECT_MINAREA	9	Minimum number of pixels above the threshold for a source detection.
DETECT_THRESH	6.0	A threshold sigma value for a source.
FILTER	N	Use filter for detection of sources?
DEBLEND_NTHRESH	32	Number of thresholds the intensity range is divided into (32 is common).
DEBLEND_MINCONT	0.02	Percentage of flux a neighbouring source has to be considered separate.
CLEAN	Y	Remove objects close to bright sources, i.e. spurious detections.
CLEAN_PARAM	1.0	Measure of cleaning.
MASK_TYPE	CORRECT	Type of masking to be done.
WEIGHT_TYPE	MAP_RMS	Type of weight map supplied.
WEIGHT_IMAGE	./[band]_IVM.fits	File path to the IVM map from ASTRODRIZZLE and corrected as in Section 3.3.5.
PHOT_APERTURES	16.7	MAG_APER aperture diameter(s) in pixels (0.5" radius).
PHOT_AUTOPARAMS	2.5, 3.5	Parameters for deriving MAG_AUTO: Kron multiplying factor and the minimum radius.
PHOT_AUTOAPERS	2.5, 3.5	Aperture parameters for deriving MAG_AUTO.
SATUR_LEVEL	500000.0	Level at which saturation occurs in Analog-Digital Units (ADUs).
MAG_ZEROPOINT	25.9463	Image zero-point AB magnitude (see Equation 3.6).
GAIN	2.5	WFC3 detector gain in electrons/ADU.
PIXEL_SCALE	0.06	Pixel scale (") set in ASTRODRIZZLE.
SEEING_FWHM	0.18	Stellar FWHM measured from the image (").
BACK_TYPE	AUTO	Type of background calculation.
BACK_VALUE	0.0, 0.0	Value of the background, 0.0 assumes a perfectly sky-subtracted image.
BACK_SIZE	64	Size in pixels of the area used to estimate the background.
BACK_FILTERSIZE	1	Type of filter used in the background.
BACKPHOTO_TYPE	LOCAL	Background estimated from a local region rather than the whole image.
BACKPHOTO_THICK	64	Value to match BACK_SIZE.

sources. The `PHOT_APERTURES` parameter dictated the aperture size that `MAG_APER` magnitude was derived from within. This was set to 16.7 pixels, which is $1''$ as was used for deriving the $Y_{105} - H_{160}$ colour. The `PHOT_AUTO*` parameters were used for the derivation of SExtractor’s total-integrated magnitude estimate – `MAG_AUTO`. The `BACK_*` parameters determined the way in which the background of the image was calculated and can have a significant effect on the number of extracted sources. The zero-point AB magnitude of the image is an important value both in SExtractor and GALAPAGOS. This was defined using the following expression where all the parameters in the equation⁵ were found in the header information of the images from ASTRODRIZZLE.

$$\text{ABMAG_ZEROPOINT} = -2.5 \log(\text{PHOTFLAM}) - 5 \log(\text{PHOTPLAM}) - 2.4079. \quad (3.6)$$

`PHOTFLAM` is the inverse sensitivity which is a scaling factor to convert instrumental flux into a physical flux density and `PHOTPLAM` is the pivot wavelength of the photometric band in Angstroms. The parameters in Table 3.3 give the segmentation map for the H_{160} -band image shown in Figure 3.6. The differences for the Y_{105} band were the AB zero-point magnitude, `MAG_ZEROPOINT` = 26.2689, and the relevant file path to the IVM map (`WEIGHT_IMAGE`; see Section 3.3.5).

3.4.2.2 Sky Estimation Setup

Postage stamps were cut out with a footprint of five times the SExtractor isophote radius (i.e. Kron radius; parameter `C03`) for each source (block C). The postage stamps are what the fits are done on, however the sky estimation is done for each source using the entire image and is not limited by the size of the stamps. The parameters used to optimise the determination of the sky (block D) for the H_{160} band within GALAPAGOS-2.2.5B are given in Table 3.4. These were determined through trial-and-error and visual verification of the fit quality. I describe a brief justification for some of those parameters here. Parameters `D03` and `D04` were used to define the masking of sources or their neighbours when determining the sky level. Parameters `D05`–`D08` dictated the starting point, size, and separation of the sky isophote (elliptical annulus) measurements. Both these sets of parameters were chosen after visual inspection to optimise the fits of the galaxies with close unresolved neighbours (e.g. ID 286) or diffuse objects (e.g., the BCG ID 272 and ID 355).

Parameters `D13` and `D14` are the slope and intercept respectively of the line on a plot of the SExtractor parameters $\log(\text{FWHM_IMAGE})$ vs. `MAG_BEST` below which

⁵Relation from http://www.stsci.edu/hst/wfc3/phot_zp_lbn.

Table 3.4: Parameters used in the GALAPAGOS setup file for the H_{160} band to estimate the sky background prior to fitting 2D models to the galaxies. See Section 3.4.2.2.

Parameter	Input	Description
D03	1.5	Enlargement scale factor for source Kron radii (from SExtractor) for sky map (see Figure 3.3).
D04	1.5	Scale factor by which the neighbouring source Kron radii from SExtractor are enlarged prior to sky estimation.
D05	10	Additional offset (pixels) applied to the scale factor for sky measurement.
D06	5	Distance between individual sky isophotes (elliptical annuli).
D07	10	Width of individual sky isophotes.
D08	10	Minimum gap between SExtractor isophote and inner sky isophote.
D09	2.5	Magnitude cut below which objects are considered as contributing to the primary source.
D10	4	Maximum number of allowed contributing sources (more is more accurate, but it slows the setup and fits).
D11	1.4	Power by which the SExtractor parameter FLUX_RADIUS is raised to convert to R_e (standard option defined in Barden et al. 2012).
D12	15	Calculate the slope of the sky from the last D12 determinations (as adopted in Barden et al. 2012).
D13	-0.25	Slope in SExtractor parameters $\log(\text{FWHM_IMAGE})$ vs. MAG_BEST below which an object is a star (see Section 3.4.2.2).
D14	6.15	Zero point in $\log(\text{FWHM_IMAGE})$ vs. MAG_BEST below which an object is a star (see Section 3.4.2.2).
D15	5	Magnitude limit below galaxies for non-secondary source detections.
D16	2	Magnitude limit below stars for non-secondary sources detections.
D17	0	Only one image used, so no neighbouring ‘tiles’ to include.

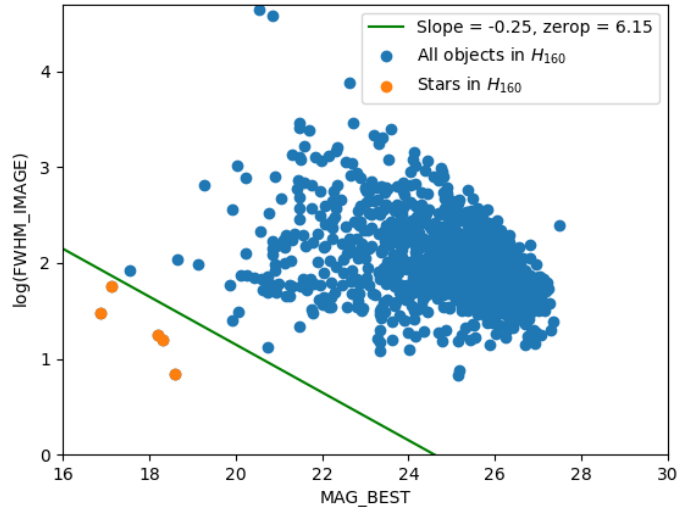


Figure 3.8: SExtractor parameters $\log(\text{FWHM_IMAGE})$ (in pixels) vs. MAG_BEST (mag) for sources in the H_{160} image of JKCS 041. Stars (orange points) and other objects (blue points) are highlighted. A line to separate these populations (green) is shown. The slope and zero point of this line are GALAPAGOS input parameters D13 and D14 respectively. They are used so GALAPAGOS can identify saturated stars to avoid fitting diffraction spikes and other artefacts that can cause the fit to crash. See Section 3.4.2.2.

GALAPAGOS treats an object as a saturated star. Bright stars have numerous secondary artefacts such as diffraction spikes which can cause the fits to fail when fitted simultaneously. Specifying this magnitude cut allows GALAPAGOS to identify sources for which secondaries should be ignored to speed up the fitting process and avoid crashing. To demonstrate how these were determined, see Figure 3.8 for these parameters for objects in the H_{160} band. The parameters derived from SExtractor are given for the stellar objects in the image (orange) and all non-stellar objects (blue). The green line separates these populations, and the slope and zero point of the relation are given by D13 and D14 respectively. For the Y_{105} -band these were determined in the same way but using SExtractor parameters for the Y_{105} band resulting in $D13 = -0.15$ and $D14 = 4.42$.

3.4.2.3 Galaxy Fitting Setup

The GALFIT setup is done in block E and executed in block D. A summary of the input parameters to GALAPAGOS for the H_{160} band that affect the galaxy fitting (and not filenames or processing options) is given in Table 3.5. The only values different for the Y_{105} band were the AB zero-point magnitude (E08; see Section 3.4.2.1) and the exposure time, $E10 = 2670.5610$. Justification for some of these parameters is

Table 3.5: Parameters used in the GALAPAGOS setup file for the H_{160} band for running GALFIT(not including filenames or processing options). See Section 3.4.2.3.

Parameter	Input	Description
E07	200	Convolution box size for PSF; this was the size of the PSF image (see Section 3.3.7) in pixels.
E08	25.9463	Image zero-point AB magnitude (see Equation 3.6).
E09	0.06	Pixel scale (") set in ASTRODRIZZLE.
E10	4509.4340	Exposure time of image (seconds).
E11	400	Constraint for the maximum R_e (pixels).
E12	-5	Constrain minimum (minus) magnitude deviation from SExtractor magnitude.
E13	5	Constrain maximum (plus) magnitude deviation from SExtractor magnitude.
E14	0.2	Constraint for the minimum Sérsic index.
E15	10	Constraint for the maximum Sérsic index.

given here. The most important parameters set were the constraints on the output parameters (E11–E15). I used 400 pixels as a generous upper limit for R_e (E11) and used the large margins (~ 5 mag) above and below the SExtractor estimate for the magnitude limits (E12 and E13) as used in [Barden et al. \(2012\)](#).

In the case of JKCS 041, I was only interested in single Sérsic profile fits to the galaxies as they were mostly quiescent, distant (meaning they were often faint or small in angular size), and for consistency with [Chan et al. \(2016, 2018\)](#) and [Beifiori et al. \(2017\)](#). When imposing an upper Sérsic index limit (E15) of $n = 8$ for my analysis (as in [N14](#)), I found that three confirmed member galaxies reached this limit with my fitting method. I therefore chose to extend my range of Sérsic indices to $0.2 < n < 10$, as it has been reported that Sérsic indices can exist up to 10 for ETGs (e.g., [Caon, Capaccioli & D’Onofrio, 1993](#); [Graham et al., 1996](#); [Kormendy et al., 2009](#)).

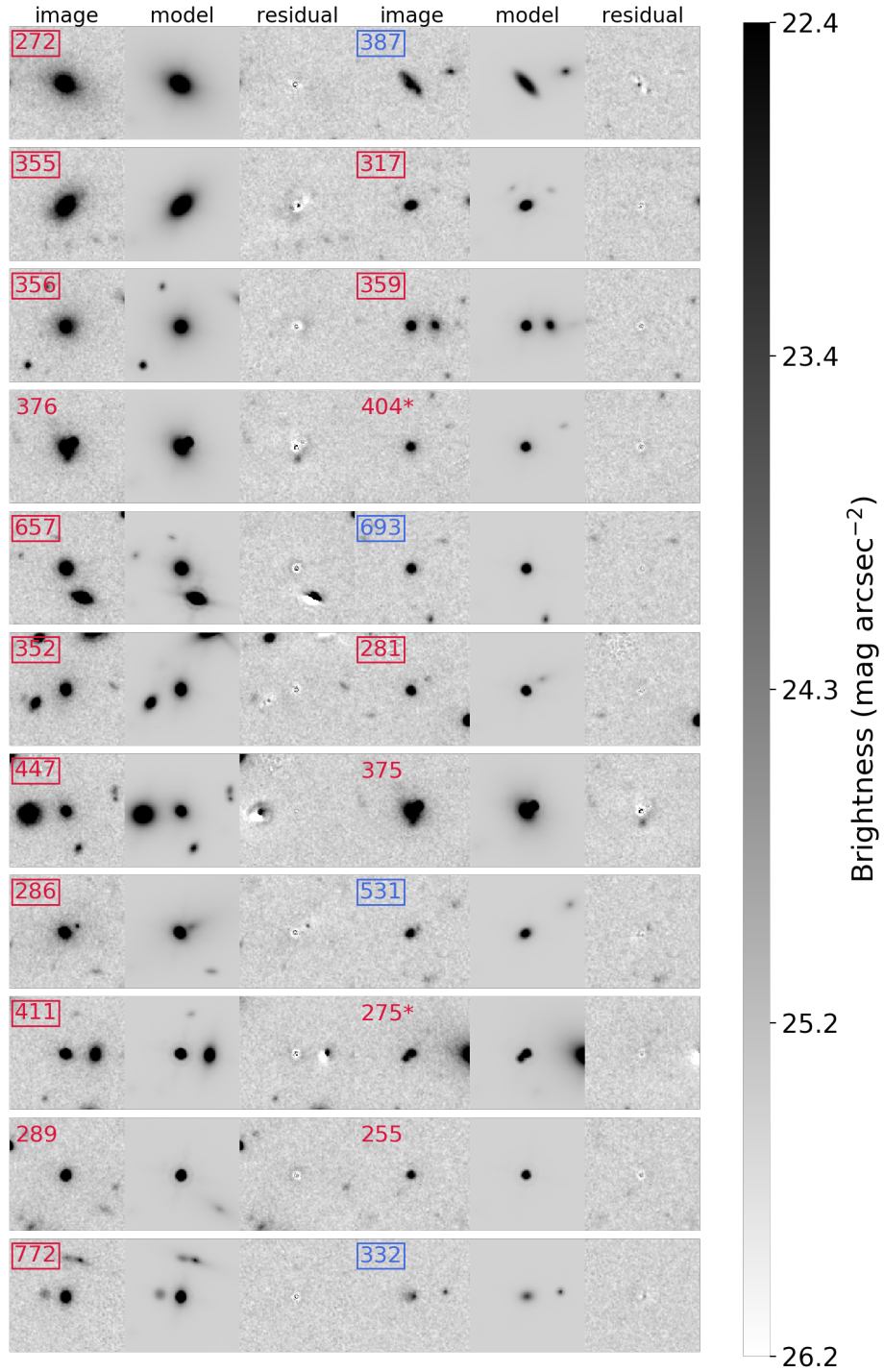


Figure 3.9: H_{160} postage stamps of all the confirmed and candidate members of JKCS 041. I indicate whether they are quiescent (red ID), SF (blue ID), observed with KMOS (boxed IDs), not observed members, or not observed candidate members (*). For each galaxy (from left to right) I plot the H_{160} -band HST image, the GALAPAGOS-2.2.5B fit to the central target galaxy and any other simultaneously fitted sources that may affect the fit, and the residual. The galaxies are ordered in columns by total-integrated magnitudes as derived from Sérsic fits (H_{160}^{tot}); brightest (BCG, ID 272) to faintest. Each postage stamp is $6.78'' \times 6.54''$. See Section 3.4.

3.4.3 Summary of Derived Properties

A number of parameters derived from the photometry using GALAPAGOS-2.2.5B are valuable for characterising the galaxies and studying their physical properties. Figure 3.9 shows postage stamps of all 20 confirmed and the two candidate members of JKCS 041 (see Section 2.3.1). I show the quiescent (red IDs) and SF members (blue IDs) that I observed with KMOS (boxed IDs), confirmed members I did not observe, and unobserved candidate members (*). In two columns, I show all members in order of total-integrated magnitude from Sérsic fits (H_{160}^{tot}); from the brightest cluster galaxy (BCG, ID 272) to the faintest. For each galaxy, I show (left to right) the input H_{160} -band HST image, the GALAPAGOS-2.2.5B model fit to the galaxy (centred) and any neighbouring sources that would affect the fit, and the residual.

Table 3.6 shows the photometric properties of the 20 spectroscopically confirmed members of JKCS 041, the 16 that I observed with KMOS (top panel), the four confirmed members that I did not observe (middle panel), and the two unobserved candidate members (bottom panel; see Section 2.3.1). The observed (= 1), and unobserved (= 0) confirmed (= 1), and unobserved and unconfirmed (= 0) galaxies are presented in order of total-integrated magnitude as derived from Sérsic fits (H_{160}^{tot} , see Section 3.4) respectively. The total-integrated magnitudes derived from GALAPAGOS were corrected for reddening by dust within the Galaxy using the EBVPY package⁶ which utilises the dust maps from Schlegel, Finkbeiner & Davis (1998) and adopting the $E(B - V)$ recalibration from Schlafly & Finkbeiner (2011). A full comparison of my derived values and those of N14 is in Section 3.4.5. In general, I found my derived parameters to be consistent to those of N14 within 1σ errors.

I show the total-integrated magnitudes derived from SExtractor ($H_{\text{tot}}^{\text{auto}}$) in Figure 2.6 (see Section 3.4). The galaxy IDs and the quiescent (Q) and SF designations come from the UVJ diagram in N14. The stellar mass estimates are derived using the total-integrated Sérsic magnitudes and the $Y_{105} - H_{160}$ colour (see Section 3.6). The $1''$ aperture colour derived from PSF matched magnitudes ($Y_{105} - H_{160}$; see Section 3.3.7), was also used to derive K -corrections (see Section 3.5). I present values of H_{160}^{tot} , R_e , Sérsic indices (n), and the projected axis ratio $q = \frac{b_e}{a_e}$ as derived from GALAPAGOS-2.2.5B (see Section 3.4). Here a_e is the semi-major axis (equivalent to R_e^{maj} as extracted from GALAPAGOS), and b_e is the semi-minor axis of the half-light isophote. In this work, I use circularised $R_e (= a_e\sqrt{q})$ values to compare my results for galaxies on the FP with those of previous studies (e.g. Jørgensen et al., 2006;

⁶Developed for PYTHON by R. J. Smethurst, <https://github.com/rjsmethurst/ebvpy>.

Table 3.6: Photometric properties of confirmed and candidate members of JKCS 041. See Section 3.4.3 for a full table description. Uncertainties are given in Section 3.4.4 for the photometric parameters and for $\log(M_*/M_\odot)$ in Section 3.6.

ID	RA	Dec	Obs.	Conf.	UVJ	$\log(M_*/M_\odot)$	$Y_{105} - H_{160}$	H_{160}^{tot}	H_{160}^{auto}	$R_{e,H160}^{\text{maj}}$ ($''$)	$R_{e,B}$ (kpc)	$\log\langle I_e \rangle$ ($L_\odot \text{ pc}^{-2}$)	q	n
272	36.681717	-4.689343	1	1	Q	11.98	1.52	20.01	20.90	1.61	14.38	2.60	0.69	8.1
355	36.686442	-4.692394	1	1	Q	11.57	1.29	20.64	20.85	0.41	3.70	3.59	0.52	3.3
356	36.694234	-4.692352	1	1	Q	11.69	1.51	20.72	21.55	1.30	11.63	2.50	0.97	9.6
657	36.675567	-4.702566	1	1	Q	11.36	1.47	21.47	21.64	0.15	1.31	4.10	0.88	3.9
352	36.690508	-4.692149	1	1	Q	11.33	1.58	21.73	21.94	0.16	1.38	3.93	0.69	4.3
447	36.691213	-4.694866	1	1	Q	10.88	1.11	21.90	22.23	0.34	3.06	3.29	0.78	4.3
286	36.687885	-4.689932	1	1	Q	11.29	1.66	21.97	21.71	0.10	0.91	4.18	0.62	3.3
411	36.673817	-4.693840	1	1	Q	11.19	1.57	22.06	22.13	0.06	0.51	4.66	0.52	1.2
772	36.675274	-4.707378	1	1	Q	11.06	1.42	22.14	22.28	0.10	0.90	4.18	0.58	3.6
387	36.682298	-4.692970	1	1	SF	10.96	1.36	22.29	22.34	0.35	3.12	3.06	0.32	0.3
317	36.699108	-4.690911	1	1	Q	10.90	1.30	22.33	22.46	0.09	0.79	4.25	0.39	1.7
359	36.676955	-4.692279	1	1	Q	10.78	1.21	22.44	22.57	0.09	0.79	4.23	0.84	6.1
693	36.677709	-4.703786	1	1	SF	10.27	0.92	22.76	22.86	0.09	0.79	4.17	0.90	1.7
281	36.690607	-4.689443	1	1	Q	10.83	1.45	22.76	22.82	0.07	0.61	4.26	0.65	0.6
531	36.679183	-4.698392	1	1	SF	9.45	0.40	22.99	23.13	0.14	1.28	3.79	0.58	1.6
332	36.671648	-4.691250	1	1	SF	8.80	0.14	23.71	23.84	0.24	2.18	3.11	0.70	1.0
376	36.675004	-4.692865	0	1	Q	11.72	1.56	20.74	21.23	0.58	5.18	3.18	0.66	9.1
289	36.689651	-4.689939	0	1	Q	11.06	1.42	22.11	22.21	0.06	0.52	4.66	0.54	0.7
375	36.674881	-4.692780	0	1	Q	10.82	1.44	22.77	22.52	0.05	0.46	4.51	0.83	0.8
255	36.687931	-4.688384	0	1	Q	-	-	-	-	-	-	4.67	-	-
404	36.689489	-4.693379	0	0	Q	10.78	1.33	22.67	22.89	0.08	0.76	4.18	0.84	8.0
275	36.682739	-4.689313	0	0	Q	10.65	1.40	23.11	23.07	0.07	0.60	4.15	0.57	0.4

Beifiori et al., 2017). As in N14, I did not resolve the smallest quiescent galaxy in the sample (ID 255) using my photometric analysis, as its R_e was smaller than one pixel ($< 0''.06$).

I show the major axis H_{160} -band sizes ($R_{e,H_{160}}^{\text{maj}}$). As the FP is in the rest- B band, and at $z = 1.80$ the H_{160} band roughly translates to the rest- V band, I needed to correct the galaxy sizes for the FP. I adopted the prescription derived for the other KCS overdensities in Chan et al. (2016) of $d \log(a_e)/d \log(\lambda) = -0.31 \pm 0.27$. This is consistent with the relation derived by van der Wel et al. (2014) and is roughly constant with redshift. This correction translated to a $\sim 5.6\%$ increase in the galaxy sizes; I plotted this B -band circularised R_e ($R_{e,B}$) on the FP (see Section 4.1). I converted the sizes to kpc assuming $z = 1.80$ in my chosen cosmology. I then used $R_{e,B}$ to derive the surface brightness within R_e ($\langle I_e \rangle$) using the K -corrected rest- B magnitudes (see Section 3.5) for the FP.

3.4.4 Uncertainties on Light-Weighted Photometric Parameters

To estimate the systematic uncertainties on my derived photometric parameters, I placed simulated galaxies in the HST images and derived properties from them using GALAPAGOS-2.2.5B as described in Section 3.4. I adapted a suite of simulations used in Chan et al. (2016, 2018) (that relied on SExtractor and GALAPAGOS) to run GALAPAGOS-2.2.5B on simulated galaxies placed into the H_{160} and Y_{105} images. There were significant differences in the file structure, program outputs, and programming mechanisms between the modified version of GALAPAGOS used in Chan et al. (2016, 2018) and GALAPAGOS-2.2.5B used for my analysis. Therefore, to upgrade the simulations to be compatible with GALAPAGOS-2.2.5B was relatively substantial, however, the functionality of the simulations remained the same.

The simulations were set up in a similar way to GALAPAGOS with a setup file with various blocks that could be executed separately. The first block (I) was for setting image parameters (AB zero-point magnitudes, exposure times, pixels scales) and file paths (image, ERR maps, and PSFs). The second block (A) was for determining a catalogue of simulated galaxy properties. The third (B) was to control the making of images with the simulated galaxies. The fourth block (S) controlled the running of SExtractor on the new images, and the fifth (G) was for running GALAPAGOS. Finally, if the bands were deep enough, errors for mass maps could be derived in the final block (M). Unfortunately for JKCS 041 the Y_{105} -band image was not sufficiently deep to provide useful spatially resolved mass properties (as done in Chan et al., 2016,

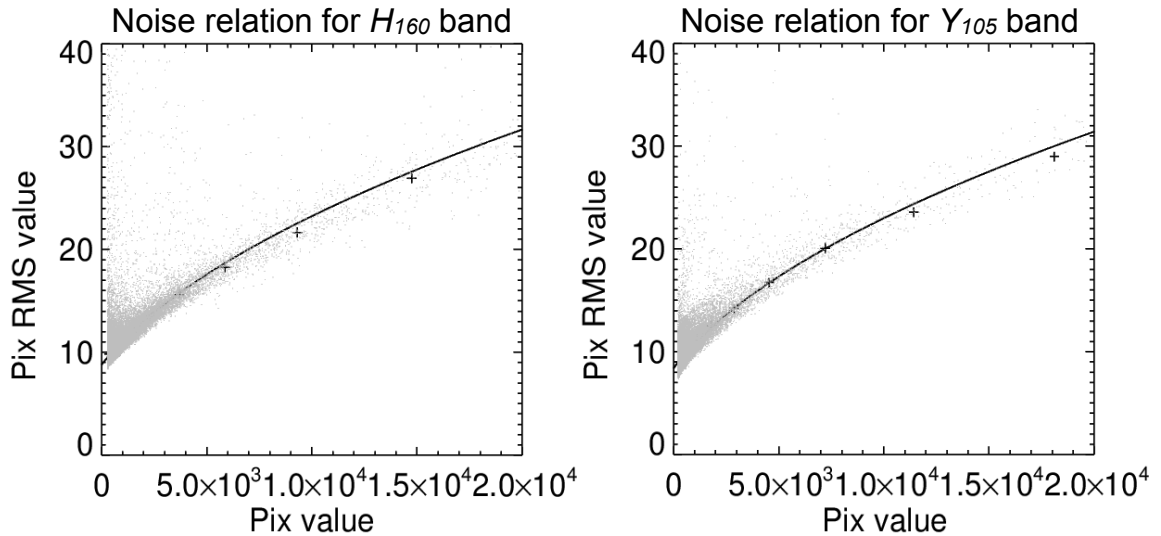


Figure 3.10: Empirical relations derived for the noise in each image, H_{160} (left) and Y_{105} (right). For each band, the RMS of each pixel is shown as a function of the value in the pixel (grey points). An empirical relation was fitted to these points (black lines). The median pixel RMS value in several pixel value bins are shown (black crosses). Sigma-cut levels were defined by the user in the simulation setup file to best match the empirical fit with the median values of the pixel RMS. This relation was then used to add noise to the simulated galaxies and the error maps to accurately represent the real galaxies in the image prior to running SExtractor and GALAPAGOS-2.25B to estimate their properties. See Section 3.4.4.

2018). I therefore only derived a total mass value (see Section 3.6) and did not use this block.

The simulations worked by creating 2D single-Sérsic profile galaxies from input parameters that represented the variety of objects in the image ($n = 0.2-10$, $R_e = 0.012-3''$, $H_{160}^{\text{tot}} = 17-24$ mag). This approach does have the limitation that the model galaxies have the form of a single Sérsic that they are fitted with. This leads to an underestimation of the errors of n , however, it is difficult to quantify the uncertainties of fitting a range of different profile forms with a single-Sérsic model. These were assigned random coordinates to be placed within (or only partially within) the image and stored in a catalogue of simulated galaxy properties. To ensure that the idealised galaxies were realistically represented in the image, a noise level was estimated from the image and added to both the image and error maps. An empirical relation for the noise in each image was derived by fitting pixel RMS values against pixel value and estimating the best fit. This relation is an approximation and does not deal with correlated noise. Figure 3.10 shows the relation (black line) fitted to the image pixels (grey), and how well it fits the median values in each pixel value bin (black crosses).

Sigma cuts of pixels to include when deriving this relation were user defined in order to best match the median bin values to the fitted empirical relation. This empirical relation was then used to add a noise to the 2D galaxy models and error maps.

The two bands were run in the simulations simultaneously. A mock image was created for the one source in both bands by adding noise corresponding to the relevant empirical relation and convolving it by the PSF of that image. I opted to simulate 1000 galaxies to ensure that useful statistics (to estimate my errors) could be obtained from their distribution. Source detection was done using SExtractor, and light-weighted parameters were derived by running GALFITM in the GALAPAGOS-2.2.5B software, as for the real galaxies. The known input parameters of the simulated galaxies and their derived outputs were then compared. Figure 3.11 shows the difference in the input simulated parameters and the output derived parameters, as a function of the true input value for total-integrated magnitude (H_{160}^{tot}), R_e , n , and q . I performed some basic cuts on the simulated galaxy outputs prior to deriving the errors to ensure that the simulated galaxy and the galaxy for which parameters were derived were the same object. This involved a cut for significant difference in magnitude, R_e , and coordinates to ensure I was comparing the same object. For each parameter I chose bins to calculate uncertainties in, to best reflect the distribution of values of the galaxies in JKCS 041 (grey arrows in Figure 3.11).

Using GALAPAGOS-2.2.5B, the uncertainties for the light-weighted parameters derived from the simulations were smaller than those presented in N14. All errors quoted below are 1σ uncertainties. For H_{160}^{tot} I found an average uncertainty across the whole range (17–24 mag) of $\langle\delta H_{160}^{\text{tot}}\rangle = 0.09$ mag. However, I adopted the incremental uncertainties of $\delta H_{160}^{\text{tot}} = 0.12$ mag for $19.5 < H_{160}^{\text{tot}} < 21.5$ mag, and $\delta H_{160}^{\text{tot}} = 0.24$ mag for $21.5 < H_{160}^{\text{tot}} < 24$ mag for the galaxies. For $R_e < 0.5''$, I found uncertainties of $\delta R_e = 7\%$, increasing to $\delta R_e = 13\%$ at $0.5'' < R_e < 1.0''$, and $\delta R_e = 17\%$ for the most extended profiles at $1.0'' < R_e < 2.0''$. For $n < 5$, I found $\delta n = 0.2$, and for the profiles with the largest Sérsic values ($5 < n < 10$), I found uncertainties of $\delta n = 1.0$. I determined errors of $\delta q = 0.01$ for all q values.

I also found some systematic trends, in that my derived output values of H_{160}^{tot} were slightly fainter than the true value at lower brightnesses, and n and R_e were slightly underestimated at larger values. However, I found that these trends over the range of values covered by the galaxies in JKCS 041 were marginal and well within the quoted 1σ errors (as shown in Figure 3.11). I also tested the effects of the ability to accurately recover galaxy properties as a function of cluster-centric radius to test the effect of potential contamination from intracluster light. I found that there were

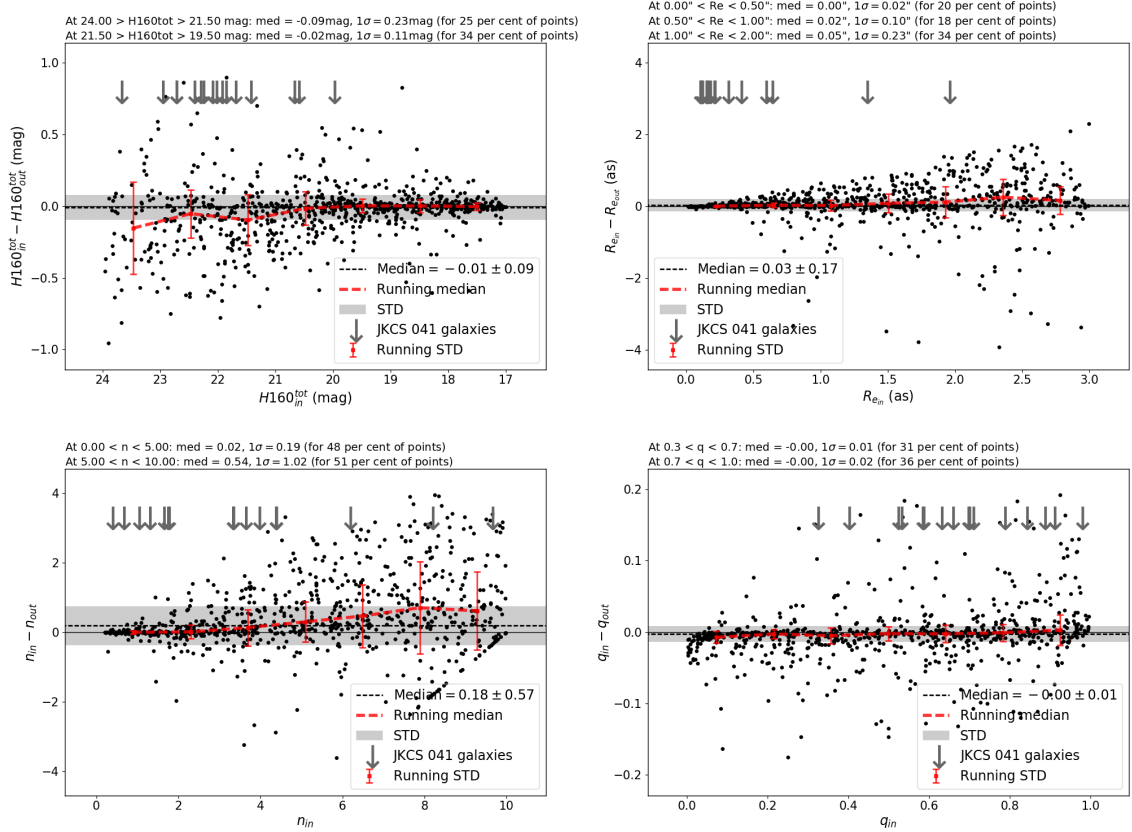


Figure 3.11: The ~ 1000 simulated galaxies that I placed in the *Hubble Space Telescope* images and extracted properties from using GALAPAGOS-2.2.5B as for the real galaxies. I derive errors from the STD of the difference between the input and output values for the simulated galaxies. I show location of JKCS 041 galaxies (grey arrows), median difference (black dashed line), and STD (grey band) for the whole sample. I also show the running median (red dashed line) and running STD (red error bars). Above each plot I show the median values (trends) and STDs (the quoted errors I give for the parameters) for bins chosen to reflect the distribution of the JKCS 041 galaxies.

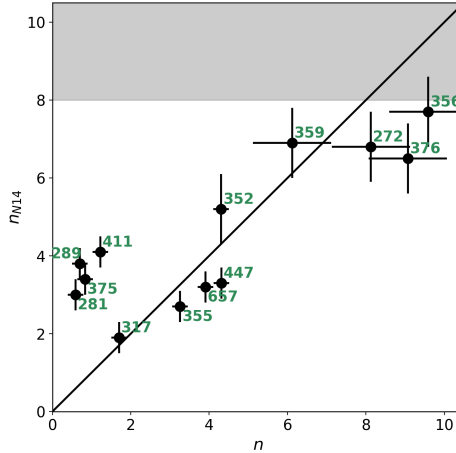


Figure 3.12: Comparison of Sérsic indices I derived (n) and those of N14 (n_{N14}) and a one-to-one line for reference (black). There is a slight trend between the n values I derived and n_{N14} . The trend at the high end may be due to the limit imposed by N14 ($n_{N14} < 8$; shaded region). The galaxies for which I derived the lowest n values, have systematically higher n_{N14} values. The photometry for these galaxies show that most are very compact (IDs 281, 289, 411), as expected for low n values ($\lesssim 1$) that I found as their light is more centrally concentrated. The other is in a close pair (ID 375) that I discuss further at the end of Section 3.4.5.

no trends of the ability to derive properties with cluster-centric radius, which for such relatively bright objects in a distant cluster was to be expected.

3.4.5 Comparison of Derived Photometric Parameters

To further test the reliability of my photometric analysis, I compared the values derived using GALAPAGOS-2.2.5B in this work to the values published in N14. I first compared the Sérsic indices I derived for the 13 quiescent galaxies for which values were published in N14 (n_{N14}) within their imposed limits of $0.2 < n_{N14} < 8.0$ in Figure 3.12. I see a slight trend between the n values I derived and those of N14 where my lowest n values tended to be lower than n_{N14} and my highest n values were higher than n_{N14} . However, my three largest n values were > 8 , which was the limit imposed by N14 (shaded region), which could explain the trend seen at the highest values. For the lowest n values I derived, the photometry showed that most of these galaxies were very compact (IDs 281, 289, 411). A lower Sérsic index might be expected for compact galaxies (as I found), however, the difference can probably be attributed to differences in sky subtraction or estimation. The other is in a close pair (ID 375) that I discuss below.

In Figure 3.13 is the comparison of my derived photometric parameters to those of

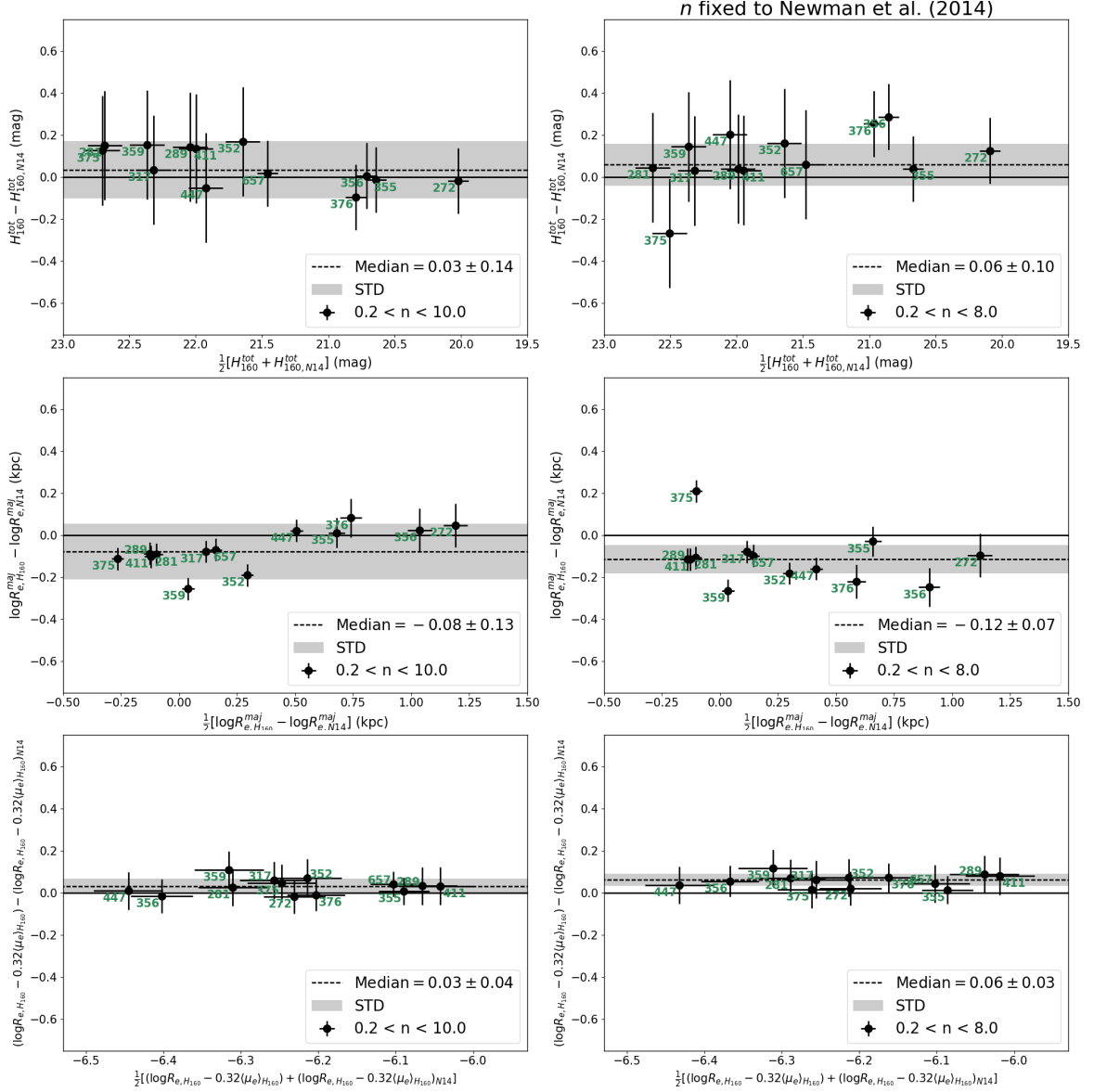


Figure 3.13: Comparison of derived photometric parameters between this work and that of N14 (N14). Both studies derived values from the same HST images but used different reduction and analyses. Here I show parameters derived from the H_{160} band. I plot the difference against the average of three parameters for 13 confirmed quiescent galaxies in JKCS 041 that were also fitted by N14. I show the galaxy IDs, and compare my derived values on the left, and values derived at fixed- n (of N14) on the right. *Top*: Total-integrated magnitude from Sérsic fits (H_{160}^{tot}). *Middle*: R_e along the major axis (R_e^{maj}). *Bottom*: FP photometric parameters (in the H_{160} band for comparison with values from N14); the circularised $R_{e,H_{160}}$ (kpc) and average surface brightness within a circularised R_e ($\langle \mu_e \rangle_{H_{160}}$; mag arcsec $^{-2}$). These are combined using typical coefficients for this definition of the FP ($R_{e,H_{160}} - 0.32\langle \mu_e \rangle_{H_{160}}$; e.g. Bender et al. 1998).

N14: total-integrated magnitude from Sérsic fits (H_{160}^{tot} ; top row), and effective radius along the major axis in the H_{160} band ($R_{e,H_{160}}^{\text{maj}}$) in kpc assuming $z = 1.80$ in my cosmology (middle row). I also show the FP parameter but in the H_{160} band (bottom row) for comparison with **N14**. I combined circularised $R_{e,H_{160}}$ (kpc) and average H_{160} surface brightness within $R_{e,H_{160}}$ ($\langle\mu_e\rangle_{H_{160}}$; mag arcsec $^{-2}$) using typical coefficients for this definition of the FP ($R_{e,H_{160}} - 0.32\langle\mu_e\rangle_{H_{160}}$; e.g. **Bender et al. 1998**). Shown on these plots is the difference against the average value of the parameters for each galaxy between the two studies (left column). As an additional test, I also show the derived parameters I obtained if I fixed the Sérsic indices for the galaxies to those from **N14**, and fitted the galaxies using GALAPAGOS-2.2.5B. I show the median difference of each parameter between the studies (dashed line) and the 1σ errors (as derived with $= 1.4826\times\text{MAD}$, to be resistant to outliers) of the distribution (shaded region). I also show the individual galaxy IDs.

In general, I found that my derived parameters were all consistent to those of **N14** within 1σ errors. I found slightly fainter H_{160}^{tot} magnitudes (positive difference), smaller R_e values (negative difference), and consistent surface brightness values. For all parameters, galaxy ID 375 is consistently marginally deviating from the rest of the galaxies. This galaxy is in a close pair with its more massive companion ID 376, so I did not prioritise these galaxies for KMOS observations due to their proximity. Using GALAPAGOS-2.2.5B I robustly determined a sky value for each object using a flux-curve growth method (see Section 3.4.1), measuring the sky in a series of elliptical annuli and rigorously masking sources (see Section 3.4.2.2). **N14** used a single region bounded by concentric rectangles and masking of sources to determine a sky level (see Section 3.2.1), and a smaller fitting region ($2.5\times\text{Kron}$ radius of the galaxy, as compared to the $5\times\text{Kron}$ radius I used). The differences between the sky estimation and fitting region is the most likely explanation of the discrepancy between our derived parameters for this galaxy.

3.5 K -Corrections

To account for redshift and any difference between the emitted and observed spectral regions, I applied K -corrections (**Hogg, 1999; Hogg et al., 2002**) to my derived magnitudes. I split the K -correction into two components (as in e.g., **Houghton et al., 2012**), such that the total K -correction is

$$K = K_b + K_c. \quad (3.7)$$

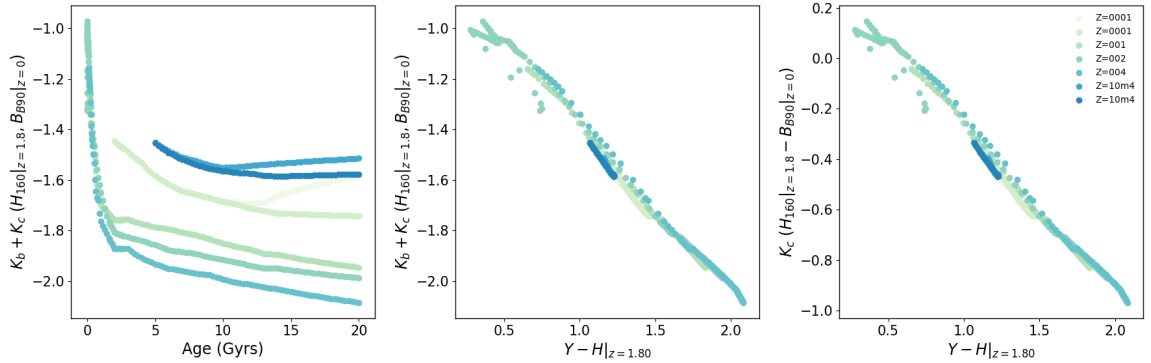


Figure 3.14: Maraston & Strömbäck (2011) SSP model (based on the MILES library) K -correction, age and colour values. I used models with a Chabrier IMF and all possible ages and metallicities in the plots. The K -correction as a function of age (left) and $Y_{105} - H_{160}$ colour (middle), and the K_c term as a function of $Y_{105} - H_{160}$ (right) are shown. I derived relations for the K -correction from these model values to determine appropriate terms to apply to the galaxies in JKCS 041. A linear relation for the K_c term was fitted to the range of model values shown in the far-right plot. The K_c term was then read off the far-right plot for each galaxy depending on the corresponding value of its PSF matched, $1''$ aperture $Y_{105} - H_{160}$. See Section 3.5.

Here the bandpass correction K_b is the reduction of the brightness by $(1+z)$ to account for cosmological expansion. The colour correction K_c accounts for the conversion between different rest-frame regions of the spectra, which depends on the underlying stellar population.

To calculate K_c terms for my galaxies, I derived a relation from SSP models (see Section 1.1.7) from which I could convert a galaxy colour into a colour-correction term. I used Maraston & Strömbäck (2011) SSP models based on the MILES library to derive the relation. I opted for a Chabrier initial mass function (IMF; Chabrier, 2003) and used all the possible ages and metallicities of the models (~ 6 Myrs–20 Gyrs, ~ 0.001 – $2.5Z_\odot$ respectively). I determined magnitudes for each age and metallicity model as observed (i.e. in the H_{160} and Y_{105} bands⁷ at $z = 1.80$) using software written by my collaborator Ryan C. W. Houghton that utilised equations from Hogg et al. (2002). The apparent magnitude m_R observed in bandpass R and absolute magnitude M_Q in bandpass Q of a source is related using

$$m_R = M_Q + DM + K_{QR}. \quad (3.8)$$

Where DM is the distance modulus given by

$$DM = 5 \log_{10} \left[\frac{D_L}{10 \text{ pc}} \right] \quad (3.9)$$

⁷Filter throughput information for HST/WFC3 was from [ftp://ftp.stsci.edu/cdbs/comp/wfc3/](http://ftp.stsci.edu/cdbs/comp/wfc3/).

and where the luminosity distance D_L (e.g., [Hogg, 1999](#)) is given by (with $1 \text{ pc} = 3.086 \times 10^{16} \text{ m}$)

$$D_L \equiv \sqrt{\frac{L}{4\pi S}}. \quad (3.10)$$

Here, S is the bolometric (integrated over all wavelengths) flux and L is the bolometric luminosity. The K -correction between bands Q and R is denoted K_{QR} .

As I wanted to compare my results to those of [Beifiori et al. \(2017\)](#) and use the local Coma FP slopes from [Jørgensen et al. \(2006\)](#), I opted to correct my galaxy magnitudes to the rest-frame Vega B band ([Bessell, 1990](#)). I therefore determined the magnitudes of all the models in the B band as observed at $z = 0$ (again using software written by my collaborator Ryan C. W. Houghton). In Figure 3.14, the values of the K -correction term (left and middle plot) and colour (K_c) term (right) are shown for the models as a function of galaxy age (left) and $Y - H$ colour as measured at $z = 1.80$ ($Y - H|_{z=1.80}$; middle and right plot). The different shades denote the different metallicity models. The $Y_{105} - H_{160}|_{z=1.80}$ colour, and the K_c term ($H_{160}|_{z=1.80} - B|_{z=0}$) for all the different age and metallicity models (right-hand plot) were then linearly fitted to give a relation to convert between the two. I calculated colours from the aperture and PSF matched magnitudes derived from both the Y_{105} and H_{160} bands as described in Section 3.3.7. I then used this relation to convert my $Y_{105} - H_{160}$ galaxy colours to colour-correction K_c terms to apply to their magnitudes for the FP (see Section 4.1). The linear relation fitted to the models is an approximation of the K -correction. I used the distribution of values derived from the models to estimate an uncertainty on my K_c terms.

3.6 Light-Weighted Stellar Masses

To estimate stellar masses for the galaxies in JKCS 041, I used an empirical relation between galaxy colour and stellar-mass-to-light ratio (M_*/L) as done in [Chan et al. \(2016, 2018\)](#). To derive this relation, I used data from the public catalogue of the NMBS ([Whitaker et al., 2011](#)). The NMBS sample has $\sim 13,000$ galaxies at $z > 1.5$ with accurate rest-frame colours, photometric redshifts (derived with EAZY, [Brammer, van Dokkum & Coppi 2008](#)), and stellar masses derived from SED fitting of 37 photometric bands using the FAST code ([Kriek et al., 2009](#)).

A M_*/L -colour relation was derived by my collaborator Jeffrey C. C. Chan in the observer frame to reduce the number of interpolations done to the data ([Chan et al., 2016, 2018](#)). The derivation was done using EAZY; utilising NMBS photometry and

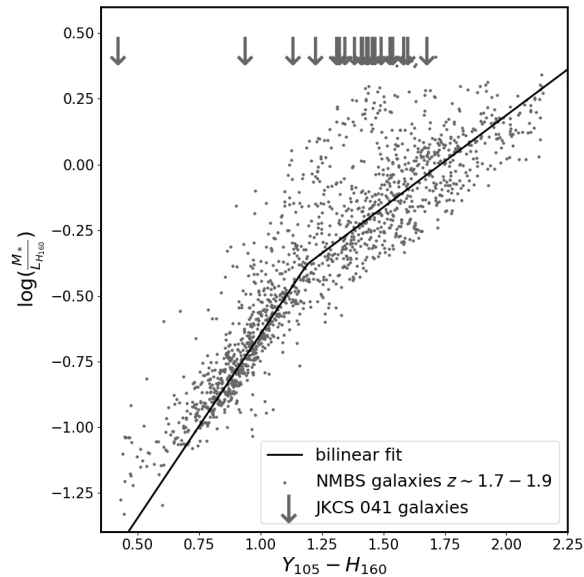


Figure 3.15: M_*/L -colour relation for galaxies from the NMBS (Whitaker et al., 2011) catalogue in the range $1.7 < z < 1.9$. The observed frame colours $Y_{105} - H_{160}$ and H_{160} -band luminosities ($L_{H_{160}}$) were derived for the NMBS galaxies as described in Chan et al. (2016, 2018). I used a bilinear fit to define a relation between $\log(M_*/L_{H_{160}})$ and $Y_{105} - H_{160}$ and used this to derive stellar masses for galaxies in JKCS 041 ($Y_{105} - H_{160}$ colours given by grey arrows). See Section 3.6.

redshifts to fit SEDs, observed-frame $Y_{105} - H_{160}$ colours, and H_{160} -band luminosities ($L_{H_{160}}$). A detailed description of this derivation can be found in Chan et al. (2016).

I selected all galaxies in the range $1.7 < z < 1.9$ from the NMBS catalogue and show their $\log(M_*/L_{H_{160}})$ against $Y_{105} - H_{160}$ values in Figure 3.15. The $Y_{105} - H_{160}$ colour is useful to constrain M_*/L as the bands straddle the 4000 \AA break in the rest frame. I fitted these galaxies with a bilinear relation. This bilinearity predominately comes from the differences between the red and blue galaxy populations at these redshifts (e.g. Mok et al., 2013; Chan et al., 2018). From this relation, I then used my $Y_{105} - H_{160}$ colours for the galaxies and derived corresponding $\log(M_*/L_{H_{160}})$ values. I subsequently estimated total stellar masses ($\log(M_*^{\text{tot}}/M_\odot)$) using $L_{H_{160}}$ derived from the total-integrated Sérsic magnitudes from GALAPAGOS-2.2.5B (H_{160}^{tot}) with

$$\frac{L_{H_{160}}}{L_\odot} = 10^{(M_\odot - M_{H_{160}})/2.5}. \quad (3.11)$$

Where $L_{H_{160}}$ and $M_{H_{160}}$ are galaxy luminosity and absolute magnitude in the H_{160} band respectively. These are scaled to solar luminosity (L_\odot) and magnitude (M_\odot) in the H_{160} band. These values are shown in Table 3.6.

There is significant scatter in the fitted NMBS relation that exists even after a magnitude cut to match the range of values for the JKCS 041 galaxies. Although

this increased scatter is expected at higher redshifts, this could have meant that my derived light-weighted stellar masses from this relation were uncertain. When deriving errors for my stellar masses, I therefore included the scatter on the relation. The uncertainties on my $\log(M_*^{\text{tot}}/M_\odot)$ values are $\delta \log(M_*^{\text{tot}}/M_\odot) \sim 0.12$ for the five brightest galaxies (IDs 272, 355, 356, 376, and 657), and $\delta \log(M_*^{\text{tot}}/M_\odot) \sim 0.15$ for all others.

To verify my mass estimates, I compared the stellar masses I derived with those from N14, that were determined using SED fits to their multi-band ground- and space-based image catalogue (see Section 3.2.1) using FAST (see Newman et al., 2012, for more details). Their masses were scaled to the total magnitude estimated from SExtractor (MAG_AUTO; see Section 3.4). I used these SExtractor total-integrated magnitudes from my images (H_{160}^{auto}) to derive MAG_AUTO scaled masses ($\log(M_*^{\text{auto}}/M_\odot)$). Comparing my masses to those of N14, I found these to be consistent, differing on average by $\log(M_*^{\text{auto}}/M_\odot) \sim 0.10$.

Chapter 4

Fundamental Plane for Galaxies in JKCS 041 and its Implications

In this final chapter of Part I, I combine the results from the KMOS spectroscopic data as derived in Chapter 2 with the photometric results derived from HST images in Chapter 3. I used the parameters I obtained to construct an FP (see Section 1.1.1) for the galaxies in JKCS 041 (see Section 4.1). From the FP, I then derived mean galaxy ages in Section 4.1.1. I quantified what the possible effect of structural evolution of the galaxies had on the derived FP ages in Section 4.2. This included investigating the mass-size and mass-velocity dispersion relations for the galaxies in Section 4.2.2. I looked at the cluster structure (Section 4.3), dynamics (Section 4.3.2), and galaxy ages (Section 4.3.3) in three dimensions. A discussion of the implications of my findings for JKCS 041 in the context of the literature is in Section 4.4. Finally, I conclude my analysis of JKCS 041 as part of KCS as presented in Part 1 of this thesis in Section 4.5.

4.1 Fundamental Plane

For the seven galaxies for which I derived reliable velocity dispersion measurements (see Section 2.5.2), I constructed the FP shown in Figure 4.1. To do this, I combined their derived photometric (see Section 3.4) and spectroscopic parameters using an expression for a 2D projection of the FP. This is the highest redshift FP constructed for galaxies within a single cluster. I used the following form of the FP (in the rest- B band) so as to compare my results with the local FP of the Coma cluster from [Jørgensen et al. \(2006\)](#) and the KCS FPs between $1.39 < z < 1.61$ from [Beifiori et al. \(2017\)](#):

$$\log R_{e,B} = a \log \sigma_e + b \log \langle I_e \rangle + c_z. \quad (4.1)$$

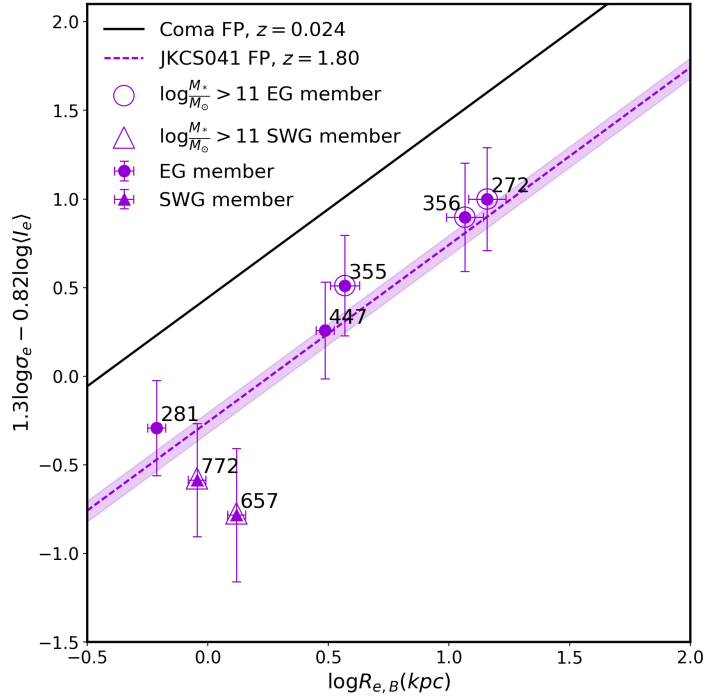


Figure 4.1: FP (in rest- B band) for the seven quiescent galaxies in JKCS 041 for which I derived stellar velocity dispersion measurements (see Section 2.5.2). The galaxies in different regions of the overdensity (as determined in 2D from Figure 2.7) are separated into a group extending eastward (EG; circles) and toward the south west (SWG; triangles; see Section 4.3). The best fit (dashed line) and 1σ error on the measurement of the FP zero point from bootstrapping (shaded region) are shown. The local fit for the Coma cluster from Jørgensen et al. (2006) is shown for comparison; I adopted the same slopes of the FP for JKCS 041. I also show the high light-weighted stellar mass ($\log(M_*^{\text{tot}}/M_\odot) > 11$; larger symbol outlines) galaxies in the sample. See Section 4.1.

Here $R_{e,B}$ is the circularised effective radius in the rest- B band (kpc), σ_e is velocity dispersion with R_e (km s^{-1}), $\langle I_e \rangle$ is average surface brightness within $R_{e,B}$ ($L_\odot \text{ pc}^{-2}$), and c_z is the redshift dependent zero point.

To understand how the galaxies in JKCS 041 might evolve from $z \sim 1.80$ to $z \sim 0$, I required a local comparison sample of galaxies. This is particularly important for the analysis of galaxies using the FP as the local galaxies are used to measure any zero-point evolution and to derive relative M/L values. As mentioned previously, the mass of JKCS 041 means that it is likely to evolve into a system of even greater mass than the Coma cluster in the local Universe (see Section 2.2.2.1). However, as the most massive nearby cluster, Coma provides the only local comparison with a rich enough data set against which to compare JKCS 041. This is also true of the other KCS clusters presented in Beifiori et al. (2017). I therefore compared the

galaxies in JKCS 041 to those in the Coma cluster and used the sample compiled by Beifiori et al. (2017). This catalogue of Coma galaxy data consisted of σ_e values from Jørgensen et al. (1999), R_e values from Holden et al. (2010), stellar masses from Maraston et al. (2013), and dynamical masses (derived from the KCS spectroscopy) from Beifiori et al. (2017).

I fixed the slopes of the FP to the coefficients found for the Coma cluster, at $z = 0.024$ in the local- B band, of $a = 1.30 \pm 0.08$ and $b = -0.82 \pm 0.03$ (Jørgensen et al., 2006). I opted to use fixed slopes of the FP, mainly because I had too few points to constrain any potential tilt. However, the assumption of a non-tilting FP, at least to $z \sim 1$, is supported by various studies (e.g., Wuyts et al., 2004; Holden et al., 2010; Bezanson, Franx & van Dokkum, 2015; Oldham, Houghton & Davies, 2017). The zero point of the FP was fitted using a least-squares method¹ that accounted for the errors in the values on both axes (dashed line). I obtained errors via a bootstrapping method (Jørgensen, Franx & Kjaergaard, 1996) by selecting random samples of the points with replacements and determining their best fit. The zero point I obtained from the fit to the FP was $c_z = -0.26^{+0.05}_{-0.07}$, with 1σ uncertainties (16th and 84th percentiles) from bootstrapping the fit (shaded region).

Using the zero-point shift of the B -band FP, the evolution in the relative change dynamical mass- (see Section 2.5.4) to-light ratio, $\Delta \log(M/L_B)$, as a function of redshift can be investigated (e.g., van Dokkum & Franx, 1996). This approach makes the assumptions that the ETGs are a homologous population, the evolution of c_z only depends on changes in M/L , and that a and b are redshift independent. The relative change in M/L is expressed as follows:

$$\begin{aligned} \Delta \log(M/L_B) &= \log(M/L)_z - \log(M/L)_{\text{Coma}} \\ &= (c_z - c_{\text{Coma}})/b. \end{aligned} \quad (4.2)$$

Where c_{Coma} is that defined in Jørgensen et al. (2006), and c_z values are calculated for each galaxy using the parameters used to construct the FP and the following equation (see e.g., van Dokkum & van der Marel, 2007),

$$c_z = \log R_e - (a \log \sigma_e + b \log \langle I_e \rangle). \quad (4.3)$$

This conversion gives a $\Delta \log(M/L_B)$ value for each of the seven galaxies on the FP that is plotted as a function of their redshifts in Figure 4.2. Again, I fitted the points using a least-squares method accounting for errors on both axes (dashed line) and derived 1σ errors from bootstrapping (shaded region). I found a relation of

¹Using the orthogonal distance regression package in SCIPY in PYTHON.

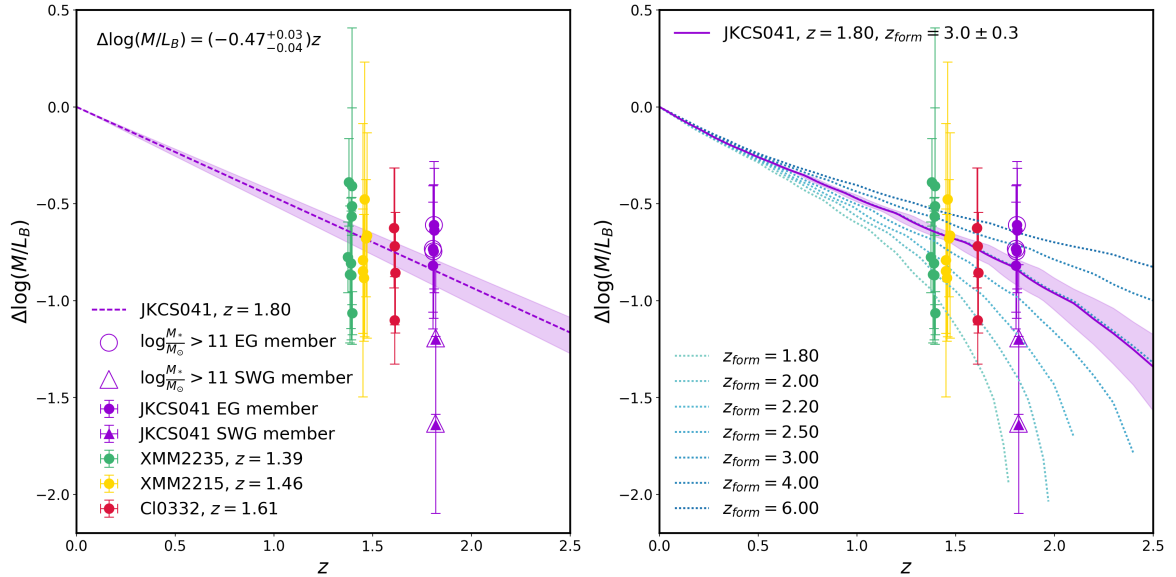


Figure 4.2: Relative M/L evolution (rest-frame B -band) derived from the FP (Equations 4.2 and 4.3) as a function of redshift for seven galaxies in JKCS 041 (violet, symbols as in Figure 4.1). Galaxies in three other KCS overdensities are shown for comparison (Beifiori et al., 2017). *Left*: The best fit (dashed line) and 1σ errors from bootstrapping (shaded region) are shown. *Right*: Interpolating SSP models (Maraston, 2005) using EZGAL (Mancone & Gonzalez, 2012), $\Delta \log(M/L)$ evolutionary tracks were built up as a function of redshift for different z_{form} values. Overplotting these tracks (dotted lines), and determining the best fitting z_{form} (solid line) and 1σ errors from bootstraps (shaded region) based on the track intersection with the best fit from the left panel, I derived a mean $z_{\text{form}} = 3.0 \pm 0.3$ ($\sim 2.1^{+0.3}_{-0.2}$ Gyrs after the Big Bang), corresponding to a mean age of $1.4^{+0.2}_{-0.3}$ Gyrs for these seven galaxies in JKCS 041. See Section 4.1.1.

$\Delta \log(M/L_B) = (-0.47^{+0.03}_{-0.04})z$ for the seven galaxies in JKCS 041 on the FP (median $z = 1.808$).

4.1.1 Derivation of FP Ages

To determine a formation epoch, and thus age of the galaxies on the FP, I interpolated SSP models at different formation redshifts (z_{form}) to get M/L values. I used EZGAL (Mancone & Gonzalez, 2012) to do this; a software that takes model SEDs of different age and stellar population properties and projects them through different observed filters to determine how parameters such as the M/L change with time. I chose to interpolate solar metallicity SSP models (a reasonable approximation for the galaxies in JKCS 041) with a Salpeter (1955) IMF from Maraston (2005) to derive model M/L values in the B band at different formation epochs. I found the age results for JKCS 041 were consistent within errors when using different models (Conroy, Gunn

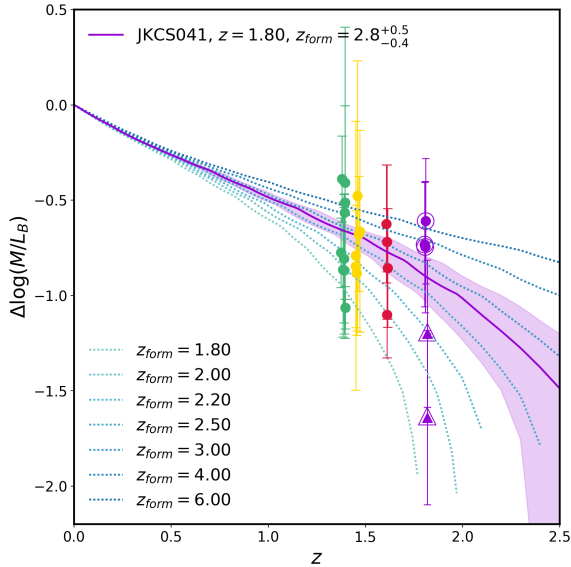


Figure 4.3: M/L evolution as a function of redshift for five high-mass ($\log(M_*^{\text{tot}}/M_\odot) > 11$) galaxies in JKCS 041 (symbols as in Figures 4.1 and 4.2). SSP models (Maraston, 2005) interpolated using EZGAL (dotted lines) and the best fitting model (solid violet line) and 1σ errors (shaded region) are shown. I derived a mean $z_{\text{form}} = 2.8^{+0.5}_{-0.4}$ ($\sim 2.3 \pm 0.4$ Gyrs after the Big Bang), corresponding to a mean age of 1.2 ± 0.4 Gyrs. This mean age is consistent with that of all seven galaxies in JKCS 041 on the FP shown in the right panel of Figure 4.2. See Section 4.1.1.

& White, 2009; Conroy & Gunn, 2010; Bruzual & Charlot, 2003) and IMFs (Salpeter, Chabrier, Kroupa 2001). As I used the relative M/L , the effects of using different IMFs is expected to be negligible. Beifiori et al. (2017) ran further tests, including with different metallicity SSP models, and found that the choice only affected the derived ages within the stated errors. This is consistent with other results from spectroscopy and photometry of galaxies at similar redshifts (Mendel et al., 2015; Chan et al., 2016).

I show some tracks of $\Delta \log(M/L_B)$ as a function of redshift for different z_{form} values calculated with EZGAL in Figure 4.2. From interpolating the models for many z_{form} values, I derived the mean best fitting formation epoch for my galaxies as determined from the intersection of the best fitting line in the left panel, and the corresponding model track (only a few of which are shown) in the right panel. The best fitting formation redshift for the seven galaxies was $z_{\text{form}} = 3.0 \pm 0.3$ (formed $\sim 2.1^{+0.3}_{-0.2}$ Gyrs after the Big Bang), with errors determined from the model tracks intersecting the 1σ uncertainties of the fit from bootstrapping. This z_{form} value corresponds to a mean age for the seven galaxies in JKCS 041 on the FP of $1.4^{+0.2}_{-0.3}$ Gyrs.

In order to compare JKCS 041 age estimates to red-sequence galaxy ages derived

in the three other KCS overdensities in Section 4.4.3, I also show the $\Delta \log(M/L_B)$ - z values for XMM2235 ($z = 1.39$; green), XMM2215 ($z = 1.46$; yellow), and Cl0332 ($z = 1.6$; red; [Beifiori et al., 2017](#)) in Figure 4.2. I investigated the FP ages for the most massive galaxies ($\log(M_*^{\text{tot}}/M_\odot) > 11$; larger outlined symbols in Figures 4.1 and 4.2) in JKCS 041 to compare my results. In Figure 4.3, I show the five most massive galaxies (as derived from stellar light; using the same plot format as Figure 4.2) and derived a comparable mean age to those I obtained for all seven galaxies of 1.2 ± 0.4 Gyrs (formed at $z_{\text{form}} = 2.8_{-0.4}^{+0.5}$, which is $\sim 2.3 \pm 0.4$ Gyrs after the Big Bang).

4.2 Structural Evolutionary Effects on the FP Zero-Point Evolution

4.2.1 FP Zero-Point and Luminosity Evolution

To understand the effects of galaxy structural evolution on the change in zero point of the FP, I used the method described in [Saglia et al. \(2010, 2016\)](#) and [Beifiori et al. \(2017\)](#). The FP zero point can be defined by the change with redshift of the structural evolutionary terms of R_e , σ_e , and luminosity ($L_{\text{FP,SE}}$, where SE is structural evolution). The variation of the luminosity from this structural evolution can be expressed as

$$\Delta \log L_{\text{FP,SE}} = \frac{2b+1}{b} \Delta \log R_e - \frac{a}{b} \Delta \log \sigma_e - \frac{1}{b} \Delta c_z. \quad (4.4)$$

Here a and b are the FP coefficients in Equation 4.1 (from [Jørgensen et al., 2006](#)) and c_z values were derived with Equation 4.3 using the FP parameters. Each structural evolutionary term can be defined as a function of redshift so that $\Delta \log R_e = \nu \log(1+z)$ (where $\Delta \log R_e = \log R_e(z) - \log R_e(0)$), $\Delta \log \sigma_e = \mu \log(1+z)$ (where $\Delta \log \sigma_e = \log \sigma_e(z) - \log \sigma_e(0)$), and $\Delta c_z = \eta' \log(1+z)$. Here ν and μ are the slopes of the evolution of sizes and velocity dispersions with redshift respectively, and η' is related to the slope of the $\log(M/L)$ evolution with $\log(1+z)$ by $\eta' = \eta \times b$. Equation 4.4 can therefore be rewritten as

$$\begin{aligned} \Delta \log L_{\text{FP,SE}} &= \left(\frac{2b+1}{b} \nu - \frac{a}{b} \mu - \frac{1}{b} \eta' \right) \log(1+z), \\ &= \chi \log(1+z), \end{aligned} \quad (4.5)$$

where $\chi = \left(\frac{2b+1}{b} \nu - \frac{a}{b} \mu - \frac{1}{b} \eta' \right)$.

Table 4.1: Slopes derived for FP luminosity zero-point and structural evolutionary parameters. I show the slopes for the change in FP luminosity without accounting for structural evolution of the galaxies ($\Delta \log L_{\text{FP}}$) and with ($\Delta \log L_{\text{FP,SE}}$). I also show the slopes derived for the change in the mass-normalised R_e (ν) and σ_e (μ) values with redshift for both the M_{dyn} - and M_*^{tot} -normalisations used to determine $\Delta \log L_{\text{FP,SE}}$. See Section 4.2.

Relation	Slope	
	M_{dyn}	M_*^{tot}
$\Delta \log L_{\text{FP}} = -\eta \log(1+z)$	1.88	$^{+0.13}_{-0.17}$
$\Delta \log R_{e,\text{MN}} \propto \nu \log(1+z)$	$-0.61^{+0.41}_{-0.20}$	$-1.00^{+0.20}_{-0.19}$
$\Delta \log \sigma_{e,\text{MN}} \propto \mu \log(1+z)$	$0.26^{+0.07}_{-0.13}$	$-0.01^{+0.08}_{-0.14}$
$\Delta \log L_{\text{FP,SE}} = \chi \log(1+z)$	1.82 ± 0.42	1.08 ± 0.33

To test the contribution of each structural evolution parameter to the FP zero point, I first determined the value of just the change in luminosity due to the evolving stellar population. This assumption is made for most studies of the FP. To do this, I assumed that $\Delta \log R_e$ and $\Delta \log \sigma_e$ were zero, leaving $\Delta \log L_{\text{FP}} = -\frac{1}{b}\eta' \log(1+z) = -\eta \log(1+z)$. The slope I derived ($\eta = 1.88^{+0.13}_{-0.17}$) is given in Table 4.1 for comparison with the other slopes determined in the following sub-section.

4.2.2 Mass-Sigma and Mass-Size Relations for JKCS 041

I used the mass-velocity dispersion (M - σ_e) and mass-size (M - R_e) relations to study the effects of structural evolution with redshift, as compared to Coma, for the seven galaxies in JKCS 041 with reliable σ_e measurements (following the method of [Saglia et al., 2010, 2016](#); [Beifiori et al., 2014, 2017](#)). The mass plane (MP) is the narrow relation between mass, σ_e , and R_e , and it follows the scalar virial relation $M \propto \sigma^2 R_e$ (see Section 2.5.4; [Cappellari et al., 2013a](#)). The FP for galaxies in the local Universe was found to be due to the virial relation and a smooth variation of galaxy properties ([Cappellari et al., 2013a](#)). As a result, useful information about the properties of galaxies comes from inhomogeneities about the plane, and specifically non-edge-on projections (e.g., [Cappellari et al., 2013b](#); [Cappellari, 2016](#); [Beifiori et al., 2017](#)). I show two such projections of the MP in Figure 4.4, the M - σ_e (left panels) and M - R_e (right panels) relations, with circularised $R_{e,B}$ values as used for the FP. The relations for both the stellar masses derived from my total integrated Sérsic magnitudes (M_*^{tot} - σ_e and M_*^{tot} - $R_{e,B}$ in the top panels of Figure 4.4; see Section 3.6), and the dynamical masses derived from the σ_e values (M_{dyn} - σ_e and M_{dyn} - $R_{e,B}$ in the bottom panels of

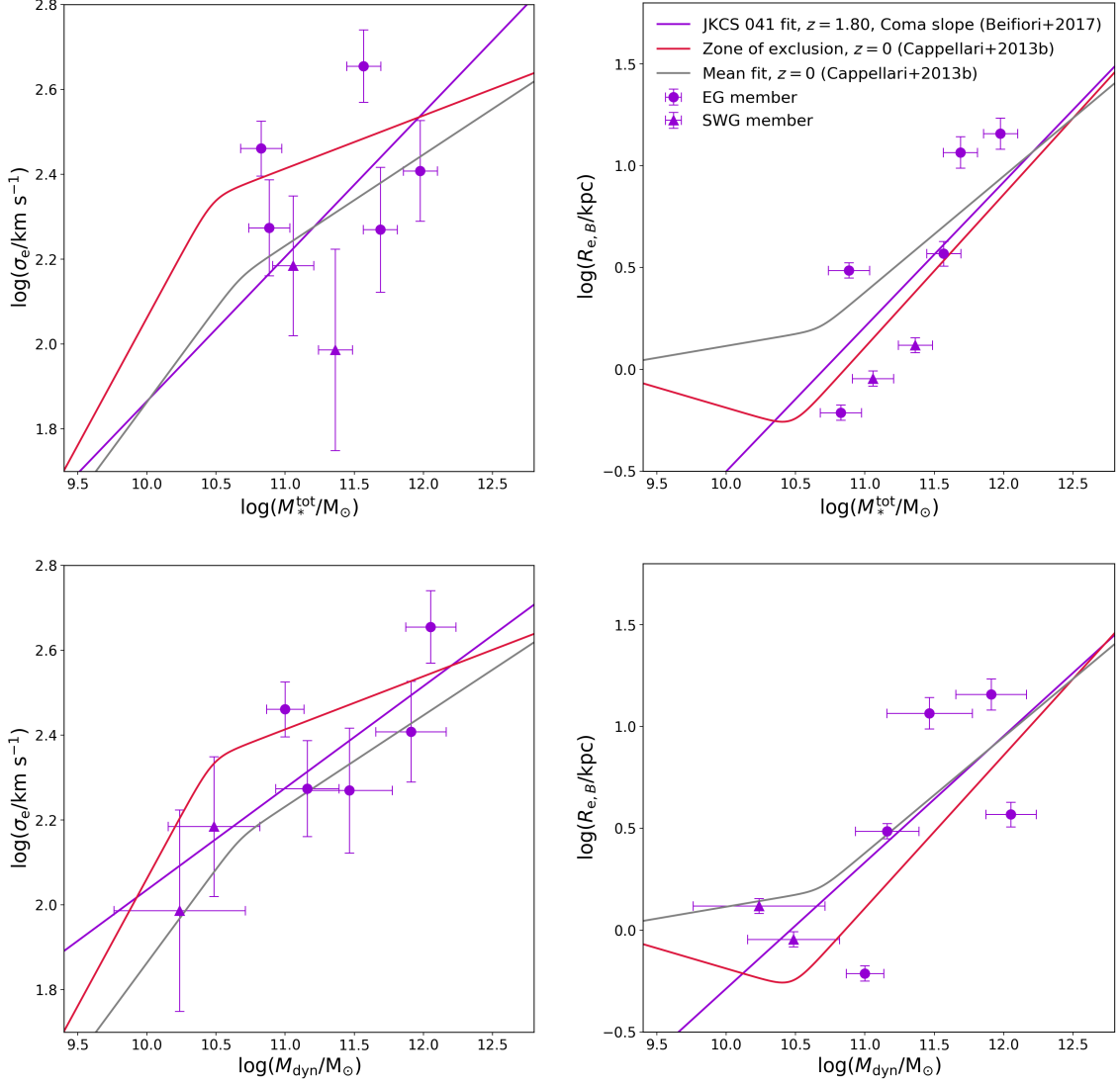


Figure 4.4: Mass-velocity dispersion (M - σ_e ; left panels) and mass-size (M - R_e ; right panels) relations for the seven galaxies in JKCS 041 with reliable σ_e measurements in the EG (circles) or SWG (triangles). *Top*: Relations derived using the M_*^{tot} mass estimate from total integrated magnitude from Sérsic fits (see Section 3.6). *Bottom*: M - σ_e and M - R_e relations derived using dynamical masses (M_{dyn} ; see Section 2.5.4). For reference, I show the zone of exclusion (red line) and mean fit to local galaxies (grey line) from Cappellari et al. (2013b). I linearly fit the galaxies to the local slopes of galaxies in the Coma cluster as derived in Beifiori et al. (2017) (violet lines). See Section 4.2.2.

Figure 4.4; see Section 2.5.4) are shown.

For reference, I show the zone of exclusion for local galaxies (red lines in Figure 4.4), where local ETGs are not found below certain sizes or above certain densities (e.g., [Bender, Burstein & Faber, 1992](#); [Burstein et al., 1997](#)). This is given by the following relation from [Cappellari et al. \(2013b\)](#),

$$R_e^{\text{maj}} = R_{e,b} \left(\frac{M}{M_b} \right)^\gamma \left[\frac{1}{2} + \frac{1}{2} \left(\frac{M}{M_b} \right)^\alpha \right]^{(\beta-\gamma)/\alpha}. \quad (4.6)$$

Here, M is either my M_*^{tot} or M_{dyn} mass estimate, $R_{e,b} = 0.7$ kpc, $\alpha = 8$, $\beta = 0.75$, and $\gamma = -0.20$. The clear break in the zone of exclusion was found by [Cappellari et al. \(2013b\)](#) to be at $M_b = 3.0 \times 10^{10} M_\odot$. I show the mean fit (that also follows a double power law form) for local galaxies in these projections (grey lines in Figure 4.4; [Cappellari et al., 2013b](#)), that has the form

$$\sigma_e^{\text{maj}} = \sigma_{e,b} \left(\frac{M}{M_b} \right)^\gamma \left[\frac{1}{2} + \frac{1}{2} \left(\frac{M}{M_b} \right)^\alpha \right]^{(\beta-\gamma)/\alpha}. \quad (4.7)$$

This relation has the derived best-fitting parameters of $\log(M_b/M_\odot) = 10.675 \pm 0.090$, $\log(\sigma_{e,b}/\text{kms}^{-1}) = 2.153 \pm 0.031$, $\alpha = 8$, logarithmic slope $\beta = 0.215 \pm 0.027$ at large masses and $\gamma = 0.442 \pm 0.028$ at small masses. I converted between the two projections of the relations from [Cappellari et al. \(2013b\)](#) using a version of the scalar virial relation from [Cappellari et al. \(2006\)](#):

$$M = \frac{5.0\sigma_e^2 R_e}{G}. \quad (4.8)$$

For the relations from [Cappellari et al. \(2013b\)](#), I rescaled R_e to circularised values using the median axis ratio of galaxies in Coma (~ 0.65), as done in [Beifiori et al. \(2017\)](#). Here I show a linear fit to the galaxies in JKCS 041 on the M - σ_e and M - R_e planes using the fixed slopes found for the Coma sample on these projections, as derived in [Beifiori et al. \(2017\)](#). As can be seen from the points in my sample, they extend beyond the zone of exclusion, as is expected for dispersion and size evolution.

To understand the change in properties of the galaxies in my sample with redshift, I again compared them to the Coma cluster (as before with the FP; see Section 4.1). To study the evolution of the scaling relations, I followed the method of [Newman et al. \(2012\)](#); [Cimatti, Nipoti & Cassata \(2012\)](#); [Delaye et al. \(2014\)](#); [van der Wel et al. \(2014\)](#); [Beifiori et al. \(2017\)](#); [Chan et al. \(2018\)](#). In order to compare how much galaxy size or σ_e has changed with redshift, I needed to account for the different mass distributions of my two samples. I did this by removing the M - σ_e and M - R_e correlations in order to compare mass-normalised parameters, with which I could measure

any structural evolution. I normalised σ_e and $R_{e,B}$ by a mass of $\log(M/M_\odot) = 11$ for both my mass estimates (M_{dyn} and M_*^{tot}) using the relations:

$$R_{e,\text{MN}} = \frac{R_{e,B}}{(M/10^{11} M_\odot)^{\beta_{M-R_e}}}, \quad (4.9)$$

$$\sigma_{e,\text{MN}} = \frac{\sigma_e}{(M/10^{11} M_\odot)^{\beta_{M-\sigma_e}}}. \quad (4.10)$$

Where $R_{e,\text{MN}}$ and $\sigma_{e,\text{MN}}$ are mass-normalised R_e and σ_e , M is the mass (either M_{dyn} or M_*^{tot}), and the β values are the local slopes of Coma as derived from the respective $M-R_e$ and $M-\sigma_e$ planes (Beifiori et al., 2017).

Using the Coma sample as the local comparison, I then derived the evolution of these mass-normalised structural parameters as a function of redshift. To address the issue of progenitor bias (see Section 1.1.5; van Dokkum & Franx, 1996) and attempt to best match the JKCS 041 sample to the Coma sample, I selected all galaxies with ages > 10 Gyrs from Coma, leaving a sample of five (following the approach of Beifiori et al. 2017; Chan et al. 2016, 2018). Accurately comparing samples of galaxies between different redshifts requires careful comparison of a number properties to best link their evolutionary paths. Although taking an age cut improves this matching of high-redshift galaxies to their possible descendants, this cut was fairly limiting as there were not ages for all the galaxies in the Coma sample. Refining the comparison further, for example by matching the data to models, was not feasible on the remaining small sample of five galaxies, so I was unable to address progenitor bias more accurately and this may affect the relations derived to quantify structural evolutionary effects on the shift of the FP zero point.

I derived slopes (ν and μ) from the mass-normalised relations $\Delta \log R_{e,\text{MN}} \propto \nu \log(1+z)$ and $\Delta \log \sigma_{e,\text{MN}} \propto \mu \log(1+z)$. These values and their respective relations are summarised in Table 4.1, their 1σ errors are from bootstrapping. I compared the weighted-mean mass-normalised sizes and dispersions of galaxies in JKCS 041 to those of galaxies in the Coma cluster. I found that M_{dyn} -normalised sizes of JKCS 041 galaxies were $\sim 69\%$ smaller and M_*^{tot} -normalised sizes were $\sim 74\%$ smaller than Coma. For the mass-normalised σ_e values, I found M_{dyn} -normalised dispersions were $\sim 25\%$ larger in JKCS 041 than in Coma, and for M_*^{tot} -normalised dispersions I found them to be $\sim 19\%$ smaller than in Coma.

4.2.3 Effects of Structural Evolution on FP Ages

I summarise the derived slopes necessary to determine the contribution of structural evolution to the change in FP zero point in Table 4.1. From Equation 4.5, I derived

the contribution to the evolution of the FP of just the structural evolution of the size and dispersion using $\chi_{\text{SE}} = \left(\frac{2b+1}{b}\nu - \frac{a}{b}\mu\right)$. I determined $\chi_{\text{SE}} = -0.06 \pm 0.42$ and $\chi_{\text{SE}} = -0.80 \pm 0.28$ for M_{dyn} -normalised and M_{*}^{tot} -normalised parameters respectively. When comparing to an FP zero point that evolves entirely due to an aging stellar population (η), I found that the effects of structural evolution may contribute between $\sim 3\%$ and up to $\sim 42\%$ from the M_{dyn} and M_{*}^{tot} normalisations respectively. If I did not apply an age cut to the local Coma sample, this contribution from structural evolution becomes $\sim 2\%$ and $\sim 50\%$ from the M_{dyn} - and M_{*}^{tot} -normalised parameters respectively. As a comparison of these effects, [Beifiori et al. \(2017\)](#) found comparable contributions of structural evolution to the FP zero-point shift of the other KCS clusters of $\sim 6\%$ and $\sim 35\%$ for M_{dyn} and M_{*} normalisations respectively.

To test what effect this had on the age values I derived, I used the percentage difference between the slope derived for luminosity evolution depending entirely on an aging stellar population (η) and the slope accounting for structural evolution of galaxies (χ) in Table 4.1. This then translated to a percentage difference in $\Delta \log(M/L)$ which I applied to my sample of seven galaxies using both the M_{dyn} -normalised and M_{*}^{tot} -normalised slopes.

For the large structural evolutionary effects I derived for the M_{*}^{tot} -normalised parameters ($\sim 42\%$), I found this translated to ages older than the Universe, as also found for XMM2235 in [Beifiori et al. \(2017\)](#). I therefore capped this maximum age to that of the Universe at $z \sim 1.80$, meaning my derived FP age could be larger by a factor ~ 2.5 when accounting for structural evolution as derived from M_{*}^{tot} -normalised parameters. This significant increase could imply that the structural evolution is overestimated for stellar-mass normalised values of $R_{e,B}$ and σ_e . As [Beifiori et al. \(2017\)](#) suggested, this could be due to a stronger progenitor bias when normalising by M_{*}^{tot} . Given the range of properties of the Coma galaxies, my comparison sample of five old (> 10 Gyrs) galaxies may not be ideal descendant matches to my sample from JKCS 041 ([van Dokkum & Franx, 2001](#); [Valentinuzzi et al., 2010a](#); [Saglia et al., 2010](#); [Poggianti et al., 2013](#); [Carollo et al., 2013](#); [Beifiori et al., 2014](#)). However, with my limited sample size, I was unable to address the effects of progenitor bias further than this. I estimated that the minimal evolutionary effects of the M_{dyn} -normalised structural parameters ($\sim 3\%$) on my derived FP ages led to an increase of only ~ 0.2 Gyrs, which is within my derived errors on the ages.

4.3 Overdensity Structure, Dynamics, and Ages in 3D

4.3.1 Structure of JKCS 041

To best understand the structure of the overdensity, I first explain the other sources that are apparent in the HST image as identified by N14. N14 confirmed 19 (two from emission lines, 17 from continuum and photometric data) members of JKCS 041 and determined HST grism redshifts for a further 79 objects (61 from emission lines and 18 from continuum). To aid the discussion of the overdensity structure, I have marked all those 79 objects with spectroscopic (in the case of the emission-line objects with $H_{160} < 25.5$ mag) or spectrophotometric (for the continuum sample of galaxies with $H_{160} < 23.3$) redshifts that are confirmed non-members of JKCS 041 in Figure 2.7 (small red circles). The remaining objects in the image fall into the following four categories:

1. Faint non-emission line objects ($H_{160} > 23.3$ mag).
2. Any objects with $H_{160} > 25.5$ mag.
3. Bright ($H_{160} < 23.3$ mag) non-emission-line objects that are at $z_{\text{phot}} < 1.4$.
4. Bright ($H_{160} < 23.3$ mag) non-emission-line objects for which grism spectra could not be extracted, that are in the range $1.4 < z_{\text{phot}} < 3$ but are NOT on the red sequence (16 objects).

Unfortunately, the photo- z catalogue used by (N14) is not public, and the coordinates of the 16 non-emission-line objects in category (4) are not known. Without these remaining objects identified, I was unable to draw strong conclusions about the 3D structure of the overdensity. However, due to the increased accuracy of my redshifts derived from the KMOS spectra as compared to the grism spectra, I was able to study the 3D structure of the confirmed overdensity members.

As can be seen from the confirmed (green squares) and candidate members (yellow squares) of the overdensity in Figure 2.7, JKCS 041 appears to be elongated and seems to extend in two distinct directions. In Figure 4.5, I show the spatial extent of the 16 observed galaxies (filled squares), again with the quiescent (red ID labels) and SF (blue ID labels) members indicated. As a third dimension, I show the velocity relative to the median redshift of the overdensity (blue to red) of the observed galaxies. I also show the confirmed members of JKCS 041 with no KMOS observations (dashed green

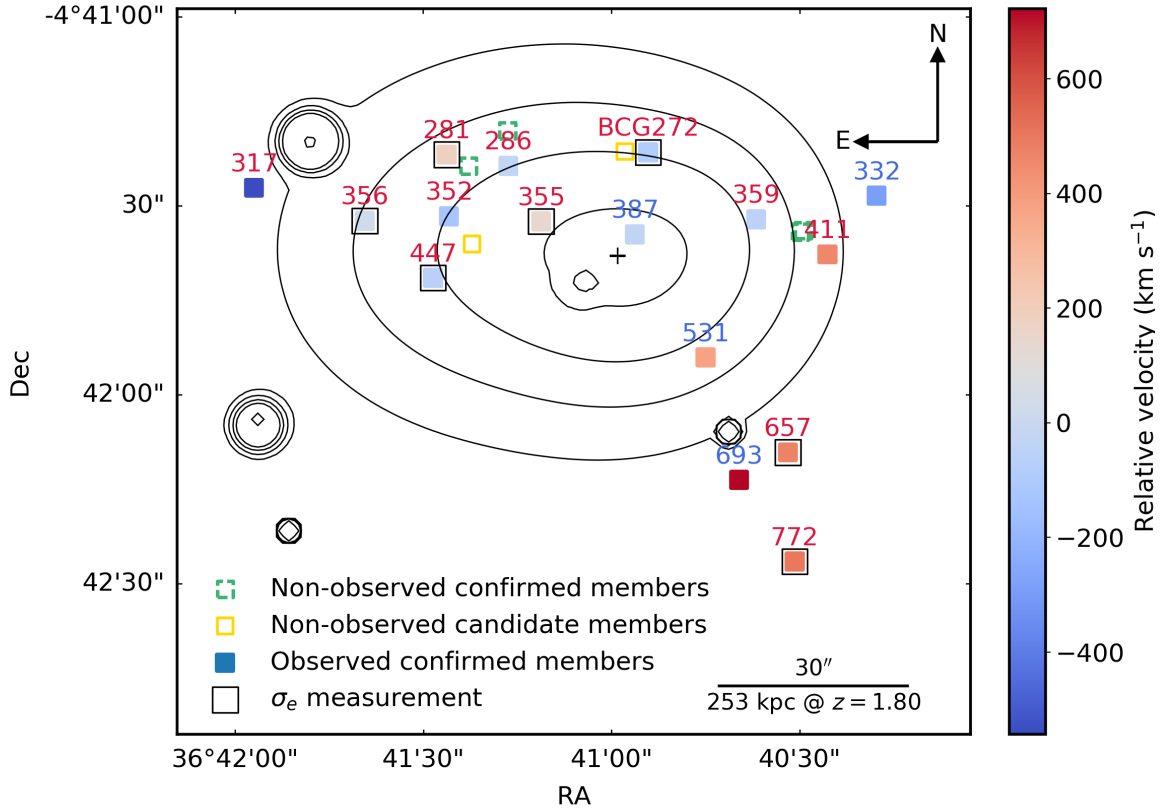


Figure 4.5: Spatial extent of the confirmed and candidate members of JKCS 041 with the relative velocity of the 16 observed members indicated. The observed galaxies are marked as quiescent (red IDs) or SF (blue IDs). The non-observed confirmed members (dashed green squares) and non-observed candidate members (yellow squares) are all quiescent. The X-ray contours from [Andreon et al. \(2009\)](#) are shown, and the geometric centre of the galaxies is shown by the ‘+’. The galaxies to the south west of the overdensity show systematically higher relative velocities. See Section 4.3.

squares) and unobserved candidate members (unfilled yellow squares), all of which are quiescent. Those galaxies for which I have velocity dispersion measurements are highlighted (black square outlines). Again I show the X-ray contours (from [Andreon et al. 2009](#)) and the geometric centre of the galaxies (‘+’; as in Figure 2.7).

Given the improved accuracy of the spectroscopic redshifts I derived (see Section 2.5.3), I was able to investigate the three-dimensional properties of both the quiescent and SF galaxies in JKCS 041. At these redshifts, this is the first study of its kind to investigate the dynamics in a cluster of both the quiescent and SF galaxies. Generally SF galaxies are more easily observed at greater distances due to their bright emission lines. The observed confirmed members of JKCS 041 that are in the group that extends east (EG) are mostly quiescent, while the group toward the south west (SWG) are 50% SF galaxies, however this is only four galaxies in total (IDs 531, 657, 693,

772). The X-ray contours overlaid in Figure 4.5 (from [Andreon et al., 2009](#)) show that the hot diffuse ICM is elongated along the EG. In a relaxed cluster, the hot ICM and spatial distribution of galaxies should both approximately trace the potential well of the overdensity. The fact that the X-ray component is offset from the observed galaxies in the SWG could imply that it is not relaxed, that I am not probing the full distribution of members, or that the centring of the contours is incorrect. The image contains a number of bright X-ray point sources, which, if any un-subtracted emission remains, could bias the position of the X-ray contour centroid (as discussed in Section 2.2.2.1).

4.3.2 Overdensity Dynamics

As is evident from the symbol colours in Figure 4.5, galaxies in the SWG have systematically higher positive relative velocities. These galaxies could be in front of the cluster and more rapidly moving away as they fall towards the cluster centre. The galaxies could also be being flung out of the cluster after a first pass. This sample of galaxies with a systematic higher positive velocity could therefore indicate a group of galaxies that is in the process of merging with the other confirmed members. The EG galaxies show lower absolute relative velocities and some of these galaxies also have systematically higher negative relative velocities, implying that they are moving toward us. This could imply that there is a more relaxed group of predominantly quiescent galaxies (those in the EG) and an infalling group of galaxies (those in the SWG) with a higher proportion of SF galaxies.

To investigate the cluster dynamics further, I plotted a phase-space diagram and histogram of the relative velocities of the observed galaxies in Figure 4.6. In the left panel, I show the relative velocities of the galaxies (from the median measured redshift) as a function of their radius from the geometric centre of the galaxies (average in RA and Dec, marked by the ‘+’ symbol in Figure 4.5). I show the four galaxies in the SWG (IDs 531, 657, 693, 772; triangles), as identified in 2D on Figure 4.5, the EG galaxies (circles), and galaxies for which I derived σ_e measurements (outlined squares). The SWG galaxies mostly occupy a distinct region of the phase-space diagram at higher relative velocities and larger radii for three of the galaxies, with one interloper (ID 447), which in 2D space is close to the SWG and may form part of the same population.

I show a histogram of the relative velocities of the galaxies in the right panel of Figure 4.6. I fitted the distribution of velocities with both a double and single Gaussian and found that it was best fitted by a double Gaussian. Although this

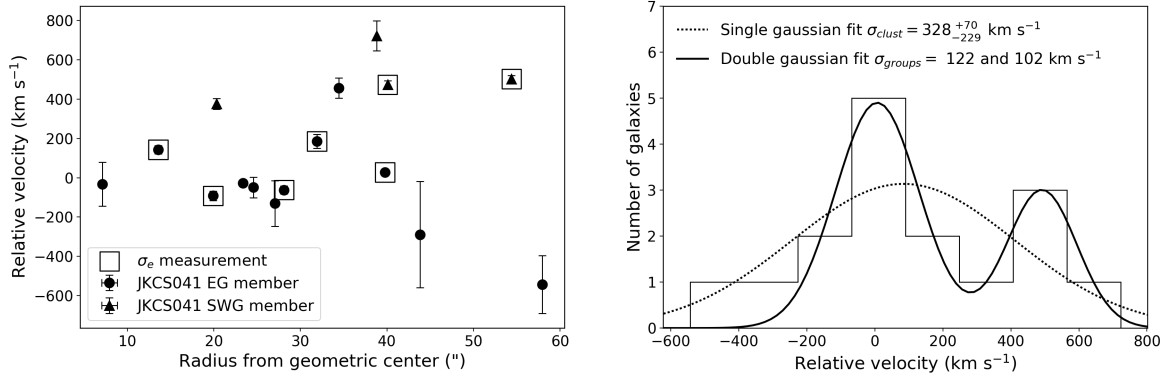


Figure 4.6: Velocities of the galaxies in JKCS 041 relative to the median redshift of the observed sample. *Left:* Phase-space diagram showing all 16 observed galaxies as a function of radius from their geometric centre (shown by the ‘+’ in Figure 4.5). I show the four galaxies in the SWG (triangles; identified in 2D from Figure 4.5), the EG galaxies (circles), and galaxies with σ_e measurements (square outlines). *Right:* Histogram of relative velocities of the 16 observed galaxies. I show the best-fitting double Gaussian (solid line, and corresponding dispersions measured from the two peaks), and the single Gaussian fit (dotted line), from which I estimated a σ_{clust} . See Section 4.3.2.

implies the overdensity is not virialised, I used the histogram of galaxy velocities to investigate how a derived virial mass compared to other mass estimates for this overdensity. The virial mass of a relaxed overdensity, originally presented by Limber & Mathews (1960) and modified by Carlberg et al. (1996), is given by

$$M_v = \frac{3\pi}{2} \frac{\sigma_{\text{clust}}^2 R_h}{G}. \quad (4.11)$$

Where R_h is the ring-wise projected harmonic mean radius, defined by

$$R_h = \frac{N(N-1)}{\sum_{i<j} \frac{1}{2\pi} \int_0^{2\pi} \frac{d\theta}{\sqrt{R_i^2 + R_j^2 + 2R_i R_j \cos\theta}}} \quad (4.12)$$

$$= \frac{N(N-1)}{\sum_{i<j} \frac{2}{[\pi(R_i + R_j)]} K(k_{ij})}.$$

Here R_i and R_j are the distances of galaxies i and j from the central point of the overdensity (which I have defined as the geometric centre of the galaxies; ‘+’ in Figure 4.5), $k_{ij}^2 = 4R_i R_j / (R_i + R_j)^2$, and $K(k_{ij})$ is the complete elliptical integral of the first kind in Legendre’s notation (form from Irgens et al., 2002).

For all 20 confirmed members of JKCS 041, I derived $R_h = 493 \pm 20$ kpc. For the 16 observed galaxies, I obtain $\sigma_{\text{clust}} = 328^{+71}_{-229}$ km s⁻¹ from a single Gaussian fit to the galaxies (Figure 4.6), and 1σ errors from randomly sampling the observed

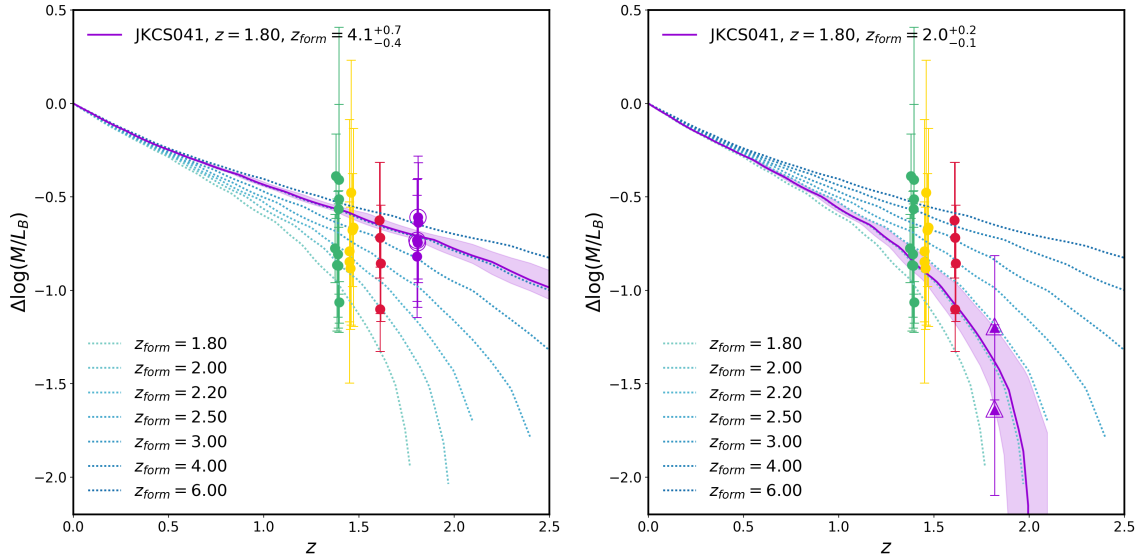


Figure 4.7: Relative M/L evolution as a function of redshift for galaxies in JKCS 041 (symbols as in Figures 4.1, 4.2, and 4.3). SSP models (Maraston, 2005) interpolated using EZGAL (dotted lines) and the best fitting model (solid violet line) and 1σ errors (shaded region) are shown. *Left*: Five EG galaxies from which I derived an older mean age $2.1^{+0.3}_{-0.2}$ Gyrs ($z_{\text{form}} = 4.1^{+0.7}_{-0.4}$, $\sim 1.5^{+0.2}_{-0.3}$ Gyrs after the Big Bang) than the mean age of all seven galaxies in JKCS 041. *Right*: Two SWG galaxies that I found to have a significantly younger mean age compared to the EG of 0.3 ± 0.2 Gyrs ($z_{\text{form}} = 2.0^{+0.2}_{-0.1}$, $\sim 3.2 \pm 0.2$ Gyrs after the Big Bang). See Section 4.3.3.

galaxies and refitting. This gives a poorly constrained total mass for the overdensity $\log(M_{\text{clust}}/M_{\odot}) = 13.8 \pm 0.6$. Within errors, this is consistent with the value found by Andreon et al. (2014) of $\log(M/M_{\odot}) \gtrsim 14.2$. However, as discussed, it appears that the observed galaxies from which I derived a σ_{clust} value form two dynamically distinct groups, meaning that the overdensity is not virialised, making this an unreliable measure of its total mass. When measuring the virial masses of the two groups separately, I derived a mass of the SWG of $\log(M_{\text{SWG}}/M_{\odot}) = 12.3 \pm 0.6$ and $\log(M_{\text{EG}}/M_{\odot}) = 12.8 \pm 0.6$ for the EG. The total cluster mass as measured from the sum of the two groups is $\log(M_{\text{groups}}/M_{\odot}) = 13.0 \pm 0.6$. This is lower but still in agreement with the mass derived from the single Gaussian fit within their large errors but significantly lower than the mass estimated by Andreon et al. (2014).

4.3.3 Galaxy Ages

To further test the properties of the galaxies in the two spatially and dynamically distinct groups, I investigated the ages I could derive from the seven galaxies on the FP that reside in the EG and SWG separately (indicated in Figures 4.1, 4.2 and 4.7

with circles and triangles respectively). With the seven galaxies in total, I realise that I am dealing with very small numbers and that splitting the sample in this way based on their location in the overdensity causes large uncertainties. Deriving ages from the FP as described in Section 4.1.1 and as shown in Figure 4.7, I took the five galaxies that were in the EG (left panel) and the two in the SWG (IDs 657 & 772; right panel) that were on the FP and determined mean ages for the two groups. I found that the EG galaxies had a significantly older mean age $2.1_{-0.2}^{+0.3}$ Gyrs ($z_{\text{form}} = 4.1_{-0.4}^{+0.7}$, formed just $\sim 1.5_{-0.3}^{+0.2}$ Gyrs after the Big Bang) than the two SWG galaxies with mean age 0.3 ± 0.2 Gyrs ($z_{\text{form}} = 2.0_{-0.1}^{+0.2}$, formed $\sim 3.2 \pm 0.2$ Gyrs after the Big Bang). To check this was not a direct effect of mass, I determined average light-weighted stellar masses of the EG ($\langle \log(M_*^{\text{tot}}/M_\odot) \rangle = 11.36$) and SWG ($\langle \log(M_*^{\text{tot}}/M_\odot) \rangle = 11.18$) populations and found that these populations had similar masses. However, if I look just at the dynamical masses then this age difference may also be attributed to the fact that the SWG galaxies have lower dynamical masses.

4.4 Discussion

4.4.1 Absorption-Line Spectroscopy at $z \gtrsim 1.80$

For JKCS 041 at $z \simeq 1.80$, I have derived seven σ_e values for individual galaxies. In the literature, dispersion measurements of 16 individual galaxies at $z \gtrsim 1.8$ have been confirmed (van Dokkum, Kriek & Franx, 2009; Onodera et al., 2010; Toft et al., 2012; van de Sande et al., 2013; Belli et al., 2014; Belli, Newman & Ellis, 2017; Newman, Belli & Ellis, 2015; Hill et al., 2016; Toft et al., 2017). Most of these observations were of the brightest, most massive galaxies spanning a wide range of redshifts. These seven stellar velocity dispersions for galaxies in JKCS 041 increases the sample in the literature by $> 40\%$. I also present the largest number of galaxy velocity dispersions within a single overdensity at comparable redshifts, as no previous survey has systematically targeted quiescent galaxies to these depths and distances.

4.4.2 Comparison of Ages for JKCS 041

The mean age obtained for the seven JKCS 041 galaxies on the FP is 1.4 ± 0.2 Gyrs ($z_{\text{form}} = 3.0 \pm 0.3$, $\sim 2.1_{-0.2}^{+0.3}$ Gyrs after the Big Bang), this is consistent within 1σ errors of previous results for this overdensity (Newman et al., 2014; Andreon et al., 2014). N14 obtained ages from spectral fitting of stellar absorption lines with Bruzual & Charlot (2003) SSP models (BC03) of stacked HST grism spectra of the

15 quiescent galaxies. They fitted the galaxies in two mass bins; for the high mass ($\log(M_*/M_\odot) > 11$) quiescent members, their models gave an age of $1.45^{+0.24}_{-0.18}$ Gyrs ($z_{\text{form}} = 3.0^{+0.4}_{-0.2}$, formed $\sim 2.11^{+0.18}_{-0.24}$ Gyrs after the Big Bang) and for the lower mass sample $10.5 < \log(M_*/M_\odot) < 11$, they obtained a luminosity-weighted age of $0.90^{+0.19}_{-0.10}$ Gyrs ($z_{\text{form}} = 2.4^{+0.2}_{-0.1}$, $\sim 2.7^{+0.10}_{-0.19}$ Gyrs after the Big Bang).

Using the same HST grism data, [Andreon et al. \(2014\)](#) derived SFH-weighted (see Section 1.1.7) average ages for average masses (as defined in [Longhetti et al., 2005](#)) in the bins of [N14](#). Assuming a simple exponentially declining SFH model, solar metallicity, and using BC03 models, [Andreon et al. \(2014\)](#) found average ages of 1.4 Gyrs at $\log(M_*/M_\odot) \sim 11.5$, and 0.7 Gyrs at $\log(M_*/M_\odot) \sim 10.5$, and found a mean age of all the galaxies of 1.1 ± 0.1 Gyrs ($z_{\text{form}} \approx 2.6 \pm 0.1$) for the mean mass of $\log(M_*/M_\odot) \sim 11$. These studies show that there is a trend of galaxy age with mass as found by other studies (e.g., [Nelán et al., 2005](#); [Treu et al., 2005](#); [Thomas et al., 2010](#)). However, my results indicate that the picture may not be as simple as an effect of just mass in the case of JKCS 041 at $z \approx 1.80$; see Section 4.4.4 for further discussion of galaxy ages in the context of cluster dynamics and galaxy properties.

4.4.3 Comparison of FP Ages to Other KCS Overdensities

The mean formation redshift I derived for the seven galaxies on the FP in JKCS 041 ($z_{\text{form}} = 3.0 \pm 0.3$), is consistent within errors of just the five high-mass $\log(M_*/M_\odot) > 11$ galaxies ($z_{\text{form}} = 2.8^{+0.5}_{-0.4}$). This formation epoch ($\sim 2.1^{+0.3}_{-0.2}$ Gyrs after the Big Bang) is consistent with that determined for the richest and most virialised KCS overdensity analysed in [Beifiori et al. \(2017\)](#); XMM2235 at $z \sim 1.39$ ($z_{\text{form}} \sim 2.95$, $\sim 2.16 \pm 0.50$ Gyrs after the Big Bang; see Section 2.2.3.2). [Beifiori et al. \(2017\)](#) found that XMM2235 had a slightly older formation epoch than the other two clusters, which they suggested might indicate more rapid galaxy evolution in this more massive and relaxed cluster. JKCS 041, one of the most massive overdensities at $z \sim 1.8$ and with a high passive fraction, has the same formation epoch. This adds weight to the indicative results found by [Beifiori et al. \(2017\)](#), that there is some accelerated formation in more massive overdensities at earlier times (as also found by e.g., [Gebhardt et al., 2003](#); [Saglia et al., 2010](#); [Strazzullo et al., 2013](#); [Lani et al., 2013](#); [Delaye et al., 2014](#)). As can also be seen from the total cluster mass versus redshift plot for the KCS sample in Figure 2.5 taken from [Beifiori et al. \(2017\)](#), XMM2235 and JKCS 041 lie on the same model mass-accretion evolutionary track of a massive local cluster ($\log(M_{200}/h^{-1}M_\odot) = 16$) implying that JKCS 041 and XMM2235 could have similar cluster evolution.

4.4.4 Structure and Evolution of JKCS 041

When looking at just the 16 confirmed members of JKCS 041 that I observed with KMOS, I found that the EG contained the oldest galaxies (as measured from the FP of five galaxies), while the younger SWG (as determined from the FP ages of two galaxies) contained a higher proportion of SF galaxies. The EG is a larger, more relaxed group of galaxies and if the centroid of the X-rays can be relied upon then these EG galaxies are more centred on this emission. It is tempting to say that the EG is the central core of the galaxy cluster, however due to the uncertainty of the exact location of the X-ray component, I instead term these galaxies the EG. The age results for the two groups of galaxies, although based on very small numbers of galaxies, were found to be independent of light-weighted stellar mass. This does not directly conflict with the differing age results of JKCS 041 galaxies in high- and low-mass bins found by N14 and Andreon et al. (2014) as they were looking at stacks of subsets of all the 15 (then confirmed) quiescent galaxies. However, it does indicate that the effect of mass may not be the only factor in the determination of galaxy ages. The two younger SWG quiescent galaxies, have very young ages that were significantly reducing the mean age for all seven galaxies on the FP. The mean age I derived for all seven galaxies is consistent with a more massive and virialised overdensity, however these results suggest that JKCS 041 is made up of two different age populations. It could well be that the younger SWG is infalling into the cluster core represented by the EG.

Coupling the young stellar mean age of the SWG galaxies (0.3 Gyr) with their relatively compact sizes (~ 1 kpc) but considerable masses ($\log(M_*/M_\odot) \sim 11$) means that these galaxies fit the description of red nuggets (see Section 1.1.5; e.g., van Dokkum et al., 2008; Damjanov et al., 2009). It could well be that interactions of the galaxies within the infalling group could have triggered a compaction event of a red-nugget progenitor dusty turbulent disc. This could have occurred either through a gas rich merger (Barnes & Hernquist, 1991), tidal interaction with another infalling galaxy, or rapid accretion onto a turbulent disc along a gas rich filament resulting in a violent disc instability (e.g., Dekel et al., 2009; Elmegreen & Burkert, 2010; Dekel & Burkert, 2014; Forbes et al., 2014). These extremely compact high-redshift galaxies can then rapidly deplete their gas reservoirs in a starbursting ‘blue nugget’ phase (e.g., Barro et al., 2013, 2014). The very young age of the infalling red nuggets in the SWG is consistent with the rapid quenching timescale of a red nugget due to a dissipative compaction event triggering a short period of intense star formation (e.g., Dekel & Burkert, 2014). An infalling group provides the optimum conditions to trigger rapid

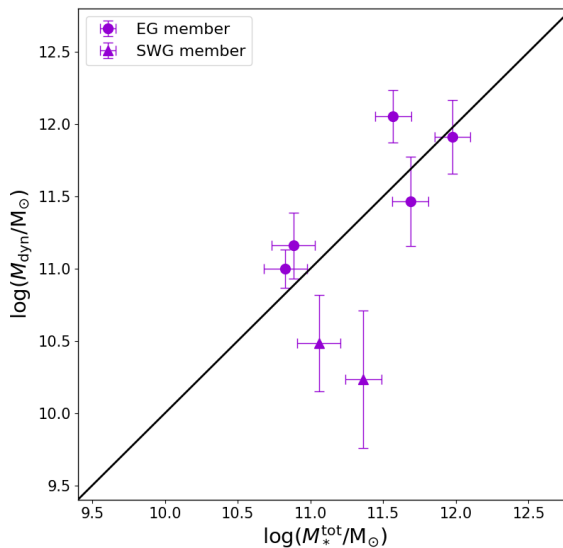


Figure 4.8: Comparison of the mass estimates of the galaxies derived using two methods. The M_{dyn} values were derived from the velocity dispersions of the galaxies (Section 2.5.4) and the M_*^{tot} were derived using their photometry (Section 3.6). The two estimates are not in agreement for all galaxies and this could be due to systematics of each method or a difference in the total mass (derived from the dynamics) and the light-weighted component of the galaxy. See Section 4.4.4.

compaction as once within a massive overdensity the cluster dispersion becomes too large for efficient merging (e.g., [Ostriker, 1980](#)) or gas accretion (e.g., [Larson, Tinsley & Caldwell, 1980](#)). This is consistent with the earlier hypothesis that the cluster environment can trigger starburst events to rapidly consume gas and quench star formation as measured at $z \lesssim 0.3$ (e.g., [Dressler & Gunn, 1983](#); [Couch & Sharples, 1987](#); [Barger et al., 1996](#); [Poggianti et al., 1999](#)). The formation of the massive and compact red nuggets could form via similar interactions while falling into clusters in the high-redshift Universe. This is also consistent with the idea of ‘preprocessing’ galaxies in a group environment prior to it merging with a massive cluster (e.g., [Zabludoff & Mulchaey, 1998](#); [Mihos, 2004](#); [Fujita, 2004](#)). In the hierarchical model, groups merging with clusters should peak around $z \sim 0.5$ (e.g., [Dressler, 2004](#)), so JKCS 041 may represent the early stages of group infall.

As can be seen from Figure 4.8, the SWG galaxies have smaller M_{dyn} values than the other five galaxies in the dispersion sample but comparable light-weighted stellar masses. The FP age results indicate that the SWG galaxies are significantly younger than the EG galaxies. Trends seen in the field indicate that lower mass ETGs have younger ages ([Treu et al., 2005](#); [Thomas et al., 2010](#)), which is more consistent with the M_{dyn} values. However, for the light-weighted stellar masses, although there is

significant scatter in the NMBS relation that they were derived from, their errors reflect this uncertainty and I find them to be consistent with those that N14 derived from SED fits. For three of the seven galaxies the two mass estimates are not in agreement with each other. The possible difference between the two mass determinations may be explained by the different observational limitations associated with each. It could also be that the total mass (measured from the dynamics) differs from the light-weighted mass as either the dark matter contribution cannot be quantified, there are a higher number of low-mass stars than expected, or there is considerable mass in the form of ionized gas that causes the disparity. If the low-dynamical mass SWG galaxies were formed from a turbulent disc, then one would expect that there is some residual rotational support that would make the virial mass a poor measure of its total mass with R_e .

From the overdensity dynamics, I see two distinct groups of galaxies, separated both spatially and in relative velocity, with the SWG having systematically higher relative velocities. Given the velocities of the 16 observed galaxies and age results (of the seven galaxies on the FP) of the confirmed members of JKCS 041, I suggest that these results could indicate an overdensity in formation that is made up of two distinct merging groups of galaxies. This tentative result could still be consistent with the work done by N14 who showed a mass matched field sample (from Whitaker et al., 2013) at the same redshift as JKCS 041 were not as quiescent, and that environmental quenching was responsible for the increased number of quiescent galaxies in JKCS 041. The lower proportion of quiescent galaxies in the SWG could potentially be a merging group that represents a transition population between typical field and overdensity populations at this redshift. This is also consistent with the difference in ages of the two groups, as it has been found that ETGs in the field contain younger stellar populations than cluster ETGs (e.g., van Dokkum & Ellis, 2003). Firm conclusions require more galaxies to be measured.

4.4.5 Speculation on the Lives of the Most Massive ETGs

For JKCS 041, I found an infalling galaxy group that had a higher proportion of SF galaxies. Those that were quenched were extremely compact and massive red nugget galaxies with young ages indicative of a recent starburst phase. It could be that as the galaxies fall into the deep potential well of the cluster they undergo compaction into red nuggets. Extremely high SFRs seen in higher redshift clusters ($z \sim 2.2$ – 2.5 ; Hatch et al., 2011; Wang et al., 2016) are consistent with this picture. Other studies also find evidence that the cores of quiescent galaxies formed in short periods of

intense SF at $z \gtrsim 2$ (e.g., [Bezanson et al., 2009](#); [Oser et al., 2010](#); [Barro et al., 2013](#); [Nelson et al., 2014](#); [Kriek et al., 2016](#)). Results from the local Universe have shown that at the centres of very massive ETGs in the Virgo and Coma clusters have a very bottom-heavy IMF (see Section 1.1.6; [van Dokkum & Conroy, 2010, 2011](#)). It has been speculated that a bottom-heavy IMF could be the result of this extreme mode of starbursting SF seen in these massive ETGs at high redshift (e.g., [van Dokkum et al., 2015](#); [Zolotov et al., 2015](#); [Barro et al., 2016](#)). This is the most detailed study of a high-redshift cluster and its individual members. My results for JKCS 041 tentatively show that an environment triggered starburst phase is a viable formation mechanism for at least some of the ETGs in this dense cluster environment at $z \approx 1.80$. My results also add weight to this possible picture of formation for some of the most massive ETGs in the local Universe.

4.5 Conclusions

In this part of the thesis, I present new KMOS spectra for the overdensity JKCS 041 at $z = 1.80$ as part of KCS. KCS is a GTO KMOS programme, which aimed to constrain the evolution of galaxies in dense environments between $1 < z < 2$. [N14](#) confirmed 19 members of JKCS 041 using HST grism spectra and identified three candidate members. I observed 16 galaxies with KMOS (12 quiescent and four SF), 15 confirmed members and one candidate member (ID 772), which I subsequently spectroscopically confirmed, bringing the total number of confirmed members of JKCS 041 to 20.

I reduced and analysed HST images of the overdensity in the H_{160} and Y_{105} bands (presented in [N14](#)). To determine photometric parameters of the galaxies, I fitted 2D Sérsic profiles to galaxies using GALAPAGOS-2.2.5B. From the spectra, I determined improved spectroscopic redshift measurements for the 16 observed galaxies using either kinematic fits (for 14 galaxies using PPAFF), or emission lines (in the case of two SF galaxies). From kinematic fits of the quiescent galaxies in my sample, I was able to determine stellar velocity dispersions for seven galaxies. I combined these dispersions with the photometric parameters to construct a fundamental plane of individual galaxies in JKCS 041. I then used the FP to derive ages of galaxies. With the improved redshifts, I was able to investigate the three-dimensional dynamics of observed galaxies in the overdensity. The main results of this work are summarised below.

1. I derived velocity dispersion measurements for seven quiescent galaxies in my spectroscopic sample. This sample of dispersions is the largest for a single overdensity at comparable redshifts by a significant margin.
2. Using photometric parameters derived from the HST images and the derived σ_e values, I was able to construct an FP for seven quiescent galaxies in JKCS 041. This is the highest redshift FP constructed for a single overdensity. It further supports studies suggesting that the FP holds to $z \sim 2$ (e.g. [Bezanson et al., 2013](#)).
3. From the shift in zero point of the FP, I estimated M/L evolution with z for the galaxies in JKCS 041. Overlaying derived $\Delta \log(M/L_B)$ evolutionary tracks from interpolated SSP ([Maraston, 2005](#)) models, I derived a mean age of the seven galaxies to be 1.4 ± 0.2 Gyrs ($z_{\text{form}} = 3.0 \pm 0.3$). Comparisons with the literature showed that these results were consistent with other studies of JKCS 041, and results of the other KCS overdensities ([Beifiori et al., 2017](#)).
4. Testing the effects of structural and stellar velocity dispersion evolution on these values, I found very little effect when using M_{dyn} -normalised parameters (~ 0.2 Gyrs), but up to a factor of ~ 2.5 larger ages when using M_{\star}^{tot} -normalised parameters. The large difference between the effects from different mass normalisations could mean an overestimation of structural evolution from M_{\star}^{tot} -normalised values; this could be due to progenitor bias.
5. From the dynamics of 16 confirmed members of JKCS 041, I saw a distinct group of galaxies extending south west in the overdensity. These few galaxies, with a higher SF proportion, have systematically higher relative velocities. As a further investigation into the structure of JKCS 041, I determined ages for those galaxies on the FP in the east and south-west groups. I found significantly older ages of the galaxies making up the EG ($2.1_{-0.2}^{+0.3}$ Gyrs, $z_{\text{form}} = 4.1_{-0.4}^{+0.7}$), than the two quiescent galaxies in the SWG (0.3 ± 0.2 Gyrs, $z_{\text{form}} = 2.0_{-0.1}^{+0.2}$). These tentative dynamic and age results might indicate that the overdensity is in formation and is made up of two merging groups of galaxies. I found that this result was independent of light-weighted stellar mass.

Part II – Unravelling the Origin of the Counter-Rotating Core in IC 1459 with KMOS and MUSE

*“When you consider things like the stars, our affairs don’t seem to matter very
much, do they?”*

— Virginia Woolf, *Night and Day*, 1919

Abstract

The massive early-type galaxy (ETG) IC 1459 is the archetypal slowly rotating galaxy that exhibits a rapidly counter-rotating kinematically decoupled core (KDC). To investigate the origin of its KDC, I coupled a large mosaic of data from the near-infrared (NIR) integral field unit (IFU) instrument K-band Multi-Object Spectrograph (KMOS), obtained using the little-utilised ‘Mosaic Mode’, with an equally large mosaic from the wide field-of-view optical IFU Multi-Unit Spectroscopic Explorer (MUSE). The large local ETG was observed with a combined broad wavelength coverage of $\sim 4750\text{--}10400 \text{ \AA}$. By measuring the stellar kinematics, I discovered high velocity dispersions along the major axis of the galaxy and some asymmetry in its dispersion map. Radially binning the spectra across the NIR and optical mosaics, I was able to study the stellar populations and spatially resolved initial mass function (IMF) of IC 1459 across regions that exhibited different kinematics. Using the strong optical absorption indices, I determined a radially constant mass-weighted age of ~ 12 Gyrs and a negative metallicity gradient. I discovered that the metallicity gradient was driven by an extremely metal-poor population in the outer parts of the galaxy superpositioned onto the metal-rich population found in the rest of the radial bins. This is the first time this has been seen for a KDC host galaxy. The constant radial age supports results from orbital modelling which suggest that the KDC is not an orbitally distinct feature of the galaxy but is in fact the superposition of smooth distributions of prograde and retrograde stars orbiting on thick short-axis tube orbits. Distinctive KDC net rotation is observed where there is a mass-fraction imbalance of the prograde and retrograde stellar populations, and the blending of their kinematic distributions explains the higher dispersion along the major axis observed in IC 1459. Fixing the stellar populations measured in the optical, I measured the spatially resolved IMF from the NIR dwarf-sensitive features for the first time for a KDC. I discovered a surprising relatively bottom-light Milky Way-like IMF and no gradient which is in contradiction to other studies of massive ETGs. The tentative result could indicate a significantly different evolutionary path for ETGs with KDCs, potentially involving major mergers of gas-rich spirals (as also supported by the asymmetrical dispersion and other observational evidence) or counter-rotating accretion of cold streams in the early Universe.

Chapter 5

KMOS and MUSE Data and Analysis of IC 1459

In part II of this thesis, I detail the analysis of the massive local ETG, IC 1459. In this chapter, I give information on the KMOS data (Section 5.1.1) and MUSE data (Section 5.1.2) I used to investigate the properties of IC 1459. I then describe the analysis of the mosaics of data to measure the kinematics (Section 5.2.1), stellar populations (Section 5.2.3) and IMF (Section 5.2.4) of IC 1459 in order to understand its evolution. I discuss the possible implications of this analysis in Section 5.3 and summarise the conclusions of this work in Section 5.4.

5.1 Mosaic Data

For the analysis of IC 1459, I used data from two IFU instruments. I reduced and analysed the KMOS data of the bright local ETG. I later included an available reduced MUSE data cube of IC 1459 to strengthen the analysis. In this section, I cover the KMOS data in Section 5.1.1, including the observations (Section 5.1.1.1) and reduction (Section 5.1.1.2). I then detail the MUSE data in Section 5.1.2 including the observations (Section 5.1.2.2) and preparing the cube for analysis (Section 5.1.2.3).

5.1.1 KMOS Data

5.1.1.1 KMOS Observations

IC 1459 is a bright ($M_V \simeq -22.3$, from LEDA), local, massive ETG (see Section 1.2.2) with an angular size $R_e = 46.2''$ (Läsker, Ferrarese & van de Ven, 2014). Due to the size and magnitude of the galaxy, IC 1459 makes the ideal backup target for variable weather conditions or poor seeing. For a lot of the KMOS GTO programs,

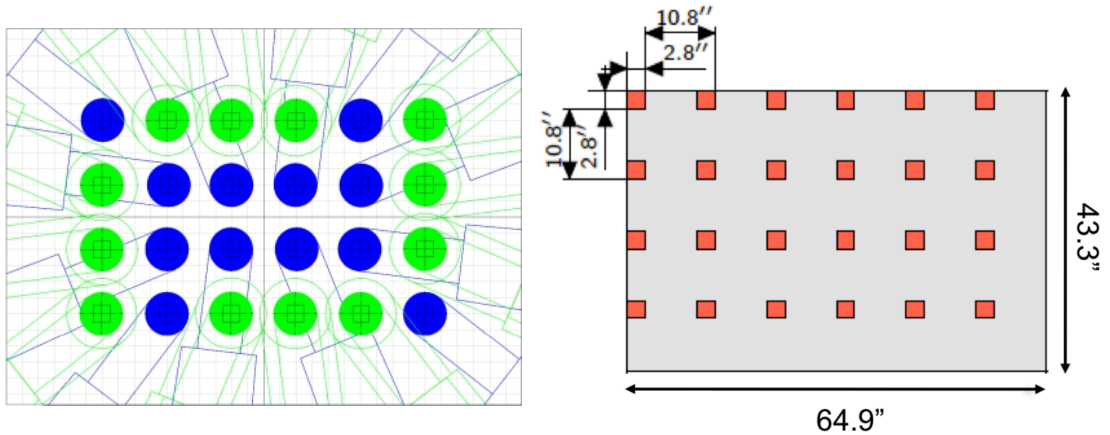


Figure 5.1: *Left:* Image from KARMA of the upper layer (green) and lower layer (blue) arms forming a 6×4 grid in the ‘mapping24’ mode, utilising all 24 arms. Shifting both across and down, a contiguous area of $\sim 64.9'' \times 43.3''$ is covered in 16 pointings. Image credit: <http://www.usm.uni-muenchen.de/people/wegner/kmos/en/observation.php>. *Right:* Diagram to show IFU positions (red) at the start of the OB. The whole contiguous region (grey) is covered in a single OB. Image credit: The [KMOS User Manual P97](#).

good seeing ($\lesssim 1''$) and clear skies were required to achieve the precision and depth for the science goals (as was the case for KCS, see Section 2.2). Therefore, if the observing conditions became sub-optimal, a bright (to observe through cloud) and large angular size (if one does not require resolving detail below the seeing limit) target makes for the ideal backup and maximises the use of telescope time.

It would take $\sim 16.5 \times 16.5$ KMOS IFUs (each $2.8'' \times 2.8''$, with $14 \times 14 0''.2$ pixels) to span the half-light radius of IC 1459. In order to cover a sufficient area, one can use KMOS’s highly under-utilised ‘Mosaic Mode’. Here the 24 arms of KMOS can be arranged in a grid of fixed dimensions (as automated in KARMA) and moved across the surface of a target to create a complete mosaic of data. In the ‘mapping24’ mode, the arms are arranged in a 6×4 grid and with 16 successive pointings (with a 1 pixel overlap) can cover a contiguous region of $\sim 64.9'' \times 43.3''$. See Figure 5.1 for an example of the arm configuration (left panel) and mosaic dimensions (right panel).

The KMOS data for IC 1459 that I reduced and analysed in this chapter were taken in two different observing periods. The useable observations across both periods were taken in two OBs in the first period and one OB in the second period. For simplicity, I will call these mosaics 1a and 1b (taken in P93) and mosaic 2 (taken in P95). Mosaics 1a and 1b were observed on 10th July 2014 in P93 as a poor seeing ($\sim 1.5''$ – $2''$) backup target for KCS (during ESO programme ID: 093.A-0051(A)).

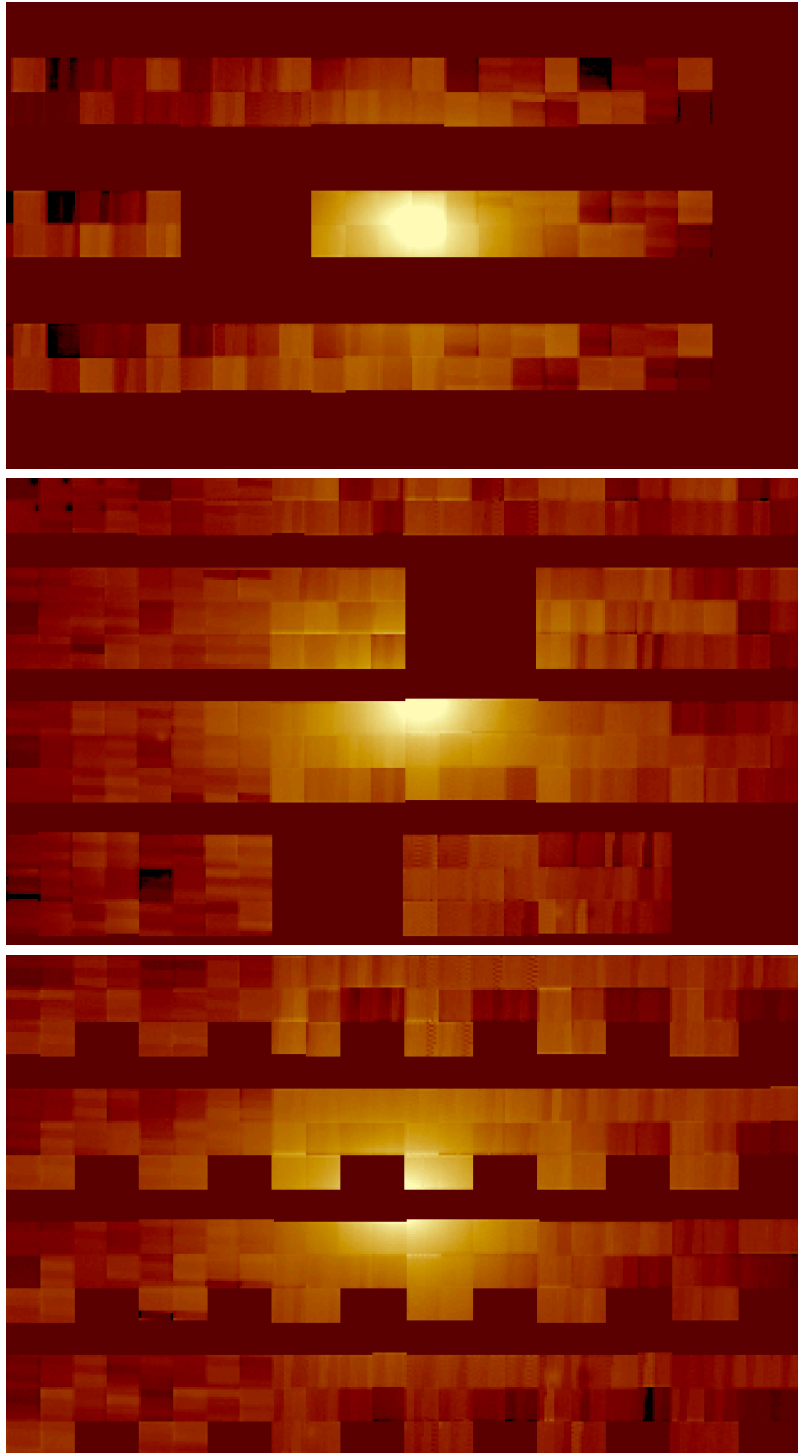


Figure 5.2: Median images of the three reduced KMOS mosaics of IC 1459 as displayed in QFITSVIEW¹. The images have a logarithmic scaling to exaggerate features in order to show the IFU footprints. The smooth colour background represents NaN values. *Top*: Mosaic 1a with 99.5% logarithmic image scale and size $65'' \times 38''$. *Middle*: Mosaic 1b with same scaling and size as mosaic 1a. *Bottom*: Mosaic 2 with same scaling as mosaic 1a and size $65'' \times 40.8''$. The galaxy is not centred on the same location as the first two mosaics as its core (central brightest pixel) is missing. See Sections 5.1.1.1 and 5.1.1.2.

During this observing period, three of the 24 arms were not functioning (arms 4, 11 and 15). To fill in the gaps in the mosaic from the missing IFUs, the mosaic was observed in two parts with two position angles differing by 180° . The OBs for IC 1459 could not be completed for either position angle, despite a few attempts to do so, due to the loss of guide-star tracking through thick cloud. As a result, the mosaics of useable data from P93 had some gaps. In an effort to fill some of these gaps, IC 1459 was observed again as a backup target in P95. Mosaic 2 was observed on 7th August 2016 as a poor-seeing ($\sim 1''$ – $1.5''$) backup for the KROSS survey (see Section 1.1.10; during ESO programme ID: 095.B-0035(B)). All the arms were functioning at the time of the observations. However, again due to the variable weather conditions the telescope lost tracking at multiple times and still only a partial mosaic of data could be obtained. The KMOS data for all three mosaics were taken during dark time.

For all three mosaics, the galaxy was observed in the *IZ* band (0.8 – $1.08 \mu\text{m}$, see Section 2.1) with 300 s exposures. This meant that for every one of the 16 pointings to build a complete mosaic, the exposure time was 300 s. The mosaic was observed using the standard nod-to-sky mode. From the observations, I selected all the useable data to be those mosaics taken within a single OB that was at least 50% complete (leaving mosaics 1a, 1b and 2) to ensure that the data covered a sufficiently large contiguous region for analysis. Discarding all the data where the telescope had lost tracking left me with three partial mosaics. Median images of the mosaics (top to bottom: 1a, 1b and 2) in Figure 5.2 show the footprints of useable data for each (following the reduction described in Section 5.1.1.2). I show the images in a logarithmic scaling to enhance the features, and the variations in brightness between the IFUs is exaggerated. Any differences in brightness between the IFUs is likely to be due to the variability of the sky and any intrinsic differences between the response of the IFU pixels. I did not flux-calibrate the images shown as this was not integral to my analysis.

5.1.1.2 KMOS Data Reduction

The data for IC 1459 was downloaded from the ESO archive². Using the query form for raw data, I selected the KMOS science observations by searching the object name

¹Version 3.3, written by Thomas Ott, available <http://www.mpe.mpg.de/~ott/dpuser/qfitsview.html>.

²From <http://archive.eso.org/cms.html> under the ‘LPO Raw Data’ category and the ‘Raw data query form’.

(IC 1459) and the instrument (KMOS). I then selected the relevant KMOS calibration files i.e. taken over the same night and with the same exposure time (header keyword: `EXPTIME = 300 s`) and filter (header keyword: `INS.FILT1.NAME = IZ`) as the observations where necessary. The calibration files I needed to reduce the KMOS data are summarised below.

- Dark frames (header keyword: `DPR.TYPE = DARK`) from the same night and with the same exposure time as the observations.
- Flat frames from the daytime after the night of the observations with the internal flat lamp on (`DPR.TYPE = FLAT,LAMP`) for the *IZ* filter (they had `EXPTIME = 3 s`) and with the lamp off (`DPR.TYPE = FLAT,OFF`) that had the same exposure time as the `FLAT,LAMP` files. To account for instrument flexure, flats were taken at six instrument rotator angles with the flat lamp on: -60° (300°), 0° , 60° , 120° , 180° , 240° . The files were used in both the flat and illumination correction reduction steps described below.
- Wavelength calibration files with the arc lamp on (`DPR.TYPE = WAVE,LAMP`) and off (`DPR.TYPE = WAVE,OFF`) were taken from the daytime after the night of the observations and in the *IZ* filter (they had `EXPTIME = 4 s`). Arc lamp frames were taken at a number of rotator angles as with the flats to account for the effects of flexure.
- Telluric stars (`DPR.TYPE = OBJECT,SKY,STD,FLUX`) were obtained from the same night as the observations and taken in the *IZ* filter. I also checked the type of star (`OCS.STDSTAR.TYPE`) as some stellar types are better as standard stars than others (e.g., A0V; see Section 2.3.3). The observed standard stars had different exposure times that were appropriate for the stellar magnitudes and these were set when preparing the OBs.

All three mosaics were observed as different OBs and were therefore reduced separately. The data for IC 1459 was reduced using a combination of the ESO KMOS pipeline (SPARK) that was run using the ESO Recipe Execution tool (ESOREX, version 3.10.2; [Davies et al., 2013](#)), and purpose-built software that I developed. ESOREX performs many of the main reduction steps such as dark, flat, wavelength, and illumination corrections. However, if data is taken in a non-standard way, such as the two-part mosaic, the pipeline does have some limitations. The various pipeline ‘recipes’ or reduction steps had some required and some optional input files that were

given to ESOREX. Each recipe then had a list of optional parameters that could alter the way the pipeline processed the data at each stage³. I wrote shell scripts tailored to each stage in order to automate and monitor the reduction process. A summary and the order of the necessary reduction steps are detailed below.

1. Dark frames were used to correct for instrument bias and to generate maps of bad pixels. The names of the raw dark files retrieved from the ESO archive described above were compiled into a .sof file and assigned the relevant keyword for their file type (e.g., DARK) so that the file could be read by ESOREX. These were then processed using the ESOREX recipe KMOS_DARK to produce a bad pixel calibration file.
2. Flat fields were used to correct for pixel-to-pixel sensitivity variations. The flats taken from the ESO archive with the internal flat lamp on and off were processed using the dark bad pixel map calibration file and the ESOREX recipe KMOS_FLAT. Filter specific flat calibration files were produced including normalised flat fields with data and noise frames for each detector, x - and y -coordinates of every illuminated pixel on the detector, a map of bad pixels, and information about the edges of the IFU slitlets (i.e. one stripe of 14 pixels; there are 14 slitlets per IFU).
3. Wavelength calibration frames for the observations in the IZ band were taken using arc lamps. The wavelength calibrations were performed by combining the arc frames, files produced from processing the flats, KMOS reference wavelength tables for the IZ band and running the ESOREX recipe KMOS_WAVE_CAL. This produced a file that contained wavelength information for every illuminated pixel on the detector and a wavelength calibrated pseudo detector image (i.e. an arc-lamp frame projected onto slitlets for the eight IFUs feeding to each detector side-by-side as viewed in detector space).
4. Illumination corrections were done to account for instrument flexure. These were performed by processing the flats for each of the six rotator angles separately, combined with the output flat and wavelength calibration files, the KMOS band wavelength information and using the KMO_ILLUMINATION_FLAT recipe. This produced images of the internal flat field uniformity for each IFU at a specific rotator angle.

³All information regarding the recipes, necessary inputs and their file types, and optional parameters can be found in [The KMOS Data Reduction Library Design and Manual \(v3.1\)](#) and [KMOS Pipeline Cookbook](#).

5. The science frames for each OB were processed with `KMO_SCI_RED` using the illumination correction frame closest to the rotator angle at the time of observations and calibration files produced in the previous steps. It was during this step that science frames were combined into a mosaic and only observations taken within an OB could be combined in this way (i.e. header information about position angle or rotator angle was not used by the pipeline). It was therefore up to the user to distinguish exactly what data were processed by this recipe in order to make sense of the output. Provided the keyword option `no_combine` was set to `FALSE` (the default), the recipe combined the frames into a mosaic (triggered by the `mapping24` header keyword). A multi-extension `sci_combined_mapping24.fits` mosaic file was produced.
6. During the `KMO_SCI_RED`, the sky subtraction was done using a subtraction of the sky frames for each science exposure taken with the nod-to-sky observing mode. The telluric correction is described in Section 5.1.3.
7. The noise cube for the mosaics was not properly propagated in this version of the pipeline. I therefore had to use different methods to estimate the noise when fitting the spectra from the cubes as described in Section 5.2.1.
8. To analyse mosaics 1a and 1b that were taken at different position angles, I moved them onto the same reference grid as each other. I flipped mosaic 1a by 180° and then padded both mosaics 1a and 1b with NaN values in order to align the brightest pixel in each to the same central coordinates in both mosaics. I could not do the same for mosaic 2 as the centre of the galaxy was not covered in the mosaic as can be seen from the bottom panel of Figure 5.2. I was therefore unable to centre the mosaic using the brightest pixel as an approximation of its centre (which is sufficient given the relatively large seeing for all the mosaics). Due to this uncertainty in the location of the galaxy centroid, I decided not to flux calibrate the mosaics. However, this was not integral to my analysis and would have been purely for display purposes. The shifted 1a and 1b mosaics are those displayed in a logarithmic scale (to highlight the mosaic footprints) in Figure 5.2. I decided not to combine the first two mosaics at this stage as each required a different telluric correction and it simplified the analysis to treat them separately (as in Section 5.2.1). I instead combined average spectra from the separate mosaics as described in Section 5.2.2.

5.1.2 MUSE Data

5.1.2.1 Overview of MUSE

MUSE is a large FOV ($1' \times 1'$) panchromatic optical ($\sim 0.46\text{--}0.93 \mu\text{m}$) IFU instrument on the VLT (Nasmyth focus of UT4; Bacon et al., 2010). It had first light on 31st January 2014. MUSE has a resolving power $R \sim 2000$ at $0.46 \mu\text{m}$ and $R \sim 4000$ at $0.93 \mu\text{m}$ (similar to some KMOS bands). In its Wide Field Mode (i.e. that with the largest $1' \times 1'$ FOV as used and discussed here), MUSE has a pixel scale of $0.2''$, the same as KMOS. When using KMOS in Mosaic Mode, as done for IC 1459, one is able to cover an area of the sky that is comparable to the MUSE footprint. Given its wide optical spectral coverage, resolving power, FOV and pixel scale, MUSE makes the ideal optical companion to KMOS (see Section 2.1 for details of KMOS).

5.1.2.2 MUSE Observations

The MUSE data of IC 1459 were observed on 14th October 2014 under programme ID 094.B-0298(A) (P.I. C. J. Walcher). The aim of this programme was to obtain a uniform sample of stellar velocity dispersions for the host spheroids of galaxies with mass estimates of the central SMBH (see Section 1.1.3; Cappellari et al., 2002). The data were taken with the `MUSE_wfmnoao_obs_genericoffset` observing template⁴ which used a nod-to-sky observing pattern. The template included a rotation between exposures so that patterns of the image slicers could be averaged out over time to reduce instrumental effects on the output images. The observations were dithered by $\lesssim 1''$ to improve the removal of bad pixels (as with KMOS). The released reduced data cube (see Section 5.1.2.3) was made from eight raw science files and had a total integration time of 368 s exposure (as compared to 300 s for the KMOS observations). The average seeing measured by the Differential Image Motion Monitor at Paranal Observatory was $\sim 1.3\text{--}1.6''$. The MUSE observations were taken during bright time which caused increased photon noise in the data.

5.1.2.3 MUSE Cube Preparation

Unlike KMOS data, MUSE observations are reduced by the Quality Control Group at ESO in a largely automated way and released for use by the public. The reduced data can be accessed via the ESO Science Archive⁵ Phase 3 (i.e. prepared, validated and reduced) Data Products query form⁶. The data were reduced using the MUSE-

⁴More details can be found in the [MUSE User Manual v1.1](#).

⁵<http://archive.eso.org/cms.html>

⁶http://archive.eso.org/wdb/wdb/adp/phase3_main/form

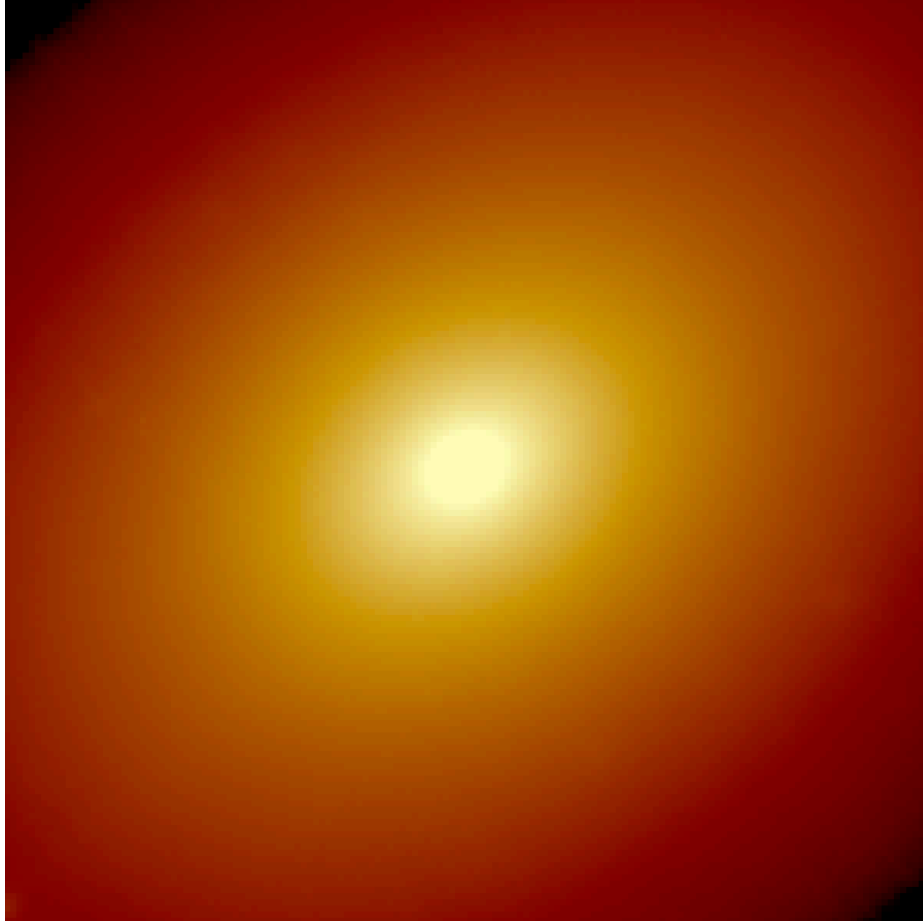


Figure 5.3: Median image of the reduced MUSE mosaic of IC 1459 as displayed in QFITSVIEW. The cube was downloaded from the ESO Science Archive and was cropped, after some additional sky subtraction, down to a size of $30'' \times 30''$, 150×150 pixels centred on the galaxy core. The major axis of this E3 galaxy is approximately from the bottom left to the top right of the image. The image has a logarithmic scaling and is displayed at a scale of 99.5% in QFITSVIEW. See Sections 5.1.2.2 and 5.1.2.3.

1.6.1 pipeline and were published as a reduced data cube on the 22nd June 2016. As described in the ESO Phase 3 Data Release Description⁷, the pipeline removes most of the observational signatures of the instrument. This includes pre-processing, de-biasing of frames, flat-fielding, astrometric calibrations, sky-subtraction, wavelength calibrations, and flux calibrations. An initial sky subtraction was performed by subtracting the sky frames from their corresponding data frames taken during the observations.

The data cube of IC 1459 was available as a FITS file that included both a data and a noise extension. In theory, this cube was a science-quality data product that was ready for analysis. However, I found that this was not the case as the data still suffered strong contamination from bright sky lines following the initial sky subtraction. It is mentioned in the Phase 3 Data Release notes that although the best calibration files available are used in the reduction, there is no universal reduction strategy that can satisfy the requirements for all the data observed. Particularly, caution is advised over the sky subtraction. To improve on the removal of the sky for the MUSE data of IC 1459, a ‘pseudo sky’ spectrum was taken from the edges of the MUSE cube (where the contribution of the galaxy was negligible) and was subtracted from the rest of the cube. This reduction step visibly improved the sky removal in some areas of the cube but residual sky features (from over- and under-subtraction) were still visible across the whole cube. This contamination can be seen in the average spectra extracted from the MUSE cube (see Section 5.2.2) shown in Figure 5.9.

Due to the large size of the data cube (~ 17 GB), to make analysing it easier, the outer regions that were worst affected by sky and had only very low-S/N galaxy data were cropped. This left the central $30'' \times 30''$, 150×150 pixels centred on the galaxy core. The subtraction of the pseudo sky and cube cropping was done by Joshua Warren and is described in his submitted DPhil thesis. As shown in Section 5.2.1, this conservative cropping does not impact on my science goals for studying this galaxy. Figure 5.3 shows the cropped MUSE cube of IC 1459 as displayed in QFITSVIEW and again with a logarithmic scale and 99.5% scaling. The major axis of the galaxy runs approximately from the bottom left to the top right of the image. It is not on the same absolute scale as the KMOS cubes (median images shown in Figure 5.2) as it has a much higher average S/N (as demonstrated in Section 5.2.1). The galaxy does not have the same orientation as in the KMOS mosaics.

⁷<http://www.eso.org/observing/dfo/quality/PHOENIX/MUSE/processing.html>

5.1.3 Telluric Correction

To correct for the telluric absorption in the reduced KMOS cubes, I again used MOLECFIT (Smette et al., 2015; Kausch et al., 2015) as before with the KCS data (Section 2.4, reduction step 2c). The software uses three-hour interval atmospheric data measured at Paranal Observatory from GDAS to model the absorption by the Earth’s atmosphere⁸. MOLECFIT derives atmospheric transmission spectra and molecular abundances using the radiative transfer code Line-by-line Radiate Transfer Model (Clough, Iacono & Moncet, 1992; Clough et al., 2005). The input for the code is an atmospheric profile constructed from a standard atmospheric model (including height, pressure, temperature, and chemical composition), regular interval GDAS data (pressure, temperature, humidity) and local weather information (taken from the data header). The model atmosphere is then fitted to the input galaxy spectrum using a χ^2 -minimisation fitting technique to find the best fit to the data. As described in the user manual, MOLECFIT was tested with fits to observed atmospheric spectra and the model was found to have relative deviations of only a few percent from the real data. I opted to use MOLECFIT for the telluric correction of the KMOS data as this level of accuracy was sufficient for the analysis I wanted to perform for IC 1459.

Given the length of the KMOS OBs (~ 1 hour as only partially completed) and interval length of the GDAS atmospheric information (3 hours), one telluric correction per cube was sufficient. In the outer regions the sky lines become extremely bright and swamp the effects of the telluric absorption. To ensure the best fit of the telluric absorption, I therefore made average spectra of the mosaics to maximise the galaxy S/N prior to fitting the atmospheric absorption. I fitted the median spectrum from each mosaic using MOLECFIT. I opted to fit the continuum of the spectra using a high-order polynomial (maximum of eight) which helped to improve the fit to the worst affected telluric absorption regions. I also chose to fit the whole spectral range simultaneously (excluding the very ends where the data was of poorer quality). I found this gave the best fit to the data which I judged by comparing the χ^2 values of each fit. MOLECFIT produced an output best-fitting model telluric spectrum which I divided through every pixel in the cube. This resulted in continuum and telluric corrected cubes for the three KMOS mosaics. Examples of the telluric fit to an average KMOS mosaic spectrum is shown in Figure 5.4.

Given that the telluric absorption in the MUSE cube had a much smaller effect on the spectrum, localised to three narrow regions, I opted not to telluric correct

⁸More details about MOLECFIT are in the [User Manual for MOLECFIT \(v3.8\)](#).

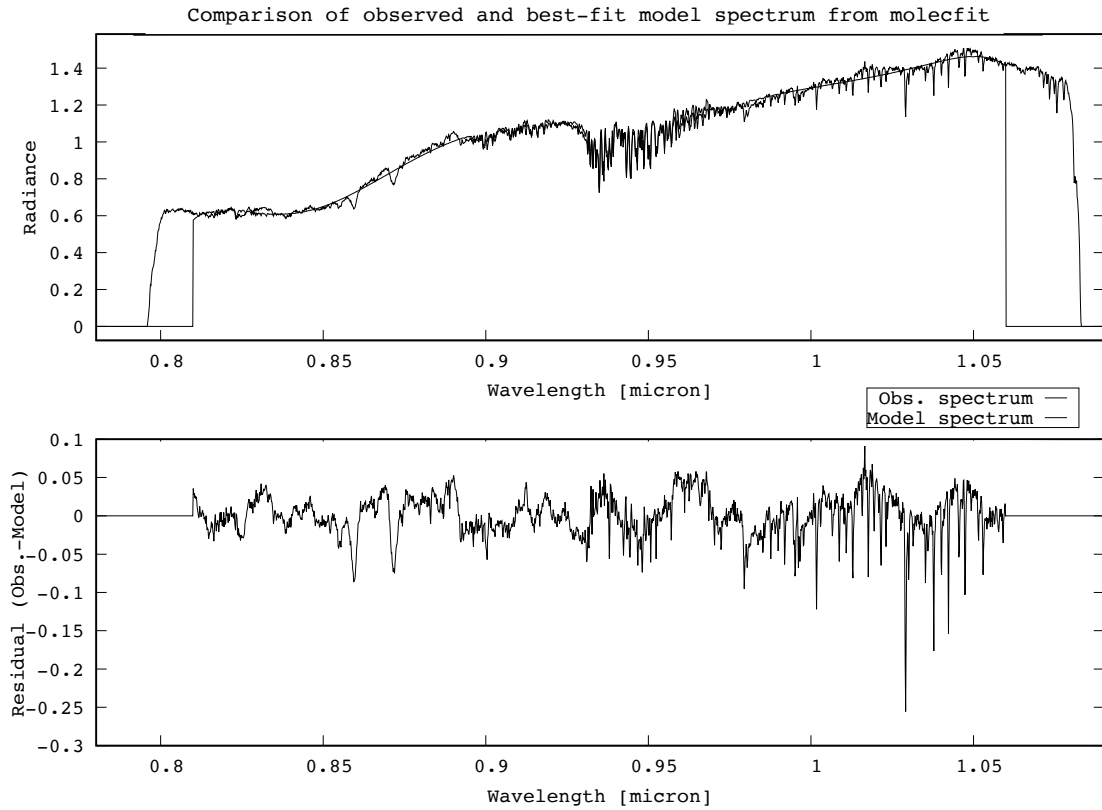


Figure 5.4: Figure produced by MOLECFIT of the median spectrum made from KMOS mosaic 1a in the top plot overlaid with the model telluric correction spectrum and fit to the continuum with an eighth order polynomial fit (straight edges and smooth continuum line). The median KMOS spectrum was normalised to one. The very ends of the KMOS spectra were not fitted (to improve the polynomial fit to the continuum) but were clipped before using the spectra for analysis. The bottom panel shows the residual of the data to the model. The worst affected region of the spectrum from telluric absorption is $\sim 0.92\text{--}0.97\ \mu\text{m}$. Note that the residual spectrum in the bottom panel does still show some effects of telluric absorption and towards the redder end the over-subtraction of the sky lines is prominent. Figure 5.9 shows the genuine galaxy features in the KMOS spectra. See Section 5.1.3.

the MUSE spectra. I show the average MUSE spectrum of the core with the narrow telluric affected regions highlighted (grey shaded bands) in Figure 5.9. This was because fitting the affected regions of the spectrum did not dramatically improve the effects of telluric absorption. However, as the continuum had already been corrected in the reduction stage, I did find that only fitting parts of the spectrum with MOLECFIT introduced new artificial features in the spectrum. As the small affected regions of the spectrum were not contaminating any of the features I used for analysis (described in Sections 5.2.1 and 5.2.3), I decided not to telluric correct the MUSE cube.

5.2 Data Analysis

5.2.1 Mosaic Kinematics

5.2.1.1 Voronoi Binning

To understand the three-dimensional structure of the galaxy, I used the spectra in the cubes to measure the stellar kinematics across the surface of the galaxy. As I had three separate KMOS mosaics and a MUSE mosaic, I used the kinematics of the galaxy to orient IC 1459 in each of them. As discussed, the data was taken in variable weather conditions for the four mosaics and often as a poor seeing backup target. Therefore, the quality of the spectra varied across the different mosaics and as one would expect, the S/N also varies from the bright central part of a galaxy to the faint outskirts where the sky becomes dominant. So as to preserve the data quality where possible, adaptive binning can be used. I adopted the Voronoi binning method of Cappellari & Copin (2003) that adaptively bins the data into regions of constant S/N. This meant that for every bin, I could normalise and median all the contributing spectra to produce a single spectrum that met a threshold S/N required to perform analysis.

To Voronoi bin the data in the different mosaics, I used the VORONOI_2D_BINNING software⁹ that implements the method outlined in Cappellari & Copin (2003). The VORONOI_2D_BINNING software required a signal and noise for each spatial pixel across the mosaic. For the MUSE mosaic, this was done simply by taking the median value of the spectrum from a spatial pixel in the data cube and noise cube to produce a signal and noise value respectively for every pixel in the MUSE cube (150×150 pixels).

⁹<http://www-astro.physics.ox.ac.uk/~mxc/software/>

For the KMOS cubes, identifying signal and noise values was more complicated as the noise cubes were not properly propagated by the pipeline. The wavelength range of the MUSE data ($\sim 0.46\text{--}0.93\ \mu\text{m}$) and KMOS data ($\sim 0.8\text{--}1.08\ \mu\text{m}$) overlap. In this region where the spectral range is covered by both instruments is a strong absorption feature that is useful for extracting kinematics called the Ca II triplet (CaT, $\lambda 8498, 8542, 8662\ \text{\AA}$). Due to the fact that the same feature appears in both the optical MUSE data and the NIR KMOS data, the CaT was an obvious choice for extracting kinematics from all the mosaics. To estimate a signal and noise value for the KMOS mosaics, I therefore used the continuum around the CaT feature. I fitted the continuum regions of the CaT (as defined in [Cenarro et al., 2001](#)) and took the average continuum level as my signal value and the standard deviation of the data to the fit as a measure of the noise. I made signal and noise arrays that matched the footprints of the KMOS mosaics shown in Figure 5.2.

Using the signal and noise arrays for each mosaic, I experimented with binning the data for S/N thresholds between 20 (that is an approximate minimum requirement for extracting kinematics) and 100 (as is roughly required to perform analysis on very faint IMF-sensitive features). Normalising and taking the median of all the spectra within these different S/N Voronoi bins gave me spectra to analyse at a common S/N value across all the mosaics from KMOS and MUSE. To measure the stellar kinematics, I again used the latest version of PPXF ([Cappellari & Emsellem, 2004](#); [Cappellari, 2017](#)). I opted to fit the kinematics with SSP models here as I needed to fit the same spectra with SSP models for extracting stellar populations and IMF information. Therefore, for consistency with the kinematic and stellar populations analysis for IC 1459 (in Sections 5.2.3 and 5.2.4) I used the same templates for all of the spectral fitting described in this chapter.

5.2.1.2 Spectral Fitting Templates

The templates I used to fit the spectra were the extended MILES (E-MILES)-based SSP models of [Vazdekis et al. \(2016\)](#)¹⁰. These have a broad spectral range ($\sim 1680\text{--}50,000\ \text{\AA}$) making them ideal for both the optical MUSE and NIR KMOS data. Between $3540\text{--}8950\ \text{\AA}$ the E-MILES SSP models are joined to the MILES-based SSP models of [Sánchez-Blázquez et al. \(2006\)](#); [Falcón-Barroso et al. \(2011\)](#). The E-MILES library (and the SSP models based upon them) therefore has the same spectral resolution of $2.54\ \text{\AA}$ FWHM ([Beifiori et al., 2011](#)) over the range $3540\text{--}8950\ \text{\AA}$ increasing to $\sigma = 60\ \text{km s}^{-1}$ at greater wavelengths. See Table 5.1 for a summary of

¹⁰Available from <http://miles.iac.es/>.

the different resolution values of the MUSE spectra, KMOS data, and SSP models over the spectral regions used for analysis. I used the E-MILES-based SSP models that were based on the Bag of Stellar Tracks and Isochrones (BaSTI; [Pietrinferni et al., 2004](#)) models due to the wide range of ages (53 ages spanning 0.03–14.00 Gyrs) and metallicities (12 spanning $[M/H] = -2.27$ – 0.40 , or $Z = 0.0001$ – 0.040)¹¹. The E-MILES-based SSP models come in only one $[\alpha/Fe]$ (see Section 1.1.7) value which is termed ‘base’ where the iron metallicity and total metallicity are assumed to be equal ($\langle[M/H]\rangle = [Fe/H]$) and it follows the abundance pattern of the Galaxy.

The SSP models of [Vazdekis et al. \(2016\)](#) come with five options for the IMF, two of which have 13 possible logarithmic slopes spanning $\Gamma = 0.3$ – 3.5 . The regular array of the [Vazdekis et al. \(2016\)](#) SSP model templates (i.e. for every age template there are the same options for metallicity and IMF) was particularly important for fitting the stellar populations and determining a best fitting IMF. These different IMF options are summarised below.

- Unimodal – a single power law with a choice of 13 different logarithmic slopes: Γ ([Vazdekis et al., 1996](#)).
- Bimodal – a fixed low-mass end slope (as defined in [Vazdekis et al., 1996](#)) and 13 different high-mass end ($\log(M_*/M_\odot) > 0.6$) slopes given by the Γ_b parameter.
- Kroupa universal IMF ([Kroupa, 2001](#)) – multi-part power law with $\log(M_*/M_\odot) > 0.5$ end logarithmic slope of $\Gamma = 1.30$.
- Kroupa revised IMF – same as Kroupa universal but accounting for unresolved binaries.
- Chabrier IMF (for individual stars; [Chabrier, 2003](#)) – multi-part power law with high-mass end logarithmic slope of $\Gamma = 1.30$.

The forms of all these IMFs are given in Figure 1.7.

5.2.1.3 Deriving the Kinematics

For extracting the kinematics from the mosaics with PPXF, the choice of IMF was not important. I used Salpeter IMF templates (unimodal function with $\Gamma = 1.30$) and all possible age and metallicity models (636 templates; see Section 5.2.1.2) to fit the kinematics of the binned spectra. Following some tests on median spectra extracted from the different cubes, I chose to fit the spectra with a fourth-order

¹¹Where Solar is $Z = 0.0198$ or $[M/H] = 0.06$.

additive polynomial (advised for extracting kinematics) to the continuum and between $\sim 8100\text{--}8800 \text{ \AA}$ for both KMOS and MUSE. This was to encompass the NaI and CaT features whilst avoiding the very end of the KMOS data and regions strongly affected by sky ($\gtrsim 8800 \text{ \AA}$). The wavelength range could also be fitted by the E-MILES-SSP based templates of fixed resolution (see Table 5.1). As could be seen clearly in the MUSE spectra, particularly toward the edges of the cube (as highlighted in the spectra shown in Figure 5.9), there was still some strong contamination from sky emission in this wavelength range. I therefore used rigorous masking of these regions (between $\sim 8100\text{--}8110, 8267\text{--}8527, 8621\text{--}8694$, and $8749\text{--}8800 \text{ \AA}$) when fitting the MUSE data which allowed many more spectra to be fitted. These regions were not as contaminated in the KMOS data, mostly likely due to the multi-epoch observations which helped to reduce variable noise in the data when stacked and also that the data were taken during dark time unlike the MUSE observations. To preserve as much information as possible when extracting kinematics from the lower-resolution KMOS spectra, I therefore decided not to mask these regions. This again allowed me to constrain fits of many more spectra in the KMOS cubes.

As before for the kinematic fitting of the KCS spectra (in Section 2.5.2), estimation of the resolution FWHM ($\Delta\lambda$, Δv) and corresponding dispersion ($\sigma = \Delta v/2.355$), had to be determined for each of the instruments and templates over the fitting region. See Table 5.1 for a summary of the resolution values over the different fitting regions used for analysis. For $\sim 8100\text{--}8800 \text{ \AA}$ used for measuring the kinematics, the MUSE data had a slightly smaller average dispersion ($\langle\sigma\rangle$) than that of the [Vazdekis et al. \(2016\)](#) SSP models. Therefore, the output velocity dispersions from PPXF (σ_{obs}) were corrected after the fit using Equations 2.1 and 2.2. The σ_{diff} value subtracted in quadrature from the σ_{obs} of the MUSE spectra to give a corrected σ_{gal} value is also given in Table 5.1. The resolution difference was small and resulted in only a $\sim 1\text{--}2 \text{ km s}^{-1}$ correction to the output value. The KMOS data had a slightly larger $\langle\sigma\rangle$ than the E-MILES SSP models over this wavelength range. The templates were therefore convolved to the resolution of the data prior to the fit and did not required further correction, i.e. $\sigma_{\text{gal}} = \sigma_{\text{obs}}$.

5.2.1.4 Kinematic Maps

From kinematic fits to the median of the normalised spectra within different S/N Voronoi bins, I mapped the kinematics of IC 1459 in each of the MUSE and three KMOS mosaics. I show the velocity relative to the median velocity of IC 1459 ($\sim 1700 \text{ km s}^{-1}$ as measured from MUSE) in Figures 5.5 and 5.7. The velocity dispersion

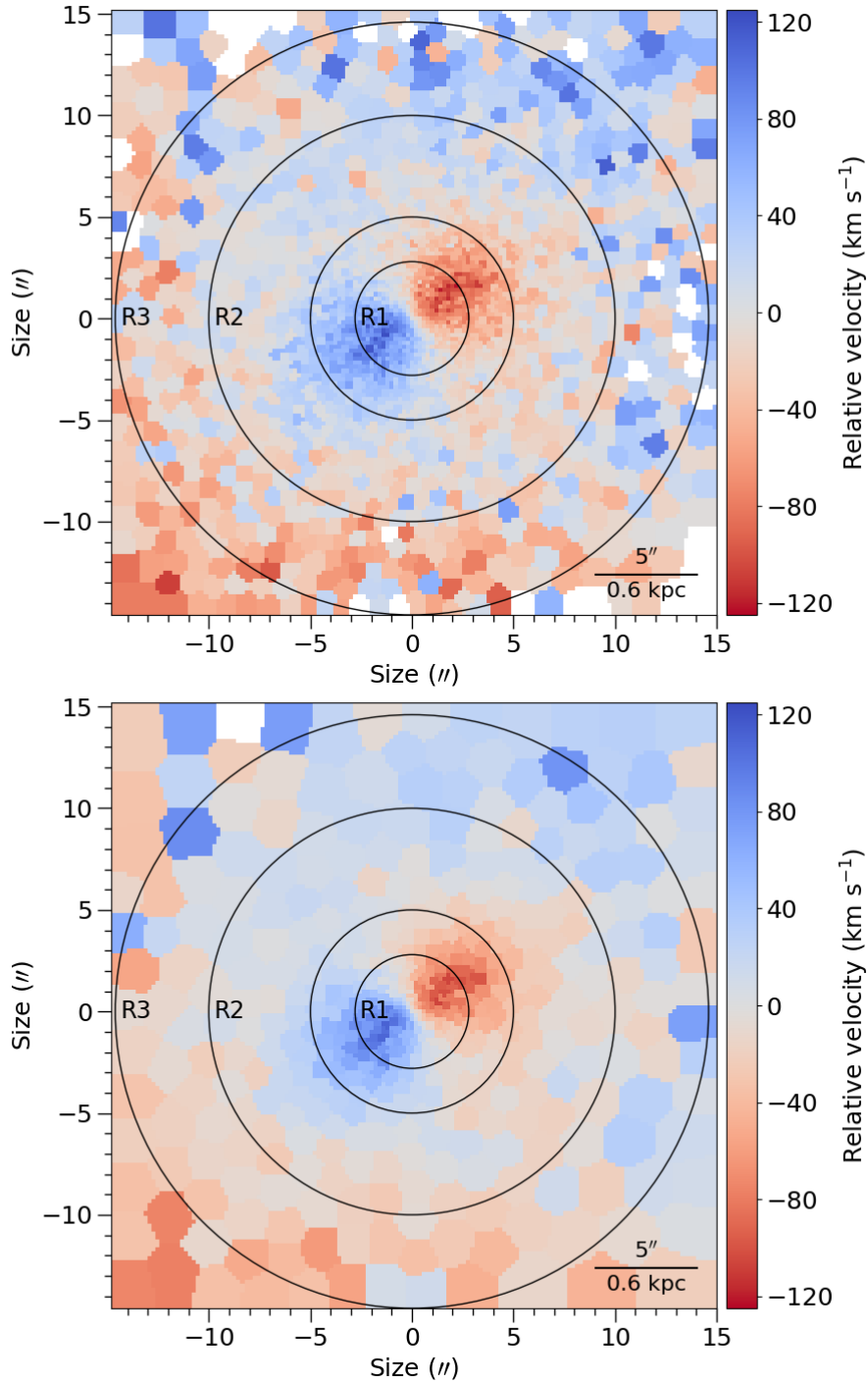


Figure 5.5: Relative velocity maps of IC 1459 as measured using PPXF on the MUSE cube. The mosaics are 150×150 pixels and $30'' \times 30''$ in size. The circles represent regions (R) from which spectra were extracted (Section 5.2.2) and properties of the stellar populations derived (see Sections 5.2.3 and 5.2.4). The white regions are NaN values where a fit to the data was not possible. Pixels in the cube were Voronoi binned to different S/N thresholds with the `VORONOI_2D_BINNING` code (Cappellari & Copin, 2003). Spectra within the bins were normalised, median stacked and their kinematics fitted. *Top*: Pixels binned to $S/N = 20$. *Middle*: Pixels binned to $S/N = 40$. Continued on the next page.

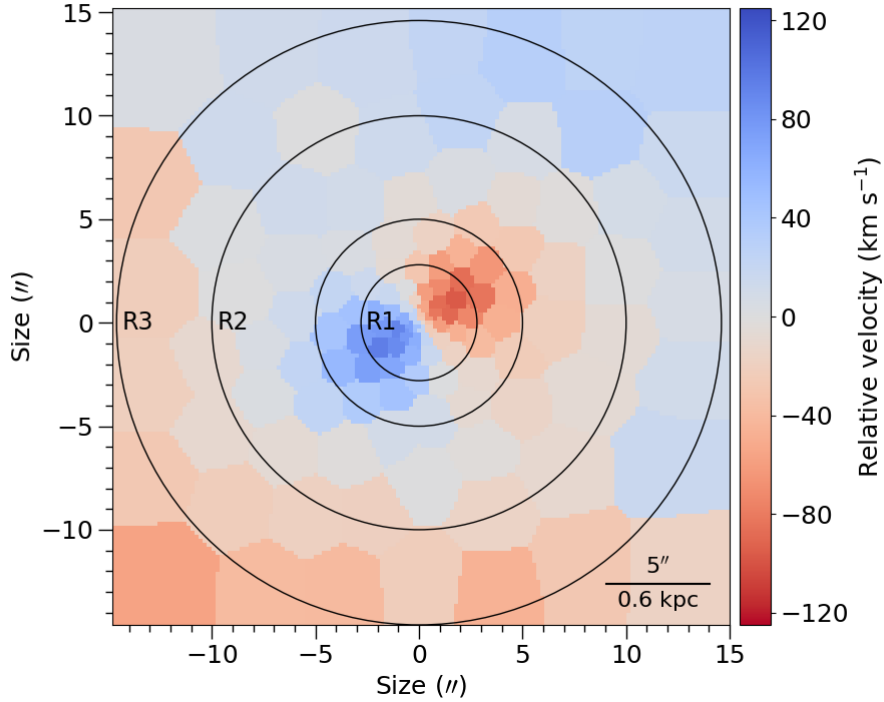


Figure 5.5: Continued. *Bottom:* Pixels binned to $S/N = 80$. See Sections 5.2.1 and 5.2.1.4.

maps for MUSE and KMOS are shown in Figures 5.6 and 5.8 respectively. The maps are shown in units of pixels and for both KMOS and MUSE the pixel scale is $0.2''$. The sizes of each map are given in the respective figure captions. The formal errors from PPXF were small compared to the resolution of the spectra. The errors on the velocities and dispersions were therefore taken to be the average spectral resolution over the fitting wavelength range ($\langle\sigma\rangle$) of the KMOS and MUSE spectra as listed in Table 5.1.

MUSE had full coverage over the central regions of the galaxy and slightly higher resolution that resulted in better fits to the data. I therefore show the MUSE mosaic with three Voronoi binning thresholds: $S/N = 20$, 40, and 80 in Figure 5.5. This is to show the quality of the data with a low $S/N = 20$ threshold, a $S/N = 40$ for comparison with the KMOS maps (Figure 5.7), and $S/N = 80$ to highlight some features of the kinematic maps more easily (discussed below). A striking feature of the relative velocity maps of MUSE is of course the strongly counter-rotating core in the central $\sim 10''$ and the slight rotation of the outer regions of the galaxy (seen starting at a radius $\sim 10''$). From the MUSE velocity maps, I measure peak rotation of the core of $\sim 125 \text{ m s}^{-1}$ and $\sim -122 \text{ m s}^{-1}$, with errors given as the $\langle\sigma\rangle$ values in Table 5.1. I show the kinematics of the three KMOS mosaics with $S/N = 40$ Voronoi

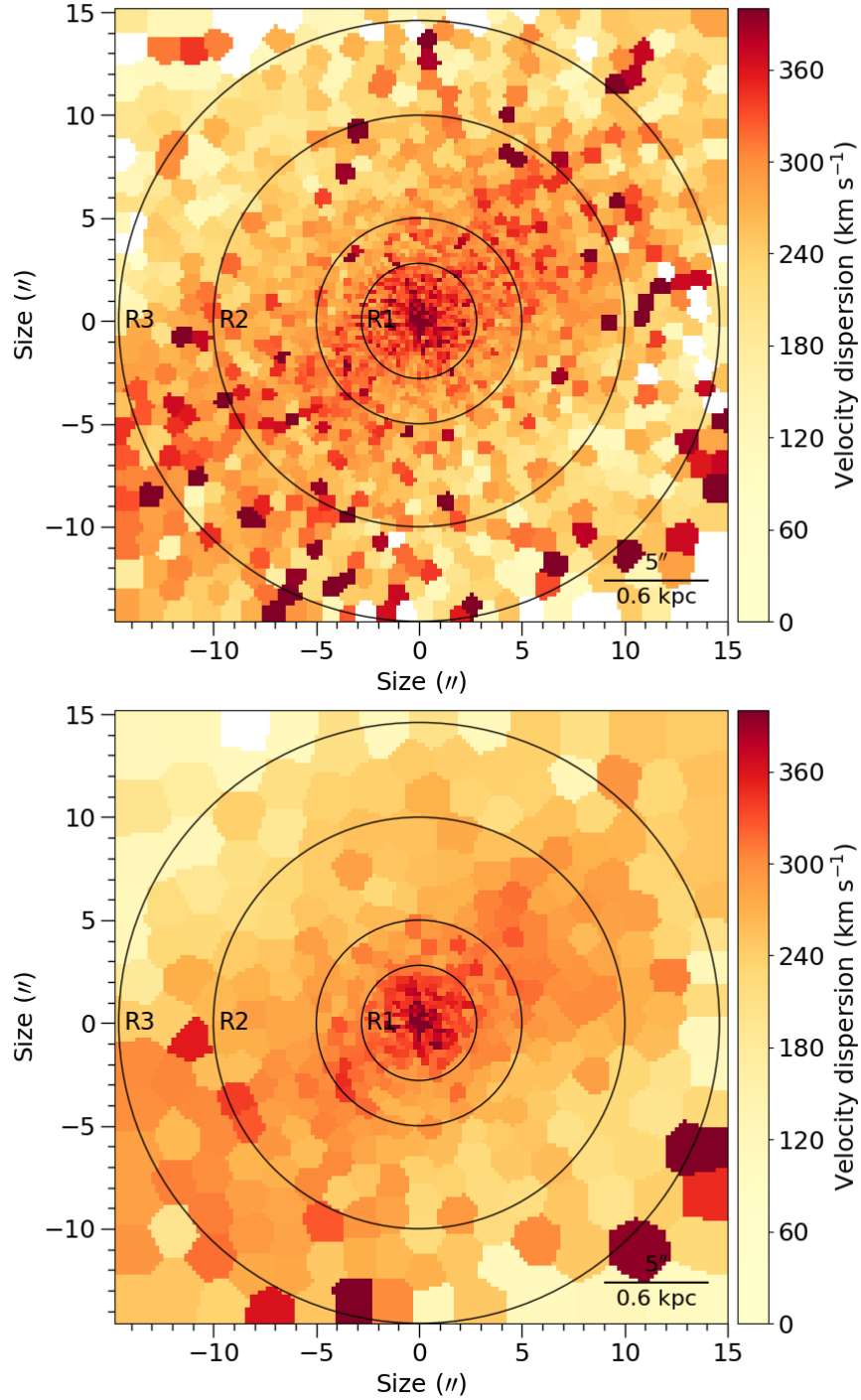


Figure 5.6: Velocity dispersion maps of IC 1459 as measured using PPF on the MUSE cube with the same scales and labelling as Figure 5.5. *Top*: Pixels binned to $S/N = 20$. *Middle*: Pixels binned to $S/N = 40$. Continued on the next page.

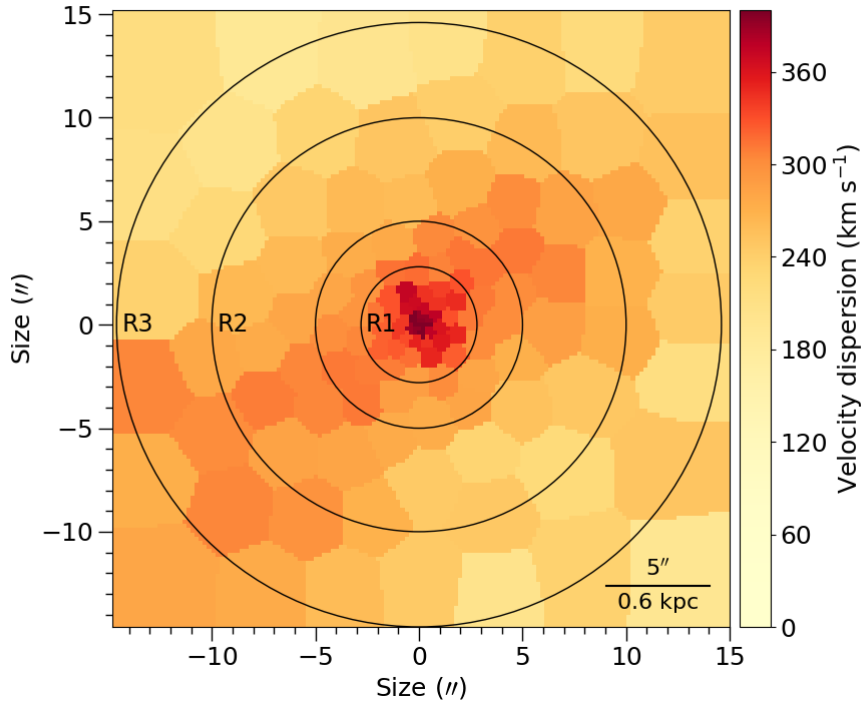


Figure 5.6: Continued. *Bottom:* Pixels binned to $S/N = 80$. See Sections 5.2.1 and 5.2.1.4.

binning in Figure 5.7. The images have different scales and the galaxy is oriented and positioned differently in each of Figures 5.5 and 5.7 (and in the different panels of the KMOS maps). With the kinematics shown it is slightly easier to distinguish the position of the galaxy in each.

The velocity dispersion maps for MUSE and KMOS (Figures 5.6 and 5.8 respectively) have the same scaling, binning, and labelling as for the relative velocity maps in Figures 5.5 and 5.7. The galaxy appears to be kinematically hotter (higher dispersion) along the major axis of the galaxy (approximately bottom left to top right). This is perpendicular to the minor axis (diagonal top left to bottom right) about which the core rotates seen in the relative velocity maps of MUSE. This is discussed further in Section 5.3.1. As can be seen from the high $S/N = 80$ binned relative velocity map on page 156, it is symmetric about the minor axis. A distinctive feature of the MUSE velocity dispersion maps, seen most easily in the high $S/N = 80$ map on the current page, is their asymmetry. The galaxy appears to have a higher dispersion towards the bottom left which extends towards the centre of the galaxy. This indicates a dynamically hotter population of stars in this region.

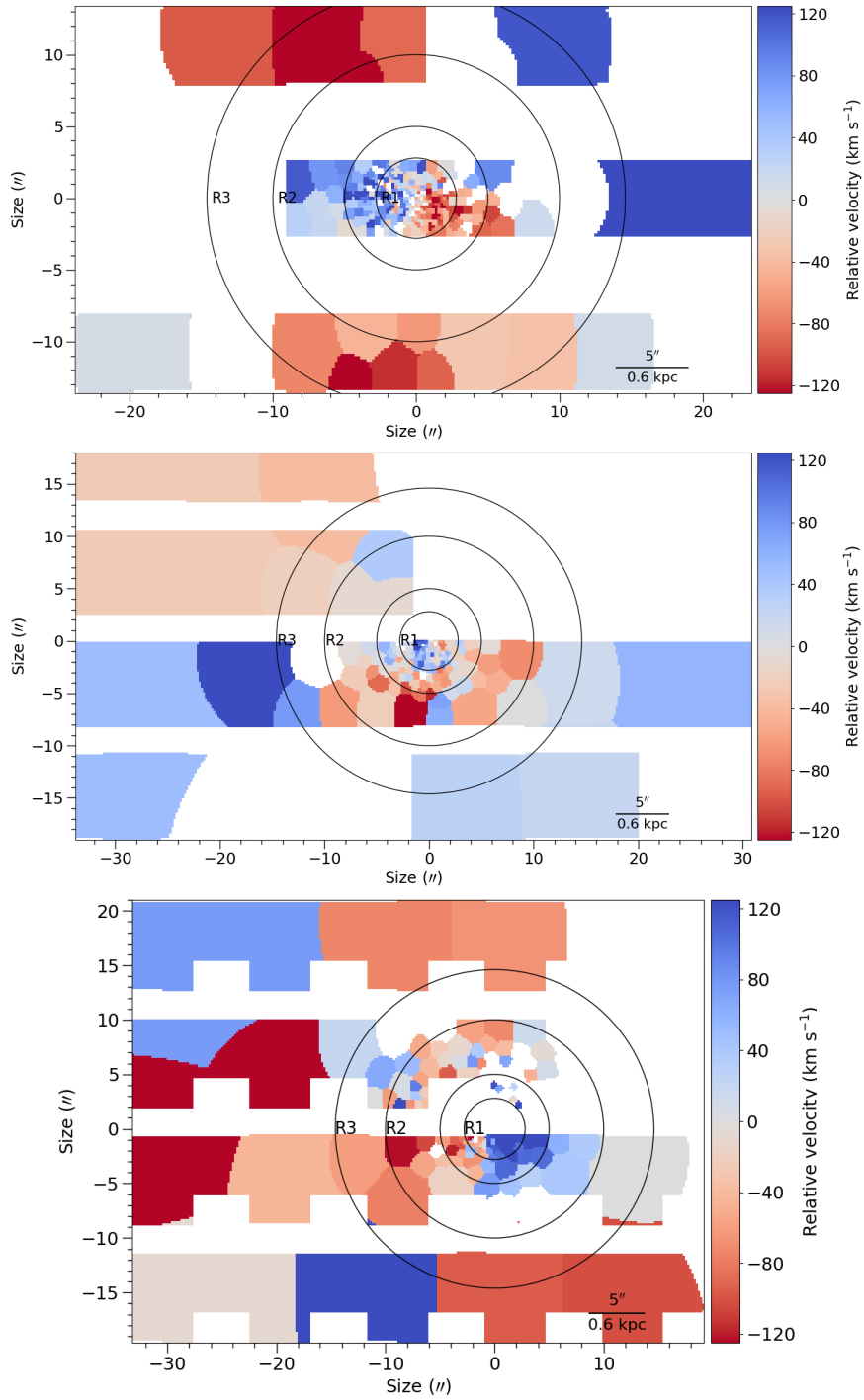


Figure 5.7: Relative velocity maps of IC 1459 as measured using PPXF on the KMOS mosaics. The circles represent regions (R) from which spectra were extracted and stellar populations and the IMF were derived across the surface of the galaxy (see Sections 5.2.2). The white regions are NaN values where there is no data or a fit to the data was not possible. The galaxy is not in the same exact location in the different mosaics. All mosaics were Voronoi binned to $S/N = 40$. *Top*: Mosaic 1a which has size $57.4'' \times 33.4''$. *Middle*: Mosaic 1b which has size $64.8'' \times 38.0''$. *Bottom*: Mosaic 2 with size $52.6'' \times 40.8''$. See Sections 5.2.1 and 5.2.1.4.

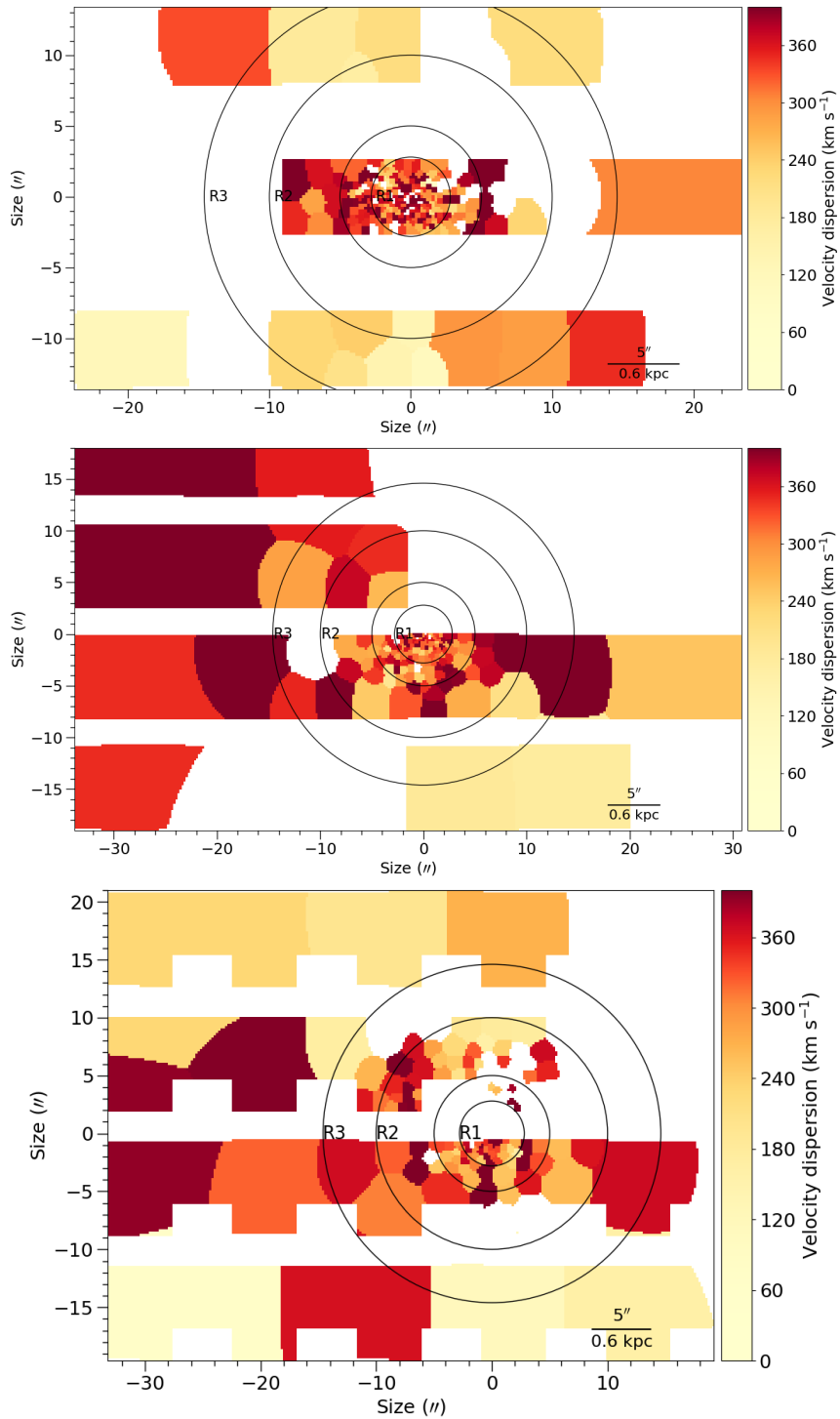


Figure 5.8: Velocity dispersion of IC 1459 as measured using PPXF on the KMOS mosaics with the same scale and labelling as Figure 5.7. All mosaics were Voronoi binned to $S/N = 40$. See Sections 5.2.1 and 5.2.1.4.

5.2.2 Extracting Average Spectra

In all of the mosaics from MUSE and KMOS in Figures 5.5, 5.6, 5.7 and 5.8, concentric circles are shown of the same scale and approximate position relative to the galaxy. These circles were determined mostly by eye using the MUSE relative-velocity maps to encompass different regions of the galaxy from which I extracted spectra. I extracted a median spectrum from each of the MUSE mosaic and three KMOS mosaics from within these regions. The inner most region (R1) was placed conservatively over the counter-rotating core of IC 1459. The radius of R1 (14 pixels, $2.8''$, i.e. one KMOS IFU) was set due to the KMOS mosaic 1a coverage which is the only contiguous KMOS data covering the counter-rotating core. Based on the MUSE kinematic map, I then determined a buffer region around the core to ensure I was not selecting spectra from within the region that showed counter-rotation (annulus of 14–25 pixels, $2.8''$ – $5.0''$). The middle region (R2) was determined from the $S/N = 20$ MUSE kinematic map (top panel of Figure 5.5) to encompass the region with no strong rotational signatures (annulus between 25–50 pixels, $5.0''$ – $10.0''$). The region with the largest radius (R3) was intended to cover the weakly rotating outer parts of the galaxy (seen most clearly in the bottom panel of Figure 5.5). The size of R3 was chosen to fill the MUSE mosaic (annulus between 50–73 pixels, $10.0''$ – $14.6''$).

For the MUSE mosaics and the KMOS mosaics 1a and 1b, the regions were centred on the brightest pixel. For KMOS mosaic 2, as the centre of the galaxy was not covered by the data, the centre was approximated using the distribution of light in the median image (Figure 5.2) and comparison with the other kinematic maps. Given the relatively high seeing ($\sim 1''$ – $2''$) of all the observations, if this positioning was off by up to $\sim 2/3$ one KMOS IFU then it shouldn't make a difference to the output spectra. Also given that all the spectra within the different regions are binned across the three KMOS mosaics, any small mismatch above the seeing limit in the centroid location of the regions would ultimately contribute only very minimally to the extracted spectra. I therefore chose to include the spectra from mosaic 2 to improve the coverage of the KMOS data.

Using these uniformly defined regions across all the mosaics, I extracted a median spectrum from each by first normalising all the spectra within them. This left me with three spectra from the MUSE cube of regions R1, R2, and R3. For the KMOS data I had three sets of spectra for each region from the mosaics. I further normalised these and made a single median KMOS spectrum for each of the three regions. In Figure 5.9 I show the final median spectra for each of the three regions as extracted from the MUSE (blue) and KMOS (red) mosaics. I indicate spectral features of the galaxy

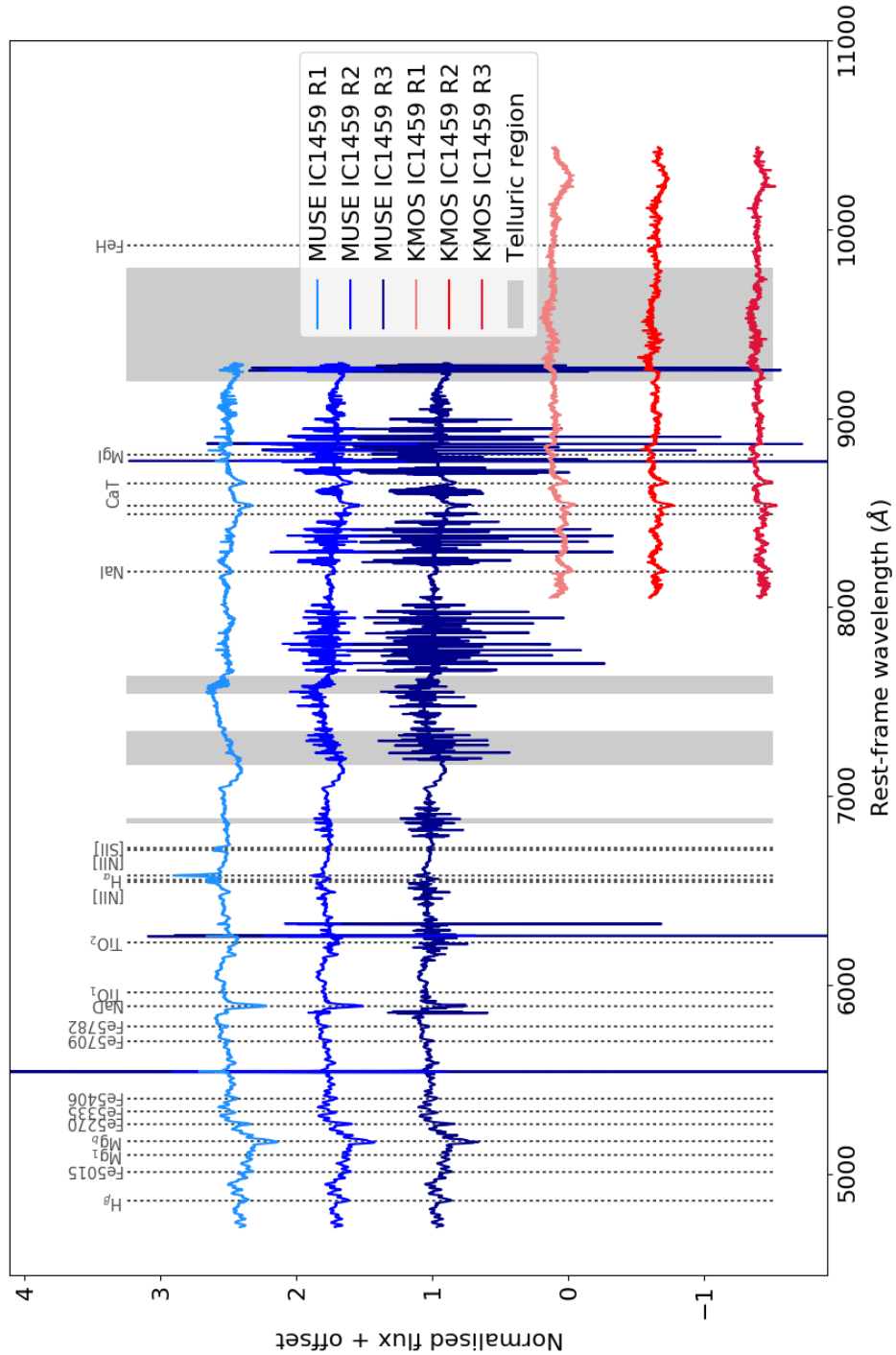


Figure 5.9: Median spectra extracted from the three regions of IC 1459 indicated in Figures 5.5 and 5.7. The MUSE spectra (blue) and KMOS spectra (combined from all three KMOS mosaics; red) are shown for the central region (R1; lightest shade), middle region (R2), and outer-most region (R3; darkest shade) of IC 1459. I show the useful spectral features of the galaxy (dotted lines) and regions of strong telluric absorption (shaded grey; see Section 5.1.3). All the strong emission not labelled is that of contamination from bright sky lines, this is strongest in the outer regions (R3) of the MUSE data. See Section 5.2.2.

Table 5.1: Table of resolution values for KMOS, MUSE and the E-MILES-based SSP models (Vazdekis et al., 2016) over the spectral ranges used for analysis. The uses are either stellar populations (SP; Section 5.2.3), kinematics (K; Section 5.2.1), or IMF (Section 5.2.4). The $\Delta\lambda$ and $\langle\Delta v\rangle$ (averaged over the wavelength range) resolution values are the FWHM and $\langle\sigma\rangle$ is the corresponding average Gaussian dispersion ($=\langle\Delta v\rangle/2.355$). The de-redshifted wavelength resolution ($\Delta\lambda_{z=0}$) was determined using $z \approx \frac{v}{c}$ with $v \sim 1700 \text{ km s}^{-1}$ (measured from the MUSE cube). The correction applied to the measured σ_{obs} from PPXF after a fit in the case of an instrument resolution that is smaller than the template resolution (i.e. $\sigma_{\text{inst}} < \sigma_{\text{temp}}$) is given by σ_{diff} (Equations 2.1 and 2.2). See Sections 5.2.1, 5.2.3 and 5.2.4.

	Wavelength Range (Å)	Use	$\Delta\lambda$ (Å)	$\Delta\lambda_{z=0}$ (Å)	$\langle\Delta v\rangle$ (km s ⁻¹)	$\langle\sigma\rangle$ (km s ⁻¹)	σ_{diff} (km s ⁻¹)
MUSE	4750–5850	SP	2.31	2.30	131	56	25
	8100–8800	K	2.31	2.30	82	35	16
KMOS	8100–8800	K	2.82	2.80	100	43	-
	8100–10400	IMF	2.82	2.80	92	39	-
E-MILES	4750–5850	SP	2.54	-	144	61	-
	8100–8800	K	2.54	-	90	38	-
	8100–10400	IMF	$\Delta\lambda = 2.54 \text{ Å}$ at $< 8950 \text{ Å}$ ($\langle\sigma\rangle = 38 \text{ km s}^{-1}$) $\sigma = 60 \text{ km s}^{-1}$ at $> 8950 \text{ Å}$ ($\langle\Delta\lambda\rangle = 4.56 \text{ Å}$)				

with dotted vertical lines. To highlight the minimal effect that a telluric correction for the MUSE data would have had, I also indicate regions of the strongest telluric features in both the optical (as spanned by MUSE) and NIR (spanned by KMOS where this correction was more important). These regions do not overlap with any of the features I used for the analysis of IC 1459.

All strong spectral features not indicated are sky lines that have resulted from poor sky subtraction. The sky features are particularly prominent in the outer regions of the MUSE mosaic (see Section 5.1.2.3) and get stronger at redder wavelengths. The NaI and CaT features used for the kinematics mostly miss the worst affected sky-line regions and are heavily masked when fitting the MUSE spectra (Section 5.2.1.3). Most of the valuable features for stellar populations are much less affected at the bluer end of the spectrum (see Section 5.2.3). The KMOS spectra appear to have much less contamination from the sky; this is helped by the fact that when combining data from all three mosaics the depth is \sim three times that of MUSE. In addition, as the KMOS data were taken with multiple pointings and at different epochs, the variable noise in each of the spectra was significantly reduced by the median stacking.

5.2.3 Spatially Resolved Stellar Populations

Using the spectra extracted from regions across the surface of IC 1459, I then wanted to measure the stellar populations of its different kinematic components. Combining the spectral range of both MUSE and KMOS, I was able to measure the stellar populations in the optical, then measure the IMF sensitive features in the NIR separately (as described in Section 5.2.4). I used PPXF to measure the properties of the stellar populations from full-spectral fitting of the MUSE spectra. I again used the E-MILES-based SSP models from [Vazdekis et al. \(2016\)](#) (see Section 5.2.1.2). The continuum was fitted with only multiplicative polynomials (as advised for PPXF with `mdegree` = 10) to avoid affecting the measured line strengths. I fitted the MUSE spectra between $\sim 4750\text{--}5850 \text{ \AA}$ as this encompassed most of the strong features for stellar populations ($H\beta$, Mgb , Fe lines). I chose not to fit the NaD ($\sim \lambda 5893 \text{ \AA}$) feature as this is a known strong absorption line of the interstellar medium. In the optical part of the spectrum, the strength of the absorption lines is driven by the stellar population parameters rather than IMF. To fit the MUSE data, I just used models with a Salpeter IMF (unimodal, $\Gamma = 1.30$; based on the BaSTI isochrones) with all possible ages (53 spanning 0.03–14.00 Gyrs) and metallicities (12 between $[M/H] = -2.27\text{--}+0.40$). I verified that the choice of IMF in this region was not important by also fitting the spectra with models that had a Chabrier, Kroupa Universal and revised, and bimodal IMF (with $\Gamma_b = 1.30$) and got the same results.

Strong Balmer and forbidden emission can be seen in the optical wavelengths spanned by the MUSE data. This is most apparent in the core of IC 1459 (R1) in the MUSE data as exhibited by the $H\alpha$, [NII] and [SII] emission in Figure 5.9. The $H\beta$ line and [OIII] $\lambda 5007 \text{ \AA}$ gas emission lines were in the fitting region I chose to fit. I therefore fitted the stars, Balmer emission, and forbidden emission simultaneously as three separate kinematic components with PPXF. This was particularly important for the populations analysis as the gas emission filled in some of the stellar absorption features. I also generously masked the strong sky line between $5570\text{--}5587 \text{ \AA}$ for the fit.

Figure 5.10 shows the PPXF fits to the MUSE spectra and corresponding grids of stellar population parameters from R1 (top two panels), R2 (middle two panels), and R3 (bottom two panels). The panels showing the spectra indicate the galaxy spectrum (black), the best fit to the stellar component (red), the best fit to the gas emission lines (light blue), the corresponding gas emission spectrum (magenta), the residuals to the fits (green points), and regions masked from the fit (navy blue). The kinematics and stellar populations derived for the fits to each of the three regions are

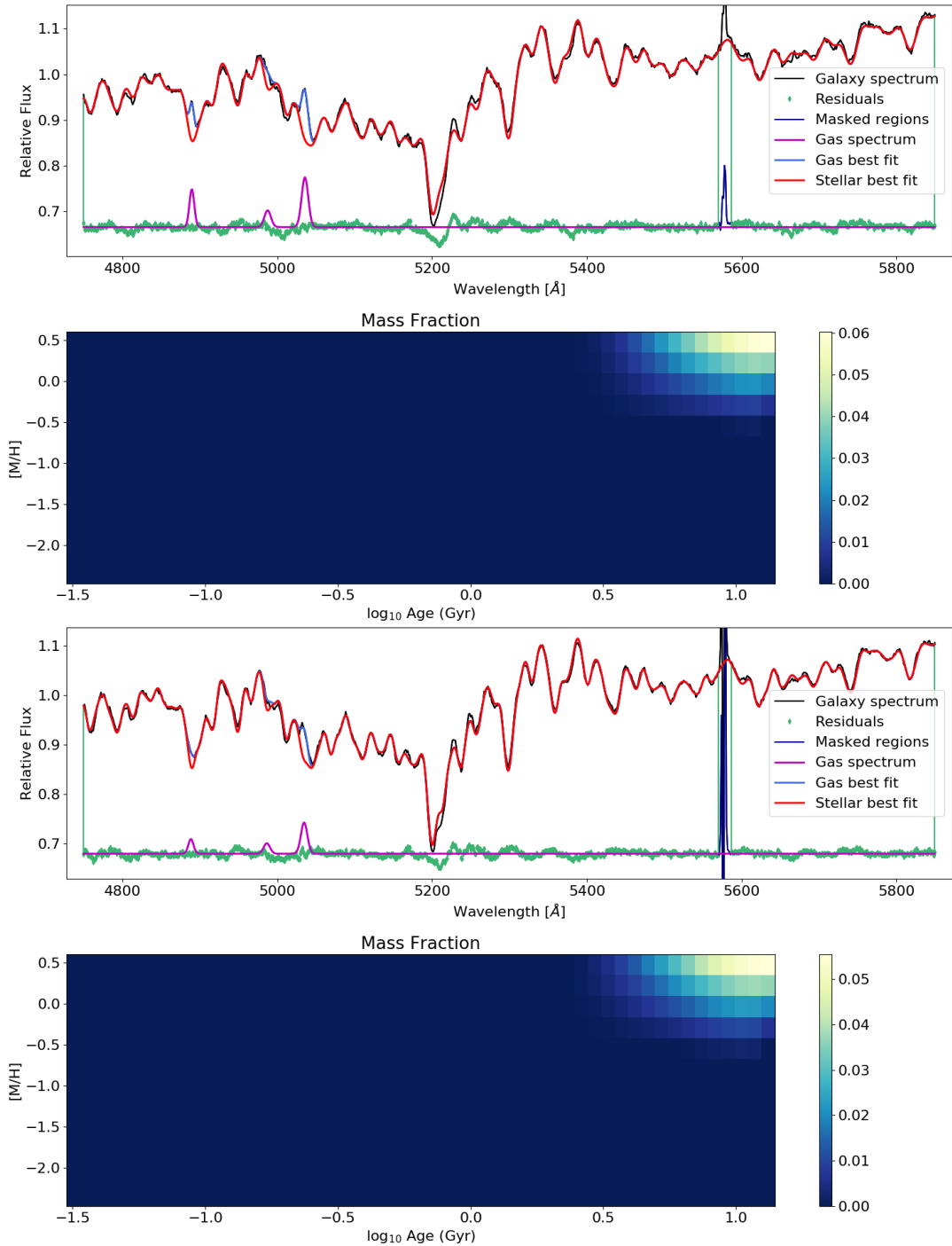


Figure 5.10: Spectral fits to the MUSE data of IC 1459 in each of the three regions across the surface (shown in e.g., Figure 5.5). The panels with the spectra show the galaxy spectrum (black), best fit to the stellar component (red), best fit to the gas emission (light blue), gas spectrum (magenta), residuals (green points), and masked region (dark blue). I show the mass fractions of the stellar populations of the fit (navy panels), derived from regularizing the weights of the best fitting templates. *Top*: R1 spectrum from which a mass-weighted age ($\langle \text{Age} \rangle$) of 11.9 Gyrs and mass-weighted metallicity $\langle [M/H] \rangle = 0.290$ were derived. *Middle*: R2 with a derived $\langle \text{Age} \rangle = 11.8$ Gyrs and $\langle [M/H] \rangle = 0.281$. Continued on the next page.

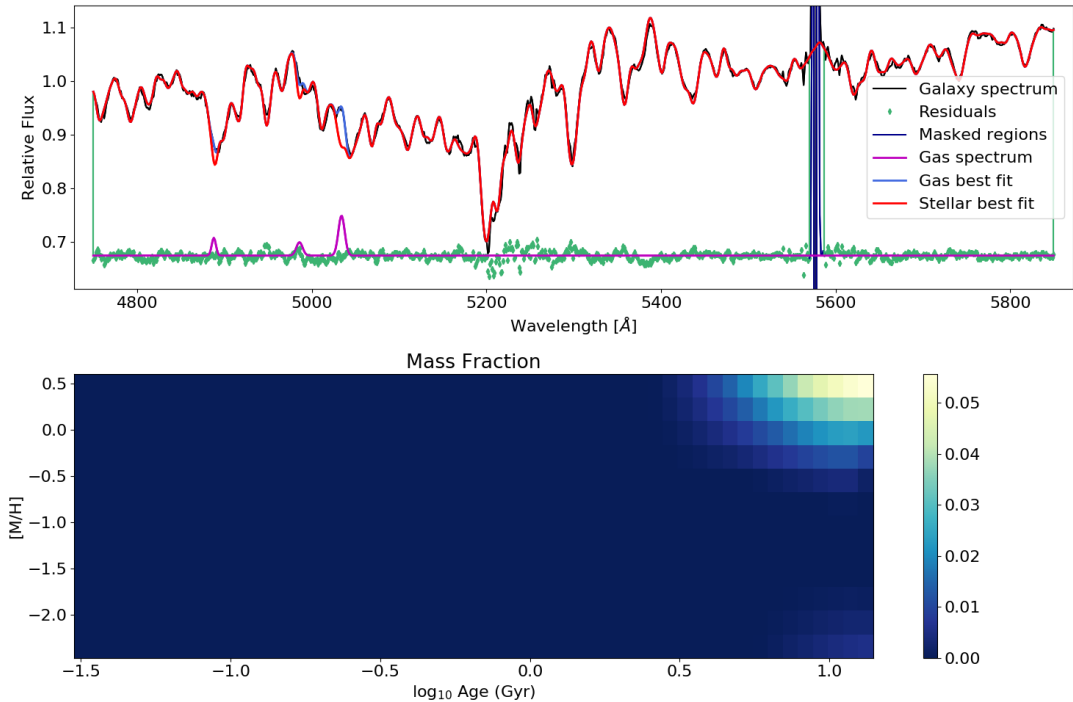


Figure 5.10: Continued. *Bottom:* R3 spectral fit from which I derived a mass-weighted age of $\langle \text{Age} \rangle = 12.0$ Gyrs and metallicity $\langle [M/H] \rangle = 0.171$. The lower metallicity compared with R1 and R2 is driven by a distinct extremely metal-poor population seen only faintly in the bottom right of the stellar population parameter grid. This secondary peak can be seen more prominently in the low-regularization grid of Figure 5.11. See Section 5.2.3.

summarised in Table 5.2. The dispersions were corrected (only by $\sim 1 \text{ km s}^{-1}$) after the fit as the template dispersion ($\langle \sigma \rangle$) was slightly higher than that of the MUSE data. See Table 5.1 for the σ_{diff} correction value (applied using Equations 2.1 and 2.2). The uncertainties for the kinematics of the fit were again assumed to be that of the average spectral resolution over the fitting range ($\langle \sigma \rangle$) for MUSE given in Table 5.1.

The navy coloured panels of Figure 5.10 show the mass-weighted properties of the stellar populations. The metallicity and age of the regions of the galaxy could be derived using the weights applied to the template library to best fit the spectrum. The grid shows these weights for the spread of metallicity (y -axis) and age (x -axis) values spanned by the E-MILES-based SSP models from [Vazdekis et al. \(2016\)](#). To use this method of measuring the stellar population parameters with PPXF, selecting models for which every age SSP had the same set of metallicity values at a fixed α -element abundance ratio was essential. The colour of the different squares in the grid is the mass fraction, i.e. the proportion of stellar mass that corresponds to that

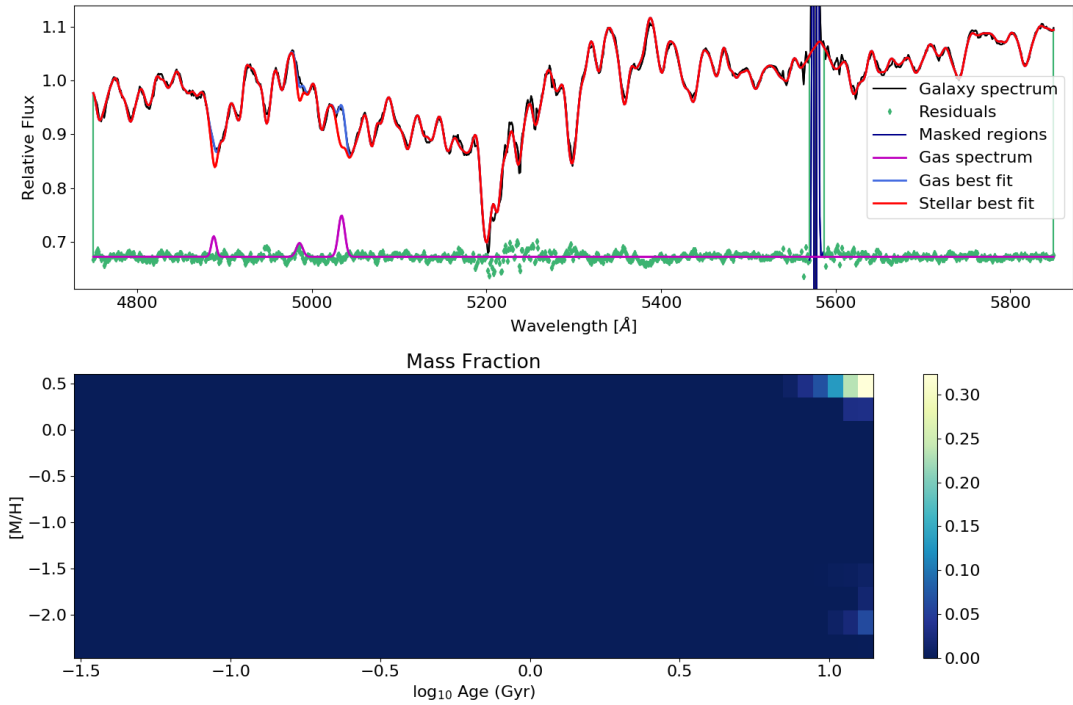


Figure 5.11: I show the same plot as displayed in the bottom panel of Figure 5.10 of the PPXF fit to the MUSE spectrum of R3 but with a regularization of one rather than 100. This plot demonstrates the effect of regularisation to the fit of the spectrum (which is slightly improved) but at the expense of information in the grid of values that characterise the stellar populations (navy panel). It is clearer to see on this grid of very little regularization that there is a secondary peak in the mass fraction of templates fitted to the R3 spectrum (seen only very faintly in Figure 5.10). The smaller peak (mass fraction ~ 0.2 if no regularization is used) appears at old ages and very low metallicity (bottom right of grid) as compared to the rest of the population (top right). See Section 5.2.3.

particular age and metallicity value. An advantage of fitting the stellar populations in this way using PPXF is that no prior assumptions about the SFH have to be made. Another useful feature of this method is that one can separate distinct populations of stars within a single galaxy spectrum based on the best-fitting templates.

An important parameter in deriving values for the stellar populations of galaxies with PPXF is the regularization (see Section 2.5.2.1). The mathematically best fitting solution is usually one that uses only a small number of templates (one, five, and four for R1, R2, R3 respectively). In order to extract useful information about the stellar populations when spectral fitting with PPXF, regularization (smoothing of the template weights whilst fitting) must be used (Cappellari, 2017). Choosing the optimal regularization (`regul`) takes careful consideration; I adopted the strategy advised in PPXF to normalise the templates (`templates/median(templates)`) and the

Table 5.2: Summary of kinematic and stellar population properties derived from the median MUSE spectra in the three regions of IC 1459 shown in Figure 5.5. The PPXF fits and grids of stellar population properties are shown in Figure 5.10. The velocity dispersions σ_{gal} were corrected using σ_{diff} values in table 5.1 and Equations 2.1 and 2.2. The mass-weighted age ($\langle \text{Age} \rangle$) and metallicity ($\langle [\text{M}/\text{H}] \rangle$) are shown along with their errors derived in Section 5.2.3.1. See Section 5.2.3.

Region	v	σ_{gal} (km s ⁻¹)	$\langle \text{Age} \rangle$ (Gyrs)	$\langle [\text{M}/\text{H}] \rangle$
R1	1710	323	11.9 ± 0.2	0.290 ± 0.003
R2	1701	279	11.8 ± 0.2	0.281 ± 0.003
R3	1686	238	12.0 ± 0.3	0.171 ± 0.013

galaxy spectrum (galaxy/median(galaxy)) such that each has a median of one. In this case, a sensible regularization was `regul` = 100 as the error on the regularization (`1/regul`) was smaller than, but on the same order as, the weights themselves. I show a fit to the R3 MUSE spectrum with a low regularization of one (fitted with 18 templates) in Figure 5.11 for comparison with the bottom panel of Figure 5.10 with the regularization of 100. Applying this regularisation forced PPXF to fit many more templates to find the best fit (62, 73, 100 for R1, R2, R3 respectively). It is from the spread of values of the weights of these templates fitted with regularization that information about the stellar populations can be derived.

Using the fits to the MUSE spectra for the three regions and the regularized grids of weights, I derived mass-weighted stellar population parameters for the three regions across the surface of the galaxy. For the core of IC 1459 (R1), I found a mass-weighted age ($\langle \text{Age} \rangle$) of 11.9 Gyrs and a mass-weighted metallicity of $\langle [\text{M}/\text{H}] \rangle = 0.290$. For the middle R2 region of IC 1459, I found consistent values with the core of $\langle \text{Age} \rangle = 11.8$ Gyrs and $\langle [\text{M}/\text{H}] \rangle = 0.281$. Finally, for the outskirts of IC 1459 (R3), I again found a similar age of $\langle \text{Age} \rangle = 12.0$ Gyrs but a lower overall mass-weighted metallicity of $\langle [\text{M}/\text{H}] \rangle = 0.171$. These values are summarised along with their errors (see Section 5.2.3.1) in Table 5.2. Interestingly, when looking at the stellar population mass-fraction grid for R3 (bottom panel of Figure 5.10), I found that this drop in metallicity was not an overall trend of the stars in this region but was instead driven by a distinct very low-metallicity population of stars. This can be seen faintly in the regularized grid used for the measuring stellar population parameters but can be seen more prominently in the grid with a regularization of one for R3 (in Figure 5.11). This grid of little regularization for R3 is used purely as a comparison for display rather than for deriving the stellar populations, however, it is useful for highlighting this secondary peak more clearly. Such a low metallicity model would have very few

spectral features and so may be used by PPXF to help fit the continuum along with the polynomial. If it was purely a problem with the fit then perhaps this should be seen in every radial bin and I do not detect the very low metal populations towards the centre.

5.2.3.1 Uncertainties on the Stellar Population Parameters

To estimate the uncertainties on the derived stellar population parameters, I adopted a method suggested by Michele Cappellari following tests he had performed (private communication). The method is a bootstrapping technique and following comparison with a more comprehensive Monte Carlo random sampling method for quantifying the uncertainties, was deemed a simpler but just as effective determination of the errors with comparable outputs. From a spectral fit to a galaxy spectrum, the best fit to the data and the residuals (= galaxy – best fit) can be used to generate bootstrapped spectra that are refitted with PPXF. The method employs the Wild bootstrap (Wu, 1986) that has the following form:

$$y_i^* = \hat{y}_i + \hat{\epsilon}_i v_i. \quad (5.1)$$

Where y_i^* is the bootstrapped value for wavelength pixel i , \hat{y}_i is the best fit to the real data for pixel i , $\hat{\epsilon}_i$ is the residual of the best fit to the real data for pixel i , and v_i is a random variable that can have a value of ± 1 with a probability of a $\frac{1}{2}$. Using this equation, I generated 100 bootstrapped spectra from the single best fit and residuals from my original fit to the data.

Using the 100 bootstrapped spectra, I then fitted each with PPXF using the same method as before for the stellar populations. However, for the fits to the bootstrapped spectra, I held the velocity and dispersion derived from the data fixed. Each bootstrapped spectrum was fitted with the same regularization (`regul` = 100) and the corresponding best-fitting mass-weighted age and metallicity was derived. I then used the distribution of values obtained from the bootstraps to estimate the uncertainties on the parameters derived from the data. As for my analysis of JKCS 041, I opted to use the STD derived from the MAD ($1\sigma = 1.4826 \times \text{MAD}$) for estimating a 1σ uncertainty from the distribution due to its resistance to outliers. The errors derived for each of the parameters of the three regions are summarised along with the derived values in Table 5.2.

Taking these uncertainties into account, I found that the mass-weighted stellar ages did not vary with radius (within errors). I found that the metallicity difference between the core (R1) and middle region (R2) of IC 1459 only varied marginally.

The difference between the inner and outer region $\langle[M/H]\rangle$ was significant. However, as shown from the distribution of values, all regions have a similar distribution of weights in the old-metal rich corner (top right) of the grids. It is in fact a distinct old and metal-poor population of stars that seems to be driving the metallicity gradient that I find in IC 1459.

5.2.4 Spatially Resolved IMF

With age and metallicity values determined for the different regions of IC 1459 using the strong stellar-population-sensitive absorption features in the MUSE data, I then wanted to measure the IMF in each region. The KMOS NIR wavelength range allowed me to probe the low-stellar mass end of the IMF where there are valuable dwarf-sensitive features. I held the age and metallicities derived from MUSE fixed when fitting for the IMF in the NIR in order to break any degeneracies between the two which can be difficult to disentangle without a broad wavelength range (e.g., [McConnell, Lu & Mann, 2016](#); [Zieleniewski et al., 2017](#)). I fitted the KMOS spectra between $\sim 8100\text{--}10400 \text{ \AA}$ which included the NaI, CaT, and FeH features that are all known to be sensitive to the IMF and avoided the poorer quality ends of the spectra. When fitting the KMOS spectra of the three regions I did not need to account for strong gas emission lines as there are none in this wavelength range, and there were also no strong sky lines to mask in the KMOS spectra. However, I chose to stringently mask between $\sim 9200\text{--}9800 \text{ \AA}$ to avoid the worst affected telluric region as it did not overlap with any of the key features I was fitting.

The high-mass end of the IMF is widely accepted to have a logarithmic slope of $\Gamma = 1.30$ (see Section 1.1.6). The E-MILES-based SSPs had the option of a Chabrier, Kroupa Universal or revised IMF all of which have high-stellar mass slopes of $\Gamma = 1.30$. There were then the unimodal and bimodal slopes in which either the high-mass slope (for bimodal) or total slope (for unimodal) could be one of thirteen options. I therefore selected just the bimodal model with $\Gamma_b = 1.30$ and unimodal IMF of $\Gamma = 1.30$ (i.e. Salpeter) so that all the IMF models I was fitting to the data had the same high-mass end slope of $\Gamma = 1.30$. This was to ensure that when fitting the templates with different IMFs, I was only measuring variations in the low-mass stellar end (as can be constrained in the NIR). For each region across the surface of IC 1459, I selected models of the closest age and metallicity derived from the MUSE data of the same region. These were models with age 12.0 Gyrs and $[M/H] = 0.26$ for R1 and R2, and age 12.0 Gyrs and $[M/H] = 0.15$ for R3. For each region, at a fixed age and metallicity corresponding to each, I therefore had five different IMF

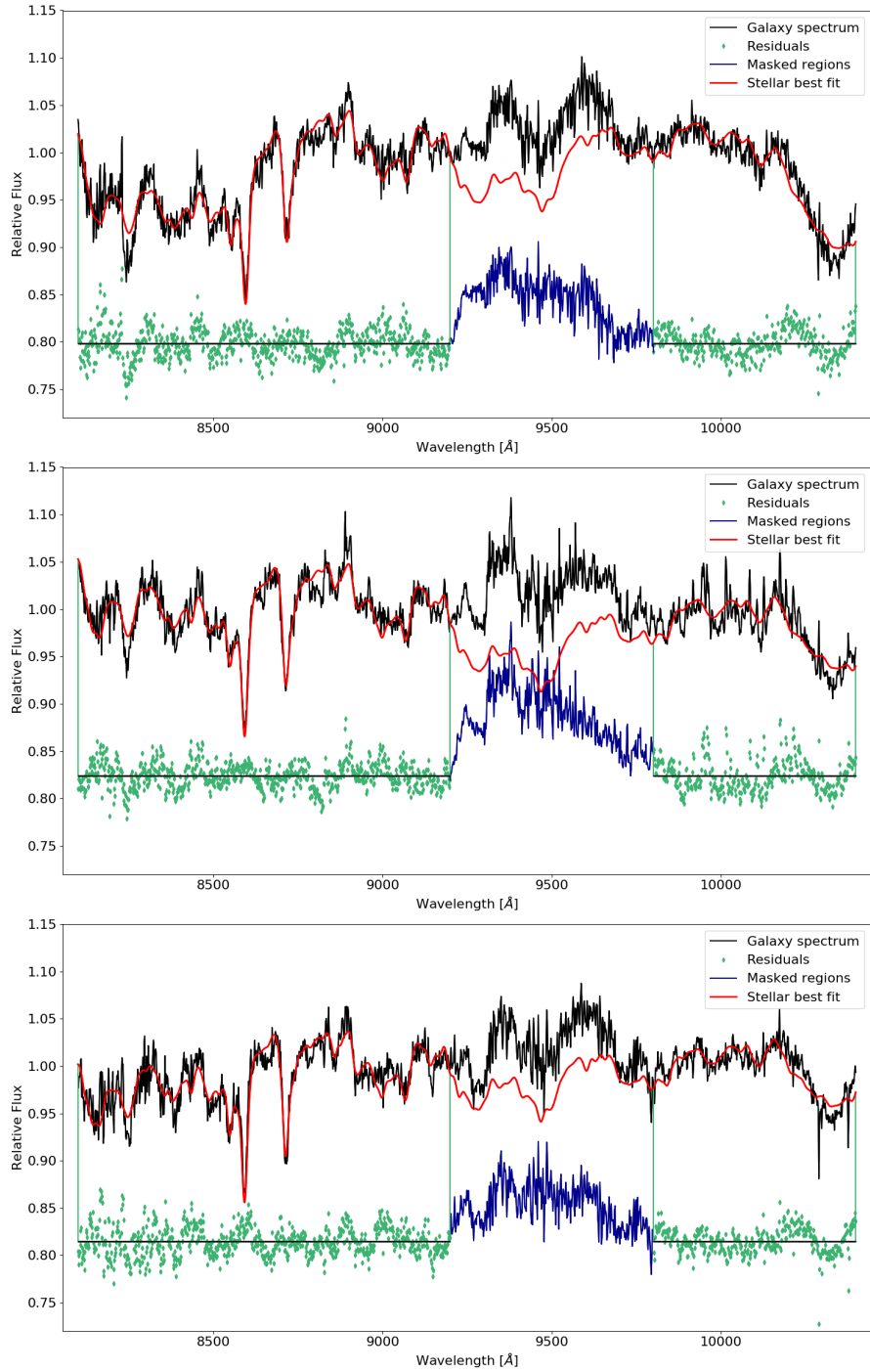


Figure 5.12: Full-spectral fit of the median KMOS spectra of IC 1459 in R1 (top), R2 (middle panel), and R3 (bottom panel) as shown in Figures 5.5 and 5.7. The spectra were fitted with PPXF (same labelling as Figure 5.10) using templates of fixed metallicity and age, as determined for the corresponding regions from the MUSE data (Figure 5.10), but with different IMFs. The fitted templates all had a fixed high-mass logarithmic slope of $\Gamma = 1.30$ but the low-mass either followed a Chabrier, Kroupa (Universal or revised), Salpeter (unimodal with $\Gamma = 1.30$) or bimodal (with $\Gamma_b=1.30$) IMF. The best fitting IMF template for all three spectra was that of a Kroupa revised IMF. See Section 5.2.4.

templates to fit to the data: Chabrier, Kroupa Universal and revised, unimodal with $\Gamma = 1.30$ (Salpeter), and bimodal with $\Gamma_b = 1.30$.

I fitted each of the three KMOS spectra with the five different IMF templates to find the best fit to the data. For all three spectra I found that they were best fitted with a relatively bottom-light multi-part power law Kroupa revised IMF. Figure 5.12 shows the PPXF best fitting IMF template (red) for the age and metallicities derived from MUSE for the KMOS spectra (black) from R1 (top panel) R2 (middle panel), and R3 (bottom panel). The residuals to the fit are shown in green and the masked bad telluric region is shown in navy blue.

A limitation of this method is that the NaI $\lambda 8183, 8195 \text{ \AA}$ doublet is not well fitted in any of the three spectra. This is a valuable dwarf-sensitive feature and may mean that the contribution of dwarf stars determined using the fixed age and metallicity derived from the MUSE spectra is not well measured. It could also be that the telluric correction was done poorly for this feature which causes it to be artificially deepened. There is some apparent correction done at the exact wavelength of NaI seen in Figure 5.4. Finally, there is the issue that the E-MILES-based SSP library does not have a fixed resolution over the fitted wavelength range (as summarised in Table 5.1). Over the fitted region, the template resolution is either comparable to that of KMOS between 8100–8950 \AA ($\langle\sigma_{\text{inst}}\rangle = 39 \text{ km s}^{-1}$, $\langle\sigma_{\text{temp}}\rangle = 38 \text{ km s}^{-1}$) or lower ($\langle\sigma_{\text{temp}}\rangle = 60 \text{ km s}^{-1}$ at 8950–10400 \AA). For this reason, I did not convolve the templates before the fit as they had the higher dispersion. Although this is important when deriving kinematics from the spectra, it is unclear exactly what effect this would have on the fit to the IMF as this is not a standard use of PPXF. It may be that an alternative spectral library or different spectral fitting technique could provide a cleaner result. This is discussed further as part of my plans for future work in Section 6.2.

5.3 Discussion

5.3.1 Kinematics of IC 1459

IC 1459 is the central galaxy in a gas-rich spiral-dominated group of 11 galaxies (Huchra & Geller, 1982; Serra et al., 2015). It is a massive galaxy ($M \sim 4\text{--}6 \times 10^{11} M_{\odot}$; Cappellari et al., 2002; Samurović & Danziger, 2005) which places it above the $M_{\text{crit}} \approx 2 \times 10^{11} M_{\odot}$ value that typically divides fast- and slow-rotators (Emsellem et al., 2011). IC 1459 is in the minority of ETGs that belong to the slow-rotator class ($\sim 15\%$; Krajnović et al., 2008; Krajnović et al., 2011); these show irregular rotation and low

specific angular momentum (Cappellari et al., 2007; Emsellem et al., 2007). It is a classic example of a galaxy with a KDC (see Section 1.1.2) and these make up $\sim 7\%$ of the total ETG population but a higher proportion ($\sim 42\%$) among just the slow rotators (Krajinović et al., 2011). KDCs typically show strong rotation relative to the outer parts of the galaxies that show little to no rotation. IC 1459 exhibits a core that is counter-rotating with respect to the outer parts of the galaxy (Franx & Illingworth, 1988) which is shown prominently in the MUSE relative velocity maps in Figure 5.5. The counter-rotating core is around $\sim 10''$ in size and is approximately bounded by the inner radius of R2 (as shown on the relative velocity maps) in order to separate the kinematic components of the galaxy. I derived a peak positive rotation velocity of the core from the Voronoi-binned to $S/N = 20$ mosaic (and with conservative errors) of $\sim 125 \pm 35 \text{ km s}^{-1}$. This is smaller than the value of $170 \pm 20 \text{ km s}^{-1}$ from Franx & Illingworth (1988), however the two are consistent within their errors. Any offset between the two estimates is likely to be an effect of the Voronoi binning that would ‘dilute’ the maximum velocity.

The dispersion maps of IC 1459 as measured from the complete MUSE mosaic (Figure 5.6) show a couple of interesting features. I noticed a higher dispersion along the major axis of the galaxy (i.e. bottom left to top right of the map) which is perpendicular to the rotation axis of the core (i.e. the minor axis). This can be seen most clearly in the large Voronoi bins of the high S/N ($= 80$) threshold dispersion map on page 158. This broadening of the spectroscopic features (i.e. higher dispersion) is to be expected for sharp velocity gradients (as seen perpendicular to the axis of rotation). If a galaxy’s stellar population is made up of multiple components travelling at different velocities, then if the different component distributions cannot be spectrally resolved, their Gaussians are blended together into broader lines.

The higher stellar dispersion along the major axis was also found for strikingly similar massive ETGs with KDCs: NGC 5813 (Krajinović et al., 2015) and NGC 4365 (Davies et al., 2001; van den Bosch et al., 2008). NGC 5813 is a central galaxy in a multi-part group (Mahdavi, Trentham & Tully, 2005) and was the first object discovered to have a KDC (Efstathiou, Ellis & Carter, 1980, 1982). Unlike IC 1459, it shows no rotation in the outer parts of the galaxy. NGC 5813 was also observed with MUSE but for a much longer exposure time (~ 80 min on source). This was to enable the modelling of the galaxy using a Schwarzschild (1979, 1982) orbital super position method that was similar to that used by van den Bosch et al. (2008) for modelling the KDC of NGC 4365. The kinematic maps of the higher- S/N MUSE data of NGC 5813 revealed a higher dispersion along the major axis but showed that it was actually in

two peaks symmetrically separated from the core. They found a strong central peak in the dispersion (also seen in the maps of IC 1459), followed by a very low dispersion ring around the centre with a radius that was coincident with the strongly rotating core. The two peaks occurred just outside the rotationally dominated region of the core.

Directly comparing the two galaxies, it is clear from the lower S/N MUSE data for IC 1459 that a lower dispersion region outside the core (lying approximately in the region between R1 and R2) would not be spatially resolved. If the double peak feature existed in IC 1459, the two peaks would lie in the R2 region along the major axis (bottom left to top right of the map). Interestingly to the top right of the dispersion maps there does seem to be a trend towards being kinematically colder outside of R2. The peak of the dispersion along the major axis in the top right appears to be in R2, coincident with that seen in NGC 5813. The other striking feature of the MUSE dispersion maps for IC 1459 is the asymmetry in contrast to the highly axisymmetric velocity maps. This asymmetry shows as a kinematically hotter region extending to the bottom left of the map and approximately along the major axis. If there are symmetrical peaks in the dispersion map for IC 1459 (which higher S/N MUSE data would reveal), it could be that this asymmetry to the bottom left is an additional kinematic component that masks the potential secondary peak. Possible causes of a double sigma peak and the implications of the derived kinematics of IC 1459 to the formation of KDCs are discussed further in Section 5.3.7.

5.3.2 Stellar Populations of IC 1459

Using the spatial information from MUSE and KMOS, I was able to extract spectra from different regions across the surface of the galaxy that showed distinct kinematics. I used the optical MUSE spectra to measure the properties of the stellar populations. Using PPXF and fitting E-MILES-based SSP models with a wide range of ages (53 possible templates) and metallicities (12 metallicities for each age; [Vazdekis et al., 2016](#)), I determined ages and metallicities for each region. I measured a metallicity gradient in IC 1459 going from metal rich in the centre to metal poor in the outer regions (as determined in previous studies e.g., [Carollo, Danziger & Buson, 1993](#); [Amblard et al., 2017](#)). This radial trend in metallicity has also been reported for several other KDCs (e.g., [Efstathiou & Gorgas, 1985](#); [Franx & Illingworth, 1988](#); [Gorgas, Efstathiou & Aragon Salamanca, 1990](#); [Bender & Surma, 1992](#); [Mehlert et al., 1998](#); [Davies et al., 2001](#); [Emsellem et al., 2004](#); [Kuntschner et al., 2010](#)).

Using regularization of the templates in PPXF for deriving stellar population parameters, I was able to derive stellar properties of the separate regions without prior assumptions (e.g. SFH or composition). What I found was that the metallicity gradient in IC 1459 did not arise from the smooth variation of stellar properties but was in fact driven by a distinct metal-poor population of stars in its outskirts. This result was hinted at in another study of a KDC (NGC 5813; [Krajnović et al., 2015](#)) when finding that a region of the galaxy could be fitted by two templates with different metallicities. They suggested their results might indicate two distinct metallicity populations but emphasised the low significance of the finding. Adopting the method of regularization, I was able to visually identify a distinct population on the mass-weighted grid of stellar population parameters. The low-metal population was coincident with where the retrograde motion of the outer parts of the galaxy becomes visible. The result could imply that the retrograde stellar population has a lower-metallicity component that drives the drop in metallicity. This would explain why it is only measured where the retrograde stars become more dominant ($R > 10''$) seen by the rotation in the outskirts.

From the stellar-population sensitive lines in the optical MUSE data, I determined ages in the three regions across the surface of IC 1459. I found a constant (within errors) and old mass-weighted age of ~ 12 Gyrs (radial values and errors are summarised in Table 5.2). Interestingly, this old stellar population and lack of age gradient has been measured for several KDCs (e.g., [Franx & Illingworth, 1988](#); [Bender, Doebereiner & Moellenhoff, 1988](#); [Rix et al., 1992](#); [Davies et al., 2001](#); [McDermid et al., 2006](#); [Kuntschner et al., 2010](#); [McDermid et al., 2015](#); [Krajnović et al., 2015](#)). If one supposed that the stars within the KDC had an external origin or that the core was a spatially decoupled component, as the kinematics suggest, then this homogeneity of stellar ages is surprising. However, the orbital superposition modelling done for two galaxies with KDCs shows a very different picture ([van den Bosch et al., 2008](#); [Krajnović et al., 2015](#)).

5.3.3 Results from Orbital Modelling of KDCs

The [Schwarzschild \(1979, 1982\)](#) orbit-based dynamical modelling method consists of constructing a library of stellar orbits with a potential derived from the luminosity distribution assuming constant M/L . The combined orbits can then be projected onto the sky and observable quantities derived. This method was used in an attempt to isolate the orbital information of just the KDC in the E3 elliptical NGC 4365 by modelling data from SAURON ([van den Bosch et al., 2008](#)). The outer parts of NGC

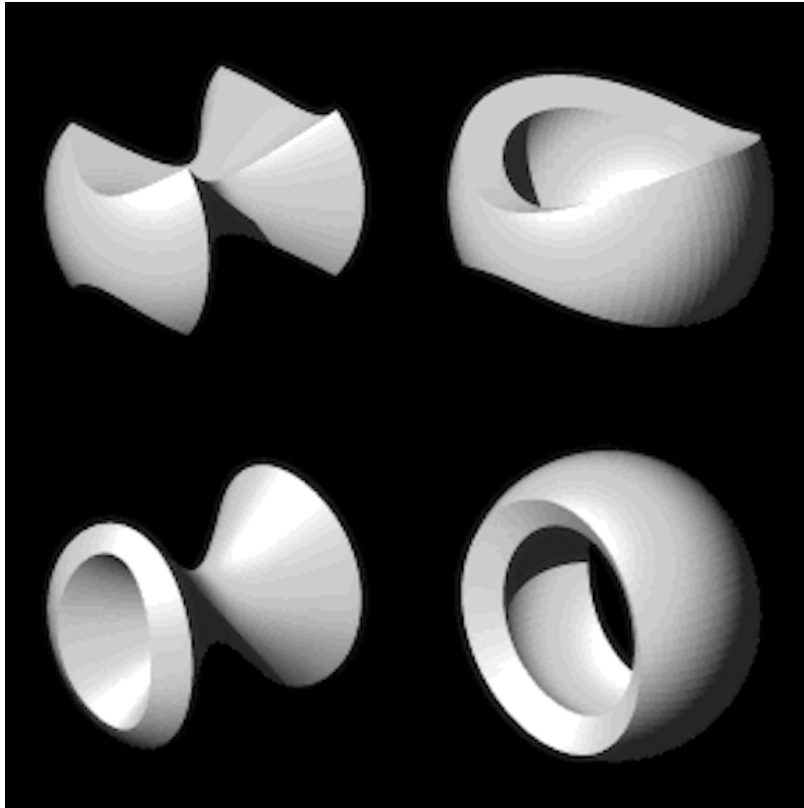


Figure 5.13: Volumes occupied by the four orbital families in a perfect triaxial galaxy (Statler, 1987). The four families are box orbits (top left), short-axis tube (top right), inner long-axis tube (bottom left), and outer long-axis tube (bottom right). Image credit: http://www.phy.ohiou.edu/~astro/dyn_theory.html. See Section 5.3.3.

4365 are rotating around the major axis while the core rotates about the minor axis (Surma & Bender, 1995), i.e. not counter-rotating around the minor axis as with IC 1459, and a constant radial age (Davies et al., 2001). van den Bosch et al. (2008) made the surprising discovery that there was no distinct orbital component in NGC 4365. Instead it was found that the galaxy was well modelled by the superposition of two counter-rotating thick tubes of orbits, each of which had a smooth distribution with radius. The same conclusion was found for NGC 5813 (Krajnović et al., 2015).

In a separable model of a triaxial system (three different length axes) there are four distinct orbital families: i) box orbits, ii) short-axis tube orbits, iii) inner long-axis tube orbits, and iv) outer long-axis tube orbits (e.g., Binney & Tremaine, 1987). The regions occupied by these four orbital families in an idealised triaxial system are shown in Figure 5.13 (Statler, 1987). Statler (1991) showed that KDCs could be observed as projections of major families of circulating orbits in a triaxial potential. A more realistic orbit library used for the accurate modelling of galaxies includes

these four stable major families of orbits, a host of minor orbit families and chaotic orbits (e.g., [van den Bosch et al., 2008](#)).

The results of the best-fitting orbit model for NGC 4365 showed that short-axis tube orbits were dominant within the central $\sim 30''$ (where the core lies within $\sim 6''$), accounting for $\sim 75\%$ of the mass. The long-axis orbits dominated outside $\sim 30''$. To understand the observed kinematics, [van den Bosch et al. \(2008\)](#) then split the orbits into prograde and retrograde orbits (the choice of which is arbitrary) where the KDC was assigned prograde rotation. The models showed that the stars on short-axis prograde and retrograde orbits both showed high rotation speeds in opposite directions and that when combined showed little net rotation. The superposition short-axis orbits showed high dispersion along the major axis due to the blending of their Gaussian distributions with positive and negative velocities. The long-axis orbits showed rapid rotation about the major axis but their rotation was only seen at large radii where they dominated the mass. From similar analysis of NGC 5813, [Krajnović et al. \(2015\)](#) found that within the KDC prograde orbits (direction of the KDC) were slightly faster than the retrograde orbits and accounted for $\sim 70\%$ of the total mass. This proportion became about ~ 50 at the edge of the KDC. At the dispersion peaks, the retrograde component was slightly more dominant. However, the angular momentum was roughly balanced with the prograde component and showed no net rotation.

In summary, from dynamical orbital modelling, KDCs do not seem to be distinct components but the superposition of prograde and retrograde short-axis orbits ([van den Bosch et al., 2008](#); [Krajnović et al., 2015](#)). Where the contributing mass of stars travelling in one direction is equal to that of the opposing rotating group, no net rotation is seen but a large dispersion is measured. At radii where the mass fractions of stars on prograde and retrograde orbits do not balance each other, a net rotation is detected, such as within the radii of the KDCs. The cause of the imbalance of stellar mass on different orbits is not clearly understood and possible formation mechanisms are discussed in Section 5.3.7.

5.3.4 The Profile of the Counter-Rotating Core

A fit to V -band photometry of the core of IC 1459 showed an excess of light at the centre ([Rusli et al., 2013](#)). A younger stellar population formed late that dominated the light of the galaxy in the core would explain this feature. However, old stellar populations are constant throughout the galaxy, so perhaps this excess can instead be attributed to the bright optical emission from ionized gas (see Section 5.3.6). From

2D photometric fits to the galaxy with the core masked and in the NIR (K -band, i.e. similar to that of KMOS and probing the stellar content), [Läsker, Ferrarese & van de Ven \(2014\)](#) found a high Sérsic index of $n = 8.25$ in the outskirts of the galaxy. When fitting the NIR light of the core, they found that it was a ‘core’ galaxy, i.e. it has a depletion of light towards its centre that is best fit by a shallower slope than its outskirts (e.g., [Ferrarese et al., 1994](#); [Lauer et al., 1995](#); [Ferrarese et al., 2006](#)). The core/coreless (those with no light deficit) classes are thought to trace a similar phenomenon as the fast and slow rotators, i.e. an ETG that has been built up from dry mergers (as hypothesised for slow rotators) rather than gas accretion. The core inner profile is typical for massive slow rotator galaxies and is found in almost all of the population (e.g., [Emsellem et al., 2011](#); [Lauer, 2012](#); [Krajnović et al., 2013](#)). The creation of the core galaxies is thought to require binary SMBH interaction in a dissipationless merger to remove some of the stars ([Begelman, Blandford & Rees, 1980](#); [Milosavljević & Merritt, 2001](#)). However, from the discovery of a small number of fast rotators (that form through gas-rich processes) with depleted cores, it could be that there are unexplored formation paths that would explain the removal of central stars in discs like systems and slow rotators ([Krajnović et al., 2013](#)).

5.3.5 Spatially Resolved IMF in IC 1459

Determining the IMF of a galaxy with a KDC could hold answers as to its formation. The results from measuring the stellar populations from the MUSE data imply that the age of the stars does not change with radius. They also indicated that the apparent metallicity gradient is in fact the superposition of a metal-poor population of stars in the outskirts of the galaxy rather than a gradual change in metallicity. Based on these results and those of other studies, there remains no clear understanding of how galaxies with KDCs form. Measuring the contribution of low-mass stars across the different regions of IC 1459 may hold key information about the possible evolutionary path of an ETG that exhibits a KDC. With the KMOS mosaics of data from which I extracted median-stacked NIR spectra at different radii, for the first time I was able to attempt to constrain the spatially resolved IMF for a galaxy with a KDC. The effects of metal abundance variations and the IMF can be difficult to separate (e.g., [McConnell, Lu & Mann, 2016](#); [Zieleniewski et al., 2017](#)), however by measuring the two separately with the optical and NIR data I could break this degeneracy. I found that all three radial bins of IC 1459 favoured a relatively bottom-light Kroupa revised IMF. The Kroupa revised IMF (i.e. the Kroupa Universal with a correction for the treatment of binary stars) is measured from individual stars in the solar

neighbourhood and is thought to be a good description of Milky Way-like massive spiral galaxies. As previously mentioned, this method of determining the IMF (i.e. holding the stellar population parameters measured in the optical fixed and solely varying the IMF in the NIR) is not a standard use of PPXF and does have some limitations. Therefore, this result is viewed as preliminary and will be further tested (see Section 6.2).

A recent study of six slowly-rotating massive ETGs (typically centrals in groups; [van Dokkum et al., 2017](#)) showed bottom-heavy IMFs in the central regions of the galaxies that rapidly become more bottom-light with radius and flatten to a Milky Way-like IMF at $R > 0.4R_e$ (see also [Sarzi et al., 2017](#)). A limiting factor for IC 1459 is the footprint of useable MUSE and KMOS data for analysis shown by the outer boundary of R3 ($R \sim 15''$) in Figure 5.5. The effective radius of IC 1459 is $R_e = 46.2''$ ([Läsker, Ferrarese & van de Ven, 2014](#)), therefore I measured properties out to $\sim \frac{1}{3}R_e$. From the results in [van Dokkum et al. \(2017\)](#), this radius should at least be sufficient to probe some gradient in the IMF if it exists; however, it would not reach the average radius at which they found that the IMF gradient flattens. Several studies have found bottom-heavy IMFs (i.e. with a higher slope than Salpeter) for the centres of massive ETGs and radial gradients (e.g., [van Dokkum & Conroy, 2010, 2011](#); [Conroy & van Dokkum, 2012b](#); [La Barbera et al., 2016](#); [Sarzi et al., 2017](#); [van Dokkum et al., 2017](#)) while others do not (e.g., [McConnell, Lu & Mann, 2016](#); [Alton, Smith & Lucey, 2017](#)).

Both the bottom-light Milky Way-like nature of the IMF and the lack of an IMF gradient found for IC 1459 are surprising in light of the majority of findings in the literature. The results could indicate that the formation of IC 1459 differs from these other massive slow-rotator ETGs in that it may not have been through the classic two-phases of evolution (e.g., [Oser et al., 2010](#)). The radially constant Milky Way-like IMF may suggest that this galaxy has been built up entirely of massive spirals. This may be a possible explanation for the strength of the counter-rotation seen in the KDC and would help to explain the Kroupa revised IMF measured for IC 1459. Possible formation mechanisms are discussed in Section 5.3.7. This work will be developed further as discussed as part of my future research (Section 6.2).

5.3.6 The AGN and Gas Content

IC 1459 is known to host an AGN; exhibiting strong radio core emission arising from a parsec-scale source and symmetrical jets (e.g., [Ekers et al., 1989](#); [Slee et al., 1994](#); [Verdoes Kleijn et al., 2000](#); [Tingay & Edwards, 2015](#)). It is classified as a

low-ionization nuclear emission-line region (LINER) galaxy as identified by strong emission lines from ionized gas (Phillips et al., 1986b,a). This radio loud AGN is surrounded by a nucleus of hot dense interstellar medium (ISM), and from weak X-ray emission was found to be accreting well below the Eddington limit (Fabbiano et al., 2003). The X-ray emission seen at the centre of IC 1459 was found to be jet dominated (Yuan, Yu & Ho, 2009). It could be that the present-day AGN plays a role in regulating star formation in this gas-rich ETG (Vaddi et al., 2016; Terrazas et al., 2017). Results have shown that there is substantial flow of gas in and out of the galaxies in the IC 1459 group and $\sim 10\%$ of the group gas mass is found outside the galaxies Serra et al. (2015). This provides a source of fuel for the AGN. Within the IC 1459 galaxy there is known to be neutral HI (Serra & Oosterloo, 2010) and molecular gas (Prandoni et al., 2012), and dust (Malin, 1985; Sparks et al., 1985; van Dokkum & Franx, 1995). The dust is shown not to map regularly onto the stellar component of the galaxy (Amblard et al., 2017).

IC 1459 exhibits strong emission from ionized gas within its core as shown by the Balmer and forbidden emission lines in the optical MUSE spectra (Figure 5.9). The central ionized gas is known to rotate in the opposite direction to the stellar KDC and thus in the same direction as the outer envelope of the galaxy (e.g., Franx & Illingworth, 1988; Forbes, Reitzel & Williger, 1995). The MUSE spectra from all three radial regions of IC 1459 exhibited emission and these lines were fitted as separate kinematic components when deriving stellar population parameters. Given the old stellar age of the core and the counter rotation of the gas to the stars, it is likely that the two components do not have a common origin. An AGN (Condon et al., 1998; Krajnović & Jaffe, 2002) and similar dust (Carollo et al., 1997b; Tran et al., 2001) and emission features are seen in the old stellar age KDC host galaxy NGC 5813 (Krajnović et al., 2015). Analysis of emission-line strength maps and kinematics using the MUSE data led the authors to a similar conclusion, that the gas was not of the same origin as the KDC. Future work investigating the properties of the ionized gas using the emission lines in the MUSE cube will be discussed in Section 6.2.

5.3.7 Possible Formation Mechanisms of IC 1459

The high velocity dispersion measurement along the major axis in the high-S/N MUSE data of the KDC galaxy NGC 5813 (Krajnović et al., 2015) showed two peaks in the dispersion maps symmetrically separated to the core. I measured this increase in major axis dispersion for IC 1459, as did van den Bosch et al. (2008) for NGC 4365.

However, if dispersion peaks similar to NGC 5813 existed in these galaxies, they are not possible to resolve with either data set. Based on the unusual kinematics of NGC 5813, (Krajnović et al., 2015) argued for the similarity with the much less massive ($< 5 \times 10^{10} M_{\odot}$; Cappellari et al., 2013a), fast-rotating 2σ galaxies whose kinematics display similar symmetrically offset dispersion peaks (Krajnović et al., 2011). 2σ galaxies are the superposition of two thin discs as verified by studying the stellar populations (Cocato et al., 2011, 2013; Johnston et al., 2013) and from modelling (Cappellari et al., 2007). They are thought to form from the accretion of gas onto a disc but with opposite angular momentum. This could occur through an interacting pair of galaxies (Vergani et al., 2007; Cocato et al., 2011) or two cold streams that supply gas to the galaxy and exert torques to produce counter-rotating discs (Algorry et al., 2014). These galaxies are clearly not the same as the very massive slow-rotator ETGs that host KDCs that are unlikely to have thin discs (Krajnović et al., 2015) and show no radial age gradient (e.g., Franx & Illingworth, 1988; Bender, Doebereiner & Moellenhoff, 1988; Rix et al., 1992; Davies et al., 2001; McDermid et al., 2006; Kuntschner et al., 2010; McDermid et al., 2015; Krajnović et al., 2015). However, the 2σ galaxies could help to provide some clues as to the formation of KDCs.

IC 1459 is a convincing case for a galaxy that has undergone at least one gas-rich major merger. It has a high gas content and shows both dust features (Sparks et al., 1985) and ionised gas emission (Phillips et al., 1986b; Franx & Illingworth, 1988) in its core. A deep image of IC 1459 (Figure 1.8) revealed tidal features in the galaxy (Malin, 1985), while Forbes, Reitzel & Williger (1995) found shell-like remnants. The long tidal tails, high gas content and shells are indicative of two merging spirals (e.g., Toomre & Toomre, 1972; Toomre, 1977; Malin & Carter, 1980). Saponara et al. (2018) found large HI clouds near IC 1459, concluding these were likely to be debris from tidal interactions with neighbouring galaxies. Being the central galaxy in a relatively small group would mean a high probability of mergers due to the low dispersion of the group (Ostriker, 1980; Tremaine, 1981). Comparing dynamical models derived from long-slit spectra of IC 1459 to simulations (Bendo & Barnes, 2000) revealed the outer parts of the galaxy were well matched to a merger of disc galaxies with a 3:1 mass ratio (Samurović & Danziger, 2005). The asymmetry in the dispersion map towards the outskirts of IC 1459 may be a sign of tidal interactions or even a major merger. The bottom-light Milky Way-like IMF of IC 1459 also supports this scenario.

Arguments against IC 1459 being made up entirely of merged spirals include the fact that ETGs tend to be more compact than spirals and merger remnants are generally less compact, and generally velocity dispersions are higher and scale

lengths are longer in ETGs than discs (Ostriker, 1980). IC 1459 has a high Sérsic index ($n \sim 8.25$ when masking the core; Läsker, Ferrarese & van de Ven, 2014) which is indicative of intermediate to minor mergers (with mass ratios 1:5 to 1:10; Hilz, Naab & Ostriker, 2013). This is in contrast to the otherwise similar KDC system NGC 5813 that has an exponential disc-like profile at large radii that conflicts with this merger scenario (Krajnović et al., 2015). The photometric profile of IC 1459 adds weight to its formation via a two-phase evolutionary path (e.g., Oser et al., 2010) that has undergone the accretion by smaller gas-poor satellites at later stages of formation (e.g., Naab et al., 2007; Naab, Johansson & Ostriker, 2009; Hopkins et al., 2009). The presence of a metal-poor population detected in the outer regions of the galaxy also adds weight to this view of the history of IC 1459. Also, it is thought that X-ray emission would still be visible from the first rapid phase of evolution in the centres of local massive ETGs (e.g., Bender et al., 1989). X-rays are detected in IC 1459; however, these are found to be dominated by the AGN jets (Yuan, Yu & Ho, 2009). There may be residual extended X-ray emission from an initial collapse and starburst phase of a progenitor, however, it would be difficult to separate the contributions to the X-ray emission seen today.

There could well be numerous possible formation processes as is suggested by the wide range of stellar populations (Bender & Surma, 1992; Carollo et al., 1997b; Kuntschner et al., 2010) and kinematic properties (Krajnović et al., 2008; Krajnović et al., 2011) for galaxies with KDCs. What are the possible mechanisms that could lead to the imbalance of stellar mass in the prograde and retrograde orbits that would result in a radially constant age? The possible mechanisms would have to include either an early assembly or a late assembly of systems with similarly aged populations (e.g., Davies et al., 2001; Kuntschner et al., 2010). The results contradict a scenario of a late accretion of a compact merger remnant (Kormendy, 1984; Franx & Illingworth, 1988). The orbital modelling also contradicts a classical definition of the two-phase evolution of a compact high-redshift ETG that builds up its mass via a series of dry mergers (e.g., Naab, Johansson & Ostriker, 2009; Hopkins et al., 2009; Oser et al., 2010). Some possible formation scenarios discussed in Krajnović et al. (2015) are summarised below.

1. The accretion of gas from a gas-rich companion in a similar formation mechanism to a 2σ galaxy. The lack of evidence for thin discs somewhat contradicts this model. Additional mechanisms of disc disturbance and dynamical heating (potentially via interactions within the group environment) are required to explain the formation of counter-rotating tube orbits.

2. The major merger (with mass ratio 1:1) of gas-rich spirals or a spiral and ETG (e.g. [Bender & Surma, 1992](#); [Surma & Bender, 1995](#)). Simulations have shown that gas-rich binary mergers can result in KDCs ([Hoffman et al., 2010](#); [Bois et al., 2011](#); [Moody et al., 2014](#)). Subsequent mergers may then lead to the destruction ([Bois et al., 2011](#)) or even enhancement of the observed KDC ([Moody et al., 2014](#)). Simulations have shown that a progenitor spinning retrograde to the merger could create a KDC with 2σ -like dynamics ([Bois et al., 2011](#)). Other simulations have shown that even prograde rotation relative to the merger can result in a KDC due to strong reactive forces creating counter rotation prior to coalescence ([Tsatsi et al., 2015](#)).

3. Massive galaxies that form in the early Universe towards the centres of group dark matter haloes are thought to form at the intersection of cold streams ([Kereš et al., 2005, 2009](#); [Dekel et al., 2009](#)). If there is sufficient time delay between the arrival of the streams (to avoid collision), two counter-rotating components could potentially form. As there is no age difference measured radially in KDCs, the feeding of the streams would have to be short, happen early, and occur within a few Gyrs of each other. In this scenario it would be difficult to distinguish between the counter-rotating stellar populations if they were formed at epochs separated by $\sim 2-3$ Gyrs around 12 Gyrs ago. Rapid accretion of cold gas streams causes strong turbulence leading to clumpy galaxies (e.g., [Dekel, Sari & Ceverino, 2009](#)). These very turbulent discs could then feasibly form the basis of the thick tube-like prograde and retrograde orbits.

These formation scenarios are all very gas rich which make explaining the depleted stellar core profile of IC 1459 (and NGC 5813) hard to explain. There is required to be some removal of the stars from the centre rather than a build-up of core stellar mass through a gas rich formation path. Also interesting is that this core like profile is very similar to that of massive slow-rotator ETGs that have gone through a two-phase evolutionary path (e.g., [Oser et al., 2010](#)). Despite the use of new data, instruments, broader wavelength coverage and new techniques to study the KDC in IC 1459, the results highlight that more research is required to understand the formation mechanisms of these interesting galaxies and that it may have major consequences for our understanding of massive ETG formation. The current explanations of possible KDC formation from observations and theory fail to come up with a clear and comprehensive evolutionary picture for this class of galaxy.

5.4 Conclusions

In Part II of this thesis, I performed analysis on IC 1459, a massive local E3 ETG with a rapidly counter-rotating core. This galaxy is part of the more general class of massive slow-rotator galaxies that have KDCs. I coupled IFU data in the optical from MUSE with KMOS data in the NIR to study the spatially resolved kinematics, stellar populations and IMF in order to understand its evolution. The key findings of this work are summarised below.

1. The distinctive counter-rotating core of IC 1459 can be seen in the optical MUSE stellar kinematic maps. It has a radius of $\sim 5''$ and peak rotation of $\sim 125 \pm 35 \text{ km s}^{-1}$ measured from the $S/N = 20$ Voronoi-binned data. Although consistent within errors of previous estimates (Franx & Illingworth, 1988), the lower rotational velocity measured here is likely to be due to the binning.
2. The velocity dispersion maps show that the galaxy is dynamically hot along the major axis, as found for other IFU studies of KDCs (van den Bosch et al., 2008; Krajnović et al., 2015). However, unlike other studies I see a hint of asymmetry in the velocity dispersion map which may be the result of a major merger or tidal interaction as evidenced by other observational features of the galaxy.
3. From the stellar populations, I measured a radially constant mass-weighted age of ~ 12 Gyrs for IC 1459. The lack of an age gradient across the galaxy is consistent with other studies of KDCs. This adds weight to the theory found through orbital modelling that the KDC is not an orbitally distinct feature of a galaxy but is in fact the superposition of two co-spatial permeating prograde and retrograde populations of stars on short-axis tube orbits. Each of the populations varies smoothly with radius and the kinematic signatures in the galaxy are apparent when the mass ratio of the prograde and retrograde populations is unbalanced.
4. I found a metallicity gradient in this galaxy, as also found in other galaxies with KDCs. However, for the first time I have been able to identify that the metallicity gradient may actually be being driven by an extremely metal-poor population present in the outer parts of the galaxy rather than by a gradual change in metallicity. This result could indicate that there is a metal-poor retrograde population of stars that dominates in mass fraction at radii $> 10''$ where the counter-rotation is seen.

5. Holding the stellar population parameters measured in the optical fixed, I measured the radial variation of the IMF in IC 1459 using the NIR data; the first time this has been done for a galaxy with a KDC. For all three radial bins, I found a bottom-light Milky Way-like IMF. This preliminary result requires further investigation but appears to contradict many studies of the IMF in massive ETGs. If confirmed, it could add weight to the formation mechanism of purely merging spirals for this galaxy. As IC 1459 deviates in other ways from massive ETGs thought to have undergone a classical two-phase evolution (e.g., [Oser et al., 2010](#)), this may be a viable formation scenario for this galaxy and its KDC.

The observational evidence for this galaxy in the context of the literature does not point to one clear solution to explain its observed strongly counter-rotating core. It is clear that more studies of similar systems would help to build a more complete picture of the formation of KDCs. Particularly, I highlight that efforts to measure the radial variations in the IMF could prove interesting for this subset of massive slow rotators. Combining the broad wavelength coverage of MUSE and KMOS with their large FOV (with KMOS in Mosaic Mode) provides valuable tools to answer some of these questions. With deeper observations (even by a factor of two) of local galaxies with MUSE and KMOS a clearer picture of KDC formation will emerge.

Chapter 6

Conclusions

In this thesis, I have studied the evolution of ETGs from different aspects and via different approaches. I looked at both the high-redshift Universe and locally, and from ETGs in a massive cluster environment to a central galaxy in a local group to understand their evolution. Utilising KMOS, the NIR multi-IFU, I was able to probe the rest frame optical at $z \sim 2$ and the NIR locally to understand different physical processes occurring in the galaxies. Using the large FOVs of KMOS in the under-utilised Mosaic Mode and the large optical IFU MUSE, I was able to study the spatially resolved properties of a massive local galaxy over a large wavelength range. The diversity of methods, approaches, wavelengths, instruments, environments, and redshifts have enabled me to build up a comprehensive picture of the evolution of ETGs. This thesis highlights the importance of diverse approaches and maintaining a broad perspective when studying galaxies in order to further our understanding of how they evolve. The work presented in this thesis goes towards filling some gaps in our understanding of how ETGs evolve but equally it raises some interesting questions that remain to be answered. I summarise the research and key results of this thesis in Section 6.1. I then discuss some interesting avenues of future work in Section 6.2 in which to further the analysis presented in this thesis.

6.1 Summary of this Thesis

Part I of the thesis detailed my work on the massive high-redshift ($z \simeq 1.80$) ETG-rich cluster JKCS 041. In Part II, I looked to the local Universe and to the fossil record of a massive ETG with a rapidly counter-rotating core, IC 1459, to understand its evolutionary path. The main results of the thesis are summarised below.

6.1.1 Part I – The KMOS Cluster Survey: Fundamental Plane of Cluster Galaxies at $z \simeq 1.80$ in JKCS 041

From the local distribution of galaxies, it is clear that the cluster environment plays a key role in the formation of ETGs. It is therefore important to probe high-redshift galaxy clusters to study the processes at play in the early Universe that change the fate of their member galaxies. Utilising the multiplexed nature of the NIR IFU instrument KMOS to perform efficient observations of cluster galaxies meant that I was able to build up a more complete picture of how massive ETGs in dense environments evolve at this redshift. As part of the KMOS Cluster Survey, 16 galaxies in JKCS 041 were observed with KMOS. Through long exposures, the stellar continua of galaxies in this distant cluster were probed in order to measure rest-frame optical stellar-absorption features in the quiescent galaxies. No previous survey had systematically targeted galaxies in clusters out to these distances and depths. KCS pushed the boundaries of what is possible using current facilities to study distant ETGs. From the KMOS spectra of the 16 observed galaxies, I determined stellar velocity dispersions for seven galaxies. This expands the sample of like measurements in the literature by $> 40\%$ and is the largest sample of dispersions for galaxies within a single cluster at this redshift. I analysed HST photometry to measure the structural properties of the galaxies. Using this unique sample of spectra and the HST data, I was able to construct a fundamental plane. This was the highest-redshift FP constructed for a single cluster and allowed me to determine mean ages of the quiescent galaxies in JKCS 041. The mean age for all the galaxies in JKCS 041 indicated a more rapid evolution in more massive and virialised cluster environments, supporting other results from KCS.

I discovered that the cluster consisted of two groups; one larger, more relaxed and older population that is likely to represent the cluster core. I then found a population of galaxies with higher relative velocities that is likely to be an infalling group of galaxies towards the south west (i.e. ‘SWG’). The SWG of galaxies contained a higher proportion of SF galaxies. From the FP, I deduced that ETGs in this infalling group were significantly younger than those in the rest of the cluster. This result links the ages of galaxies to large-scale structure of the cosmic web for the first time at this redshift. I noticed that the very young infalling quiescent galaxies were extremely compact and massive galaxies (i.e. red nuggets). These dense galaxies that are significantly more common at high redshift. The young mean age derived for these infalling galaxies was consistent with the formation of red nuggets from a dusty turbulent disk that becomes unstable, compacts, and sparks a period of extremely

rapid star formation that causes the galaxy to quench. The finding could indicate that the group falling into the large potential well of the cluster provides the ideal environment to destabilise a dusty turbulent disc (e.g. via merging, tidal interaction or rapid gas accretion).

This comprehensive view of a high-redshift cluster from ages and kinematics has revealed that the group environment at the edge of a massive cluster could play a vital role in sparking the formation of red nuggets. These red nuggets are then thought to produce the bottom-heavy IMF galaxies that form the seeds of the most massive ETGs. These massive galaxies often reside in the centres of massive galaxy clusters or groups in the local Universe. In this unique investigation, I have explored the interplay of the quiescent and SF galaxies in a massive cluster in the early Universe. Utilising both kinematic and age results, I have built up a comprehensive and complex picture of early cluster evolution. I have linked the infalling group environment to very young ages and suggest that this may be a key mechanism for facilitating the first stage in a two-phase build-up of massive slow-rotator ETGs that are found at the centres of low-redshift clusters. This investigation of JKCS 041 is the most detailed study of a high-redshift cluster performed to date. It has provided valuable insights into both high-redshift galaxy evolution and the formation of the most massive galaxies and clusters in the Universe.

6.1.2 Part II – Unravelling the Origin of the Counter-Rotating Core in IC 1459 with KMOS and MUSE

From large IFU surveys of local ETGs, it was revealed that the relatively photometrically regular morphology ellipticals harboured a wealth of interesting kinematics. These studies revealed our ignorance of how this diverse range of kinematic systems could have formed. The rarer massive slowly rotating ellipticals can exhibit interesting kinematic features. One of the most striking characteristics is galaxies with KDCs and many mysteries surround their nature and formation. In Part II of this thesis, I performed analysis on the local massive central ETG, IC 1459, in a gas-rich group dominated by spiral galaxies. This E3 elliptical galaxy exhibits a rapidly counter-rotating core and belongs to the KDC class. Using KMOS in the little utilised Mosaic Mode, I was able to observe a large region of the galaxy using the NIR IFUs. I then coupled the KMOS mosaic data with a large FOV mosaic of optical data from MUSE. The spatial coverage combined with the wide wavelength range of MUSE and KMOS makes them ideal companion instruments for studying large local galaxies.

This is the first study to use the two instruments in this way. The coverage of the instruments along all axes allowed me to investigate the kinematics, stellar populations, and for the first time for a KDC, the spatially resolved IMF.

Measuring the stellar kinematics, the strongly counter-rotating core and weakly rotating outer parts of the galaxy were mapped with KMOS and MUSE. From the contiguous MUSE data, I measured a high velocity dispersion along the major axis. This high major-axis dispersion was similar to the two dispersion peaks found for another KDC with higher-S/N MUSE data. Interestingly, I found that the dispersion maps showed some asymmetry that had not been seen before in other KDC host galaxies. Measuring the stellar populations of the optical MUSE data, I found a radially constant age of ~ 12 Gyrs as also observed for many other galaxies with KDCs. This homogeneity in the ages of the stars with radius supports the results found from orbital modelling of galaxies that the KDCs in galaxies are not orbitally distinct components. Results from dynamical modelling suggest that a KDC can arise from the superposition of co-spatial and permeating prograde and retrograde populations of stars on thick orbits in a triaxial system. The models show that the strong velocity gradients arise when there is an imbalance in the mass fraction of stars on prograde and retrograde orbits. Where the mass fractions are balanced, no net velocity is observed. The prograde and retrograde populations are smoothly radially varying populations and hence show little radial variation in their stellar age. The high dispersion along the major axis is explained by the blending of the velocity distributions of the opposing direction tube orbits in these models.

I found a metallicity gradient in the galaxy going from metal rich in the centre to metal poor in the outskirts which is also supported by many studies. Interestingly however, utilising a regularization method when fitting templates to the spectra, I was able to see that this metallicity gradient did not arise from a smooth variation in the stellar populations. What I discovered was that this gradient was actually driven by an extremely metal-poor population in the outskirts of the galaxy that was onto the metal-rich population found throughout the galaxy. This feature is the first time this has been confirmed for a KDC galaxy and could hold valuable information about the formation mechanisms of these types of galaxies.

Holding the derived stellar population parameters fixed, I then fitted the IMF sensitive features in the NIR with different IMF templates. I found that the spectra in three radial bins across the surface of the galaxy were best fitted by a bottom-light Kroupa revised IMF. Both the Milky Way-like IMF and its lack of radial gradient is a surprising result when comparing these results to those in the literature. This

method of IMF measurement does have some limitations and will be tested further as part of my proposed future work (Section 6.2). If this result does hold it shows that galaxies with KDCs may have had very different evolutionary paths compared to other slow rotators.

Although the KDC may not be an orbitally distinct component, it is still not understood what mechanisms would cause the imbalance of mass fractions of stars on different orbits whilst also maintaining a radially constant age. Current theories rely heavily on the accretion of gas to explain the counter rotation. There is strong observational evidence that IC 1459 has had at least one gas-rich merger which has been hypothesised as a possible formation scenario of a KDC. The asymmetry in the dispersion map could indicate evidence of a past major merger or tidal interaction. The relatively bottom-light IMF with no radial change could also support this theory of formation. However, the core profile of IC 1459, high Sérsic index outskirts, and potentially distinct low-metal population in its outer rotating envelope favour the more standard two-phase method of growth expected for these massive slow rotator ETGs. Clearly more work has to be done to understand the evolution of this class of massive ETG, and this study shows that radial IMF measurements may be able to unlock some interesting information regarding their evolution. I have shown that MUSE and KMOS are ideally suited to this task and to the study of massive local ETGs in general.

6.2 Future Work

6.2.1 Full-Spectral Fitting of Individual Galaxies in JKCS 041

The quality and size of the data obtained for the cluster galaxies in JKCS 041 enables further investigation into their properties beyond the FP age analysis. The wavelength range of the data spans the so-called ‘blue indices’ (e.g., [Thomas, Maraston & Bender, 2003](#); [Thomas, Maraston & Korn, 2004](#); [Jørgensen et al., 2005](#); [Sánchez-Blázquez et al., 2009](#)). Only recently have spectral libraries allowing the variation of $[M/H]$, ages, and $[\alpha/Fe]$ in order to predict SSPs been made available in this spectral range (e.g. [Vazdekis et al., 2015, 2016](#)). At least for some of the brightest galaxies in the sample, age, metallicity and α -element abundance ratios could be determined from full-spectral fitting. Typically, this has only been achieved for the BCGs or stacks of galaxies at this redshift. The data set therefore provides the potential to derive stellar population parameters for individual galaxies (beyond the BCG) for the first time at this redshift. This will be a valuable study to shed light on the SFHs, metallicities and

ages of the individual galaxies. The work will build upon the interesting picture of the formation of this cluster that has been revealed so far by the work presented in this thesis.

6.2.2 A Different Approach to Full-Spectral Fitting of IC 1459

Constraining the IMF from spectra can be done by measuring line strengths or by full-spectral fitting. Recent studies have moved toward the full-spectral fitting method so as to maximise the available data in the spectrum. The method is useful for breaking degeneracies between stellar population parameters (i.e., age and metallicity) and the IMF by simultaneously fitting them. A common approach and one that is becoming the gold standard for studies of the IMF is to fit the spectra using a Monte Carlo Markov Chain (MCMC) algorithm to explore the parameter space of a large number of variables. The large spectral range spanned by the median stacked MUSE and KMOS spectra means that I am able to break the degeneracies of stellar population parameters and the IMF as the spectral range spans valuable indices that are sensitive to each. Therefore, to test the method presented in this thesis and further investigate the IMF of IC 1459, I plan to use full-spectral fitting with an MCMC implementation. This will provide a useful comparison to results in the literature that are derived in a similar way. It will also be valuable for understanding the possible evolutionary path of IC 1459, which as concluded in this work, remains unclear.

6.2.3 Emission-Line Analysis of IC 1459

The bright emission lines in IC 1459 will be the focus of a future study. The prominent emission from ionized gas in IC 1459 could be of relevance to past merger activity and of importance to studying the AGN at the centre of the galaxy. The MUSE spectra exhibit bright Balmer and forbidden emission that can be used to study the spatial distribution and kinematics of the ionized gas. Adopting similar techniques to those used to analyse the high-S/N MUSE data of another KDC ([Krajinović et al., 2015](#)), I can create narrow band ‘images’ from the MUSE data by summing the flux around different emission features. Also, from spectral fitting different kinematic features in the spectrum, I can measure kinematics of the gas to understand its origin, morphology and any link to the AGN activity or SF in the galaxy. Although not likely to be critical to the formation of the old stellar KDC, the study of the ionized gas will be a complementary study to the work presented in this thesis.

6.2.4 Future Facilities

As demonstrated in this thesis, efforts to correct for sky contamination can be challenging and if done poorly can limit analysis from ground-based facilities. The ideal solution to avoid contamination from the Earth’s atmosphere is to take observations from space. The costs of this are understandably significantly greater than telescopes of the same size on the ground, however the gains in the data quality are vast. This will be the strength of the new space-based NIR multi-instrument facility: the James Webb Space Telescope (JWST; [Gardner et al., 2006](#)). JWST will provide a number of instruments to study galaxies at NIR wavelengths free from sky contamination. JWST will include the first multi-object spectrograph and NIR IFU in space. Studies similar to those performed for JKCS 041 will be possible to much greater quality and for larger samples of galaxies extending to lower masses at $z \sim 2$. It will therefore provide an extremely valuable resource for study galaxy evolution in clusters at high-redshift. In the lower-redshift Universe, constraining the IMF using dwarf-sensitive features should be possible for massive galaxies out to $z \sim 0.5$. Clean and vastly more detailed spatially resolved measurements of ETGs will be possible for local galaxies. It will therefore be a valuable tool for understanding the nature of the IMF in galaxies across the age of the Universe.

Future facilities will implement adaptive optics systems, that provide real time monitoring and corrections for atmospheric turbulence, for improving ground-based NIR observations; e.g. the Extremely Large Telescope and the Thirty Meter Telescope. With this new class of massive telescope, the IFU galaxy surveys performed locally will be possible to around $z \sim 2$, i.e. for a cluster like JKCS 041. This will greatly expand our understanding of these key early and transformative stages in an ETG’s life. There are certainly many exciting facilities on the horizon that provide the opportunity to keep asking questions about the formation and evolution of galaxies in our Universe. I will end this thesis as it began, with a quote from the late and great Vera Rubin — *“No observational problem will not be solved by more data.”*

Bibliography

- Abel T., Bryan G. L., Norman M. L., 2002, *Science*, 295, 93
- Algorry D. G., Navarro J. F., Abadi M. G., Sales L. V., Steinmetz M., Piontek F., 2014, *MNRAS*, 437, 3596
- Alton P. D., Smith R. J., Lucey J. R., 2017, *MNRAS*, 468, 1594
- Amblard A., Temi P., Gaspari M., Brighenti F., 2017, *ApJ*, 834, 20
- Andreon S., Maughan B., Trinchieri G., Kurk J., 2009, *A&A*, 507, 147
- Andreon S., Newman A. B., Trinchieri G., Raichoor A., Ellis R. S., Treu T., 2014, *A&A*, 565, A120
- Auger M. W., Treu T., Bolton A. S., Gavazzi R., Koopmans L. V. E., Marshall P. J., Moustakas L. A., Burles S., 2010a, *ApJ*, 724, 511
- Auger M. W., Treu T., Gavazzi R., Bolton A. S., Koopmans L. V. E., Marshall P. J., 2010b, *ApJL*, 721, L163
- Bacon R. et al., 2010, in *SPIE*, Vol. 7735, Ground-based and Airborne Instrumentation for Astronomy III, p. 773508
- Bacon R. et al., 2001, *MNRAS*, 326, 23
- Barden M., Häußler B., Peng C. Y., McIntosh D. H., Guo Y., 2012, *MNRAS*, 422, 449
- Barger A. J., Aragon-Salamanca A., Ellis R. S., Couch W. J., Smail I., Sharples R. M., 1996, *MNRAS*, 279, 1
- Barnes J. E., Hernquist L. E., 1991, *ApJL*, 370, L65
- Barro G. et al., 2016, *ApJ*, 820, 120

Barro G. et al., 2013, ApJ, 765, 104

Barro G. et al., 2014, ApJ, 791, 52

Bastian N., Covey K. R., Meyer M. R., 2010, ARA&A, 48, 339

Bauer A. E., Grützbauch R., Jørgensen I., Varela J., Bergmann M., 2011, MNRAS, 411, 2009

Begelman M. C., Blandford R. D., Rees M. J., 1980, Nature, 287, 307

Beifiori A., Maraston C., Thomas D., Johansson J., 2011, A&A, 531, A109

Beifiori A. et al., 2017, ApJ, 846, 120

Beifiori A. et al., 2014, ApJ, 789, 92

Bell E. F. et al., 2004, ApJ, 608, 752

Belli S., Newman A. B., Ellis R. S., 2017, ApJ, 834, 18

Belli S., Newman A. B., Ellis R. S., Konidaris N. P., 2014, ApJL, 788, L29

Bender R., Burstein D., Faber S. M., 1992, ApJ, 399, 462

Bender R., Doebereiner S., Moellenhoff C., 1988, A&AS, 74, 385

Bender R., Saglia R. P., Gerhard O. E., 1994, MNRAS, 269, 785

Bender R., Saglia R. P., Ziegler B., Belloni P., Greggio L., Hopp U., Bruzual G., 1998, ApJ, 493, 529

Bender R., Surma P., 1992, A&A, 258, 250

Bender R., Surma P., Doebereiner S., Moellenhoff C., Madejsky R., 1989, A&A, 217, 35

Bendo G. J., Barnes J. E., 2000, MNRAS, 316, 315

Bernardi M., Meert A., Vikram V., Huertas-Company M., Mei S., Shankar F., Sheth R. K., 2014, MNRAS, 443, 874

Berry D., Currie M., Jenness T., Draper P., Bell G., Tilanus R., 2013, in Astronomical Society of the Pacific Conference Series, Vol. 475, Astronomical Data Analysis Software and Systems XXII, Friedel D. N., ed., p. 247

- Bertin E., Arnouts S., 1996, *A&AS*, 117, 393
- Bertin E., Mellier Y., Radovich M., Missonnier G., Didelon P., Morin B., 2002, in *Astronomical Society of the Pacific Conference Series*, Vol. 281, *Astronomical Data Analysis Software and Systems XI*, Bohlender D. A., Durand D., Handley T. H., eds., p. 228
- Bertin G., Ciotti L., Del Principe M., 2002, *A&A*, 386, 149
- Bertola F., Buson L. M., Zeilinger W. W., 1988, *Nature*, 335, 705
- Bessell M. S., 1990, *PASP*, 102, 1181
- Bezanson R., Franx M., van Dokkum P. G., 2015, *ApJ*, 799, 148
- Bezanson R., van Dokkum P. G., Tal T., Marchesini D., Kriek M., Franx M., Coppi P., 2009, *ApJ*, 697, 1290
- Bezanson R., van Dokkum P. G., van de Sande J., Franx M., Leja J., Kriek M., 2013, *ApJL*, 779, L21
- Bielby R. et al., 2012, *A&A*, 545, A23
- Binney J., Merrifield M., 1998, *Galactic Astronomy*
- Binney J., Tremaine S., 1987, *Galactic Dynamics*
- Birnboim Y., Dekel A., 2003, *MNRAS*, 345, 349
- Bleem L. E. et al., 2015, *ApJS*, 216, 27
- Boch T., Fernique P., 2014, in *Astronomical Society of the Pacific Conference Series*, Vol. 485, *Astronomical Data Analysis Software and Systems XXIII*, Manset N., Forshay P., eds., p. 277
- Bois M. et al., 2011, *MNRAS*, 416, 1654
- Bolton A. S., Burles S., Treu T., Koopmans L. V. E., Moustakas L. A., 2007, *ApJL*, 665, L105
- Bond H. E., 1981, *ApJ*, 248, 606
- Bonnarel F. et al., 2000, *A&AS*, 143, 33

Borucki W. J. et al., 2010, *Science*, 327, 977

Boselli A., Gavazzi G., 2006, *PASP*, 118, 517

Brammer G. B., van Dokkum P. G., Coppi P., 2008, *ApJ*, 686, 1503

Brammer G. B. et al., 2012, *ApJS*, 200, 13

Bruzual G., Charlot S., 2003, *MNRAS*, 344, 1000

Buitrago F., Trujillo I., Conselice C. J., Bouwens R. J., Dickinson M., Yan H., 2008, *ApJL*, 687, L61

Burke C., Collins C. A., 2013, *MNRAS*, 434, 2856

Burkert A. et al., 2010, *ApJ*, 725, 2324

Burstein D., Bender R., Faber S., Nolthenius R., 1997, *AJ*, 114, 1365

Butcher H., Oemler, Jr. A., 1978, *ApJ*, 219, 18

Caon N., Capaccioli M., D'Onofrio M., 1993, *MNRAS*, 265, 1013

Cappellari M., 2016, *ARA&A*, 54, 597

Cappellari M., 2017, *MNRAS*, 466, 798

Cappellari M. et al., 2006, *MNRAS*, 366, 1126

Cappellari M., Copin Y., 2003, *MNRAS*, 342, 345

Cappellari M. et al., 2009, *ApJL*, 704, L34

Cappellari M., Emsellem E., 2004, *PASP*, 116, 138

Cappellari M. et al., 2007, *MNRAS*, 379, 418

Cappellari M. et al., 2011a, *MNRAS*, 413, 813

Cappellari M. et al., 2011b, *MNRAS*, 416, 1680

Cappellari M. et al., 2012, *Nature*, 484, 485

Cappellari M. et al., 2013b, *MNRAS*, 432, 1862

Cappellari M. et al., 2013a, *MNRAS*, 432, 1709

Cappellari M., Verolme E. K., van der Marel R. P., Verdoes Kleijn G. A., Illingworth G. D., Franx M., Carollo C. M., de Zeeuw P. T., 2002, *ApJ*, 578, 787

Carlberg R. G., 1984, *ApJ*, 286, 403

Carlberg R. G., Yee H. K. C., Ellingson E., Abraham R., Gravel P., Morris S., Pritchet C. J., 1996, *ApJ*, 462, 32

Carollo C. M. et al., 2013, *ApJ*, 776, 71

Carollo C. M., Danziger I. J., 1994, *MNRAS*, 270, 523

Carollo C. M., Danziger I. J., Buson L., 1993, *MNRAS*, 265, 553

Carollo C. M., Danziger I. J., Rich R. M., Chen X., 1997a, *ApJ*, 491, 545

Carollo C. M., Franx M., Illingworth G. D., Forbes D. A., 1997b, *ApJ*, 481, 710

Casertano S. et al., 2000, *AJ*, 120, 2747

Castellano M. et al., 2007, *ApJ*, 671, 1497

Cenarro A. J., Cardiel N., Gorgas J., Peletier R. F., Vazdekis A., Prada F., 2001, *MNRAS*, 326, 959

Cenarro A. J., Gorgas J., Vazdekis A., Cardiel N., Peletier R. F., 2003, *MNRAS*, 339, L12

Chabrier G., 2003, *PASP*, 115, 763

Chan J. C. C. et al., 2016, *MNRAS*, 458, 3181

Chan J. C. C. et al., 2018, *ApJ*, 856, 8

Cimatti A. et al., 2008, *A&A*, 482, 21

Cimatti A., Nipoti C., Cassata P., 2012, *MNRAS*, 422, L62

Clough S. A., Iacono M. J., Moncet J.-L., 1992, *JGR*, 97, 15

Clough S. A., Shephard M. W., Mlawer E. J., Delamere J. S., Iacono M. J., Cady-Pereira K., Boukabara S., Brown P. D., 2005, *JQSRT*, 91, 233

Cocato L., Morelli L., Corsini E. M., Buson L., Pizzella A., Vergani D., Bertola F., 2011, *MNRAS*, 412, L113

- Coccatto L., Morelli L., Pizzella A., Corsini E. M., Buson L. M., Dalla Bontà E., 2013, *A&A*, 549, A3
- Condon J. J., Cotton W. D., Greisen E. W., Yin Q. F., Perley R. A., Taylor G. B., Broderick J. J., 1998, *AJ*, 115, 1693
- Conroy C., 2013, *ARA&A*, 51, 393
- Conroy C., Gunn J. E., 2010, *ApJ*, 712, 833
- Conroy C., Gunn J. E., White M., 2009, *ApJ*, 699, 486
- Conroy C., van Dokkum P., 2012a, *ApJ*, 747, 69
- Conroy C., van Dokkum P. G., 2012b, *ApJ*, 760, 71
- Correa C. A., Wyithe J. S. B., Schaye J., Duffy A. R., 2015a, *MNRAS*, 450, 1514
- Correa C. A., Wyithe J. S. B., Schaye J., Duffy A. R., 2015b, *MNRAS*, 450, 1521
- Correa C. A., Wyithe J. S. B., Schaye J., Duffy A. R., 2015c, *MNRAS*, 452, 1217
- Couch W. J., Sharples R. M., 1987, *MNRAS*, 229, 423
- Culverhouse T. L. et al., 2010, *ApJL*, 723, L78
- Daddi E. et al., 2010, *ApJ*, 713, 686
- Daddi E. et al., 2005, *ApJ*, 626, 680
- Damjanov I. et al., 2009, *ApJ*, 695, 101
- Darvish B., Mobasher B., Sobral D., Rettura A., Scoville N., Faisst A., Capak P., 2016, *ApJ*, 825, 113
- Davies R. I. et al., 2013, *A&A*, 558, A56
- Davies R. L. et al., 2015, in *IAU Symposium*, Vol. 311, *Galaxy Masses as Constraints of Formation Models*, Cappellari M., Courteau S., eds., pp. 110–115
- Davies R. L. et al., 2001, *ApJL*, 548, L33
- De Lucia G., Blaizot J., 2007, *MNRAS*, 375, 2
- de Zeeuw P. T. et al., 2002, *MNRAS*, 329, 513

Dekel A., Birnboim Y., 2006, MNRAS, 368, 2

Dekel A. et al., 2009, Nature, 457, 451

Dekel A., Burkert A., 2014, MNRAS, 438, 1870

Dekel A., Sari R., Ceverino D., 2009, ApJ, 703, 785

Delaye L. et al., 2014, MNRAS, 441, 203

Deustua S., 2016, WFC3 Data Handbook, Version 3.0. (Baltimore, MD: STScI)

Djorgovski S., Davis M., 1987, ApJ, 313, 59

Dressel L., 2017, Wide Field Camera 3 Instrument Handbook, Version 9.0. (Baltimore, MD: STScI)

Dressler A., 1980, ApJ, 236, 351

Dressler A., 2004, Carnegie Observatories Astrophysics Series, Vol. 3, Star-Forming Galaxies in Clusters, Mulchaey J. S., Dressler A., Oemler A., eds. (Cambridge University Press), p. 206

Dressler A., Gunn J. E., 1983, ApJ, 270, 7

Dressler A., Gunn J. E., 1990, in Astronomical Society of the Pacific Conference Series, Vol. 10, Evolution of the Universe of Galaxies, Kron R. G., ed., pp. 200–208

Dressler A., Lynden-Bell D., Burstein D., Davies R. L., Faber S. M., Terlevich R., Wegner G., 1987, ApJ, 313, 42

Dressler A. et al., 1997, ApJ, 490, 577

Dreyer J. L. E., 1888, MmRAS, 49, 1

Dreyer J. L. E., 1895, MmRAS, 51, 185

Driver S. P. et al., 2009, Astronomy and Geophysics, 50, 5.12

Dye S. et al., 2006, MNRAS, 372, 1227

Efstathiou G., Ellis R. S., Carter D., 1980, MNRAS, 193, 931

Efstathiou G., Ellis R. S., Carter D., 1982, MNRAS, 201, 975

Efstathiou G., Gorgas J., 1985, MNRAS, 215, 37P

Eggen O. J., Lynden-Bell D., Sandage A. R., 1962, ApJ, 136, 748

Ekers R. D. et al., 1989, MNRAS, 236, 737

Ellis R. S., Smail I., Dressler A., Couch W. J., Oemler, Jr. A., Butcher H., Sharples R. M., 1997, ApJ, 483, 582

Elmegreen B. G., Burkert A., 2010, ApJ, 712, 294

Elmegreen D. M., Elmegreen B. G., Ravindranath S., Coe D. A., 2007, ApJ, 658, 763

Emsellem E. et al., 2011, MNRAS, 414, 888

Emsellem E. et al., 2007, MNRAS, 379, 401

Emsellem E. et al., 2004, MNRAS, 352, 721

Fabbiano G. et al., 2003, ApJ, 588, 175

Faber S. M., French H. B., 1980, ApJ, 235, 405

Faber S. M., Jackson R. E., 1976, ApJ, 204, 668

Faber S. M. et al., 2007, ApJ, 665, 265

Falc3n-Barroso J., S3nchez-Bl3zquez P., Vazdekis A., Ricciardelli E., Cardiel N., Cenarro A. J., Gorgas J., Peletier R. F., 2011, A&A, 532, A95

Fan L., Lapi A., Bressan A., Bernardi M., De Zotti G., Danese L., 2010, ApJ, 718, 1460

Fan L., Lapi A., De Zotti G., Danese L., 2008, ApJL, 689, L101

Fan X., Carilli C. L., Keating B., 2006, ARA&A, 44, 415

Feldmann R., Carollo C. M., Mayer L., 2011, ApJ, 736, 88

Felten J. E., Gould R. J., Stein W. A., Woolf N. J., 1966, ApJ, 146, 955

Ferrarese L. et al., 2006, ApJL, 644, L21

Ferrarese L., Merritt D., 2000, ApJL, 539, L9

Ferrarese L., van den Bosch F. C., Ford H. C., Jaffe W., O'Connell R. W., 1994, AJ, 108, 1598

Finoguenov A. et al., 2015, A&A, 576, A130

Forbes D. A., Reitzel D. B., Williger G. M., 1995, AJ, 109, 1576

Forbes J. C., Krumholz M. R., Burkert A., Dekel A., 2014, MNRAS, 438, 1552

Franx M., Illingworth G., Heckman T., 1989, ApJ, 344, 613

Franx M., Illingworth G. D., 1988, ApJL, 327, L55

Fruchter A. S., Hook R. N., 2002, PASP, 114, 144

Fujita Y., 2004, PASJ, 56, 29

Gabor J. M., Davé R., 2015, MNRAS, 447, 374

Gammie C. F., 2001, ApJ, 553, 174

Gardner J. P. et al., 2006, SSR, 123, 485

Gavazzi G., Fumagalli M., Cucciati O., Boselli A., 2010, A&A, 517, A73

Gebhardt K. et al., 2003, ApJ, 597, 239

Genzel R. et al., 2008, ApJ, 687, 59

Genzel R. et al., 2006, Nature, 442, 786

Gerhard O. E., 1993, MNRAS, 265, 213

Giavalisco M. et al., 2004, ApJL, 600, L93

Gilbank D. G., Gladders M. D., Yee H. K. C., Hsieh B. C., 2011, AJ, 141, 94

Gilbank D. G., Yee H. K. C., Ellingson E., Gladders M. D., Barrientos L. F., Blindert K., 2007, AJ, 134, 282

Gladders M. D., Yee H. K. C., 2000, AJ, 120, 2148

Gladders M. D., Yee H. K. C., 2005, ApJS, 157, 1

Gobat R. et al., 2011, A&A, 526, A133

Gobat R. et al., 2013, ApJ, 776, 9

Gonzaga S., Hack W., Fruchter A., Mack J., 2012, The DrizzlePac Handbook. (Baltimore, MD: STScI)

Gorgas J., Efstathiou G., Aragon Salamanca A., 1990, MNRAS, 245, 217

Graham A., Lauer T. R., Colless M., Postman M., 1996, ApJ, 465, 534

Grützbauch R., Bauer A. E., Jørgensen I., Varela J., 2012, MNRAS, 423, 3652

Gunn J. E., Gott, III J. R., 1972, ApJ, 176, 1

Gustafsson B., Edvardsson B., Eriksson K., Jørgensen U. G., Nordlund Å., Plez B., 2008, A&A, 486, 951

Haiman Z., Mohr J. J., Holder G. P., 2001, ApJ, 553, 545

Hatch N. A., Kurk J. D., Pentericci L., Venemans B. P., Kuiper E., Miley G. K., Röttgering H. J. A., 2011, MNRAS, 415, 2993

Häußler B. et al., 2013, MNRAS, 430, 330

Häußler B. et al., 2007, ApJS, 172, 615

Hayashi M., Kodama T., Koyama Y., Tadaki K.-I., Tanaka I., 2011, MNRAS, 415, 2670

Hayashi M. et al., 2014, MNRAS, 439, 2571

Hayashi M., Kodama T., Koyama Y., Tanaka I., Shimasaku K., Okamura S., 2010, MNRAS, 402, 1980

Heavens A., Panter B., Jimenez R., Dunlop J., 2004, Nature, 428, 625

Hill A. R., Muzzin A., Franx M., van de Sande J., 2016, ApJ, 819, 74

Hilton M. et al., 2007, ApJ, 670, 1000

Hilton M. et al., 2010, ApJ, 718, 133

Hilton M. et al., 2009, ApJ, 697, 436

Hilz M., Naab T., Ostriker J. P., 2013, MNRAS, 429, 2924

Ho L. C., Li Z.-Y., Barth A. J., Seigar M. S., Peng C. Y., 2011, ApJS, 197, 21

Hoffman L., Cox T. J., Dutta S., Hernquist L., 2010, ApJ, 723, 818

Hogg D. W., 1999, ArXiv Astrophysics e-prints

Hogg D. W., Baldry I. K., Blanton M. R., Eisenstein D. J., 2002, ArXiv Astrophysics e-prints

Holden B. P., Stanford S. A., Eisenhardt P., Dickinson M., 2004, AJ, 127, 2484

Holden B. P., van der Wel A., Kelson D. D., Franx M., Illingworth G. D., 2010, ApJ, 724, 714

Hopkins P. F., Bundy K., Murray N., Quataert E., Lauer T. R., Ma C.-P., 2009, MNRAS, 398, 898

Hopkins P. F., Hernquist L., Cox T. J., Di Matteo T., Robertson B., Springel V., 2006a, ApJS, 163, 1

Hopkins P. F., Kereš D., Oñorbe J., Faucher-Giguère C.-A., Quataert E., Murray N., Bullock J. S., 2014, MNRAS, 445, 581

Horne K., 1986, PASP, 98, 609

Houghton R. C. W., Davies R. L., Dalla Bontà E., Masters R., 2012, MNRAS, 423, 256

Hoyle F., Fowler W. A., 1963, Nature, 197, 533

Huang S., Ho L. C., Peng C. Y., Li Z.-Y., Barth A. J., 2016, ApJ, 821, 114

Hubble E., Humason M. L., 1931, ApJ, 74, 43

Hubble E. P., 1922, ApJ, 56, 162

Hubble E. P., 1926, Contributions from the Mount Wilson Observatory / Carnegie Institution of Washington, 324, 1

Huchra J. P., Geller M. J., 1982, ApJ, 257, 423

Irgens R. J., Lilje P. B., Dahle H., Maddox S. J., 2002, ApJ, 579, 227

Jedrzejewski R., Schechter P. L., 1988, ApJL, 330, L87

- Jee M. J. et al., 2011, ApJ, 737, 59
- Johansson P. H., Naab T., Ostriker J. P., 2012, ApJ, 754, 115
- Johnston E. J., Merrifield M. R., Aragón-Salamanca A., Cappellari M., 2013, MNRAS, 428, 1296
- Jørgensen I., Bergmann M., Davies R., Barr J., Takamiya M., Crampton D., 2005, AJ, 129, 1249
- Jørgensen I., Chiboucas K., Flint K., Bergmann M., Barr J., Davies R., 2006, ApJL, 639, L9
- Jørgensen I., Franx M., Hjorth J., van Dokkum P. G., 1999, MNRAS, 308, 833
- Jørgensen I., Franx M., Kjaergaard P., 1996, MNRAS, 280, 167
- Kausch W. et al., 2015, A&A, 576, A78
- Kereš D., Katz N., Fardal M., Davé R., Weinberg D. H., 2009, MNRAS, 395, 160
- Kereš D., Katz N., Weinberg D. H., Davé R., 2005, MNRAS, 363, 2
- Kneib J.-P., Natarajan P., 2011, ARA&A, 19, 47
- Koekemoer A. M. et al., 2011, ApJS, 197, 36
- Koekemoer A. M., Fruchter A. S., Hook R. N., Hack W., 2002, The 2002 HST Calibration Workshop: Hubble after the Installation of the ACS and the NICMOS Cooling System, Arribas S., Koekemoer A., Whitmore B., eds. (Baltimore, MD: STScI), p. 337
- Kormendy J., 1977, ApJ, 218, 333
- Kormendy J., 1984, ApJ, 287, 577
- Kormendy J., 1989, ApJL, 342, L63
- Kormendy J., Fisher D. B., Cornell M. E., Bender R., 2009, ApJS, 182, 216
- Kormendy J., Ho L. C., 2013, ARA&A, 51, 511
- Kormendy J., Sanders D. B., 1992, ApJL, 390, L53
- Krajinović D. et al., 2008, MNRAS, 390, 93

Krajinović D. et al., 2011, MNRAS, 414, 2923

Krajinović D., Jaffe W., 2002, A&A, 390, 423

Krajinović D. et al., 2013, MNRAS, 433, 2812

Krajinović D. et al., 2015, MNRAS, 452, 2

Kriek M. et al., 2016, Nature, 540, 248

Kriek M., van Dokkum P. G., Labbé I., Franx M., Illingworth G. D., Marchesini D., Quadri R. F., 2009, ApJ, 700, 221

Kron R. G., 1980, ApJS, 43, 305

Kronberger T., Kapferer W., Ferrari C., Unterguggenberger S., Schindler S., 2008, A&A, 481, 337

Kroupa P., 2001, MNRAS, 322, 231

Krumholz M., Burkert A., 2010, ApJ, 724, 895

Kuntschner H. et al., 2010, MNRAS, 408, 97

Kurk J. et al., 2013, A&A, 549, A63

Kurk J. et al., 2009, A&A, 504, 331

La Barbera F., Ferreras I., Vazdekis A., de la Rosa I. G., de Carvalho R. R., Trevisan M., Falcón-Barroso J., Ricciardelli E., 2013, MNRAS, 433, 3017

La Barbera F., Vazdekis A., Ferreras I., Pasquali A., Cappellari M., Martín-Navarro I., Schönebeck F., Falcón-Barroso J., 2016, MNRAS, 457, 1468

Lackner C. N., Cen R., Ostriker J. P., Joung M. R., 2012, MNRAS, 425, 641

Lani C. et al., 2013, MNRAS, 435, 207

Larson R. B., 1974, MNRAS, 166, 585

Larson R. B., Tinsley B. M., Caldwell C. N., 1980, ApJ, 237, 692

Läscher R., Ferrarese L., van de Ven G., 2014, ApJ, 780, 69

Lauer T. R., 2012, ApJ, 759, 64

Lauer T. R. et al., 1995, *AJ*, 110, 2622

Lawrence A. et al., 2007, *MNRAS*, 379, 1599

Leavitt H. S., 1908, *Annals of Harvard College Observatory*, 60, 87

Lidman C. et al., 2008, *A&A*, 489, 981

Limber D. N., Mathews W. G., 1960, *ApJ*, 132, 286

Łokas E. L., Mamon G. A., 2003, *MNRAS*, 343, 401

Longhetti M. et al., 2005, *MNRAS*, 361, 897

Lonsdale C. J. et al., 2003, *PASP*, 115, 897

Lotz J. M. et al., 2013, *ApJ*, 773, 154

Lynden-Bell D., 1969, *Nature*, 223, 690

Lynden-Bell D., 1978, *Phys. Scr.*, 17, 185

Lynden-Bell D., Rees M. J., 1971, *MNRAS*, 152, 461

Ma C.-J. et al., 2015, *ApJ*, 806, 257

Madau P., Dickinson M., 2014, *ARA&A*, 52, 415

Madau P., Ferguson H. C., Dickinson M. E., Giavalisco M., Steidel C. C., Fruchter A., 1996, *MNRAS*, 283, 1388

Mahdavi A., Trentham N., Tully R. B., 2005, *AJ*, 130, 1502

Malin D. F., 1985, in *Lecture Notes in Physics*, Berlin Springer Verlag, Vol. 232, *New Aspects of Galaxy Photometry*, Nieto J.-L., ed., pp. 27–32

Malin D. F., Carter D., 1980, *Nature*, 285, 643

Mancone C. L., Gonzalez A. H., 2012, *PASP*, 124, 606

Maraston C., 2005, *MNRAS*, 362, 799

Maraston C. et al., 2013, *MNRAS*, 435, 2764

Maraston C., Strömbäck G., 2011, *MNRAS*, 418, 2785

- Martín-Navarro I., Barbera F. L., Vazdekis A., Falcón-Barroso J., Ferreras I., 2015a, MNRAS, 447, 1033
- Martín-Navarro I., La Barbera F., Vazdekis A., Ferré-Mateu A., Trujillo I., Beasley M. A., 2015b, MNRAS, 451, 1081
- McConnell N. J., Lu J. R., Mann A. W., 2016, ApJ, 821, 39
- McDermid R. M. et al., 2015, MNRAS, 448, 3484
- McDermid R. M. et al., 2006, MNRAS, 373, 906
- Mehlert D., Saglia R. P., Bender R., Wegner G., 1998, A&A, 332, 33
- Mendel J. T. et al., 2018a, in prep., ApJ
- Mendel J. T. et al., 2018b, in prep., ApJ
- Mendel J. T. et al., 2015, ApJL, 804, L4
- Meyers J. et al., 2012, ApJ, 750, 1
- Mihos J. C., 2004, Carnegie Observatories Astrophysics Series, Vol. 3, Interactions and Mergers of Cluster Galaxies, Mulchaey J. S., Dressler A., Oemler A., eds. (Cambridge University Press), p. 277
- Mihos J. C., Hernquist L., 1996, ApJ, 464, 641
- Milosavljević M., Merritt D., 2001, ApJ, 563, 34
- Mo H., van den Bosch F. C., White S., 2010, Galaxy Formation and Evolution
- Mok A. et al., 2013, MNRAS, 431, 1090
- Moody C. E., Romanowsky A. J., Cox T. J., Novak G. S., Primack J. R., 2014, MNRAS, 444, 1475
- Moore B., Katz N., Lake G., Dressler A., Oemler A., 1996, Nature, 379, 613
- Moorwood A., 2006, in SPIE, Vol. 6269, Society of Photo-Optical Instrumentation Engineers (SPIE) Conference Series, McLean I. S. Iye M., ed.
- Mullis C. R., Rosati P., Lamer G., Böhringer H., Schwobe A., Schuecker P., Fassbender R., 2005, ApJL, 623, L85

Munari U., Sordo R., Castelli F., Zwitter T., 2005, *A&A*, 442, 1127

Muzzin A., van Dokkum P., Franx M., Marchesini D., Kriek M., Labbé I., 2009, *ApJL*, 706, L188

Muzzin A., Wilson G., Demarco R., Lidman C., Nantais J., Hoekstra H., Yee H. K. C., Rettura A., 2013, *ApJ*, 767, 39

Naab T., Johansson P. H., Ostriker J. P., 2009, *ApJL*, 699, L178

Naab T., Johansson P. H., Ostriker J. P., Efstathiou G., 2007, *ApJ*, 658, 710

Nantais J. B. et al., 2017, *MNRAS*, 465, L104

Nelan J. E., Smith R. J., Hudson M. J., Wegner G. A., Lucey J. R., Moore S. A. W., Quinney S. J., Suntzeff N. B., 2005, *ApJ*, 632, 137

Nelson E. et al., 2014, *Nature*, 513, 394

Newman A. B., Belli S., Ellis R. S., 2015, *ApJL*, 813, L7

Newman A. B., Ellis R. S., Andreon S., Treu T., Raichoor A., Trinchieri G., 2014, *ApJ*, 788, 51

Newman A. B., Ellis R. S., Bundy K., Treu T., 2012, *ApJ*, 746, 162

Newman A. B., Ellis R. S., Treu T., Bundy K., 2010, *ApJL*, 717, L103

Oke J. B., Gunn J. E., 1983, *ApJ*, 266, 713

Oldham L. J., Houghton R. C. W., Davies R. L., 2017, *MNRAS*, 465, 2101

Onodera M. et al., 2010, *ApJL*, 715, L6

Oser L., Ostriker J. P., Naab T., Johansson P. H., Burkert A., 2010, *ApJ*, 725, 2312

Ostriker J. P., 1980, *Comments on Astrophysics*, 8, 177

Overzier R. A., 2016, *A&ARv*, 24, 14

Papovich C. et al., 2010, *ApJ*, 716, 1503

Patel S. G. et al., 2013, *ApJ*, 766, 15

Paturel G. et al., 1997, *A&AS*, 124, 109

Peng C. Y., Ho L. C., Impey C. D., Rix H.-W., 2002, *AJ*, 124, 266

Peng C. Y., Ho L. C., Impey C. D., Rix H.-W., 2010, *AJ*, 139, 2097

Phillips M. M., Jenkins C. R., Dopita M. A., Sadler E. M., Binette L., 1986a, *AJ*, 92, 503

Phillips M. M., Jenkins C. R., Dopita M. A., Sadler E. M., Binette L., 1986b, *AJ*, 91, 1062

Pietrinferni A., Cassisi S., Salaris M., Castelli F., 2004, *ApJ*, 612, 168

Piffaretti R., Arnaud M., Pratt G. W., Pointecouteau E., Melin J.-B., 2011, *A&A*, 534, A109

Planck Collaboration et al., 2016a, *A&A*, 594, A27

Planck Collaboration et al., 2016b, *A&A*, 594, A13

Poggianti B. M., Moretti A., Calvi R., D’Onofrio M., Valentinuzzi T., Fritz J., Renzini A., 2013, *ApJ*, 777, 125

Poggianti B. M., Smail I., Dressler A., Couch W. J., Barger A. J., Butcher H., Ellis R. S., Oemler, Jr. A., 1999, *ApJ*, 518, 576

Postman M. et al., 2005, *ApJ*, 623, 721

Prandoni I., Laing R. A., de Ruiter H. R., Parma P., 2012, in *Journal of Physics Conference Series*, Vol. 372, *Journal of Physics Conference Series*

Press W. H., Schechter P., 1974, *ApJ*, 187, 425

Prichard L. J. et al., 2017b, *ApJ*, 850, 203

Prugniel P., Soubiran C., 2001, *A&A*, 369, 1048

Prugniel P., Soubiran C., Koleva M., Le Borgne D., 2007, *ArXiv Astrophysics e-prints*

Quadri R. F., Williams R. J., Franx M., Hildebrandt H., 2012, *ApJ*, 744, 88

Ragone-Figueroa C., Granato G. L., 2011, *MNRAS*, 414, 3690

Renzini A., 2006, *ARA&A*, 44, 141

Rix H.-W., Franx M., Fisher D., Illingworth G., 1992, *ApJL*, 400, L5

Roeser S., Demleitner M., Schilbach E., 2010, *AJ*, 139, 2440

Rosati P. et al., 2009, *A&A*, 508, 583

Rubin V. C., Graham J. A., Kenney J. D. P., 1992, *ApJL*, 394, L9

Rusli S. P., Erwin P., Saglia R. P., Thomas J., Fabricius M., Bender R., Nowak N., 2013, *AJ*, 146, 160

Saglia R. P. et al., 2016, *ApJ*, 818, 47

Saglia R. P. et al., 2010, *A&A*, 524, A6

Salpeter E. E., 1955, *ApJ*, 121, 161

Salpeter E. E., 1964, *ApJ*, 140, 796

Samurović S., Danziger I. J., 2005, *MNRAS*, 363, 769

Sánchez-Blázquez P. et al., 2009, *A&A*, 499, 47

Sánchez-Blázquez P. et al., 2006, *MNRAS*, 371, 703

Santos J. S. et al., 2011, *A&A*, 531, L15

Saponara J., Koribalski B. S., Benaglia P., Fernández López M., 2018, *MNRAS*, 473, 3358

Sarzi M., Spiniello C., La Barbera F., Krajnović D., van den Bosch R., 2017, *ArXiv e-prints*

Schiavon R. P., Barbuy B., Bruzual A. G., 2000, *ApJ*, 532, 453

Schiavon R. P., Barbuy B., Rossi S. C. F., Milone, A., 1997, *ApJ*, 479, 902

Schiavon R. P., Barbuy B., Singh P. D., 1997, *ApJ*, 484, 499

Schlafly E. F., Finkbeiner D. P., 2011, *ApJ*, 737, 103

Schlegel D. J., Finkbeiner D. P., Davis M., 1998, *ApJ*, 500, 525

Schwarzschild M., 1979, *ApJ*, 232, 236

Schwarzschild M., 1982, *ApJ*, 263, 599

Serra P. et al., 2015, *MNRAS*, 452, 2680

Serra P., Oosterloo T. A., 2010, MNRAS, 401, L29

Sérsic J. L., 1963, Boletin de la Asociacion Argentina de Astronomia La Plata Argentina, 6, 41

Sharples R. et al., 2013, The Messenger, 151, 21

Slee O. B., Sadler E. M., Reynolds J. E., Ekers R. D., 1994, MNRAS, 269, 928

Smette A. et al., 2015, A&A, 576, A77

Smith R. J., Lucey J. R., 2013, MNRAS, 434, 1964

Smith R. J., Lucey J. R., Conroy C., 2015, MNRAS, 449, 3441

Smith R. J., Lucey J. R., Price J., Hudson M. J., Phillipps S., 2012, MNRAS, 419, 3167

Sparks W. B., Wall J. V., Thorne D. J., Jordan P. R., van Breda I. G., Rudd P. J., Jorgensen H. E., 1985, MNRAS, 217, 87

Springel V., 2005, MNRAS, 364, 1105

Stanford S. A. et al., 2012, ApJ, 753, 164

Stanford S. A., Eisenhardt P. R., Dickinson M., 1998, ApJ, 492, 461

Stanford S. A. et al., 2006, ApJL, 646, L13

Statler T. S., 1987, ApJ, 321, 113

Statler T. S., 1991, ApJL, 382, L11

Stott J. P., Collins C. A., Burke C., Hamilton-Morris V., Smith G. P., 2011, MNRAS, 414, 445

Stott J. P. et al., 2010, ApJ, 718, 23

Stott J. P. et al., 2016, MNRAS, 457, 1888

Strazzullo V. et al., 2013, ApJ, 772, 118

Strazzullo V. et al., 2010, A&A, 524, A17

Sunyaev R. A., Zeldovich Y. B., 1972, Comments on Astrophysics and Space Physics, 4, 173

- Surma P., Bender R., 1995, *A&A*, 298, 405
- Tanaka M., Finoguenov A., Ueda Y., 2010, *ApJL*, 716, L152
- Tanaka M. et al., 2013, *ApJ*, 772, 113
- Terrazas B. A., Bell E. F., Woo J., Henriques B. M. B., 2017, *ApJ*, 844, 170
- Thomas D., Maraston C., Bender R., 2003, *MNRAS*, 339, 897
- Thomas D., Maraston C., Bender R., Mendes de Oliveira C., 2005, *ApJ*, 621, 673
- Thomas D., Maraston C., Johansson J., 2011, *MNRAS*, 412, 2183
- Thomas D., Maraston C., Korn A., 2004, *MNRAS*, 351, L19
- Thomas D., Maraston C., Schawinski K., Sarzi M., Silk J., 2010, *MNRAS*, 404, 1775
- Tingay S. J., Edwards P. G., 2015, *MNRAS*, 448, 252
- Toft S., Gallazzi A., Zirm A., Wold M., Zibetti S., Grillo C., Man A., 2012, *ApJ*, 754, 3
- Toft S. et al., 2017, *Nature*, 546, 510
- Tokunaga A. T., Vacca W. D., 2005, *PASP*, 117, 421
- Toomre A., 1977, in *Evolution of Galaxies and Stellar Populations*, Tinsley B. M., Larson D. Campbell R. B. G., eds., p. 401
- Toomre A., Toomre J., 1972, *ApJ*, 178, 623
- Tran H. D., Tsvetanov Z., Ford H. C., Davies J., Jaffe W., van den Bosch F. C., Rest A., 2001, *AJ*, 121, 2928
- Tremaine S., 1981, in *Structure and Evolution of Normal Galaxies*, Fall S. M., Lynden-Bell D., eds., pp. 67–84
- Treu T., Auger M. W., Koopmans L. V. E., Gavazzi R., Marshall P. J., Bolton A. S., 2010, *ApJ*, 709, 1195
- Treu T., Ellis R. S., Liao T. X., van Dokkum P. G., 2005, *ApJL*, 622, L5
- Trujillo I., Conselice C. J., Bundy K., Cooper M. C., Eisenhardt P., Ellis R. S., 2007, *MNRAS*, 382, 109

Trujillo I., Ferreras I., de La Rosa I. G., 2011, MNRAS, 415, 3903

Trujillo I. et al., 2006a, MNRAS, 373, L36

Trujillo I. et al., 2006b, ApJ, 650, 18

Tsatsi A., Macciò A. V., van de Ven G., Moster B. P., 2015, ApJL, 802, L3

Tully R. B., Fisher J. R., 1977, A&A, 54, 661

Vaddi S., O’Dea C. P., Baum S. A., Whitmore S., Ahmed R., Pierce K., Leary S., 2016, ApJ, 818, 182

Valdes F., Gupta R., Rose J. A., Singh H. P., Bell D. J., 2004, ApJS, 152, 251

Valentinuzzi T. et al., 2010a, ApJ, 712, 226

Valentinuzzi T. et al., 2010b, ApJL, 721, L19

van de Sande J., Kriek M., Franx M., Bezanson R., van Dokkum P. G., 2014, ApJL, 793, L31

van de Sande J. et al., 2013, ApJ, 771, 85

van den Bosch R. C. E., van de Ven G., Verolme E. K., Cappellari M., de Zeeuw P. T., 2008, MNRAS, 385, 647

van der Marel R. P., Franx M., 1993, ApJ, 407, 525

van der Wel A., Franx M., van Dokkum P. G., Rix H.-W., Illingworth G. D., Rosati P., 2005, ApJ, 631, 145

van der Wel A. et al., 2014, ApJ, 788, 28

van der Wel A., Holden B. P., Zirm A. W., Franx M., Rettura A., Illingworth G. D., Ford H. C., 2008, ApJ, 688, 48

van Dokkum P., Conroy C., Villaume A., Brodie J., Romanowsky A. J., 2017, ApJ, 841, 68

van Dokkum P. G., Conroy C., 2010, Nature, 468, 940

van Dokkum P. G., Conroy C., 2011, ApJL, 735, L13

van Dokkum P. G., Ellis R. S., 2003, ApJL, 592, L53

van Dokkum P. G., Franx M., 1995, AJ, 110, 2027

van Dokkum P. G., Franx M., 1996, MNRAS, 281, 985

van Dokkum P. G., Franx M., 2001, ApJ, 553, 90

van Dokkum P. G. et al., 2008, ApJL, 677, L5

van Dokkum P. G., Kriek M., Franx M., 2009, Nature, 460, 717

van Dokkum P. G. et al., 2015, ApJ, 813, 23

van Dokkum P. G., van der Marel R. P., 2007, ApJ, 655, 30

van Dokkum P. G. et al., 2010, ApJ, 709, 1018

Vaughan S. P., Davies R. L., Zieleniewski S., Houghton R. C. W., 2018, MNRAS, 475, 1073

Vazdekis A., Casuso E., Peletier R. F., Beckman J. E., 1996, The Astrophysical Journal Supplement Series, 106, 307

Vazdekis A. et al., 2015, MNRAS, 449, 1177

Vazdekis A., Koleva M., Ricciardelli E., Röck B., Falcón-Barroso J., 2016, MNRAS, 463, 3409

Verdoes Kleijn G. A., van der Marel R. P., Carollo C. M., de Zeeuw P. T., 2000, AJ, 120, 1221

Vergani D., Pizzella A., Corsini E. M., van Driel W., Buson L. M., Dettmar R.-J., Bertola F., 2007, A&A, 463, 883

Wang T. et al., 2016, ApJ, 828, 56

Wegner M., Muschiok B., 2008, in SPIE, Vol. 7019, Advanced Software and Control for Astronomy II, p. 70190T

Whitaker K. E., Kriek M., van Dokkum P. G., Bezanson R., Brammer G., Franx M., Labbé I., 2012, ApJ, 745, 179

Whitaker K. E. et al., 2011, ApJ, 735, 86

Whitaker K. E. et al., 2013, ApJL, 770, L39

White S. D. M., Rees M. J., 1978, MNRAS, 183, 341

Wing R. F., Ford, Jr. W. K., 1969, PASP, 81, 527

Wisnioski E. et al., 2015, ApJ, 799, 209

Wu C. F. J., 1986, Ann. Statist., 14, 1261

Wuyts S., van Dokkum P. G., Kelson D. D., Franx M., Illingworth G. D., 2004, ApJ, 605, 677

Yuan F., Yu Z., Ho L. C., 2009, ApJ, 703, 1034

Zabludoff A. I., Mulchaey J. S., 1998, ApJ, 496, 39

Zehavi I. et al., 2005, ApJ, 630, 1

Zeimann G. R. et al., 2012, ApJ, 756, 115

Zel'dovich Y. B., 1964, Soviet Physics Doklady, 9, 195

Zieleniewski S., Houghton R. C. W., Thatte N., Davies R. L., 2015, MNRAS, 452, 597

Zieleniewski S., Houghton R. C. W., Thatte N., Davies R. L., Vaughan S. P., 2017, MNRAS, 465, 192

Zolotov A. et al., 2015, MNRAS, 450, 2327

Zwicky F., 1933, Helvetica Physica Acta, 6, 110

Zwicky F., 1937, ApJ, 86, 217

“No one tells you the truth about writing a book.... The truth is, writing is this: hard and boring and occasionally great but usually not. Writing this book has been like... hacking away at a freezer with a screw driver.... Honestly, I have moments when I don’t care if anyone reads this book. I just want to finish it. If you are reading this it means I have “finished”.”

— Amy Poehler, *Yes Please*, 2014